8TH MIDDLE EAST SIMULATION MULTICONFERENCE

MESM'2006

EDITED BY

Professor Marwan Al-Akaidi

AUGUST 28-30, 2006

Alexandria, Egypt

A Publication of

EUROSIS

8TH MIDDLE EAST SIMULATION MULTICONFERENCE

AUGUST 28-30, 2006

Organised by

ETI

Sponsored by

EUROSIS

De Montfort University

IEEE UKRI - SPC

Ghent University

EXECUTIVE EDITOR

PHILIPPE GERIL
(BELGIUM)

EDITORS

General Conference and Programme Chair

Professor Dr M. Al-Akaidi
De Montfort University,
Leicester, United Kingdom

INTERNATIONAL PROGRAMME COMMITTEE

Modelling Methodology and Modelling Tools
Jose Antonio Barata Oliveira, Universidade Nova de Lisboa, Caparica, Portugal
Fabrice Bernardi, Universite de Corse, Corte, France
Ana M. Camacho, UNED, Madrid, Spain
Frantisek Capkovic, Slovak Academy of Sciences, Bratislava , Slovak Republic
John Dalseng, Finnmark College, Alta, Norway
Juan de Lara, Universidad Autonama de Madrid, Madrid, Spain
Jesus Felez, Universidad Politecnica de Madrid, Madrid, Spain
Frederic Grimaud. Ecole Nat Superieure de Mines de St.Etienne, France
Helge Hagenauer, Universitaet Salzburg, Salzburg, Austria
Brian Hollocks, Bournemouth University, Bournemouth, United Kingdom
Bjoern Johansson, Chalmers University of Technology, Goteborg, Sweden
Panajotis T. Katsaros, Aristotle University Thessaloniki, Thessaloniki, Greece
Yan Luo, NIST, Gaithersburg, USA
Thomas O Mathuna, Cork Institute of Technology, Cork, Ireland
Michel Minoux, Universite P. et M. Curie-CNRS, Paris cedex 05, France
Tudor Niculiu, University Politecnica Bucharest, Bucharest, Romania
Marc Parenthoen, CERV, Plouzan, France
Zdravko Terze, University of Zagreb, Zagreb, Croatia
Dmitry Zaitsev, Odessa National Telecommunications Academy, Odessa, Ukraine

Analysis Methodology
Abdel Aitouche, Hautes Etudes Industrielles, Lille, France
Bruno Ciciani, Universita di Roma "La Sapienza", Rome, Italy
John Dalton, University of Newcastle, Newcastle-upon-Tyne, United Kingdom
Julie Dugdale, Universite Paul Sabatier, Narbonne, France
Mauro Iacono, SUN - II Universita di Napoli, Aversa (CE) Italy
Jens Kohlmeyer, Universitaet Ulm, Ulm, Germany
Francesco Moscato, Seconda Universita di Napoli, Aversa, Italy
Jairo R. Montoya-Torres, Ecole Nationale Superieure des Mines de Saint-Etienne, Gardanne, France
Nadia Zanzouri, ENIT, Tunis, Tunisia

Simulation of Networks and Communication
Salvatore D'Antonio, Consorzio Interuniversitario Nazionale per l'Informatica, Naples, Italy
Mahmoud Al-Qutayri, Etisalat University College, Sharjah, UAE
Med Salim Bouhlel, Sfax University, Sfax, Tunisia
Dirk Brade, FOI, Stockholm, Sweden
Eugen Dedu, LIFC, Montbelliard, France
Carlos Palau, UPV, Valencia, Spain
Rob Pooley, University of Edinburgh, Edinburgh, United Kingdom
Djamel Sadok, The Federal University of Pernambuco - Brazil
Ahmad A. Sharieh, University of Jordan, Amman, Jordan
Veronique Veque, Universite de Paris Sud LRI, Orsay, France

Complex Systems Simulation
Zdzislaw Bubnicki, Wroclaw University of Technology, Wroclaw, Poland
Marta Pla Castells, Universidad de Valencia, Valencia, Spain
Michele Colajanni, Unviersita di Modena, Modena, Italy
Krzysztof Fujarewicz, Silesian University of Technology, Gliwice, Poland
Tom Dhaene, University of Antwerp, Antwerp, Belgium
Alessandro Genco, University of Palermo, ICAR / CNR, Palermo, Italy
Jean-Christophe Guyot, EADS SPACE Transportation, Les Mureaux Cedex, France
Daniel Huber, Heinz Nixdorf Institute, University of Paderborn, Paderborn, Germany
Abder Koukam, Universite de Technologie de Belfort-Montbeliard, France
Jan Lemeire, VUB, Brussels, Belgium
Brian Mayoh, Aarhus University, Aarhus N, Denmark
Jorge M. Perez, ITP, S.Fernando de Hernares, Spain
Panos Periorellis, University of Newcastle Upon Tyne, Newcastle, United Kingdom
Fatima Rateb, University College London, London, United Kingdom
Marco Remondino, University of Turin, Turin, Italy
Marc Rouff, University of Caen Basse-Normandie, Caen, France
Jan Studzinski, Systems Research Institute of Polish Academy of Science

INTERNATIONAL PROGRAMME COMMITTEE

Simulation of Signal and Image Processing
Bruno Ciciani, Universita di Roma "La Sapienza", Rome, Italy
Aboul Ella Hassanine, Kuwait University, Safat, Kuwait
Tania Jimenez, Universidad de Los Andes, Merida, Venezuela
Viorel Nicolau, "Dunarea de Jos" University of Galati, Romania
Bogdan Raducanu, UAB, Cerdanyola, Spain
Renate Sitte, Griffith University, Gold Coast Mail Centre, Australia
Joao Manuel R. S. Tavares, University of Porto, Porto, Portugal
Hanene Trichili, University of Sfax, Sfax, Tunisia
Ahmed M. Zeki, International Islamic University Malaysia (IIUM), Kuala Lumpur, Malaysia

Energy Systems Simulation
Paulo Maciel, UFPE, Recife, Brazil
Musleh B. AL-Otaibi, Alahmadi, Kuwait
Ahmad Jammal, Ministry of Education & Higher Education, Beirut, Lebanon
Janos Sebestyen Janosy, KFKI, Budapest, Hungary
Carlos Ramos, Polytechnic of Porto (ISEP/IPP), Porto, Portugal
Tzanko Tzanov, Technical University of Sofia, Sofia, Bulgaria
Patrick Wager, EMPA, St. Gallen, Switzerland

Simulation in the Chemical and Petrochemical Industry
Ammar Al Khani, Espoo, Finland
Diganta Bhusan Das, University of Oxford, Oxford, United Kingdom
Eugenio Ferreira, Universidade do Minho, Braga Portugal
Vahid Nassehi, Loughborough University, Loughborough, United Kingdom
Mohammad Al-Nawafleh, Tafila Applied University College, Al-Balqa' Applied University, Tafila, Jordan
Cornel Resteanu, Research Institute of Informatics, Bucharest, Romania
M R Riazi, Kuwait University, Safat, Kuwait

Multimedia and Virtual Reality Systems
Ahmed Bin Subaih, University of Sheffield, Sheffield, United Kingdom
Christos Bouras, University of Patras, Rion, Patras, Greece
Eckhard C. Bollow, Software Technology and IT-Project Management, Lueneburg, Germany
Richard Chbeir, Universite de Bourgogne, Dijon CEDEX FRANCE
Paule Ruiz del Puerto, University of Oviedo, Oviedo, Spain
Zhisheng Huang, Vrije University Amsterdam, The Netherlands
Christoph Laroque, University of Paderborn, Paderborn, Germany
Ahmed Mostefaoui , Laboratoire d'Informatique de Franche-Comte, Montbeliard Cedex, France
Dorin-Mircea Popovici, Centre Europeen de Realite Virtuelle, Plouzane, France
Christian Reimann, C-LAB, Paderborn, Germany
Marco Roccetti, University of Bologna, Bologna, Italy
Zasriati Azla Sabot, University Tun Abdul Razak (UNITAR) Selanngor, Malaysia
Mike Sips, University of Konstanz, Konstanz, Germany
Charles van der Mast, Delft University of Technology, Delft, The Netherlands

Decision Processing in Management
Hadhoum Boukachour, Le Havre University, Le Havre, France
Naoufel Cheikhrouhou, Ecole Polytechnique Federale de Lausanne, Lausanne, Switzerland
Joel Colloc, Le Havre University, Le Havre, France
Jeanne Schreurs, Universiteit Hasselt, Diepenbeek, Belgium
Christine Sybord, Lyon 2 Lumiere University, Lyon, France
Behrouz Zarei, Sharif University of Technology, Tehran, Iran

Modelling and Simulation in Biomedical Systems
Syed Afaq Husain, International Islamic University, Islamabad, Pakistan
Manuel Alfonseca, Escuela Politecnica Superior, Universidad Autonoma de Madrid, Madrid, Spain
Clemens Heitzinger, Arizona State University (ASU), USA
Manuel Gonzalez Hidalgo, Edf. Anselm Turmeda, Palma de Mallorca, Baleares, Spain
Tomislav Pribanic, University of Zagreb, Zagreb, Croatia
Oliver Straub, University of Ulm, Ulm, Germany
Jean-Pierre Thomesse, Institut National Polytechnique de Lorraine, Vandoeuvre Les Nancy, France
Olaf Tietje, Systaim GmbH, Zurich, Switzerland

Modelling and Simulation for Industrial Applications
Track Chair: Prof. David Stockton, de Montfort University, Leicester, United Kingdom
Luis Felipe Acebes Arconada, Universidad de Valladolid, Valladolid, Spain
Leopoldo Arnesto, UPV, Valencia, Spain
Andre Astolfi, Naval Academy Research Institute, Brest Naval, France
Michel Benne, Sucreries de Bois Rouge, Saint-Andre, France
Pascal Berruet, Universite Bretagne Sud, Lorient cedex, France
Christelle Bloch, Universite de Technologie de Belfort-Montbeliard, Belfort Cedex, France
PJ Byrne, Enterprise Research Centre, University of Limerick, Ireland
A. Chatzinikolaou, Bosch Rexroth SA, Athens, Greece
Olaf Diegel, Massey University, Albany Campus, North Shore Mail Centre, Auckland, New Zealand
S Collart Dutilleul, LAGIS-EC-LILLE, Villenneuve d'Ascq, France
Christoph Hartmann, The German University in Cairo, New Cairo City, Egypt
Sergej Kalaschnikow, VA TECH ELIN EBG Elektronik GmbH & Co, Vienna, Austria
Markus Koch, C-LAB, Paderborn, Germany
Habtom Mebrahtu, Anglia Polytechnica University, Chelmsford, United Kingdom
Pascal Meyer, Forschungszentrum Karlsruhe, Karlsruhe, Germany
Lars Moench, TU Ilmenau, Ilmenau, Germany

INTERNATIONAL PROGRAMME COMMITTEE

Carlos E. Pereira, Universidad Federal do Rio Grande Do Sul, Porto Alegre, Brazil
Caterina Rizzi, Universita degli Studi di Bergama, Dalmine, Italy
Amir Shirkhodaie, Tennessee State University, Nashville, USA
Hans Veeke, TU Delft, Delft, The Netherlands
Ramiro Velazquez, Universite Paris 6 - CNRS, Fontenay aux Roses, France
Val Vitanov, Cranfield University, Cranfield, United Kingdom
Ursula Wellen, Deutsche Post AG, Bonn, Germany
Joao de Silva Wellington, UFPE, Recife, Brazil

Simulation in Logistics, Traffic, Transport and Harbour Simulation
Paul Davidsson, Blekinge Institute of Technology, Ronneby, Sweden
Isabel Garcia Gutierrez, Universidad Carlos III de Madrid, Leganos, Madrid, Spain
Thomas Hanne, Fraunhofer-Institut ITWM, Kaiserslautern, Germany
Daniel Krajzewicz, GermanAerospace Centre, Berlin, Germany
Herve Manier, Universite de Technologie de Belfort-Montbeliard (UTBM), Belfort Cedex, France
Vittorio Maniezzo, Universita di Bologna, Bologna, Italy
Rafael J. Martinez, Universitat de Valencia, Valencia, Spain
Philippe Mussi, INRIA Sophia Antipolis, France Frederic Serin, IUT du Havre, Le Havre, France

Web based Simulation
Victor Bassilious, University of Abertay Dundee, United Kingdom
Jorge Marx Gomez, Otto-von-Guericke-Universitat Magdeburg, Magdeburg, Germany
Wolfgang Kuehn, University of Wuppertal Wuppertal, Germany
Jose Machado, Unviersidade do Minho, Braga Codex, Portugal
Mara Nikolaidou, University of Athens, Ilissia, Athens, Greece
Francesco Quaglia, Universita' di Roma "La Sapienza", Roma, Italy
Stefan Sarstedt, University of Ulm, Ulm, Germany
Jaroslav Sklenar, University of Malta, Msida, Malta
Alfonso Urquia,UNED, Madrid, Spain

Simulation in Information Processing
Julien Bourgeois, LIFC, Montbelliard, France
Christophe Claramunt, Naval Academy Research Institute, Brest Naval, France
Patrick De Causmaecker, University of Nottingham, Nottingham, United Kingdom
Khalil Drira, LAAS-CNRS, Toulouse Cedex 04, France
Laurent Guillon, Naval Academy Research Institute, Brest Naval, France
Jean-Claude Hochon, GFI Consulting, Toulouse, France
Majed Khodr, Manar University, Lebanon
Peter Lawrence, Monash University, Clayton, Australia
Christophe Roche, Universite de Savoie, Le Bourget du Lac cedex, France
Christian Siemers, TU Clausthal, Clausthal-Zellerfeld, Germany
Jim Torresen, University of Oslo, Oslo, Norway
Nagi Wakimm, Saint Esprit University, Beirut, Lebanon

Simulation in Fuzzy Systems, Neural Networks and Genetic Algorithms
Chrissanthi Angeli, Technological Education Institute of Piraeus, Athens, Greece
Ulrich Bodenhofer, Software Competence Center Hagenberg GmbH, Hagenberg, Austria
Sabine Bostelmann, TU Clausthal, Clausthal, Germany
Luc Boullart, Ghent University, Ghent, Belgium
Maroua Bouzid, University of Caen, Caen, France
Paulo Alexandre Ribeiro Cortez, University of Minho, Guimaraes, Portugal
Analacia Schiaffino Morales De Franceschi, ULBRA, Canoas - RS, Brazil
Rashidy Kanan, University of Amirkabir, Tehran, Iran
Nashat Mansour, Lebanese American University, Beirut, Lebanon
Seung Man Lee, NASA Ames Research Center, Moffett Field, USA
Antoni Ligeza, AGH - University of Science and Technology, Krakow, Poland
Marie-Ange Manier, Universite de Technologie de Belfort-Montbeliard (UTBM), Belfort Cedex, France
Paulo Moura Oliveira, UTAD-Universidade de Tres-os-Montes e Alto Douro, Vila Real, Portugal
S.Tauseef Ur Rehman, Pakistan
Kifah Tout, The Lebanese University, Beirut, Lebanon
Angus Wu, City University of Hong Kong, Hong Kong

Simulation in the Built Environment
Bernadette O'Regan, University of Limerick, Limerick, Ireland
Agustin Yague, Universidad Politicnica de Madrid, Madrid, Spain

Simulation in Archaeology
Jean Yves Blaise, UMR CNRS/MCC 694 MAP, Marseille, France
Anders Hast, University of Gavle, Gavle, Sweden
Wolfgang Kreutzer, University of Canterbury, Christchurch, New Zealand
Marcos A Rodrigues, Sheffield Hallam University, Sheffield , United Kingdom

Simulation Projects in the Arab World
Saleh Al-Jufout, Tafila Technical University, Tafila, Jordan
Mohamed-Aly O. Louly, University of Technology, Troyes, France

Local Arrangements Chairs
Dr. Ghada M. Amer, Higher Institute of Technology, Benha, Egypt
Prof. Kasim Al-Aubidy, Philadelphia University, Amman, Jordan

MESM’2006

EUROSIS is a Division of ETI Bvba, The European Technology Institute, Torhoutsesteenweg 162, Box 4, B-8400 Ostend, Belgium

Printed in Belgium by Reproduct NV, Ghent, Belgium
Cover Design by Grafisch Bedrijf Lammaing, Ostend, Belgium

EUROSIS-ETI Publication
ISBN: 90-77381-28-7

PREFACE

Dear conference delegate,

I have the pleasure to welcome you all to the 8th Middle Eastern Modeling & Simulation Multiconference (MESM2006) **Organized** by Eurosis and the European Technology Institute **Hosted** at the Mercure Romance Hotel in Alexandria Egypt.. The MESM2006 is **sponsored** by the IEEE – UKRI SPC & De Montfort University (UK).

We decided to run our 8th MESM06 in Alexandria and in particular in Egypt, based on the success of our previous conferences as the first one was MESM'99 (hosted by Jordan University) and MESM2000 (hosted by Philadelphia University) conferences. The MESM2000 already enjoyed greater renown as it was opened by H.R.H. Crown Prince AlHassan Ben Talal of Jordan.

Our aim is to bring people from various parts of the Middle East and Europe in contact with colleagues working in Modeling & Simulation from around the world.

Although a number of studies have found simulation & modeling to be one of the most practical and effective problem-solving techniques there is, however, little practical study literature available to guide those interested in the field. Modeling and Simulation make a powerful combination to improve the systems and organisations of the future.

The Conference highlights recent and significant advances in many research areas of modeling and simulation related to Methodology, Networks Communications, Signal & Image Processing, Biomedical Applications, Industrial Applications, Software Engineering, Neural Network, and Fuzzy Systems.

Your presence at this conference emphasizes an important fact: namely the challenge and opportunities that surround the Modeling and Simulation practices anywhere in the world. We in Eurosis believe strongly that Modeling & Simulation make a powerful combination to improve the systems and organisation of the 21st century. It will continue to contribute to increase public awareness of the quality of life, and show the growing need to improve this through better organizations and systems.

As a General Conference & Programme Chair, I would like to express my thanks to De Montfort University (UK) to give me the time to chair this conference and thanks also due to committee members for reviewing the papers and thanks due to our local chair Dr Ghada Amer of Benha University in organizing this event.

Thanks to my colleague Philippe Geril executive director of the Eurosis office for supporting the event and for his time.

Last but not least thanks to all authors without whom the conference would not be a successful conference.

I take this opportunity to express my wish that this conference will be an important step in our continuous efforts to establish the Eurosis chapter in the Middle East and get more people interested in Modeling & Simulation in the region. I wish you all of the success in reaching for that aim.

August / 2006

Professor Dr Marwan Al-Akaidi
General Conference and Programme Chair
Eurosis – M. East Chair
School of Engineering & Technology,
De Montfort University,
Leicester, LE 1 9BH, UK.
Email: mma@dmu.ac.uk

CONTENTS

CONTENTS

ELECTRONIC NETWORKS SIMULATION

ELECTRONIC APPLICATIONS SIMULATION

ELECTRONICS SIMULATION IN MEDICINE

MULTIMEDIA SIMULATION

SCICOS

CONTENTS

SCIENTIFIC PROGRAMME

SIMULATION METHODOLOGY

SOLVING STOCHASTIC PROJECT SELECTION PROBLEMS BY COMBINING SIMULATION AND NEIGHBORHOOD SEARCH

M. Minoux
University Paris 6,
4 Place Jussieu, 75005, Paris, France
E-mail : Michel.Minoux@lip6.fr

KEYWORDS
Operations Research models, Stochastic Decision models, Combined Simulation and Optimization, Neighborhood Search.

ABSTRACT

We consider a class of stochastic optimal project selection problems where a subset of a given set of projects has to be selected in order to satisfy various resource constraints, while maximizing expected return on investment (ROI).
We propose a solution approach combining neighborhood search on the (discrete) space of decision variables and simulation for finding good (near-optimal) solutions to instances of this class of problems. Computational results validating the approach are presented, and we conclude by mentioning a few possible directions for future research.

1 INTRODUCTION

We consider a class of stochastic optimal project selection problems where a subset of a given set of n projects has to be selected in order to:
- satisfy various resource constraints (there are m such constraints, numbered
  i=1,...m, corresponding e.g. to budget, available personnel, energetic resource, etc.) ;
- maximize expected return on investment (ROI).

For each project j = 1,...n, the return on investment b_j and the various quantities $a_{i,j}$ of resources necessary to carry out the project are assumed to be independent (though not necessarily identically distributed) continuous and bounded random variables with known distribution functions. Also, the quantities q_i of available resources of each type i are assumed to be independent (bounded) continuous random variables with known distribution functions. We also make the usual assumption of complete recourse by considering that, whenever needed, additional amounts of each of the resources considered can be obtained at some given (usually high) unit cost (for instance, when the budget constraint turns out to be slightly violated, it is realistic to assume that loans can be obtained at an interest rate depending on the current situation of the financial markets).

In section 2 we describe a heuristic solution approach to the optimal project selection problem combining neighborhood search on the (discrete) space of decision variables and simulation for finding good (near-optimal) solutions to instances of this class of problems. In section 3 we present the results of a number of computational experiments aimed at validating the proposed approach on a set of instances ranging from 15 projects and 3 resource constraints, to 20 projects and 3 resource constraints, under special assumptions enabling one to compute exact optimal solutions (for the sake of comparison).
We conclude section 3 by mentioning some relevant directions for future research.

2 APPROXIMATE SOLUTIONS VIA COMBINED SIMULATION AND NEIGHBORHOOD SEARCH

Obviously, solving a stochastic project selection problem as the one described above can be achieved by enumerating all $2^n - 1$ possible solutions, each time computing (by simulation) an estimate of the expected solution value. Assuming that a sufficiently large number of random samples is used in the simulation each time an estimate of the objective has to be computed (the right minimum number has to be determined on the basis of the usual estimate of std deviation) an optimal solution value, as close as desired to the exact (unknown) optimal solution value can be deduced. However such an approach would obviously not be practically feasible for large problems, typically involving a number of projects larger than 15 to 20. For such 'large' problems exact optimality is most likely out of reach, and we have to limit ourselves to finding *approximate solutions.*

For that purpose we propose here to use a neighborhood search technique which only requires to define, for each possible solution, the set of so-called neighboring solutions.

A natural way, in our context, to define the neighborhood N(x) of a solution $x \in \{0,1\}^n$ is to consider all the solutions x' such that $|x'-x|=1$ in the sense of the Hamming distance.
The algorithm proposed below combines the idea of applying neighborhood search with a 'best neighbor' strategy (at each step, move to the solution achieving the best objective function value in the neighborhood of the current solution), with the additional idea of performing multiple starts to better explore the solution space.

It makes repetitive use of the following basic procedure, denoted ***Search(x)***, which takes some solution x as starting

solution, and after carrying out a specified number of moves (the parameter *nmoves* is typically chosen between n/2 and n, in our experiments we took *nmoves=n/2*) outputs a new solution x1, taken to be the best solution encountered during the search. x1 may eventually be chosen as the starting point for a new application of the same procedure.
We note that such an approach is closely related to the so-called 'Variable Depth Search' heuristics (see e.g. Reeves 1993) and may be viewed as a variant of the Kernighan-Lin heuristic (see Kernighan & Lin, 1970).

Basic search procedure: x1 ← Search(x)

Set bestval = -∞ ;
for j=1 to n do
status[j] ←1; (the variables x_j such that status[j] =1 are the so-called 'free' variables, this indicates that their value may be changed – if profitable- ; each variable is allowed to change value only once, so status[j] is set to 0 as soon as the value of x_j has been changed)
endfor
for p = 1 to nmoves do
zmax ← -∞ ;
Let F(x) denote the set of indices i ($1 \le i \le n$) such that status[i] = 1 (the set of 'free' variables).

for all $j \in F(x)$ do :
define $y \in N(x)$ as the solution in the neighborhood of x such that :
$y_i = x_i \ \forall i \neq j$, and $y_j = 1-x_j$;
compute (using simulation) v the objective function value corresponding to y ;
If ($v > z_{max}$) then
set : $z_{max} \leftarrow v$;
$y_{max} \leftarrow y$;
$j_{max} \leftarrow j$;
endif
endfor

if(zmax > bestval) then
bestval ← zmax ;
x1 ← y_{max} ;
endif
x ← y_{max} ;
status[j_{max}] ← 0 ;
endfor

2 COMPUTATIONAL EXPERIMENTS

The computational results reported in Table 1 have been obtained by applying only 4 times , for each instance considered, the above neighborhood search procedure, starting with the solution [0, 0, ...0] , each additional round being initialized with the solution produced by the previous one. 15 instances of the stochastic project selection problem have been considered with sizes ranging from n=15, m=3 to n=20 , m=3. Each instance is described by specifying the mean values of the ROI coefficients b_j , the mean values of the technical coefficients $a_{i,j}$, and the values of the right handside coefficients c_i (assumed to be deterministic in the experiments). For each stochastic coefficient, the std. value heas been taken to be 0.1 times the mean value.

In order to be in a position to validate the proposed approach, we have assumed that each random coefficient has gaussian distribution (remember that the mean value is given and the std. equals 0.1 times the mean value). For each possible solution to the project selection problem, each component of the Ax vector is therefore a gaussian distribution with easily computable mean and std. ; observe that it can thus take any value on $]-\infty, +\infty[$ with nonzero probability. As a result, every solution has nonzero probability to be infeasible. To handle this situation, we decided to penalize infeasibilities by subtracting from the the objective function b.x a penalty term proportional to the expected value of the amount of constraint violation (in our experiments the weighting factor is taken to be equal to 100 for each constraint). Since, for each solution x, the left handside of each constraint is a gaussian distribution with known mean value and known std., the *exact* computation of the penalty term is easily carried out using the classical error function.
Table 1 displays :

(a) the exact optimal solution value to the deterministic version of each instance (i.e. the project selection problem in which each random coefficient is replaced by its mean value). These exact optimal values are obtained by complete enumeration of the 2^n solutions.
(b) The exact solution value to each instance of the stochastic problem (again these are obtained by complete enumeration of the 2^n solutions).
(c) The approximate solution value for the stochastic problem obtained by a single application of the Search(x) procedure, starting from the solution [0, 0, ...0].
(d) The best approximate solution value obtained by applying 4 rounds of the Search(x) procedure successively.
(e) The relative differences (in percents) between the exact values (b) and the best approximate solution values (d).
(f) The relative difference (in percents) between the optimal solution values of the deterministic version versus the stochastic version of each instance. This provides a measure of how much the stochastic version of the problem differs from its deterministic (averaged) version.

These results clearly confirm that the proposed combined neighborhood search / simulation algorithm leads to reasonably good solutions within reduced computing times (note that 4 applications of the Search(x) procedure with nmoves=n/2 only require $2n^2$ function evaluations) . Indeed column (e) of Table 1 shows that the solutions

Instance	(a) exact sol value (deterministic)	(b) exact sol value (stochastic)	(c) 1 round of Search(x)	(d) 4 rounds of Search(x)	(e) % difference (b) – (d)	(f) % difference (a) – (b)
P1 (15 x 3)	39	32.07	31	31	3.4%	21.6%
P2 (15 x 3)	74	66.97	65	66.97	0%	10.5%
P3 (15 x 3)	90	84.13	81.35	81.35	3.4%	6.9%
P4 (15 x 3)	58	52.96	46	50.99	3.8%	9.5%
P5 (15 x 3)	96	88.59	81.83	81.83	8.2%	8.3%
P6 (15 x 3)	85	76.08	68.75	69.21	9.9%	11.7%
P7 (15 x 3)	61	51.51	35	51.51	0%	18.4%
P8 (15 x 3)	59	49.49	46.82	47.49	4.2%	19.2%
P9 (15 x 4)	85	63.96	63.96	63.96	0%	32.8%
P10 (15 x 4)	78	70.98	70.98	70.98	0%	9.8%
P11 (18 x 3)	65	68.74	47.66	57.99	1.2%	10.6%
P12 (18 x 3)	109	103.78	73.64	86.98	19.3%	5.0%
P13 (18 x 3)	84	77.83	55.86	76.99	1.1%	7.9%
P14 (20 x 3)	100	87.99	63.54	81.99	7.3%	13.6%
P15 (20 x 3)	229	220.75	189.36	211.31	4.2%	3.7%

Table 1 : computational results showing the quality of solutions produced by 4 rounds of the procedure Search(x).

produced are optimal in 4 cases over 15, and the deviation from exact optimality is less than 5% on average. Note however that the quality of solutions are likely to be further improved by systematically applying the above-described procedure from *several randomly chosen starting solutions*, but of course at the expense of increasing computation time accordingly. Further investigation along this line is left for future research.

Among other possible directions for future research on the subject of the present paper, we can also mention investigation of a variant of the stochastic project selection problem where some measure of risk (such as variance, or the so-called 'Value at Risk') is taken into account, either as an additional constraint, or as an additional term in the objective function.

REFERENCES

Reeves C.R. (Editor). 1993. 'Modern Heuristic Techniques for Combinatorial Problems', Blackwell Scientific Publ.

Kernighan B.W., Lin S. 1970. 'An Efficient Heuristic Procedure for Partitioning Graphs', Bell Syst. Techn . J., 49,2,pp. 291-307.

AUTHOR BIOGRAPHY

MICHEL MINOUX is a Professor at the University of PARIS-6 and his research activities concern theory and applications of continuous and discrete optimization techniques, graph theoretical models and combinatorial optimization. He is the author of 'Mathematical Programming' (Wiley 1986), co-author of 'Graphs and Algorithms' (Wiley 1984). During the last 15-20 years he has been involved in numerous research projects requiring advanced optimization techniques, in particular in connection with telecommunications network optimization, energy networks and air transportation systems. Among his recent research interests is the investigation of connections between stochastic optimization techniques and what is referred to as robust optimization.

New Model for Asphaltene Precipitation with Modified Virial Equation of State

Sabbaghi S. [a] **, Sh. Ayatollahi** [a] **, M. Shariaty-Niassar** [b]**, A. Jahanmiri** [a]

[a] Shiraz University, Department of Chemical Engineering

[b] Tehran University, Department of Chemical Engineering

E-mail: sabbaghi@shirazu.ac.ir

KEYWORDS

Model, State Equation, Precipitation, Asphaltene, Nanotechnology.

ABSTRACT

A new model was developed to predict asphaltene precipitation. The virial equation of state (VEOS) was modified using group contribution methods of asphaltenes which are assumed to be polymeric-like compounds consisting of aggregates of monodisperse asphaltene monomers. The modified VEOS with the Peneloux correction was used to estimate the molar volume and solubility parameter. The modified VEOS was then used for the prediction of the onset and amount of asphaltene precipitation. The modified VEOS successfully predicted density and molar volume of asphaltene. The proposed model shows that the density and solubility parameter of asphaltene depend on molecular weight and temperature. Correlations of density, solubility parameter and structure coefficient as a function of molecular weight and temperature are developed. The correlations facilitate the calculation of these parameters numerical methods. The modified VEOS were tested against density calculated by SRK and PR EOS. A set of fitted data is used to check the validity of the calculated results of model.

INTRODUCTION

The structure and stability of petroleum is based on the manner in which the asphaltene and resin constituents interact. Hence, the disturbance of these interactions plays a major role in the formation of sediment and the deposition of asphaltenic material. Asphaltene precipitation in the reservoir has proved to be a problem in oil production. Asphaltene deposition can occur in surface facilities and pipelines. Treatment of the deposited solids increases operating costs. Therefore, it is desirable to prevent or mitigate asphaltene deposition. As a first step, it is necessary to predict the onset and amount of asphaltene precipitation. Knowing the mechanism of asphaltene precipitation is a key element to develop a realistic model in predicting asphaltene aggregates greatly limited the development of asphaltene models. Since 1980's many models of asphaltane precipitation have been developed to predict the onset and the amount of asphaltene precipitation [David, A., Lichaa, P.M., Mansoori, G.A.]. The use of cubic equations of state (CEOS) such as those of SRK and PR, is popular in for calculation of phase equilibrium values like temperature-pressure-composition relationships, as they are simple and convenient to be used [Andersen, S. L., et. al.]. These models are very successful for vapor-liquid as well as liquid-liquid equilibrium calculations [Pedersen, K.S., et. al.]. In 1986, Gupta used a combination of the SRK and PR equations to calculate asphaltene solubility [Gupta, A.K.]. The SRK EOS is used in combination with a structural correlation for estimation of the critical properties and acentric factor of asphaltenes. These properties are then introduced into the PR EOS and a solid-liquid-equilibrium calculation was then performed for a non_associating single component with fixed molar mass [Alexander, G.L., et. al.]. In the other model, the precipitated asphaltenes were considered as pure solid while the oil and gas phases were modeled with a CEOS. A correlation including eight parameters was introduced for calculation the fugacity of asphaltene fraction. Thomas' model employed large number of parameters and must be tuned in order to match experimental data [Thomas, F.R, et. al.]. In the year 2000, Wu et al. used their thermodynamic model to predict asphaltene precipitation in reservoir fluids [Wu, J., et. al.]. The calculated results were in good agreement with the experimental measurements. However, the model includes many parameters that are estimated and is not easy to be applied. In 2002, Akbarzadeh et al. developed a new thermodynamic model for predicting asphaltene precipitation at various conditions. Correlations were developed for the critical properties and acentric factor of each solubility class [Akbarzadeh, K., et. al.]. The aim of this article is to present a correlation for solubility, density and structure coefficients. It is important to note that in the previous studies the structure coefficient was evaluated by trial and error method and also density and solubility parameter were evaluated just as a function of molecular weight while in this study these parameters are evaluated as function of temperature and molecular weight, without trial and error.

COMPUTATIONAL DETAILS OF PROPOSAL MODEL

The intraction of forces between molecules in macromolecules is very critical that can't be ignored. These systems are dense and molecules are very near to each other such that most of their properties are governed by this interaction forces. Figure (1) show molecular structure of

asphaltene proposed for 510 $^{\circ}C$ residue of Venezuelan Crude by Carbognan [Carbognani]. It has been tried that measurable macroscopic quantities are related to microscopic intractions between molecules. For the calculation of chemical potential, complicated numerical calculations are needed that can be evaluated by quantum mechanics. A rather general function that are used in intraction potential energy is the Mie potential function [Mc Quarrie, D.A., Hirschfelder, J.O., et. al.].

$$U(r)=\frac{n\varepsilon}{n-m}\left(\frac{n}{m}\right)^{\frac{m}{n-m}}\left[\left(\frac{\sigma}{r}\right)^{n}-\left(\frac{\sigma}{r}\right)^{m}\right] \qquad (1)$$

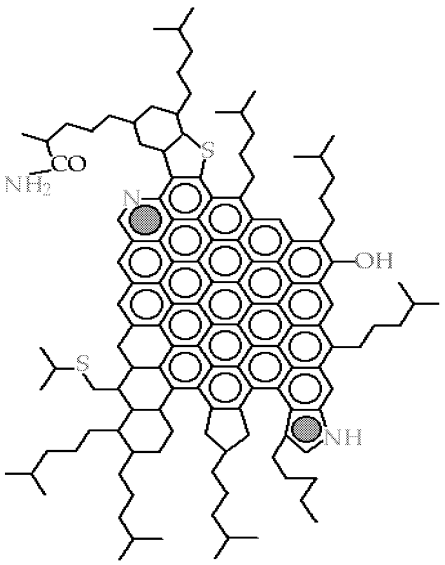

Figures 1: Molecular Structure of Asphaltene[Carbognani]

The costants ε and σ are obtained from intermolecular potential energy data. The curve of intermolecular pair potentials (U) versus distance (r) is drawn in Figure (2) by using the proposed function of intermolecular pair potential. Method of semi-empirical equations and PM3 is used to calculate the parameters associated with the chemical structure. It solves an approximate form of the Schrodinger equation that depends on having appropriate parameters available for the type of chemical system in question. Two different models are proposed for the potential function of asphaltene, one of those resulted in better agreement with the calculated parameters from the EOS which will be discussed later [Sabbaghi S., et. al.]. To work with Equation (1) and in order to determine the constants of potential function, calculated data have been fitted. The resultes are such as, n=18, m= 9, σ =16.0399 and ε = 23.057 then the model are defined by Equation (2):

$$U(r)= 92228\times\left[\left(\frac{16.0399}{r}\right)^{18}-\left(\frac{16.0399}{r}\right)^{9}\right] \qquad (2)$$

For many purposes, it suffices to distinguish two principal forces:(A) a repulsive force primarily due to the electrostatic repulsions between outer electron clouds of the molecular structure,(B) an attractive forces due to correlations for the positions of the electrons in one molecule with those in the other, which occur in such a way that cause a net electrical attraction. Repulsive and attractive potential energy are show equations (2a, 2b). In Figure(3), each of the terms in Equation(2) as well as the sumation, the total intermolecular potential energy, for the general case[Cark Nyeland, Akiyoshi S., et. al., Yu Zhang, et. al.].

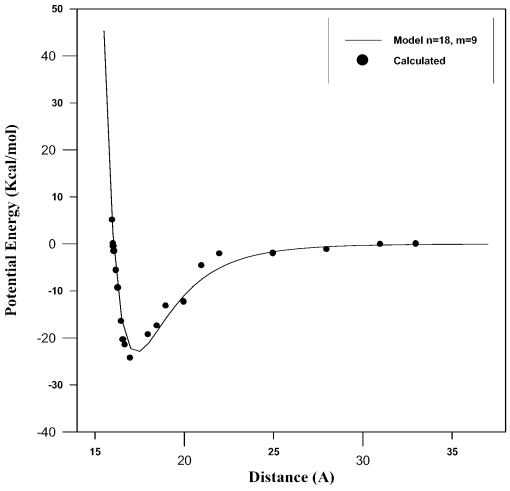

Figures 2: Intermolecular Potential of Asphaltene from Eq. (2)

$$\text{Repulsive Potential Energy} = 92.228\times\left[\left(\frac{16.0399}{r}\right)^{18}\right] \qquad (2a)$$

$$\text{Attractive Potential Energy} = -92.228\times\left[\left(\frac{16.0399}{r}\right)^{9}\right] \qquad (2b)$$

SECOND-VIRIAL COEFFICIENT

Equation (3) shows a general form of virial equation:

$$\frac{PV}{RT}=1+\frac{B_2(T)}{V} \qquad (3)$$

Here the second-virial coefficient $B_2(T)$ is a function of temperature which can be obtained by the interaction between pairs of molecules. Previous works using the statistical mechanics showed that the second-virial coefficient for intermolecular pair potential can be calculated by [Mc Quarrie, D.A., Hirschfelder, J.O., et. al.]:

$$B_2(T)=-2\pi\int_0^{\infty}\left(e^{-\beta u}-1\right)r^2dr \qquad (4)$$

$$\beta=\frac{1}{KT} \qquad (5)$$

Figure (4) shows second-virial coefficient as a function of temperature based on Equation (4). These results

were fitted using an exponential model with the values for: $x = -1407780.7$ and $y = -.035$.

$$B_2(T) = x\,e^{yT} \tag{6}$$

To find the best function for the chemical potential, a structure for the asphaltene was proposed first and the molecular dynamic method was used the chemical potential as a function distances between the atoms [Mc Quarrie, D.A., Hirschfelder, J.O., et. al].

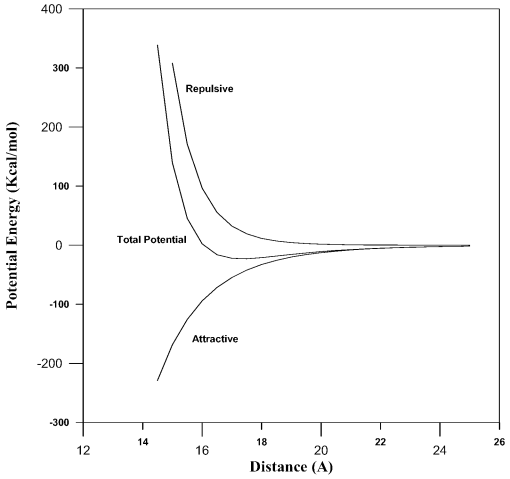

Figures 3: Intermolecular Separation of Asphaltene for Model from Eqs. (2a, 2b)

A MODIFIEDFORM OF THE VEOS FOR ASPHALTENE

The Virial Equation of State (VEOS) is used here to predict the asphaltene precipitation. The VEOS a modified version of equation(3):

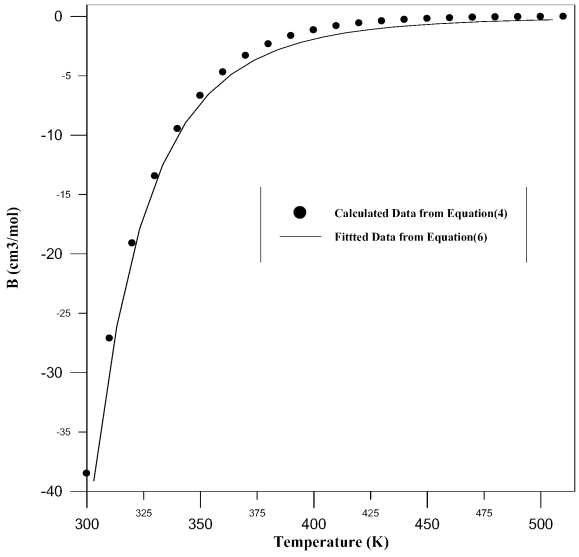

Figures 4: Second-Virial Coefficient vs. Temperature for Asphaltene from Eq. (4)

$$P = \frac{RT}{V}\left(1 + \frac{B_2(T)}{V}\right) \tag{7}$$

It is proved that the VEOS with a Peneloux correction gives the best estimates of liquid molar volume, obtained as follows [Peneloux, A., et. al.]:

$$V^L = V^{Virrial} - C \tag{8}$$

Where C is the Peneloux correction term which can be estimated by:

$$C = 1.377\left(M_W\right)^{1.27}\left(.29 - Z_{RA}\right) \tag{9}$$

Where Z_{RA} is the Racket compressibility factor proposed by Spencer and Danner for saturated liquid molar volume [Spencer, C.F., et. al.]. If these parameters are not available, it may be estimated from[Reid, RC., et. al.]:

$$Z_{RA} = 0.29 - 0.088\,w \tag{10}$$

$$w = C_f\left[0.587\,Ln(M_w) - 2.54\right] \tag{11}$$

Replacing $V^{Virrial}$ in Equation (8) by that in Equation (7) will result in the following form of the EOS:

$$P = \frac{RT}{\left(V^L + C\right)}\left(1 + \frac{B_2(T)}{\left(V^L + C\right)}\right) \tag{12}$$

If $\bar{r}$ is the average number of monomers in a given aggregate then the equation of state parameter for the aggregates related to the monomer parameter will be:

$$C = \bar{r}\,Cm \tag{13}$$

$$B = \bar{r}\,Bm \tag{14}$$

$$V^L = \bar{r}\,v^L \tag{15}$$

Where Cm, Bm are the monomer parameters. The modified VEOS is obtained by replacing C in equation (12):

$$P = \frac{RT}{\bar{r}\left(v^L + C\right)}\left(1 + \frac{B_2(T)}{\left(v^L + C\right)}\right) \tag{16}$$

The value of $\bar{r}$ can be estimated by the following relation:

$$\bar{r} = \frac{\overline{M}_W^{agg}}{M_W^{mon}} \tag{17}$$

$\overline{M}_W^{agg}$ and M_W^{mon} are the average molar mass of the asphaltene aggregate and the monomer molar mass, respectively.

EOS CALCULATION OF SOLUBILITY PARAMETER

Solubility parameter is one of the key parameters in modeling of thermodynamic solutions. This parameter

can be estimated by either a correlation or an EOS. Here, we have used the modified form of the VEOS to derive a relation for estimating the solubility parameter of asphaltene. In 1970, Hildebrand, Prausnitz and Scott related the liquid solubility parameter of non-polar solvents (δ^L) to the internal energy of vaporization $\left(\Delta U^{LV}\right)$ and the molar volume of the liquid phase $\left(v^L\right)$ to obtain:

$$\delta^L = \left(\frac{\Delta U^{LV}}{v^L}\right) \qquad (18)$$

To calculate the internal energy of vaporization the following equation was used [Hildebrand, J., et. al]:

$$\Delta U^{LV} = \int_{v^l}^{v} \left[\left(T\frac{\partial P}{\partial T}\right)_v - P\right].dv \qquad (19)$$

Therefore, the solubility parameter can be obtained by Equations (18), (19) that is:

$$\delta^L = \frac{T}{v^l}\left[R\,\frac{dB}{dT}\right]^{1/2} \qquad (20)$$

Note that the number of monomers ($\bar{r}$) indirectly affects the solubility parameter (Equation 20) as the monomer molar volume $\left(v^L\right)$, determined from Equation (16) is a function of ($\bar{r}$).

EFFECT OF TEMPERATURE AND MOLAR MASS ON DENSITY

Effect of temperature on pridicted density of asphaltene by modefied VEOS for different molecular weight is shown in Figure (5). As it is shown there as the tepmperature increases, the density of asphaltene decrease. Figure (6) shows effect of molecular weight on density asphaltene. According to these results the density increases sharply with the increase in molecular weight and then approaches a constant amount at very high molecular weight value.

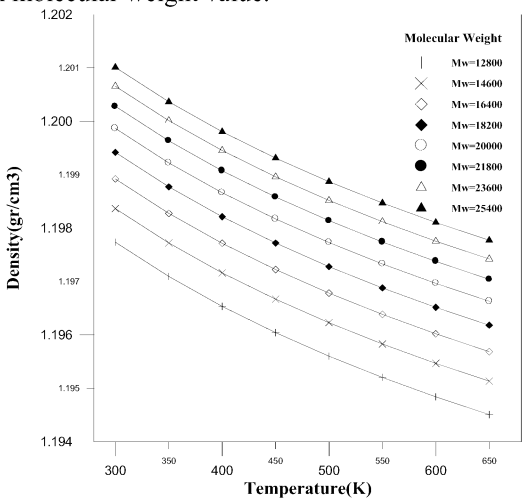

Figures 5: Density vs. Temperature for Asphaltene from Eq. (3)

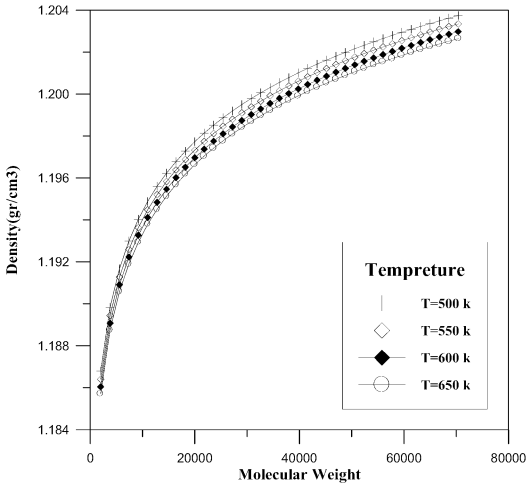

Figures 6: Density vs. Molar Mass for Asphaltene from Eq. (3)

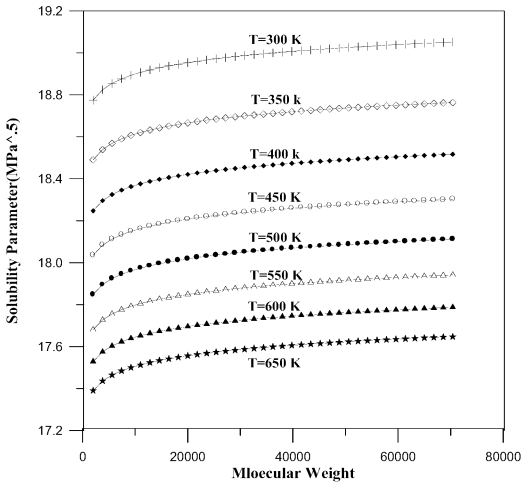

Figures 7: Solubility Parameter vs. Molar Mass for Asphaltene from Eq. (20)

EFFECT OF MOLAR MASS AND TEMPERATURE ON SOLUBILITY PARAMETER

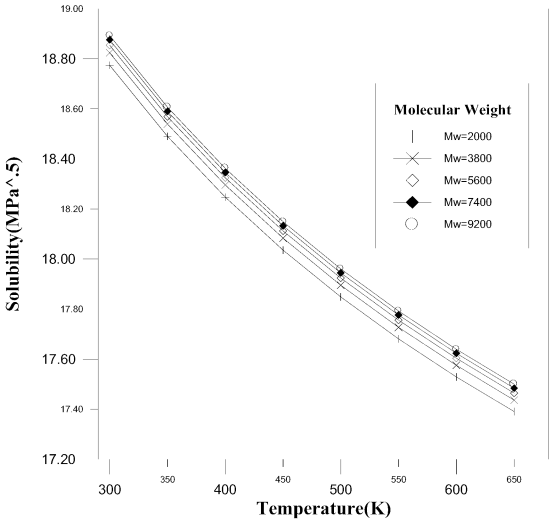

Figures 8: Solubility Parameter vs. Temperature for Asphaltene from Eq. (20)

The molar mass has a little effect on solubility parameter of asphaltene. This can be seen from Figure (7), where the predicted solubility parameter of asphaltene is plotted versus the molar mass for different temperature. For liquids, temperature affects both on internal energy of vaporization and density. The changes in these properties result in a decrease in the solubility parameter of asphaltene. Figure (8) shows this trend .

RESULTS AND DISCUSSION

According to Figure (5) to (8) it is deduced that density and solubility parameter of asphaltene are function of molar mass and temperature. Then we developed three correlations for prediction of density, solubility parameter and structure coefficient , respectively. The validity of the correlations, were tested to the data predicted by SRK and PR EOS which resulted in good agreement between the calculated parameters. Meanwhile, density and solubility parameter as the functions of temperature found from SRK and PR EOS are shown in Figures (9) and (10).

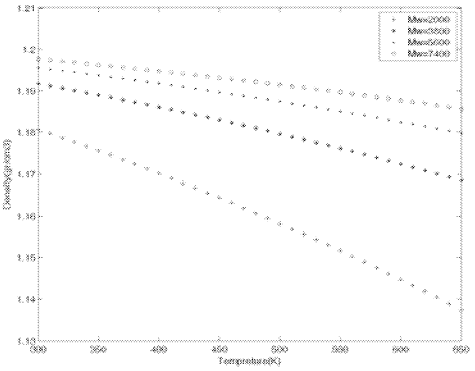

Figures 9: Density vs. Temperature for Asphaltene with SRK, PR EOS [Akbarzadeh, K., et. al]

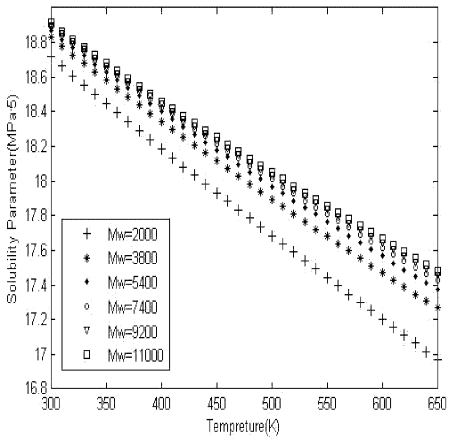

Figures 10: Solubility Parameter vs. Temperature for Asphaltene with SRK, PR EOS [Akbarzadeh, K.]

$$C_f = 77.3\left(M_W\right)^{-1.1677}\left(T\right)^{1.13} \qquad (21)$$

$$\delta = 32.02\left(M_W\right)^{.0041}\left(T\right)^{-.0991} \qquad (22)$$

$$\rho = 1.1767\left(M_W\right)^{.00398}\left(T\right)^{-.0035} \qquad (23)$$

Figures (11, 12), compare the calculated density and solubility of asphltene from proposed correlations with results of SRK, PR EOS. Figure (13), compares the calculated and measured densities of asphaltene. According to this figure, all the points scatter around the 45-degree line that means good agreement has been achieved here. To check the accuracy of the proposed model, the density measurements at different temperatures are calculated.

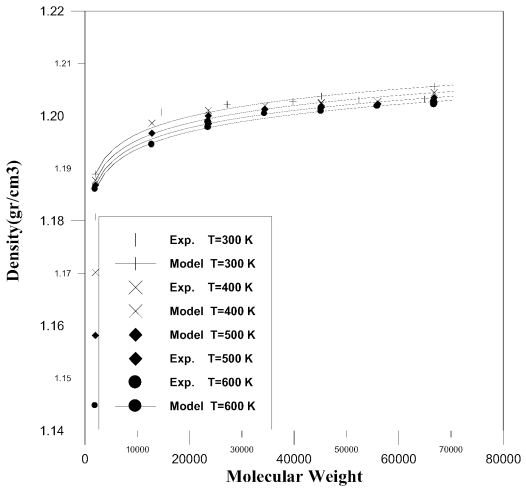

Figures 11: Compares Solubility Parameter and Density Versus Molar Mass with Data for Asphaltene from Eq.(23)

As a summary, in this study firstly a new correlation is presented for structure coefficient, secondly density and solubility parameters are presented as function of temperature and molecular weight, thirdly in the evaluation of density and solubility parameters instate of numerical solution of nonlinear state equation, we are able to use directly the presented correlations in this study.

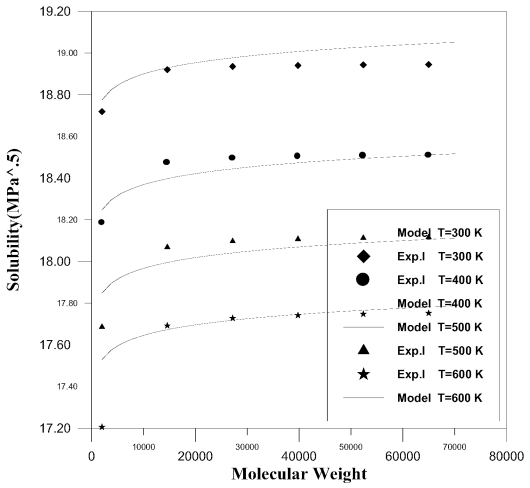

Figures 12: Compares solubility Parameter and Density Versus Molar Mass with Data for Asphaltene from Eq.(22)

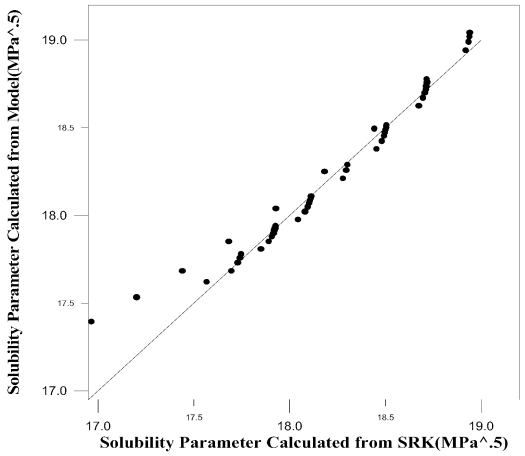

Figures 13: Comparison Solubility Parameter the Calculated and Results of SRK, PR EOS

NOMENCLATURE

$B_2(T)$: Second-virial coefficient, $\frac{cm^3}{mol}$

C_f : A correction factor that accounts for structural effect

K : Boltzmann constant, $\frac{Kcal}{mol.K}$

Mw: The molar mass of asphaltene

n, m: Dimensionless constants [-]

P: Pressure, bar

R: Gas constant

T: Temperature, K

x,y: Constants

w : The acentric factor

σ : The intermolecular distance at which the potential is zero, [$\dot{A}$]

U(r): Potential energy, [$\frac{Kcal}{mol}$]

V: Molar volume, $\frac{cm^3}{mol}$

V^L : Molar volume of liquid, $\frac{cm^3}{mol}$

v^L : Monomer molar volume of liquid, $\frac{cm^3}{mol}$

V^{Virial} : Molar volume calculated by virial Eq., $\frac{cm^3}{mol}$

ε : Well depth, [$\frac{Kcal}{mol}$]

REFERENCE

Akbarzadeh, K., Ayatollahi, Sh., Nasrifar, Kh., Yarranton, H.W., Moshfeghian M., "Equation Lead to Asphaltene Deposition Predictions", Oil & Gas Journal, Oct. 28(2002), 100, 44; ABI/INFORM Golbal.

Akbarzadeh, K., Sh. Ayatollahi, M. lMoshfeghian, H. Alboudwarej, H.W. Yarranton, "Estimation of SARA Fraction Properties With the SRK EOS. Journal of Canadian Petroleum Technology. 2004, Volume 43, No. 9.

Akiyoshi S., Satimi K., Nobuaki M., Kenro H.,2004. Potential energy surface and intermolecular vibrations of $O_2 - H_2O$, Chem. Phys. letters, pp.101-105.

Alexander, G.L., Creagh, A.L., Prausnitz, lM., "Phase Equilibria for HighBoiling Fossil-Fuel Distillates: 1. Characterization", Ind. Eng. Chem. Fund., 24(1985), 301.

Andersen, S.l., Speight, lG., "Thermodynamic Models for Asphaltene Solubility and Precipitation", J. of Petroleum Science and Engineering, 22(1999), 53-66.

Carbognani, 1992. INTEVEP S.A., Tech. Rept.

Cark Nyeland,2003. Gradient expansions in density functional calculations of intermolecular potentials, Chemical physics letters, pp.353-359.

David, A., 1973. Asphaltene flocculation during solvent stimulation of heavy oils. AIChE(Am. Inst. Chem. Eng.) Symp. Ser., 69(127):56-61.

Gupta, A.K., "A model for asphaltene Flocculation Using an Equation of State", M.Sc. Thesis, Department of Chemical and Petroleum Engineering, University of Calgary, June 1986.

Hildebrand, J., and R. Scott, Solubility of Non-Electrolytes, 3rd ed., Reinhold, New York, 1949.

Hirschfelder, J.O., Curtiss, C.F., Bird, R.B., Moleculary Theory of gases and Liquids, 2nd Printing, Wiley, New York, 1964.

Lichaa, P.M., 1977. Asphaltene deposition problem in Venezuela crudes-usage of asphaltenes in emulsion stability. In: Oil and sands. Can.Pet.Technol. J.(Jun), pp.609-624.

Mansoori, G.A., 1999. Modeling and Asphaltene and Other Heavy Organic Compound. J. of Petroleum Science Engineering,16,101.

Mc Quarrie, D.A., Statistical Mechanics, Harper Collines Publishers, 1976.

Pedersen, K.S., Skovberg, P., Ronningsen, H.P., "Wax Precipitation from North Sea Crude Oils: 4. Thermodynamic Modeling", Energy & Fules, 5(1991), 924-932.

Peneloux, A., Rauzy, E., Freeze, R., "A Consistent Correction for RedlichKwong-Soave Volumes", Fluid Phase Equilibria, 8(1982), 7-23.

Reid, RC., Prausnitz, lM., Poling, B.E., "The Properties of Gases & Liquids", 4th edition., Mc Graw-Hill, New York, p. 67, 1989.

Sabbaghi S., A. Jahanmiri, M. Shariaty-Niassar, Sh. Ayatollahi, A. Boushehri, "Theoretical Study of Potential Energy and Intermolecular Forces of Asphaltene Using a Quantum Mechanics", Accepted for Publication , Intl. J. Nanosci.&Nanotech.(IJNN), 2005.

Spencer, c.F., Danner, R.P., "Improved Equation for Prediction of Saturated Liquid Density", 1. Chem. Eng. Data, 17(1972), 236-241.

Thomas, F.R, Bennion, D.W., Hunter, RE., "Experimental and Theoretical Studies of Solids Precipitation from Reservoir Fluid", 1. Can. Pet. Tech., 31 (1992), 22-31.
Wu, J., Prausnitz, J.M., Firoozabadi, A., "Molecular Thennodynamics of Asphaltene Precipitation in Reservoir Fluids", AIChE J., 46(2000), 197-209.
Yu Zhang, Hong-Yun Shi,2002. An ab initio study of intermolecular potential for the He-Hcl complex, J. of molecular structure(Theochem), pp.89-93.

ENGINEERING SIMULATION

A SOLUTION TO THE LOW DAMPING PROBLEM OF HYDRAULIC DRIVE SYSTEMS

A. Chatzinikolaou
S. Patsi 62
GR-118 55 Athens, Greece
E-mail: achatzi@otenet.gr

C. Angeli
Department of Mathematics and Computer Science
Technological Education Institute of Piraeus
Konstantinoupoleos 38, N. Smirni
GR-171 21 Athens, Greece
E-mail: c_angeli@otenet.gr or
c.angeli@computer.org

KEY WORDS

Modelling, simulation, hydraulic systems, low damping problem

ABSTRACT

It is generally accepted that hydraulic drive systems have significant advantages in comparison to other drive systems in a range of applications, due to their compactness. The main problems of hydraulic systems are leakage and the low degree of damping due to the compressibility of the hydraulic fluid. This work proposes a method that describes efficiently the dynamic behaviour of hydraulic systems based on a reliable and useful mathematical model and suggests a method to improve their dynamic behaviour.

INTRODUCTION

Hydraulic systems have a lot of advantages as drive and control systems due to the small masses of their driving elements. A major problem of these systems is the low degree of damping due to the compressibility of the hydraulic fluid. This disadvantage has lead to an increasing competition from the relevant electrical systems.

The reduction of the problem of the low damping and the improvement of the dynamic behaviour of hydraulic drive systems can be achieved in various ways. The proposed way consists in the use of flow bypass orifices with a very small diameter that are placed at suitable positions of the hydraulic circuit and produce a small leakage. According to this method the dynamic behaviour of the system is significantly improved without great loss on the total performance.

The fact that a small amount of leakage influences the dynamic behaviour of hydraulic systems significantly more than their performance can also be used for the early fault detection of incipient faults in systems before their occurrence. The need of reliable early process fault detection in dynamical systems has received great attention and recent research work has been reported among others researchers by (Isermann 1984, Ming-Chang Shin et al 1997, Patton et al. 2000, Zhou and Paik 2000, Angeli and Chatzinikolaou 2005). The main problem regarding the reliability of the diagnostic method consists the modeling uncertainties due to process noise, parameter variations and non-linearities.

In this paper, the dynamic behaviour of hydraulic systems is studied, a method is presented that analyses and models their dynamic behaviour by presenting a reliable and useful mathematical model and a method is proposed that improves the dynamic behaviour.

MODELLING PROCESS

A hydraulic system consists of hydraulic elements connected with pipes and a hydraulic medium. As mechanical systems they are a combination of three basic elements, spring, damper and inertia. The elasticity of the oil can be considered as a spring effect and the hydraulic friction forces and the leakage of the elements as a damper.

In order to study the dynamic behaviour of hydraulic systems it should be taken into consideration that the hydraulic components are smaller dynamic systems that influence the dynamic behaviour of the total system. In addition the dynamic behaviour of the components is influenced by the dynamic behaviour of the system (Hoffmann 1978, Hoffmann and Hesse 1980, Hoffmann 1981, Backe 1986). For the description of the dynamic behaviour of hydraulic systems, most components can be considered as quasi-steady, because the volume of the incorporated hydraulic fluid is usually very small and their moving parts are so small that their inertia is unimportant. This means that the dynamic state of the components can be described as a sequence of stationary states.

The hydraulic components have been regarded in many previous research works as components that include an incompressible fluid (Chaimowitsch 1965). In this work, the components are classified in two categories: The relatively compact components, as valves, and the components with large fluid volume, as cylinders and pipes. For the description of the mathematical model of hydraulic components the technical specifications of the manufacturer instead of theoretical considerations have been used (Chatzinikolaou 1992).

Hydraulic components connected with connection pipes of short length can be considered as quasi-steady and the included fluid volume in the pipes as a unique volume where the pressure increase during a dynamic state is proportional to the difference between the incoming and outgoing flows.

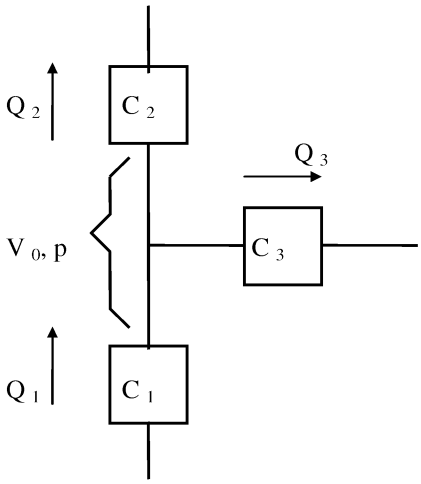

Figure 1. Connection of hydraulic components

The connection of three hydraulic components (C_1, C_2, C_3) is schematically represented in Figure 1. In this Figure, the flow rates Q_1, Q_2, Q_3 through the components can be described with mathematical equations derived from their characteristics. The basic equation for the volume compression (ΔV) as a function of pressure increase (Δp) and fluid volume (V_0) is:

$$\Delta V = (1/E_{fluid}) \cdot \Delta p \cdot V_0$$

Where $1/E_{fluid}$ is the elasticity coefficient of the hydraulic fluid.

$$\Delta p = (E_{fluid} /V_0) \cdot \Delta V$$

$$dp/dt = (E_{fluid} /V_0).(dV/dt) = (E_{fluid} /V_0).Q$$

$$\text{where } Q = \Sigma Q = Q_{in} - Q_{out}$$

In every junction or volume we have:

$$dp/dt = (E_{fluid} /V_0).\Sigma Q \qquad (1)$$

The flows Q through the components can be expressed using mathematical relations derived from the technical specifications according to the kind of the component.

The modulus of the fluid elasticity under ideal conditions in the case of hydraulic oil is:

$$E_{fluid} = E_{oil} = 1{,}4.10^{9} \text{ N/m}^2$$

If we take into consideration the elasticity of the pipes and the elasticity of the included air in the fluid we have to use another corrected value of the modulus of the oil elasticity. This value can be derived from the equation:

$$1/E = 1/E_{oil} + 1/E_{pipe} + 1/E_{air}$$

A practical useful value of the modulus of the oil is:

$$E_{oil} = 1{,}0.10^{9} \text{ N/m}^2$$

The use of the relation (1) in every junction of the circuit and the equations that express the flow rates build a system with differential equations that can be solved with various ways.

THE EXPERIMENTATION SYSTEM

A typical hydraulic system was used for the experimentation part of this work. This system is presented in Figure 2 and consists basically of a hydraulic motor (2.1), a rotated mass with a moment of inertia J_m, a hydraulic servo valve (1.3) and a power pack.

A set of flow bypass devices (orifices D_{tt} and D_{ab}) have been placed between the hydraulic motor and the servo valve. These devices produce a small leackage that influence the dynamic behaviour of the system.

The servo valve was energised with various input values I_2 [A] and the response of the hydraulic motor with the coupled mass was studied for various operating conditions and various flow bypass orifice diameters and combinations.

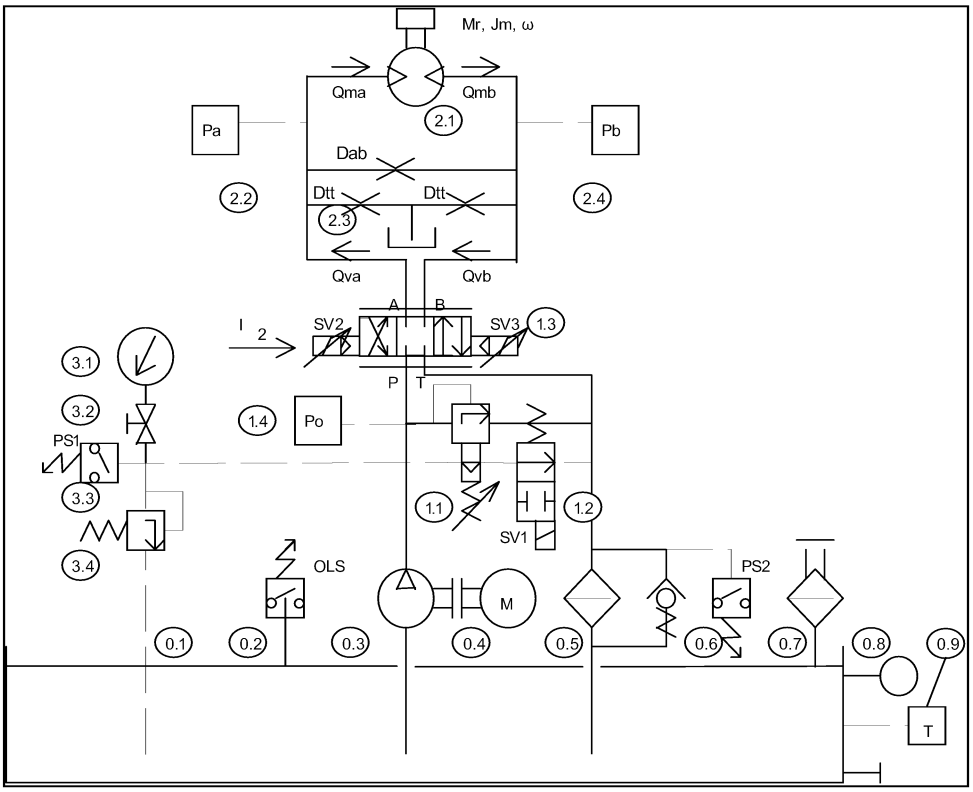

Figure 2. The experimentation system

SIMULATION RESULTS

The system “servovalve-hydraulic motor" that is illustrated in the hydraulic circuit of Figure 2 was modelled together with the load according to the proposed method. The modelling of the hydraulic elements with the coupled mass leads to a non-linear system of equations.

The method of the integration used for the simulation of the dynamic behaviour of the system was the fourth-order Runge Kutta method. The step response functions for the pressures p_a and p_b and for a command value I_2 = 15 mA and an operational parameter set that includes the system pressure p_0, the oil volume V_1 in the pipes between motor and servo valve and the diameter values of the orifices D_{tt} and D_{ab} are presented in Figure 3. In this Figure the influences of various orifices in pressures p_a, and p_b are illustrated.

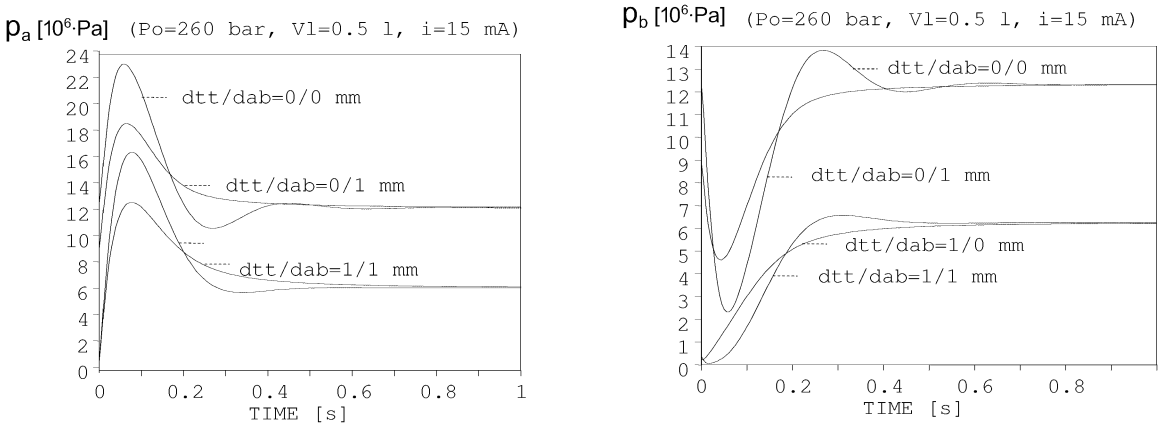

Figure 3. Simulation results

In Figure 3 a graphical representation of the pressures p_a and p_b at the ports A and B of the hydraulic motor for various bypass orifices is illustrated. In this diagram a significant influence of a small leakage to the dynamic behaviour of the hydraulic system is obvious.

The upper curve represents the response of the system without any leackage. By the second curve a bypass orifice with a diameter of 1 mm has been placed between A and B, by the third curve two bypass orifices with a diameter of 1 mm has been placed between A, B and the tank and by the fourth curve all three orifices have been placed.

It can be observed that while the increase of the damping through a leakage to the tank (two lower curves) is accompanied by a significant decrease of the performance, a small bypass from A to B (second upper curve) has as consequence the improvement of the dynamic behaviour without losses.

MODEL VALIDATION

The simulation model was validated in comparison to the real world data in order to prove the accuracy of the proposed method. For this purpose the actual hydraulic system of the experimentation part was connected through sensors with a data acquisition subsystem. The acquired data referring to the relevant system variables were compared with the simulation results. The measured quantities of the actual system were the pressure values at critical points of the hydraulic system and the values of the angular velocity of the hydraulic motor. During the validation process the estimation of uncertain parameter values, as the parameter value of the mechanical friction torque, were experimentally determined. The output of the simulation and the output of the actual system under various operating conditions using various values for the bypass orifices illustrate a satisfactory accuracy.

Data from the measurement process as well as relevant values from the simulation process referring to the pressure values are presented together for comparison reasons in Figure 4 where the consistency of the behaviour of model and system can be observed.

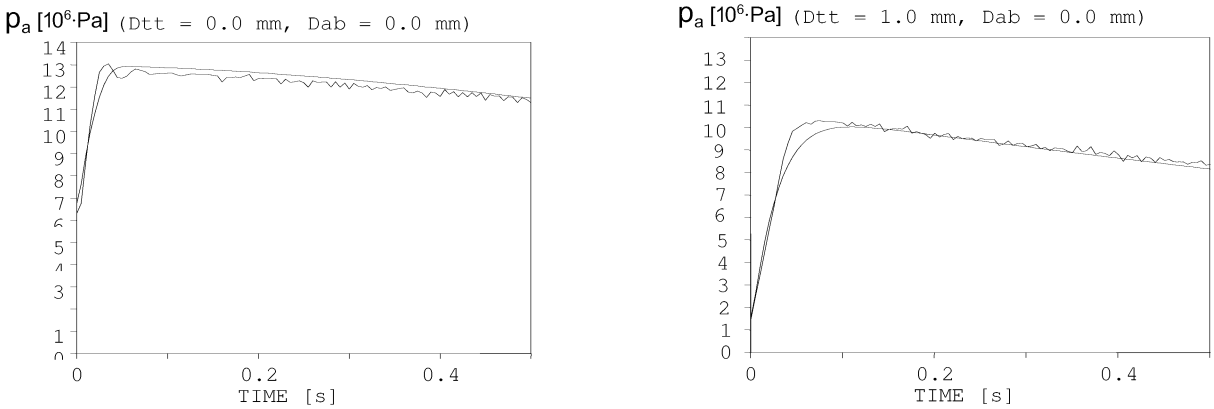

Figure 4. Comparison of measured and calculated results.

CONCLUSION

In this paper, the modelling and simulation process of a hydraulic drive system is presented. In this system suitably positioned orifices were used in order to reduce the low dumping problem of hydraulic systems. The dynamic behaviour of the actual system and the influence of a small leakage was studied.

The simulation results illustrate that the damping characteristic of the hydraulic system has been considerably improved by the proposed method. In addition, the method can be successfully applied for the modelling of real-world situations with sensitive dynamic behaviour as it was developed and implemented to a real world hydraulic system.

The results show that the dynamic behaviour of a hydraulic system can also be used for the purpose of early detection of incipient faults when these modelling observations are included in a suitable diagnostic system. The method was developed using a real hydraulic system and the corresponding mathematical model was validated using measurements of the actual system.

REFERENCES

Angeli, C. and A. Chatzinikolaou 2005. "Using modeling techniques for fault prediction in hydraulic drive systems". *Proceedings of 3rd International Industrial Simulation Conference ISC 2005*, June 9-11, Berlin, Germany.

Backe W. 1986. "Servohydraulik", Umdruck zur Vorlesung, RWTH Aachen.

Chaimowitsch E. M. 1965. "Oelhydraulik", VEB-Verlag Technik, Berlin.

Chatzinikolaou A. 1992. "Dynamic Behaviour of Hydraulic Systems in automatic machines", PhD thesis, Technical University of Athens.

Hoffmann W. 1978. "Berechnung des dynamischen Verhaltens hydraulischer Schaltungen", *o+p, Oelhydraulik und Pneumatik* Nr. 12.

Hoffmann W. 1981. "Dynamisches Verhalten hydraulischer Systeme, automatischer Modellaufbau und digitale Simulation", Dissertation RWTH Aachen.

Hoffmann, W. and K.Hesse 1980. "Digitale Simulation des dynamischen Verhaltens hydraulischer Geraete", *o+p Oelhydraulik und Pneumatik*, Nr. 3.

Isermann R. 1984. "Process Fault Detection Based on Modeling and Estimation Methods - A Survey". *Automatica*, Vol 20, Nr. 4, 387-404.

Ming-Chang Shin and Chung-Din Tsai. 1997. "Servo Hydraulic Cylinder Position Control using a NeuroFuzzy Controller", *Mechatronics*, 7/4, 355-368.

Patton, R. P. Frank and R.Clark. 2000. "Issues in Fault Diagnosis For Dynamic Systems", Springer-Verlag, New York.

Zhou, M. and J. Paik. 2000. "Integrating Neural Network and Symbolic Inference for Prediction in Food Extraction Process". *In Proceedings of 13th International Conference on Industrial and Engineering Applications of Artificial Intelligence and Expert Systems, IEA/AIE, New Orleans*, Louisiana, USA, June 19-22, 567-572.

BIOGRAPHIES

A. CHATZINIKOLAOU was for many years researcher at the Technical University of Athens in the department of Mechanical Engineering and is involved in many large projects of hydraulic systems for drive and control automatic machines. He holds a PhD in Dynamic Behaviour of Hydraulic Systems for Robots. His current research interests are the application of Artificial Intelligent Techniques to Hydraulic Systems.

C. ANGELI is a Professor at the Technological Education Institute of Piraeus. She holds a MSc in Intelligent Systems from University of Plymouth and a DPhil in Intelligent Fault Detection Techniques from University of Sussex. Her current research interest is real-time expert systems and artificial intelligent techniques in fault detection.

DYNAMIC SIMULATION MODELING OF LANDING AIRCRAFT

Zdravko Terze * , Hinko Wolf†, Dubravko Matijašević*

* Department of Aerospace Engineering
F. Mech. Eng. Naval Arch., University of Zagreb, Croatia
e-mail: zdravko.terze@fsb.hr

† Department of Applied Mechanics
F. Mech. Eng. Naval Arch., University of Zagreb, Croatia

KEYWORDS
Dynamics of Landing aircraft, Aircraft Multibody Model, Non-linear Landing Gear Dynamics, Shock Absorber Model.

ABSTRACT

Dynamical model and numerical procedures for dynamic simulation of landing and taxi of large transport aircraft are shortly presented. The simulator allows for dynamic response determination of landing aircraft for different flight and touch-down parameters. The mathematical model and computational procedures are based on non-linear dynamical model of landing aircraft, which is synthesised *via* modeling of aircraft structural systems using multibody dynamics approach. The model includes discontinuous dynamics of landing gear oleo-pneumatic shock-absorber with friction and hydraulic/thermodynamic processes. It also includes contact dynamics of non-linear tire and unilateral dynamics of assembly of nose gear elastic leg. The longitudinal and lateral aerodynamic loads are estimated by considering aircraft various system configurations (landing gears in up and down position, different control surfaces in active/inactive modes). Dynamic simulator is based on numerical processing of nonlinear dynamics of aircraft structural systems with variable kinematical structure. Mathematical model is derived as differential-algebraic (DAE) system and numerical tools are modularly shaped. Efficient numerical integration methods and original procedures for MBS constraint stabilization are applied for determination of system dynamical response. On the basis of the presented model, dynamic simulations of landing cases of large transport aircraft were performed for various initial descent velocities and different lateral wind conditions.

INTRODUCTION

During landing and taxi, a transport aircraft landing gear and parts of an airframe can be exposed to high dynamical loading. In the extreme situations even damages and loss of the stability of an airplane may be expected. During large airplane tail-down landing, all of dynamical loads are carried on the main gear first: dynamical characteristics of the main gear are of the most significant importance for the safe touchdown and landing during which an airframe load factors should be kept in the prescribed range [1], [2]. However, when the aircraft critical landing conditions and structural loads are being determined, the simplifications are often made: aerodynamic loads are oversimplified, aircraft pitching and rolling motion are neglected or tire dynamics and wheel spin-up forces are not taken into consideration [2]. Although some basic characteristics of landing aircraft dynamical response can be determined by linear dynamic analysis, dynamic simulation of landing airplane for the sake of its stability analysis or determination of structural loads requires full-scale non-linear multibody approach.
In the paper, a non-linear dynamical model of large transport aircraft that allows for dynamic simulation of airplane landing cases is shortly described. The model includes aircraft aerodynamic loads, discontinuous dynamics of shock absorbers oleo-pneumatic elements (main and nose landing gear) and aircraft tires 3D dynamics that include longitudinal and lateral loading. Because of its great influence on the aircraft ground dynamical behaviour and structural loads determination, dynamical model of main gear shock absorber is presented in more details. Based on the developed model, landing cases of large transport aircraft for different 3D flight-landing parameters are simulated and presented.

LANDING AIRCRAFT DYNAMICAL MODEL

Multibody dynamical model

The aircraft dynamical model that allows for non-linear dynamic simulation of 3D landing is designed as a multibody system (MBS) with variable kinematical structure. The 'global' model comprises aircraft main body, main landing gear consisting of two elastic legs with the upper part (upper part of shock absorber + additional masses) and the lower part (lower part of shock absorber + wheel and tire + additional masses) and nose gear consisting of the upper and lower part of the same structure. The 'local' structural sub-systems of different parts and mechanisms are independently modeled and incorporated in the 'global' scheme (Fig. 1).
The gears' upper and lower parts are connected *via* non-linear force couplers, modeled according to the shock absorbers dynamical characteristics. With this aim in view, main elastic leg and shock-absorber sub-assemblies as well as nose gear elastic leg mechanism are modeled in detail using CAD tools (Fig. 1). After defining geometry, non-linear models of their dynamical behaviour are numerically tested (Fig. 2) and built into 'global' dynamical model.

The additional non-linear force couplers are added to model aircraft tires dynamics: it is assumed that aircraft main gear is equipped with four tires of the conventional type. Two conventional tires are mounted on the aircraft nose gear as well. Mechanical properties of tires are estimated after [5] and manufacturer data. Dynamical model of tire contains its non-linear dynamical behaviour, including tire inertia effects, centrifugal growth of radius and side loads. The calculation of spin-up force of tire contact dynamics is based on variable slip-friction characteristics and a slippage factor, defined according to manufacturer data. It is assumed (and verified by the simulation results) that tire-bottoming deflections will not occur during analysed motion.
Generally, dynamical response of landing aircraft includes unsteady aspects, not only because of the external landing impact, but also with regard to the unilateral contact phenomena within landing gear mechanism. A full 3D aerodynamic loads are estimated by considering aircraft various system configurations (landing gears in up and down position, different control surfaces in active/inactive modes). The whole aircraft ('global' model) and parts of main shock absorber assembly are depicted in Fig. 1.

Mathematical model

The configuration space $\mathcal{R}^n$ of an airborne aircraft is considered to be a manifold $\mathcal{M}^n$ covered by coordinate system (local chart) $\mathbf{q}(t)$ and equipped with Riemannian metrics *via* system generalized mass $\mathbf{M}(\mathbf{q}) = [M_{ab}]$. System kinetic energy $T(\mathbf{q},\dot{\mathbf{q}}) : \mathrm{T}\mathcal{M}^n \to \mathcal{R}$ is defined on tangent bundle $T\mathcal{M}^n$ covered by the coordinates $(\mathbf{q},\dot{\mathbf{q}}) : \mathrm{T}\mathcal{M}^n = \{(\mathbf{q},\dot{\mathbf{q}}) : \mathbf{q} \in \mathcal{M}^n, \dot{\mathbf{q}} \in \mathrm{T}_{\mathbf{q}}\mathcal{M}^n\}$.
System kinetic energy is given by $T = \frac{1}{2} M_{ab}\dot{q}^a\dot{q}^b$ and manifold kinematical line element is $\mathrm{d}s^2 = M_{ab}\mathrm{d}q^a\mathrm{d}q^b$.
Consequently, dynamical equations of unconstrained system are given in the form

$$M_{ab}\ddot{q}^b + \Gamma_{a,bc}\dot{q}^b\dot{q}^c = F_a(\mathbf{q},\dot{\mathbf{q}},t),$$

where generalized mass (metric tensor) is defined as

$$M_{ab} = \sum_{k=1}^{N}\left[m_k \partial_{q^a} X^i_k \partial_{q^b} X^i_k + \psi^{ij}_k \partial_{q^a} R^i_{k\,i} \partial_{q^b} R^i_{k\,j} \right],$$

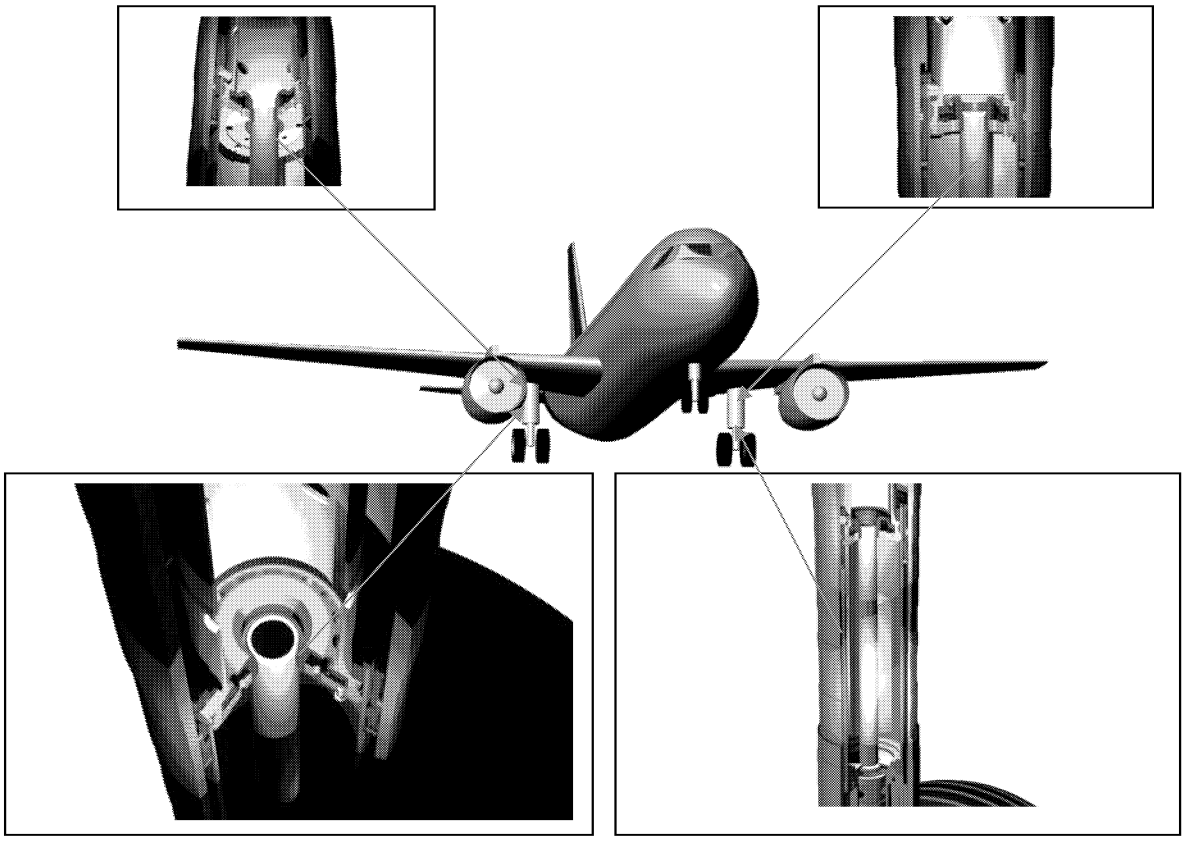

Figure 1.: *Schematic presentation of global multibody model of landing aircraft.*
Details of shock absorber assembly model - low pressure gas chamber / oil chamber, upper and lower bearings, systems of orifices.

and Christoffel symbols of the first kind

$$\Gamma_{a,bc} = \sum_{k=1}^{N}\left[m_k \partial_{q^a} X_k^i \partial_{q^b}\partial_{q^c} X_k^i + \psi_k^{ij} \partial_{q^a} R_k^i{}_i \partial_{q^b}\partial_{q^c} R_k^i{}_j \right]$$

define non-linear velocity terms (centrifugal, gyroscopic, Coriolis); symmetric Riemannian connection on $\mathcal{M}^n$ is defined by $\Gamma_{bc}{}^{a} = M^{ad}\Gamma_{d,bc}$. Inertial frame $\mathcal{E}^3$ coordinates of mass centre of the body B_k (*N*, number of bodies) are given by $X_k^{(i)}$. Mass and Binet's inertia tensor of the body B_k are m_k and ψ_k^{ij} and $R_k^i{}_i$ is rotation matrix of the body, where underlined indices refer to the inertial frame; generalized applied forces are given by F_a. By imposing system kinematical constraints (landing gear external contacts, elastic leg extension constraints)

$$\mathbf{\Phi}(\mathbf{q},t) = \mathbf{0} \ , \ \mathbf{\Phi}(\mathbf{q},t): \mathcal{R}^n \times \mathcal{R} \to \mathcal{R}^r \ ,$$

the system is forced to move on the configuration sub-manifold:

$$\mathcal{S}^{n-r}(t) = \left\{ \mathbf{q} \in \mathcal{M}^n, \mathbf{\Phi}(\mathbf{q},t) = \mathbf{0} \right\} ,$$

and velocities and accelerations of the system are given by:

$$\mathbf{\Phi}_\mathbf{q}(\mathbf{q},t)\dot{\mathbf{q}} = -\mathbf{\Phi}_t \ , \ \mathbf{\Phi}_\mathbf{q}(\mathbf{q},t)\ddot{\mathbf{q}} = \xi \ .$$

The mathematical model of the aircraft multibody system is shaped as differential-algebraic system (DAE) of index 1 (redundant coordinates formulation) [4], where Lagrangian equations of the first type and kinematical constraint equations at the acceleration level are put together:

$$\mathbf{M}(\mathbf{q})\ddot{\mathbf{q}} + \mathbf{\Phi}_\mathbf{q}^{\mathrm{T}}(\mathbf{q},t)\boldsymbol{\lambda} = \mathbf{Q}(\mathbf{q},\dot{\mathbf{q}},t) \ , \ \mathbf{\Phi}_\mathbf{q}(\mathbf{q},t)\ddot{\mathbf{q}} = \xi \ .$$

$\mathbf{M}(\mathbf{q})$ is positive-definite inertia matrix, $\mathbf{\Phi}_\mathbf{q}(\mathbf{q},t)$ is the system's Jacobian (kinematical constraint matrix), $\boldsymbol{\lambda}$ is vector of Lagrange multipliers, ξ is additional terms vector and $\mathbf{Q}(\mathbf{q},\dot{\mathbf{q}},t)$ represents the applied forces and centrifugal and gyroscopic terms [4]. Since system has variable kinematical configuration (during motion several kinematical constraints change form active to inactive mode), it was integrated using DAE numerical routines that included constraint violation stabilization procedure [4].

LANDING GEAR SHOCK ABSORBER

Most commonly, a telescopic main landing gear of a transport aircraft comprises a shock absorber of oleo-pneumatic type [3]. Considering a contemporary design, it is a several stage unit and contains four chambers: a first-stage oleo-pneumatic chamber containing low pressure gas and hydraulic fluid, a recoil chamber and compression chamber containing hydraulic fluid and a second-stage pneumatic chamber that contains high pressure gas (nitrogen) (Fig. 2).

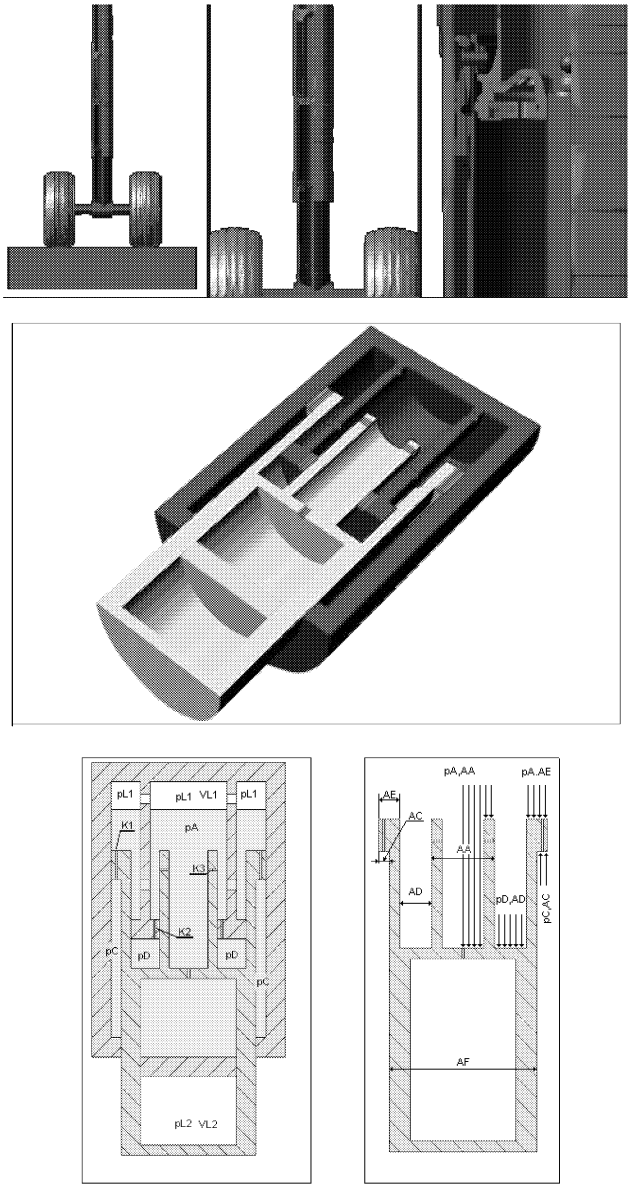

Figure 2.: *Multibody model of main landing gear elastic leg and schematic presentation of oleo-pneumatic shock absorber. Animation sequence of dynamic simulation of 'drop-test' - numerical testing of elastic leg dynamical characteristics and data validation (JAR-25).*

A floating piston in the second-stage cylinder separates hydraulic fluid and high pressured nitrogen. During a compression stroke, floating piston does not become active until gas pressures of the first-stage and second-stage chambers are equal, which happens during system increased dynamical loading. Dynamical characteristics of shock absorber are strongly influenced by systems of orifices that control hydraulic flow and by means of which net hydraulic resistance can be tuned. Considering different possibilities of activation of floating piston and orifices as the absorber closes, it can be shown that four operation stages can be identified during the compression stroke. During return stroke, primary control of recoil of shock absorber consists of fluid flow from the recoil chamber into oleo-pneumatic

chamber and from the oleo-pneumatic chamber into compression chamber. To prevent unit (and airplane!) excessive rebound, orifices hydraulic resistance increases significantly during the absorber recoil stroke.

Dynamical model

Since mechanical properties of landing gear shock absorber are mainly determined by the pneumatic spring force and oleo (hydraulic) damping force, dynamical model of the absorber are presented in the overall multibody system as a force coupling element (highly non-linear!) consisting of these terms.

All mechanical characteristics and geometrical data (AA, AC, AD etc., Fig. 2), needed to establish the mathematical model, are determined on the basis of CAD modelling according to manufacturer data. The cylinder-piston stick-slip friction phenomenon and internal seal friction are also introduced. The floating piston inertia effect is neglected in absorber dynamical model presented here.

Pneumatic spring force

Depending on the unit operational stage, pneumatic spring force is dependent on initial inflation pressure in two nitrogen chambers and influenced by change of volume of the shock absorber (variation of kinematical configuration of the unit). During modeling, it is assumed instantaneous gas compression ratio in accordance with the polytrophic law for compression. Since absorber high rate of compression is expected to occur during landing impact, a polytrophic exponential term is chosen as $n = 1.3$ during modeling of all internal processes [6]. By having considered geometrical determinations of gas chambers (volumes *VL1, VL2*, Fig. 2) in dependence of unit kinematical configuration and after determination of initial gas inflation pressure, the net pneumatic force is expressed as a non-linear function of shock absorber stroke.

Hydraulic damping force

Hydraulic damping force results from the pressure difference associated with the flow through the systems of orifices. It is assumed that jet velocities and Reynolds numbers are sufficiently large that flow is fully turbulent (orifice area is small in relation to the absorber diameter). As a result, the net damping force is expressed as a function of the stroke velocity. Since during compression stroke some orifices become active/inactive (orifices *K3* change their position as the absorber closes), the net hydraulic damping force is modeled *via* two stage discontinuous function of the absorber stroke velocity. Orifice hydraulic resistance damping coefficients *K1, K2, K3* (Fig. 2) are estimated on the basis of orifice geometry and hydraulic fluid density. Prior to dynamic simulations of landing aircraft, dynamical model of shock absorber has been validated by numerical dynamical simulations (Fig. 2) of landing gear drop test ([1] paragraphs 25.723-25.727).

DYNAMIC SIMULATION PROCEDURES

On the basis of aircraft dynamical model, dynamic simulations of landing cases of large transport aircraft were performed for various initial descent velocities and different lateral wind conditions. Mass of the aircraft is set as 64500 kg and horizontal velocity equals $v_{x1} = 67.5$ ms^{-1}. The initial aircraft pitch and roll angles prior to touchdown are 10^o and 3^o respectively, while the aircraft pitching and rolling velocity at the instant of touchdown is assumed to be approximately zero. The animation sequence of landing airplane with present lateral wind is shown in Fig. 3. Time evolution of shock absorber total force in the right elastic leg during different landing cases, when descent velocity is varied in the range from $v_{z1} = 0.25$ ms^{-1} to $v_{z1} = 1.25$ ms^{-1} is presented in Fig. 4.

Landing cases with indicated touchdown parameters do not represent demanding landing scenarios for a modern transport airplane. During simulated landing impacts, absorber stroke time evolution is well within a range of 0.45 m (max. stroke) and no upper-point cylinder-piston collision occurred during analysed landing cases (which does not mean that stick-slip transitions can not occur within shock-absorber mechanism). The undercarriage load factors are also well in the prescribed range. It is evident that diagram of time evolution of shock absorber total force is almost flat immediately after the touchdown. This is due to the fact that shock absorber pneumatics is still not active during this period of activation (pneumatic force acts as a set-up spring) and tire dynamics affects the overall system motion dominantly. This is more emphasised for lower initial descent velocities.

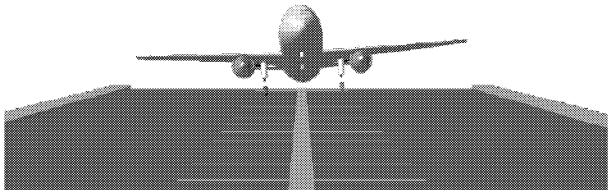

Figure 3.: *Animation sequence of landing airplane with present lateral wind – one gear landing case.*

In the cases of landing impacts with larger touchdown descent velocities, a set-up value is quickly reached and damping hydraulic component builds up very fast after the impact, provoking thus a big gradient of the absorber total force soon after the moment of touchdown. Of course, left shock absorber force and stroke diagrams (not shown here) have an additional time delay due to the fact that left elastic leg comes to the contact with the ground later on during landing process, depending on the aircraft geometry and rolling motion. Discontinuities visible at shock absorber total force characteristics in Fig. 4 are due to different working regime of the orifices (inactive/active K3 orifices, Fig. 2) and due to the change of pneumatic force at the point where floating piston of second-stage pneumatic cylinder becomes active.

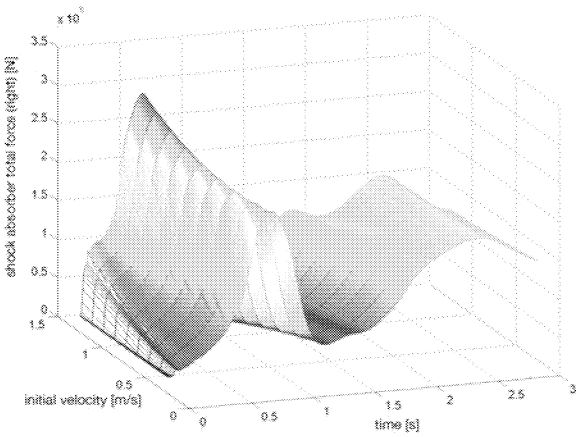

Figure 4.: *Shock absorber total force vs time (right el. leg).*

As presented shortly here, dynamic simulator is based on determination of dynamical response of the modeled aircraft for specified initial conditions, airplane aerodynamic configuration and generalized loads (schematic layout of simulator global architecture is presented in Fig. 5). The accuracy of final numerical results is well within required tolerancies, which allows for utilization of the developed mathematical model to serve as a solver of a flight procedure trainer that would focus on different landing routines.

Figure 5.: *Schematic layout of dynamic simulator 'global' architecture.*

REFERENCES

[1] Joint Aviation Requirements, 1996, JAR-25, Large Aeroplanes.

[2] Chester, D. H. 2002. "Aircraft Landing Impact Parametric Study with Emphasis on Nose Gear Landing Conditions", *Journal of Aircraft*, 39, 394-403.

[3] Currey, N. S. 1988. *Aircraft Landing Gear Design: Principles and Practices*, AIAA.

[4] Terze, Z. et al, 2001. "Null Space Integration Method for Constrained Multibody System Simulation with no Constraint Violation", *Multibody System Dynamics*, 6, 229-243.

[5] Smiley, R. F. and Horne, W. B. 1958. "Mechanical Properties of Pneumatic Tires with Special Reference to Modern Aircraft Tires", NACA Report No. 4110.

[6] Yadav, D. and Ramamoorthy, R. P. 1991. "Nonlinear Landing Gear Behaviour at Touchdown", *Journal of Dynamic Systems, Measurement, and Control*, 113, 677-683.

BIOGRAPHY

Prof. dr. Zdravko Terze, Head of Dept. of Aerospace Engineering, received Ph.D. degree (1996) from Univ. Zagreb. As invited scientist he pursued his research in domain of computational dynamics of multibody and structural systems at University of Brussels and University of Stuttgart. Prof. Teze conducted several research programmes supported by National Scientific Fund, EU research funds and industrial partners in domain of numerical modelling and computational dynamics of structures and multibody systems, aircraft system dynamics and computational aeroelasticity. Prof. Terze published number of scientific papers in int. journals and proceedings and served as organizer and member of scientific comitees of international symposia in EU and USA. Addresses: http://www.fsb.hr/aero/zterze_en.htm, zterze@fsb.hr

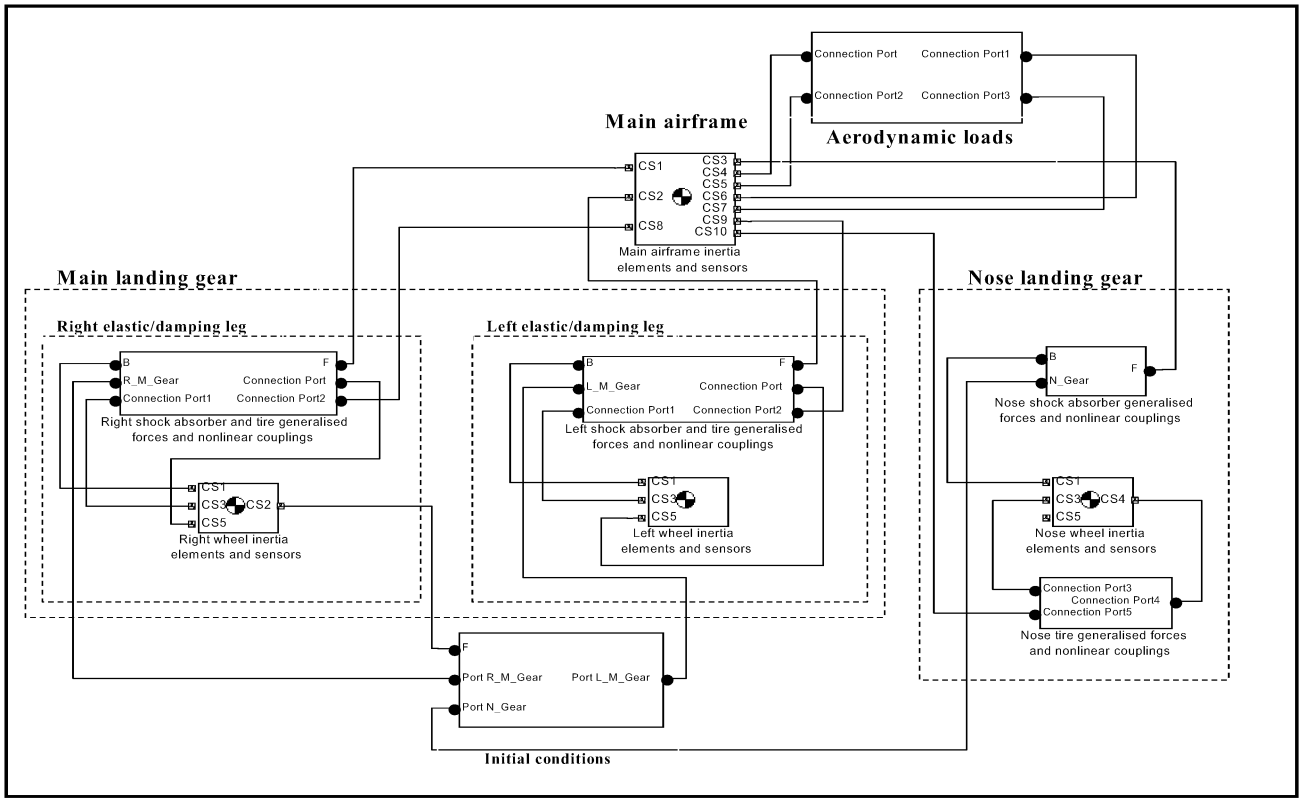

DEVELOPING A FRAMEWORK FOR DISCRETE EVENT SIMULATION OF AIRCRAFT PISTON ENGINE OVERHAUL PROCEDURES

Reza Azadegan
Maghsud Solimanpur
Department of Mechanical Engineering
Urmia University
Urmia, 57169-33111,Iran
E-mail: azadegan@engineer.com

KEYWORDS
Discrete Event Simulation, Overhaul, Aircraft Piston Engines.

ABSTRACT

In this paper aircraft piston engines overhaul procedures are studied and discussed. Then elements of the model for discrete event simulation of these operations are mentioned. Different events, required algorithms and methods are indicated and finally, parameters of interest and their gathering in the simulation model are studied. Because of the similarities among different aircraft piston engines and as a result their overhaul operations, findings of this research can be used as a framework for similar simulation studies.

INTRODUCTION

Stochastic nature of defects, failures, material and part routings, distribution of repair and inspection tasks make analytical methods difficult or impossible to observe and analyze the function of aircraft maintenance environments. Also because queues in such a complex system are usually G/G/c type, simulation is one of the few possible way to analyze the system behavior.

One of the main goals of any aircraft maintenance enterprise either civil or military is improving readiness and availability of the aircrafts. This availability is defined as:

$$A_o = \frac{MTBM}{MTBM + MDT}. \qquad (1)$$

Mean Time Between Maintenance (*MTBM*) is increased by increase of reliability and Mean Down Time (*MDT*) is reduced by reduction of repair cycle time (Blanchard 1997). Related analysis is among capabilities of simulation models.

Discrete event simulation can estimate different parameters of system such as work in process (*WIP*), throughput rate, repair cycle time, utilization rate of servers, mean queue length for servers, spare parts requirements, etc. Simulation works specially well in diagnosing how systems respond to changes done in workflow.

Estimations mentioned above provide a powerful tool for management and engineering decision-making in aviation industries. Engine overhauls are usually performed because of one of these reasons: accumulation of time between overhaul (*TBO*) which usually ranges between 800 to 1500 hrs, engine sudden stoppage, degradation in performance, excessive metal particles in the oil, any defect detection or failure (Jeppesen 1997) and (Kroes and Wild 1995). In such conditions engine is removed, packed and sent to an authorized overhaul shop. Procedures and the elements of the model, which are developed in this research, are started from this point and are continued to engine departure from system.

PISTON ENGINE OVERHAUL PROCEDURES

For modeling any system, the processes are to be understood and documented (Rus 2003). In this paper, all main procedures of overhaul operations are typically extracted from references (Jeppesen 1997) and (Kroes and Wild 1995) and documented in the form of process flow charts. As illustrated in Figure 1, after completion of reception and related inspections, a work scope is prepared. In parallel, all technical documents are reviewed and necessary procedures are arranged according to related service bulletins or documents. After this stage and in the case of confirming the computed overhaul cost, engine will be externally cleaned and disassembled. In addition, in this stage engine components will be preliminarily inspected. It is assumed that engine will be disassembled to fourteen types of parts and six types of accessories as shown in Table 1. According to Figure 1, after degreasing the main parts, some of them will go to stripping and the others will be coated with inhabiting oil. For repair and inspection of all the parts and accessories mentioned in Table 1, a separate process flow chart has been prepared in this research, though these are not reported in this paper due to space limitation.

Figure 2 shows repair and inspection flow chart of the crankshaft. Depicted work flow is explained as follows. First, crankshaft will be visually inspected. After completion of visual inspection, if the part is not rejected, it will go through other inspections. Key components must be structurally inspected to verify their integrity. If a structural inspection reveals a faulty part, it should be rejected and replaced with a new one (Jeppesen 1997). Structural inspections usually are of type NDT and piston engine parts are inspected by magnetic particles inspection for ferrous metals and penetrant liquid method for non-ferrous parts.After crankshaft is inspected by magnetic particles, if not rejected, it will go through dimensional inspection. Data from this inspection in addition to data from crankcase dimensional inspection in its temporary assembly will be recorded and compared. Figure 2 also shows that by the end of inspections, crankshaft will be sent to one of the stages of polishing, grinding or cleaning considering the defect found and required repair. If it is not accepted, the part will be rejected or repaired again regarding its condition and possibility of correction.

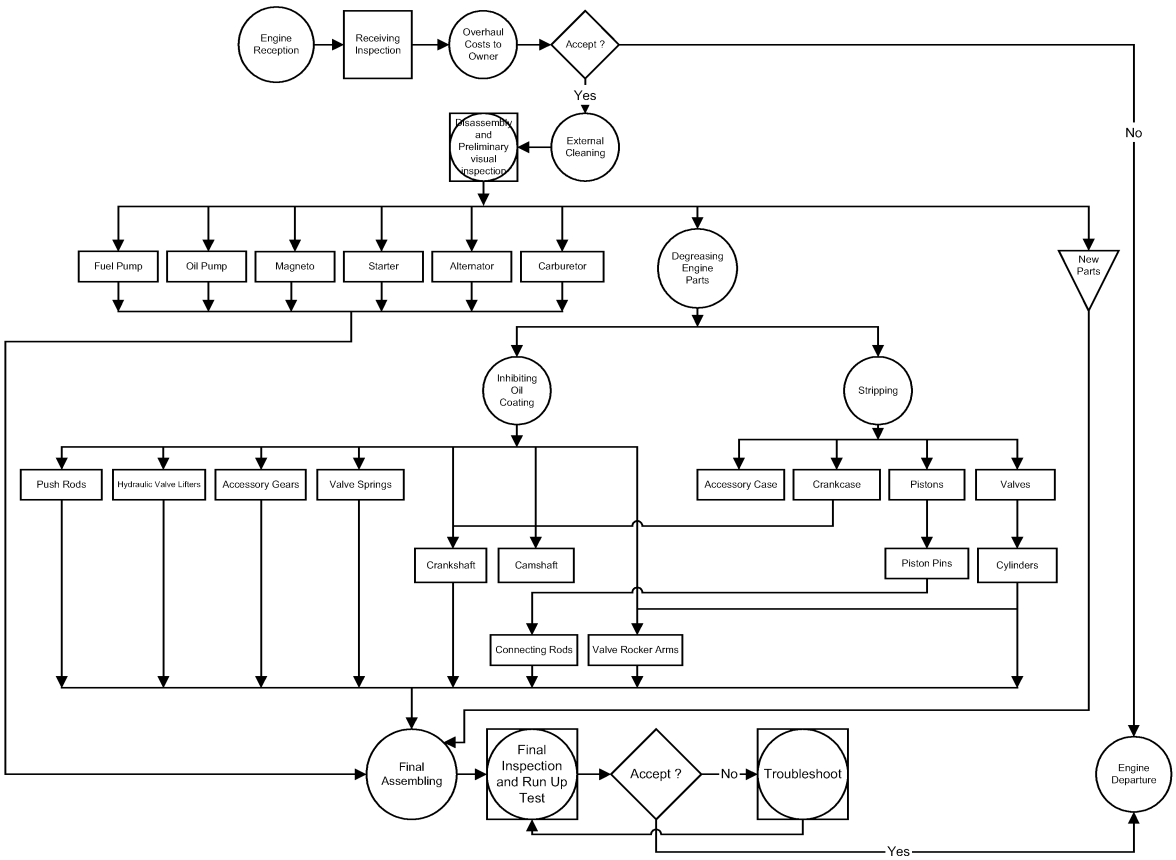

Figure 1 : Aircraft Piston Engine Overhaul Operation Procedures

Table 1 : Engine Parts and Accessories

Engine Main Parts	Accessory Case, Camshaft, Connecting Rods, Crankcase, Crankshaft, Cylinders, Accessory Gears, Hydraulic Valve Lifters, Piston Pins, Pistons, Push Rods, Valve Rocker Arms, Valves, Valve Springs
Engine Accessories	Alternator, Carburetor, Fuel Pump, Magneto, Oil Pump, Starter

A grinded part is inspected and if accepted, is nitrided. All nitrided parts as well as those, which come to polishing directly after inspections, are polished and sent to preassembly cleaning, if polishing accepted. The parts without any defect directly go to preassembly cleaning after accomplishing dimensional and magnetic particles inspections.

Finally engine parts and accessories will be assembled according to the manufacturer's instructions. Then final inspection and engine run up test are done. If engine performance is accepted, engine will leave the shop for installation on the aircraft.

Probabilities of finding defect, its repairability, and required repair type in different inspection stages are depicted by special codings. For instance, in visual inspection of crankshaft, probability of finding any defect is shown by p_1. A defected part is rejected (not repairable) with probability p_2 and it will be diagnosed to be repairable by probability $1\text{-}p_2$. A repairable part is sent to grinding with probability p_3 or to polishing with probability $1\text{-}p_3$. Table 2 contains possible defects, inspection and treatment methods for crankshaft.

MAIN ELEMENTS OF THE MODEL

It is worth to define some terms before discussing main elements of the model. These terms are as follows (Banks and Carson 1984) :

State: A collection of parameters, which contains all data to describe the system in any moment.

Entity: Any part of the system, which needs to be defined clearly in the model.

Attributes: Characteristics of an entity.

Event: A momentary event, which changes state of the system.

Activity: a time interval whose end is determined by its beginning.

This model assumes an engine as the main entity which is decomposed into elements as mentioned in Table 1. Figure 3 shows the general structure of the model. In setup stage, initial values of all parameters and variables including distribution of service times, different probabilities used in the model, initial state of the system, number of different servers, simulation termination conditions, etc. are defined. In time advancement stage, Future Events List (FEL) will be evaluated. FEL contains data about the event type, event time and related engine number.

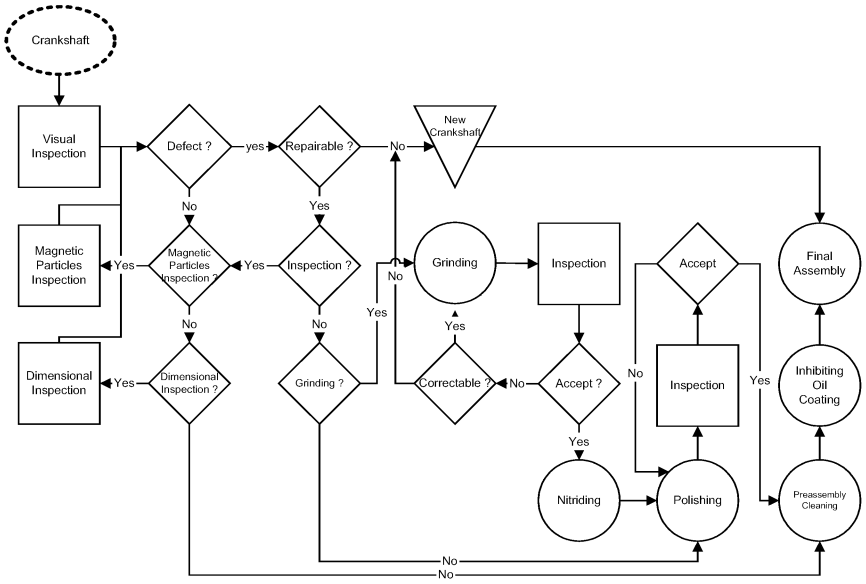

Figure 2 : Crankshaft Inspection and Repair Procedures

Table 2 : Crankshaft Possible Defects, Inspection and Treatment Methods

Possible Defects	Inspection	Treatment
Burning, Pitting, Scoring or spalling journal bearing surfaces	Visual Inspection	-Remove by polishing if it is possible. -Grind crankshaft to undersize and use undersize bearings if it is possible. -Replace crankshaft.
Fatigue & Heat Cracks	Magnetic Particle Inspection	-Replace crankshaft.
Main Bearing Journals clearances exceed Limitations	Dimensional Inspection	-Grind crankshaft to undersize and use undersize bearings if it is possible. -Replace crankshaft.
Rod Bearing Journals Clearances exceed Limitations	Dimensional Inspection	-Grind crankshaft to undersize and use undersize bearings if it is possible. -Replace crankshaft.
Crankshaft Runout exceeds Limitations	Dimensional Inspection	-Replace crankshaft.

At this stage, the earliest event is called from FEL and run, accordingly. In this research, a number of 140 events have been recognized, of which those related to crankshaft are reported in Table 3. The flow chart associated with each event is then drawn, which shows how the state of system is changed when corresponding event takes place.

For example, Figure 4 illustrates the changes in the state of system when event "Leaving Crankshaft Visual Inspection" takes place. Based on entity's recorded attributes, sending crankshaft to required repair station would be programmed after accomplishment of the last inspection stage. If there is any entity in the server queue, queue assessment will be called. Since different servers perform different jobs, each job is represented by a code.

In queue assessment stage, based on this code, future event is added to FEL. Table 4 illustrates different server types and number of jobs done by each server.

In the proposed model some delay lists (DLs) are used to keep entities whose move has been stopped. Main types of these lists are arrays that keep entities waiting in the queues of servers. However, in the simulation of overhaul procedures there might be other conditions that an entity cannot move without their satisfaction. For example, inspection of crankshaft needs the data to be obtained from inspection of crankcase. In this case, after "crankshaft inhabiting oil coating", it is kept in a delay list till fulfillment of crankcase inspections. The Delay list and the logic needed to transfer entities to and from this list is defined to manage such conditions. Evaluation of DL is done at the beginning of control stage. After examining DL and programming future events, the simulation termination conditions are checked. In report stage, gathered data and statistics are used to calculate the parameters of interest. These issues are discussed in detail in subsequent section.

PARAMETERS OF INTEREST

The main objectives of this model are to provide precise and reliable estimations about throughput rate, work-in-process inventories and repair cycle time. Their relation is explained through Little's law by equation (2) (Little 1961).

$$TH = WIP / RCT. \qquad (2)$$

Where, *TH* is the throughput rate, *RCT* is the repair cycle time, and *WIP* is the work-in-process.

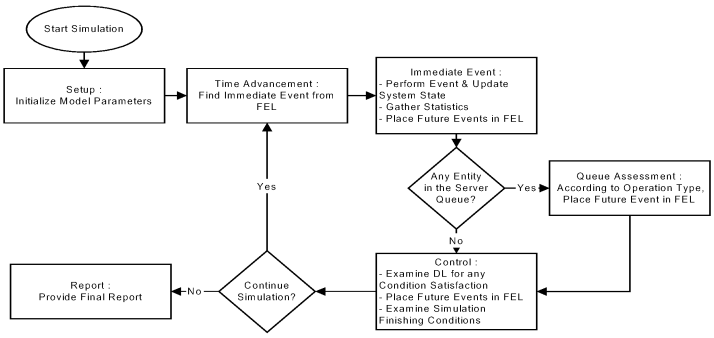

Figure 3 : General structure of the model

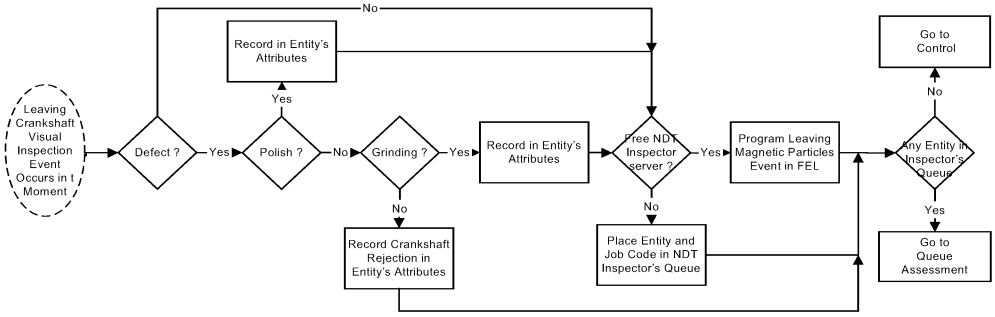

Figure 4 : Leaving Crankshaft Visual Inspection Event

Generally throughput is defined as the number of engines which have fully passed overhaul procedures. This parameter would be more important if the purpose of simulation is to evaluate whether a system has sufficient capacity to cope with the works assigned to (Hopp and spearman 2000).

Repair cycle time is defined as the time between engine arrival and departure. Repair cycle time is calculated by

$$RCT = \sum_{i=1}^{n} \frac{T_{di} - T_{ei}}{n}, \qquad (3)$$

where T_{ei} is entrance time of ith engine and T_{di} is departure time of that. The parameter n is the number of departed engines within simulation time.

Two kinds of information are recorded for calculating *WIP*. The first is the number of engines in the system and the second is the time at which this number changes. *WIP* at time t can be estimated by

$$WIP = \sum_{i=1}^{n} N_i (T_{i+1} - T_i) / t, \qquad (4)$$

Where N_i is the ith recorded number of engines, T_i is the time at which N_i is recorded. It is to be noted that in the proposed model the maximum amount of *RCT* and *WIP* are also estimated. Without loss of generality, the parameters mentioned in equations (2), (3) and (4) can be applied for each station. The proposed model also provides information about the utilization rate of servers. In long term, utilization rate of each server equals mean process time divided by mean arrival time. However, since in this model each server can do several kinds of jobs, the utilization rate is calculated by equation (5).

$$u = \frac{T_b}{ct}. \qquad (5)$$

Where T_b is the time within which servers are busy, c is the number of servers and t is the simulation time. Over long run, mean waiting time can be approximated by equation (6) (Allen 1990).

$$\varphi_q = \frac{(c_a^2 + c_e^2)}{2} \times \frac{u\sqrt{2(c+1)} - 1}{c(1-u)} \times t_e \qquad (6)$$

Where $c_a = \sigma_a / t_a$ is variability of arrival, $c_e = \sigma_e / t_e$ is variability of processing, σ_a is standard deviation of arrival and σ_e is standard deviation of processing. The parameters t_a and t_e are mean arrival and mean processing times, respectively.

Equation (6) reveals that waiting time will drastically increase in a non-linear manner, if utilization rate increases, because U term (i.e. u / (1-u)) will increase in that fashion as shown in Figure (5). If $u \geq 1$ the workstation is not stable and the queue length and waiting time go to infinity. Cycle time in any workstation is composed of waiting time calculated by equation (6), process time and any other non-productive times. Then increase of utilization will also affect on related cycle time. As described, reducing repair cycle time is the main goal of any aircraft maintenance enterprise.

Table 3 : Events Related to Crankshaft Inspection and Repair Procedures

No	Event Type	Related Server
1	Leaving Crankshaft Visual Inspection	Inspector
2	Leaving Crankshaft Magnetic Particles Inspection	NDT Inspector
3	Leaving Crankshaft Dimensional Inspection	Inspector
4	Leaving Crankshaft Polishing	General Mechanic
5	Leaving Crankshaft Polishing Inspection	Inspector
6	Leaving Crankshaft Grinding	Machinist
7	Leaving Crankshaft Preassembly Cleaning	Cleaner
8	Leaving Crankshaft Grinding Inspection	Inspector
9	Leaving Crankshaft Nitriding	Coating Mechanic
10	Leaving Crankshaft Inhabiting Oil Coating	Cleaner

Table 4 : Server Types and Number of Jobs they Perform

No	1	2	3	4	5	6	7	8	9	10	11	12
Server Type	Inspector	Cleaner	Accessory Mechanic	Accessory Inspector	Electric Mechanic	Electric Inspector	Assembly – Disassembly Mechanic	General Mechanic	NDT Inspector	Machinist	Coating Mechanic	Office Staff
Number of Jobs	40	26	12	6	12	6	3	14	8	3	2	2

Thus estimating the capacity needed to keep utilization sufficiently low to reduce RCT will be a worth objective of this simulation model. Alternatively, if high utilization is a goal of interest in an overhaul workshop, the only possible solution regarding equation (6) is controlling the process and arrival variations to eliminate effect of a large U term (Standrige 2004).

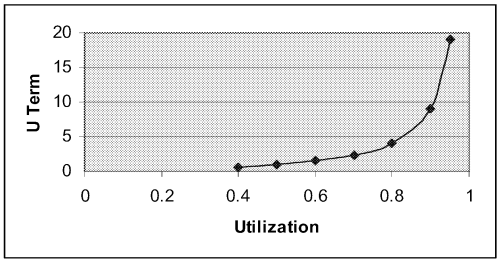

Figure 5 : U Term versus Utilization

CONCLUSION

Aircraft piston engine overhaul procedures are documented through flow charts in this paper. These charts illustrate procedures for fourteen types of parts and six types of accessories. Then events of the system are extracted and their effects on the system states are documented. This information is only provided for crankshaft in this paper. Different data required in this model are reviewed and methods to gather them in the model are discussed. Findings of this research including overhaul procedures, elements of the model, algorithms, flow charts and methods can be used as a tool in the simulation of aircraft piston engine overhaul shops.

REFERENCES

Allen, A.O. 1990. Probability, statistics, and queuing theory with complex science applications. Academic Press, NY.

Banks, J. and J.S. Carson. 1984. *Discrete-Event System Simulation,* Prentice-Hall.

Blanchard and S. Benjasmin. 1997. *Logistics Engineering and Management.* Prentic Hall.

Hopp, W.J. and M.L. Spearman. 2000. *Factory physi*cs, McGraw-Hill, Boston, MA.

Jeppesen Sanderson. 1997. *A&P Technician Poweplant Textbook* ,Englewood.

Kroes, M.J. and T.W. Wild. 1995. *Aircraft Powerplants.* McGraw-Hill.

Little, J.D.C. 1961. "A Proof for Queuing Formula $L=\lambda w$ ". *Operations Research*. Vol. 16, pp. 651-657.

Rus, I.; H. Neu; and J. Muench. 2003. "A Systematic Methodology for Developing Discrete Event Simulation Models of Software Development Process" *In Proc. of Software Process Simulation Modeling Workshop (ProSim 2003),* Portland, OR.

Standrige, C.R. 2004. "How Factory Physics Helps Simulation". In *Proc. 2004 Winter Simulation Conf.*, pp 1103-1108.

BIOGRAPHY

REZA AZADEGAN got his bachelor's from C.A.T.C., Tehran, Iran in 2003. He is currently a MS. student of mechanical engineering in the Urmia University, Urmia, Iran. His field of research is modeling and analyzing aeronautical maintenance procedures.

MAGHSUD SOLIMANPUR has got his Ph.D. from Indian Institute of Technology Delhi, New Delhi, India in 2003. He is an Assist. Prof. in the Faculty of Engineering, Urmia University, Urmia, Iran. His fields of research are Operations Research, Simulation, Production Management, Manufacturing Systems Engineering.

ANALYZING OVERHAUL CYCLE TIME OF A TYPICAL AEROENGINE OBTAINED FROM SIMULATION

Maghsud Solimanpur
Reza Azadegan
Department of Mechanical Engineering
Urmia University
Urmia, 57169-33111, Iran
E-mail: m.solimanpur@mail.urmia.ac.ir

KEYWORDS
Overhaul Cycle Time, Simulation, Point and Confidence Interval Estimations.

ABSTRACT

We have proposed a discrete event model to simulate overhaul cycle time of a typical aeroengine. In this paper, effect of initial condition of the system on cycle time is studied and then point and confidence interval estimations are obtained for cycle time. Initial conditions of the system are studied by dividing the simulation time into different groups and studying if there is a significant difference between mean cycle time of the groups. By the result first 10000 minutes of simulations are removed from further calculations. Then Number of required simulation replications are determined and estimations for cycle time are calculated.

INTRODUCTION

Aircraft maintenance environments are usually more complex than to be studied analytically. This means that computer simulations are essential in design and analysis of such systems. Stochastic nature of these simulations makes simulation output data analysis an important issue. Studying effect of initial state of the system on simulation output and giving estimations for them are among the important parts of this subject. For more information (Law and Kelton 1991) and (Banks and Carson 1984) can be seen.
We have proposed a discrete event dynamic system model to simulate overhaul cycle time of a typical aircraft piston engine. In this paper, overhaul cycle time obtained from simulation response is analyzed. Obviously, initial state of the system is among the factors which affect the cycle time obtained from the simulation model. This paper aims at analyzing the effects of this factor in the cycle time through least significant difference method.
The simulation model attempted in this paper is verified and validated by analyzing simulation behavior using some rules governing the system. This is done by gathering some parameters underlying system behavior in simple scenarios and then analyzing them. Some of these rules are number of engines, assembly requirements, conservation law, utilization, waiting time, bottleneck rate, spare parts and confirmation probability of repairs.

In the following section of this paper overhaul procedures of piston engines are generally described. Then a brief statistical background of the problem is presented. This presents how point and confidence interval estimations are done. After that effect of initial state of the system on simulation output is studied and first 10000 minutes of simulation are removed from further analysis. This is done by studying least significant difference between mean of groups. Then using ten initial simulation runs, number of replications required to give confidence interval with a desired accuracy is determined. Finally, required replications are done to compute point and confidence interval estimations for the engine overhaul cycle time.

OVERHAUL PROCEDURES

Engine overhaul procedures attempted in this paper has been developed with respect to the processes given in (Jepppesen Sanderson 1997) and (Kroes and Wild 1995). These procedures are documented in the form of process flow charts. Figure 1 illustrates a general look at the overhaul procedures of a typical aircraft piston engine. After engine reception and related inspections, a cost estimation of overhaul repairs is sent to the owner. If the cost of overhaul is economical and owner confirms it, engine will enter the workshop and go for external cleaning, disassembly and preliminary visual inspection. Dotted section of Figure 1 points to cleaning, inspection and repair of engine parts and accessories. In fact, in this stage different parts will go through different procedures. As a part of model development, for all main parts of a four cylinder opposed piston engine, flow charts are drawn to determine how their cleaning, inspection and repair operations are done.
It is assumed that final assembly will begin if all the parts and accessories are ready. By the end of final assembly, engine will go for final inspection and run up test. Finally, if engine overhaul is accepted, engine will depart the system.

STATISTICAL BACKGROUND

In this model, times between engine entrance to workshop and departure from it are gathered for cycle time estimations. Entrance point of workshop is where engine overhaul cost is confirmed by the owner and engine starts to proceed the overhaul procedures.
Both point and confidence interval estimations are done for cycle time. Let us assume that the computerized overhaul

simulation model developed in this research is run for *R* replications each with 120000 minutes length. In this experimentation each replication is further divided into 12 groups each with 10000 minutes length. Then mean cycle time of each replication is computed by Equation (1).

$$\overline{X}_{r.} = \frac{\sum_{g=1}^{12} \overline{X}_{rg}}{12}, \qquad (1)$$

where $\overline{X}_{rg}$ is the mean cycle time of group *g* of replication *r*. Finally, a consistent estimation of mean cycle time can be obtained by

$$\overline{\overline{X}} = \frac{\sum_{r=1}^{R} \overline{X}_{r.}}{R}. \qquad (2)$$

A point estimation for cycle time variance can be calculated by

$$s^2 = \frac{\sum_{r=1}^{R} (\overline{X}_{r.} - \overline{\overline{X}})^2}{R-1}. \qquad (3)$$

Due to Central Limit Theorem and with respect to long simulation runs, the distribution of $\overline{X}_{r.}$ converges to normal distribution. Therefore, an interval estimation for μ with ((1-α)×100)-percent confidence can be obtained by

$$\overline{\overline{X}} - t_{\alpha/2,R-1}\frac{s}{\sqrt{R}} \le \mu \le \overline{\overline{X}} + t_{\alpha/2,R-1}\frac{s}{\sqrt{R}}, \qquad (4)$$

where $t_{\alpha/2,R-1}$ is the corresponding Student-t value with *R-1* degree of freedom and α/2 coverage in each side.

INITIAL STATE

In any simulation run, there is a bias related to the initial state of the system. It could be eliminated by one of the following methods (Banks and Carson 1984):

(1) gathering data about the system and defining initial states
(2) dividing simulation time to two stages: initialization and data gathering. This method should be done regarding two matters. First, by the end of initial stage a stable condition should be reached and second, data gathering stage should be long enough to allow precise estimations in stable state of system.

For this reason, ten replications have been considered in this experimentation. Table 1 includes mean cycle time of each group obtained from simulation program where simulation starts with empty conditions.

It is seen that the mean cycle time of first group of each replication is less than the others. This is due to the effects of initial conditions of the system. Table 2 shows mean and accumulative mean of each group. It also contains accumulative means calculated after removing the data of first and second groups.

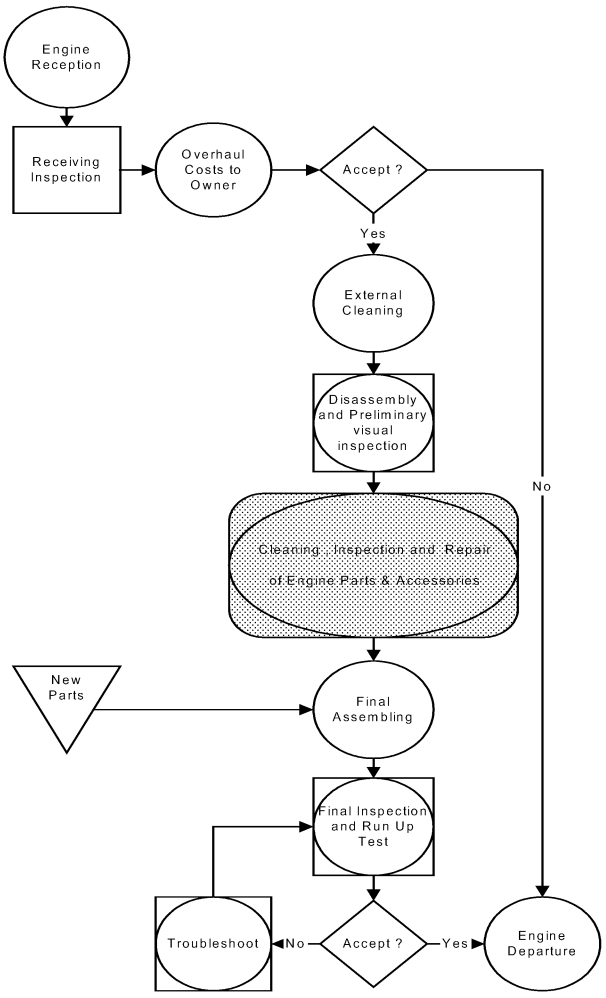

Figure 1: General Practices of Overhaul

Table 1 : Mean Cycle Time of Groups

Group	Replication									
	1	2	3	4	5	6	7	8	9	10
1	3744	3702	3781	3528	3755	3653	4140	3668	4193	3411
2	4275	3804	4265	3729	3993	3829	4306	4044	4040	4311
3	4086	3957	3730	4008	4063	4073	4570	3980	3643	4212
4	3908	4036	4071	4027	4424	4244	4220	5166	3717	3879
5	4232	4147	3620	4013	4002	4099	4161	4493	3842	4085
6	3981	3824	3574	3780	4302	4143	4206	3712	4029	4011
7	3758	3969	3818	3979	3940	3955	3970	3450	4177	4006
8	4109	4163	4184	4215	3738	4291	4088	3813	3975	3746
9	4055	4010	4279	3963	4149	4237	4053	4432	3690	3802
10	4281	3927	4012	3771	4039	4321	4080	4827	4244	3679
11	4062	4013	3785	3985	3723	3790	4212	4029	4135	4280
12	3879	3985	3820	4180	4461	3947	4287	4031	4263	3957

Table 2 : Mean and Accumulative Mean of Groups

Group	Mean	Accumulative Mean (Without removing)	Accumulative Mean (After removing group 1)	Accumulative Mean (After removing groups 1 and 2)
1	3757.5	3757.5	-	-
2	4059.6	3908.55	4059.6	-
3	4032.2	3949.77	4045.9	4032.2
4	4169.2	4004.63	4087	4100.7
5	4069.4	4017.58	4082.6	4090.267
6	3956.2	4007.35	4057.32	4056.75
7	3902.2	3992.33	4031.467	4025.84
8	4032.2	3997.31	4031.571	4026.9
9	4067	4005.06	4036	4032.629
10	4118.1	4016.36	4045.122	4043.313
11	4001.4	4015	4040.75	4038.656
12	4081	4020.5	4044.409	4042.89

Least Significant Difference (LSD) method is used to compare these group means (Fisher 1935). First, variance in different groups is studied. To do so, analyze of variance (ANOVA) (Montgomery 2004) is done for groups by :

$$SS_T = (3744)2 + (3702)2 + \ldots + (3957)2 - \frac{(482460)^2}{120} = 8082896$$

$$SS_G = \frac{(37575)^2 + (40596)^2 + \ldots + (40810)^2}{10} - \frac{(482460)^2}{120} = 1293169$$

$$SS_E = SS_T - SS_G = 6789726$$

Where SS_T is total sum of squares, SS_G is sum of the squares of groups and SS_E is sum of the squares of errors. Corresponding mean of squares are computed through dividing sum of squares by the degrees of freedom. Critical F is then calculated by

$$F_c = \frac{117560}{62867} = 1.869$$

This analysis of variance is shown in Table 3.

Table 3. Group ANOVA

Source of Variation	Sum of Squares	Degree of freedom	Mean Square	Critical F
Group	1293169	11	117560	1.869
Error	6789726	108	62867	
Total	8082896	119		

Critical F obtained from this ANOVA is less than the value given in F distribution table in both 0.05 and 0.01 levels. This reveals that there is no significant difference between variance of the groups. By this assumption, LSD can be used to compare the mean of the groups by

$$LSD_{\alpha/2} = \sqrt{\frac{2S_E^2}{R}} \times t_{\alpha/2,f} . \qquad (5)$$

Where S_E^2 is the variance of error and $t_{\alpha/2,f}$ is the corresponding Student-t value with $f = G(r\text{-}1)$ degree of freedom and covering α/2 in each side. Using Equation (5), least significant difference for 0.05 and 0.01 levels can be calculated:

$LSD_{0.025} = 222.01$ and $LSD_{0.005} = 293.44$.

Comparing mean of groups with this LSDs illustrates that only mean of the first group has significant difference with the others.

Figure 2 illustrates mean and accumulative mean of groups. It is clear that by removing data from first group, the bias resulted by initial conditions of the system will be eliminated.

ACCURACY AND REPLICATIONS

An important issue associated with a simulation run is the accuracy with which the parameter of concern is estimated. In this research, the accuracy of mean cycle time is assumed to be ε = ± 60 minutes. The Number of required replications or runs depends on the accuracy of interest.

Minimum number of required replications can be determined using Equation (6) (Banks and Carson 1984).

$$R \geq \left(\frac{t_{\alpha/2,R-1} \, S_\circ}{\varepsilon} \right)^2 , \qquad (6)$$

where $S_\circ$ is the standard deviation error obtained by the data of ten replications reported in Table 1. Since $t_{\alpha/2,R-1} \geq Z_{\alpha/2}$, Equation (7) can be used for initial estimation of R :

$$R \geq \left(\frac{Z_{\alpha/2} S_\circ}{\varepsilon} \right)^2 . \qquad (7)$$

Where $Z_{\alpha/2}$ represents the standard normal statistics covering α/2 in each side. Using equation (7), the required number of replications should be at least:

$$\frac{Z_{\alpha/2}^2 \, S_\circ^2}{\varepsilon} = \frac{(1.96)^2 \, (8290.01)}{(60)^2} = 8.84 .$$

Therefore, Equation (6) is used for 10, 11 and 12 replications as shown in Table 4.

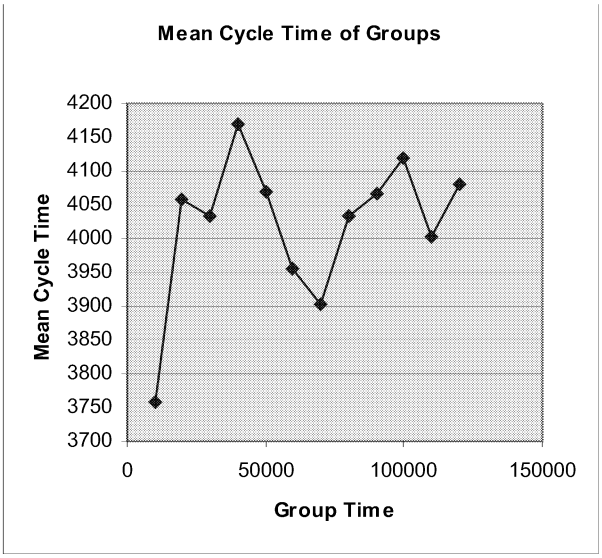

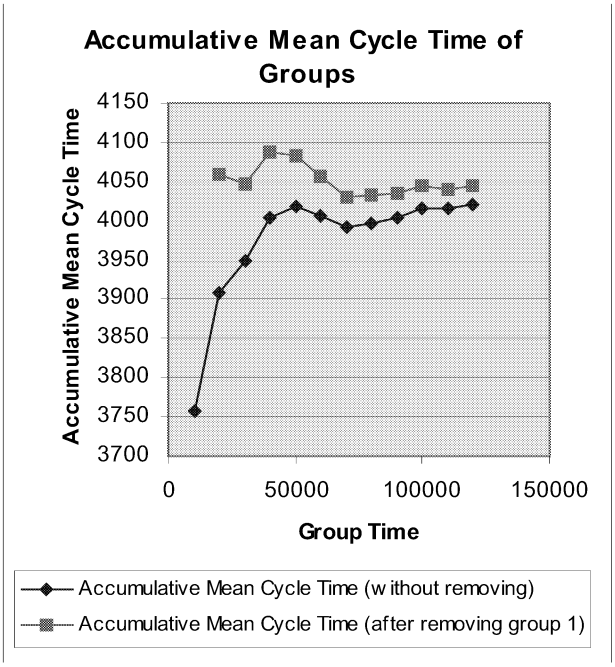

Figure 2: Mean and Accumulative Mean Cycle Time of Groups

Table 4 : Required Number of Replications

R	10	11	12
$t_{\alpha/2,\,R-1}$	2.26	2.23	2.2
$\left(\frac{t_{\alpha/2,\,R-1}\,S_\circ}{\varepsilon}\right)^2$	11.76	11.45	11.145

Since 12 is the smallest integer number satisfying Equation (7), at least 12 – 10 = 2 more replications are still required in order to estimate the mean cycle time with the specified accuracy. Since the standard deviation error, $S_\circ$, may change to some extent after inclusion of data of new replications, to assure consistency of results, three more replications have been considered in this research.

CYCLE TIME ESTIMATION

Regarding the data obtained from 13 replications of the simulation model, the point estimation of cycle time is obtained as

$\overline{\overline{X}} = 4049.98$ minutes.

Also, a 95% confidence interval with ε = ± 60 accuracy for this parameter is as follows.

$$4049.98 - 2.18 \times 22.24 \le \mu \le 4049.98 + 2.18 \times 22.24$$

This means that the mean time from entrance to departure of aircraft piston engines is between 4001.49 and 4098.46 minutes with 95% confidence.

FURTHER RESEARCH

There are different factors affecting overhaul cycle time like number of different servers, availability level of spare parts, bottleneck rate, etc. Studying the effects of these parameters on the cycle time can be scope of further researches. For example, developing methamodels, designing experiments or even doing optimizations on simulation response surface provide valuable tools to improve overhaul cycle time in aircraft piston engine maintenance workshops.

CONCLUSION

In this paper, effect of initial state of an aircraft piston engine overhaul workshop on the overhaul cycle time obtained from computer simulation is studied. By dividing simulation time to different groups, first 10000 minutes of simulation is removed from further analysis regarding its bias on cycle time estimations. Then using ten initial runs, required number of replications to give confidence interval estimation with a desired accuracy of ε = ± 60 minutes is determined as 13 replications. Finally, mean cycle time is estimated as 4049.98 minutes and a 95% confidence interval with ε = ± 60 accuracy for this parameter is given.

REFFERENCES

Banks, J. and J.S. Carson. 1984. *Discrete-Event System Simulation,* Prentice-Hall.

Fisher, R.A. 1935. *The Design of Experiments.* Edinburgh and London: Oliver and Boyd.

Jepppesen Sanderson. 1997. *A&P Technician Poweplant Textbook* ,Englewood.

Kroes, M.J. and T.W. Wild. 1995. *Aircraft Powerplants.* McGraw-Hill.

Law, A.M. and D. Kelton. 1991. *Simulation Modeling & Analysis.* McGraw-Hill.

Montgomery, Douglas C. 2004. *Introduction to Statistical Quality Control*. John Wiley.

BIOGRAPHY

MAGHSUD SOLIMANPUR was born in Urmia, West Azerbaijan Province, Iran. He has got his B.Tech and M.Tech. degrees from the Sharif University of Technology, Tehran, Iran and Ph.D. from Indian Institute of Technology Delhi, New Delhi, India in 2003. He is currently Assist. Prof. in the Faculty of Engineering, Urmia University, Urmia, Iran. His fields of research are Operations Research, Simulation, Production Management, Manufacturing Systems Engineering.

REZA AZADEGAN is an aircraft maintenance engineer. He got his bachelor's from C.A.T.C., Tehran, Iran in 2003. He is currently a MS. student of mechanical engineering in the Urmia University, Urmia, Iran. His field of research is modeling and analyzing aeronautical maintenance procedures.

USING PHYSICS OF THE SYSTEM IN VERIFICATION AND VALIDATION OF SIMULATING OVERHAUL PROCEDURES OF A TYPICAL AEROENGINE

Reza Azadegan
Maghsud Solimanpur
Department of Mechanical Engineering
Urmia University
Urmia, 57169-33111,Iran
E-mail: azadegan@engineer.com

KEYWORDS
Physics of the system, Verification, Validation, Simulation, Overhaul, Aeroengine .

ABSTRACT

We have used a discrete event dynamic system approach to simulate the work flow in a typical aircraft piston engine overhaul workshop. This paper describes how physics governing this system can help in verification and validation of its simulation model and program. Based on physics of the workshop, procedures and objectives of the simulation program, some parameters are programmed to be gathered, underlying the system behavior. These parameters provide an analytical foundation and some analytical relations between them can predict the responses of the program in simple scenarios. Discontentment of these relations, implies that either the model is not valid or the program is not correct and we showed the satisfaction of these relations and governing physics in our model.

INTRODUCTION

Aircraft maintenance environments are usually more complex than to be described by analytical methods efficiently. But analytical relations between different parameters of the system can be used to show some of the system behaviors and as a result be used in verification and validation of proposed model and simulation program. We have used a discrete event dynamic system approach to simulate the work flow in a typical aircraft piston engine overhaul workshop. This paper describes the parameters through which the verification and validity of the simulated model is tested. To do so, some data about the parameters of interest are obtained from simulation model and checked if they are correct and logical using analytical relations between them. How factory physics helps simulation is studied by (Standrige 2004), he has pointed some of the uses of this physics in verification and validation in his work. These governing physics of industrial environments are studied more by (Hopp and spearman 2000). Also verification and validation of simulation models are completely covered in (Sargent 1982, 1984, 1996, 2004) using different methods and techniques.

The remainder of this paper is organized as follows: Next section gives a view about overhaul procedures and proposed simulation model. Then, it provides some general background about verification and validation issues in simulation. The later section presents governing physics about number of engines, assembly requirements, conservation law, utilization, waiting time, bottleneck rate, spare parts and confirmation probability of repairs and the last section concludes this paper.

OVERHAUL PROCEDURES AND PROPOSED SIMULATION MODEL

The simulation model attempted in this paper has been developed with respect to the overhaul procedures given in (Jepppesen Sanderson 1997) and (Kroes and Wild 1995). These procedures are documented in the form of process flow charts. Figure 1 illustrates a general look at overhaul procedures of a typical aircraft piston engine. After engine reception and related inspections, a cost estimation of overhaul repairs is sent to the owner. If the cost of overhaul is economical and owner confirms it, engine will go for external cleaning, disassembly and preliminary visual inspection. Doted section of figure 1 points to cleaning, inspection and repair of engine parts and accessories. In fact, in this stage different parts will go through different procedures. As a part of model development, for all main parts of a four cylinder opposed piston engine, flow charts are drawn to determine how their cleaning, inspection and repair operations are done.
It is assumed that final assembly will begin if all the parts and accessories are ready. By the end of final assembly, the engine will go for final inspection and run up test. Finally, if engine overhaul is accepted, engine will depart the system.
After documenting the overhaul procedures, all events of the simulation system are identified. In this research, a number of 140 events have been recognized in a typical engine overhaul shop. The flow chart associated with each event is then drawn, which shows how the state of system is changed when corresponding event takes place. These events in addition to other elements of a discrete event simulation model have been used to write a simulation program with an event driven approach. A general purpose language (C#) were used for programming.

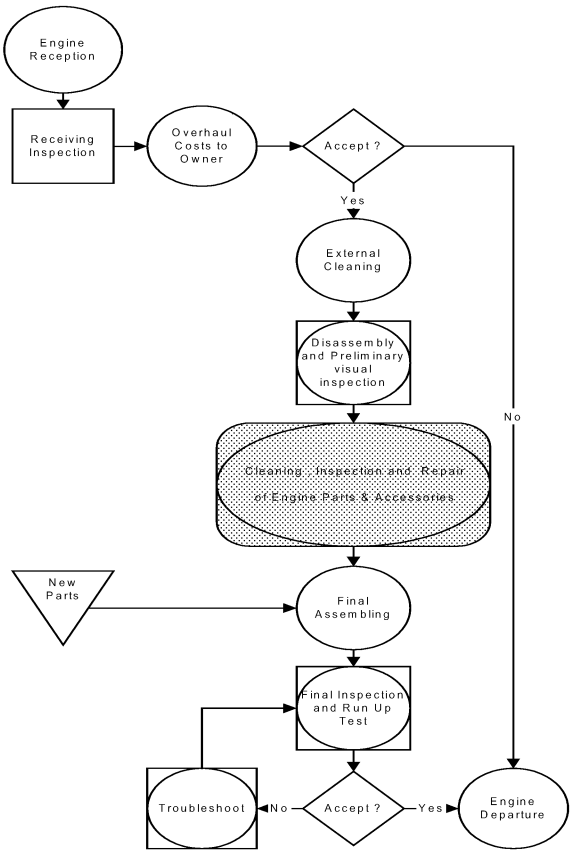

Figure 1: General Practices of Overhaul

VERIFICATION AND VALIDATION

Model validation is often defined as "substantiation that a computerized model within its domain of applicability possesses a satisfactory range of accuracy consistent with the intended application of the model" (Schlesinger et al. 1979). Verification of the model is usually explained as " ensuring that the computer program of the computerized model and its implementation are correct" (Sargent 2004).
Figure 2 shows three main steps of simulation process. It should be noted that in a complete process of modeling, each step may be repeated several times and corrections be applied (Banks and Carson 1984).
This paper is dealt with the validation of conceptual model and verification of computerized model. But, it should be added that subjects presented in this paper may be helpful from early stages of conceptual modeling to final validation or even debugging process

GOVERNING PHYSICS

There are some rules which are governing industrial environments and some parameters that explain behavior of the system. These rules are used to track and analyze the simulation process over time. In this simulation study the applied rules are number of engines, assembly requirements, conservation law, utilization, waiting time, bottleneck rate, spare parts, and confirmation probability of repairs. Application of these rules are discussed in subsequent sections.

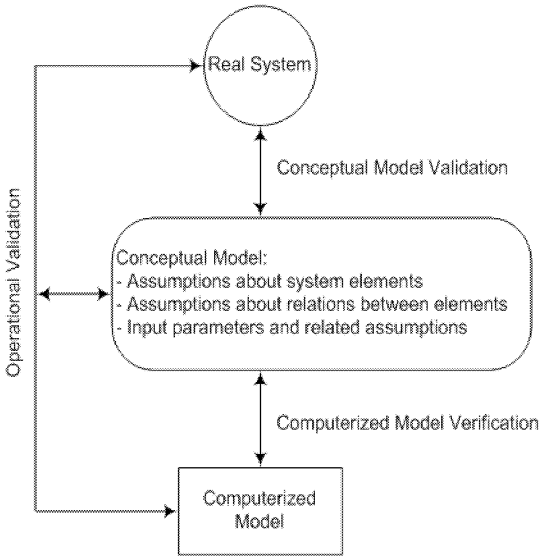

Figure 2: Modeling, Validation and Verification

Number of Engines

In a valid and verified simulation model, always input, output and remaining entities should be in balance (Hopp and Spearman 2000). Here it means that engines entered the system should equal to departed ones plus engines remained in the system. In this model, engines can depart the system in two different ways. First, the engines with high amounts of damage whose overhaul cost is not economical and they depart workshop if their costs are not confirmed by the owner after reception inspection. Second, the engines which depart the workshop after completion of overhaul process. Therefore, Equation (1) is evolved.

$$N_{in} = N_{remained} + N_{rejected} + N_{overhauled}, \qquad (1)$$

where N_{in} is the number of engines entered the workshop, $N_{rejected}$ is the number of engines rejected in the reception inspection stage, $N_{overhauled}$ is the number of engines fully passed the overhaul process and $N_{remained}$ is the number of engines being in the workshop at the time simulation terminates. The parameters N_{in} , $N_{rejected}$ and $N_{overhauled}$ are calculated by counting engines in entrance and departure points. Then $N_{remained}$ can be calculated by Equation (1) and should be equal to the number of engines which actually are in the model. It is notable that this needs specifying the places wherein an engine can be. Table 1 includes data obtained from ten replications, each executed for 500000 minutes.

Assembly Requirements

It is assumed that all parts and accessories should be ready before engine final assembly. From a simulation programming viewpoint, this needs occurrence of specific events. By collecting data about occurrence of these events in the model, it will be possible to study status of each engine entered the system. This will result in two types of engines: first, engines which all of the events required to program their final assembly have not yet happened; second,

fully assembled engines which have departed the workshop. Obviously, some parts or accessories of the first category of engines are still under repair or inspection and therefore those should be among remained engines. Checking this assures that there is not any lost part or engine in the model, additionally helps in any required debugging.

Table 1: Number of Engines

R	N_{in}	$N_{rejected}$	$N_{overhauled}$	$N_{remained}$
1	714	148	552	14
2	718	135	570	13
3	712	133	566	13
4	715	148	551	16
5	712	148	553	11
6	710	141	555	14
7	716	147	556	13
8	719	150	556	13
9	707	147	543	17
10	717	136	562	19

Conservation Law

Here conservation or Little's Law (Little 1961) can be stated as equation (2).

$$TH = \frac{WIP}{CT}. \qquad (2)$$

Where *TH* is throughput rate, *WIP* is the work-in-process and *CT* is repair cycle time. Generally, throughput is referred to as the rate at which entities complete processing. As the verification and validation are of concern, changes in reduction or increment of *WIP*, should also have the same effect on the cycle time. Additionally, in long terms, the ratio of *WIP* to cycle time, i.e. *TH*, should approximately equal to the arrival rate in a stable system (Standrige 2004). Table 2 contains arrival rates and *TH*s estimated by little's law, obtained from ten replications. Here because throughput is estimated only for fully overhauled engines, output rate of engines rejected in reception inspection stage should be subtracted from arrival rate of engines.

It worth noting that the little's law can be used for each of the servers in the system.

Table 2: Throughput from Little's Law

R	*WIP*	*CT*	*TH*	Arrival Rate
1	11.54	4156.43	0.0027	0.0028
2	11.88	4153.20	0.0028	0.0029
3	11.59	4066.72	0.0028	0.0029
4	11.31	4082.73	0.0027	0.0028
5	11.21	4031.6	0.0027	0.0028
6	11.48	4116.94	0.0027	0.0028
7	11.46	4126.65	0.0027	0.0028
8	11.72	4195.02	0.0028	0.0028
9	11.21	4095.55	0.0027	0.0028
10	11.90	4195.26	0.0028	0.0029

Utilization

Information about the utilization rate of servers can also provide a tool to interpret model behavior. Over long terms, utilization rate of each server is estimated by

$$u = \frac{\lambda}{c\mu}, \qquad (3)$$

where λ is the arrival rate, μ is the process rate of the server and c is the number of servers. By increasing the number of servers, keeping other parameters constant, utilization of those servers will decrease. This is verified by several simulation runs for all of server types. Figure 3-a illustrates utilization rate of one of the servers, viz. *general mechanic*, versus different number of servers. Figure 3-b shows increment of cycle time as utilization rate increases. It is seen from this figure that as utilization rate converges to 1, the cycle time goes to infinity.

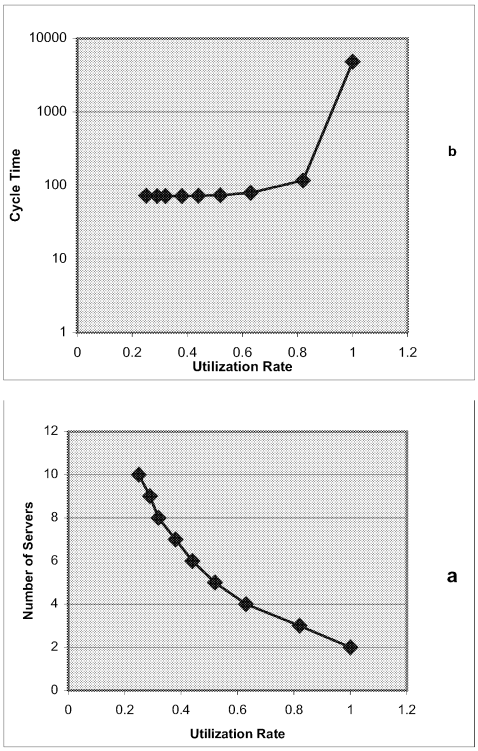

Figure 3 : Utilization Rate versus Number of Servers and Cycle Time

Waiting Time

Equation (4) presents lower and upper bounds for waiting time in queue of a multi-server station, in general (G/G/c) (Gross and Harris 1998) .

$$\frac{\lambda^2\sigma_e^2 + cu(u-2)}{2\lambda c(1-u)} - \frac{\lambda(c-1)(\sigma_e^2 + 1/\mu^2)}{2c} \le WT_q \le \frac{\lambda(c\sigma_a^2 + \sigma_e^2)}{2c(1-u)}. \qquad (4)$$

The parameter WT_q is the average waiting time in queue, σ_a is the standard deviation of arrival times, σ_e is the standard

deviation of processing times, λ and μ are arrival and processing rates respectively.
Using equation (4), it is checked if waiting time in queue of a particular station, obtained directly from the model, is between the boundaries mentioned above. Table 3 indicates this data for one of the servers in aircraft piston engine overhaul workshop called *general mechanic*. The number of general mechanics in ten replications reported in Table 3 is 3.

Table 3 : Waiting Time for General mechanic

R	λ	μ	σ_e	σ_a	u	Lower Limit	Upper Limit	WT_q
1	0.036	0.014	3714.7	779.6	0.82	8.27	201.79	58.32
2	0.037	0.014	3857.9	730.2	0.85	28.97	248.66	59.87
3	0.037	0.014	3759.4	763.8	0.84	21.53	233.21	49.40
4	0.036	0.014	3907.3	807.5	0.82	13.73	210.99	54.29
5	0.036	0.014	3747.3	786.6	0.83	11.88	215.55	45.42
6	0.036	0.014	3800.4	800.3	0.83	13.48	218.87	52.53
7	0.037	0.014	3805.3	784.4	0.83	19.54	223.40	50.59
8	0.037	0.014	3919.0	780.8	0.84	26.86	241.33	57.24
9	0.035	0.014	3775.5	847.5	0.81	2.25	193.98	48.87
10	0.036	0.014	3856.9	785.3	0.83	15.20	219.27	61.99

Bottleneck Rate

Usually throughput of a system is limited by the capacity of one or two work stations, commonly called constraints or bottlenecks (Roser et al. 2001) . By the increase of throughput from zero, WIP should also increase relatively until reaches its critical value. After that even by increase of engine arrival rate, throughput will remain constant (Spearman 2003), which means engines will be buffered in the system. This throughput value equals the bottleneck rate. To find the bottleneck server of the system, utilization of the servers are investigated. In stable systems, bottleneck is the server with biggest utilization rate (Law and Kelton 1991). To do so, some simulation runs are done and general mechanic servers are identified as the bottleneck of the system under study. Then response of the model to increase of arrival rate is studied to find if it is working logical. Figure 4-a shows converging throughput to a constant value (bottleneck rate) by increase of WIP. Figure 4-b illustrates that when the critical WIP or bottleneck rate is approached, utilization rate of the identified bottleneck station converges to 1.

Spare Parts

Logically, the number of required spares of a particular part can be calculated by multiplying the probability of rejecting that part during inspection to the number of overhauled engines. For instance cylinders may be rejected during visual inspection, dimensional inspection or inspection of accomplished repairs. In this model, we have considered a specific probability of rejection for each inspection. Summation of these probabilities in the attempted model is 0.375. Since the arrival rate of engines is assumed to be 0.0028 (28 engines enter the workshop within 10000 minutes) and having the fact that there are four cylinders in each engine, the average number of cylinders required in each 10000 minute can be calculated by

$$0.0028 \times 10000 \times 4 \times 0.375 = 42.52.$$

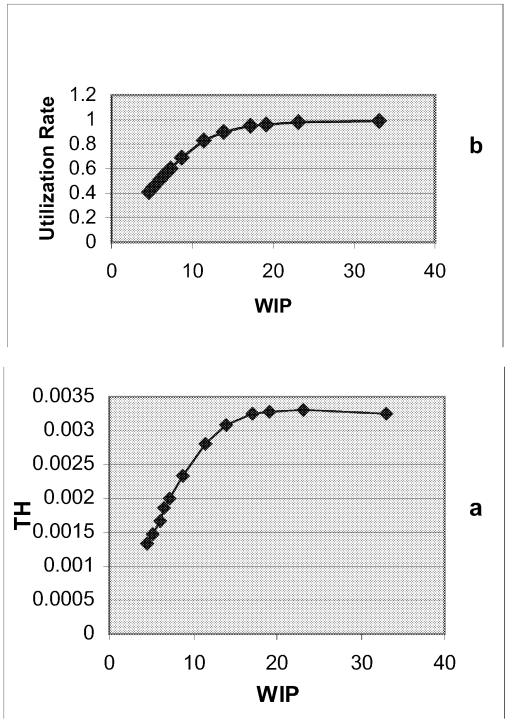

Figure 4.

Now, the value 42.52 can be used to test the validity of the computerized model. To do so, the simulation program is run for 500000 minutes. Figure 5 illustrates required number of spare cylinders obtained from the model in each 10000 minutes of the simulation period. Mean number of spare cylinder requirements obtained from simulation equals to 42.50 for each 10000 minutes. As seen in Figure 5, the number of spare cylinders obtained from model is almost about 42.5, which reveals validity of the computerized model.

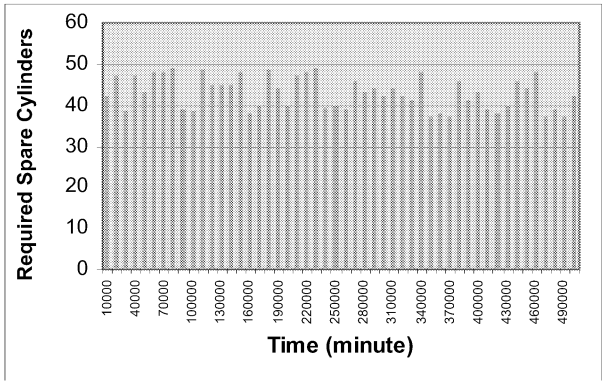

Figure 5. Spare Cylinder Requirements

Confirmation Probability of Repairs

In an aircraft maintenance environment, usually any conducted repair or work should be inspected by another person. It is obvious that the probability of confirming a repair done by the previous person affects different parameters such as overhaul cycle time and spare parts requirements. Logically, increment of this probability should result in decrement of overhaul cycle time and required spare parts. The data collected from the simulation model in Table 4 confirms this logic.

Table 4 : Effect of Acceptance Probability on Overhaul Cycle Time and Spare Part Requirements

Acceptance Probability	Overhaul Cycle Time	Required Spare Valves	Required Spare Cylinders	Required Spare Crankcase	Required Spare Crankshafts	Required Spare Accessory Cases	Required Spare Pistons	Required Spare Accessory Gears
0.3	6487	9580	2511	1015	1118	932	4004	5174
0.4	4445	9529	2423	947	1115	850	3870	5105
0.5	3784	9447	2167	898	1100	831	3761	5011
0.6	3390	9228	1982	826	1062	713	3574	4899
0.7	3186	9208	1830	757	1044	690	3423	4826
0.8	3023	9128	1626	708	1030	636	3398	4795
0.9	2864	8786	1581	648	1017	598	3232	4736

CONCLUSION

We have used a discrete event dynamic system approach to simulate overhaul procedures of a typical aircraft piston engine. In this paper, physics governing industrial environments are used for verification and validation purpose. For this reason some parameters are gathered from simulation response and analytically studied in simple scenarios. We showed the program is behaving logical by using some rules and relations about number of engines, assembly requirements, conservation law, utilization, waiting time, bottleneck rate, spare parts and confirmation probability of repairs are satisfied.

REFERENCES

Banks, J. and J.S. Carson. 1984. *Discrete-Event System Simulation,* Prentice-Hall.

Gross, D. and C. M. Harris. 1998. *Fundamentals of Queuing Theory*. John Wily & Sons, NY.

Hopp, W.J. and M.L. Spearman. 2000. *Factory physi*cs, McGraw-Hill, Boston, MA.

Jepppesen Sanderson. 1997. *A&P Technician Poweplant Textbook* ,Englewood.

Kroes, M.J. and T.W. Wild. 1995. *Aircraft Powerplants.* McGraw-Hill.

Law, A.M. and D. Kelton. 1991. *Simulation Modeling & Analysis*. McGraw-Hill.

Little, J.D.C. 1961. "A Proof for Queuing Formula $L=\lambda w$ ". *Operations Research*. Vol. 16, pp. 651-657.

Roser, C.; M. Nakano; M. Tanaka. 2001. "A Practical Bottleneck Detection Method". In *Proc. 2001 Winter Simulation Conference.* pp. 949-953.

Sargent, R.G. 1982. "Verification and Validation of simulation Models". Chapter IX in *Progress in Modeling and Simulation*, ed. F. E. Cellier, 159-169. Academic Press, London.

Sargent, R. G. 1984. "Simulation model validation". Chapter 19 in *Simulation and Model-Based Methodologies: An Integrative View*, ed. T. I. Oren, B. P. Zeigler, and M. S. Elzas, 537-555. Springer-Verlag, Heidelberg, Germany.

Sargent, R. G. 1996. "Some subjective validation methods using graphical displays of data". In *Proc. 1996 Winter Simulation Conf.*, pp 345-351.

Sargent, R. G. 2004. "Validation and Verification of Simulation Models". In *Proc. 2004 Winter Simulation Conf.*, pp 17-28.

Schlesinger, et al. 1979. "Terminology for model credibility". *Simulation* 32 (3): pp 103-104.

Spearman, M. 2003. "Measures, models, and factory physics". Presentation to the Michigan Simulation Users Group 2003 Annual Conference. Available online via <www.m-sug.org> [accessed August 20, 2006].

Standrige, C.R. 2004. "How Factory Physics Helps Simulation". In *Proc. 2004 Winter Simulation Conf.*, pp 1103-1108.

BIOGRAPHY

REZA AZADEGAN is an aircraft maintenance engineer. He got his bachelor's from C.A.T.C., Tehran, Iran in 2003. He is currently a MS. student of mechanical engineering in the Urmia University, Urmia, Iran. His field of research is modeling and analyzing aeronautical maintenance procedures.

MAGHSUD SOLIMANPUR was born in Urmia, West Azerbaijan Province, Iran. He has got his B.Tech and M.Tech. degrees from the Sharif University of Technology, Tehran, Iran and Ph.D. from Indian Institute of Technology Delhi, New Delhi, India in 2003. He is currently Assist. Prof. in the Faculty of Engineering, Urmia University, Urmia, Iran. His fields of research are Operations Research, Simulation, Production Management, Manufacturing Systems Engineering.

SIMULATION IN CIM AND LOGISTICS

USING SIMULATION MODELING IN DIAGNOSTIC OF A CAR MANUFACTURING COMPANY FUTURE EXPANSION: A CASE STUDY

Reza Zanjirani Farahani

Department of Industrial Engineering,
Amirkabir University of Technology,
424 Hafez Ave., Tehran, Iran
Email: farahan@aut.ac.ir

Nasrin Asgari
Iranian Supply Chain Management Research Group, Tehran, Iran
Department of Industrial Engineering, Tarbiat Modares university, Tehran, Iran

KEYWORDS
Diagnostics, Simulation, Logistics, Index, Standard.

ABSTRACT
In this case study, a car producer company wants to increase its production rate; so we want to investigate that which type of problems will be occurred doing that. Logistics system is one of the sub-systems that face some of the problems. In this paper, we investigate the problems that generate in the scope of logistics sub-system. Also, we diagnose future problems. Geographical scope of this study is limited from parts warehouse to assembly (trim) department. Nine parts are selected as a sample. Current state of the system, its indices and standards is documented by interviewing and visiting. Future state is guessed by simulation. Finally, some projects is defined to solve the problem.

INTRODUCTION

In this case, a methodology is presented to anticipate future problems in logistics sub-system especially in transportation and warehousing area. The case is an automobile manufacturing company that produces 450000 automobile per year and wants to increase it up to 600000. This increasing may cause some problems in warehouses like shortage of space and in transportation like heavy traffic in the factory. These problems should be diagnosed. For example, the root of the shortage of space may be bad layout of parts and we could solve this problem by doing a suitable layout; so the company doesn't need to increase its warehouses' capacity. If we want to know that the parts layout are good or not, we can apply standard indices. We can use this procedure for distinguishing problems in internal transportation and we use simulation instead of standard indices to find places of high traffic. However, first the current state of the system should be documented, then the future state should be estimated.

In the next section, problem definition is discussed. Then, a methodology is presented to solving the problem. Later section is about data gathering and then we show analysis and results. Finally, conclusion is presented.

PROBLEM DEFINATION

As we told, increasing the capacity forces on logistics and parts transportation system. If weak points of process don't distinguish, they will cause mail problems.
One of the important chains in parts transportation stages is a chain that transports from warehouse to assembly department (AD). In the chain, vehicles transport full pallets to AD and back them empty to warehouse. Parts transport by lift trucks inside the warehouses and ADs. Amount of transportation in this chain is high. Warehouses are far from ADs. Because of complexity and high amount of transportation inside the factory, there are some problems. If the production rate increases, these problems will cause new problems. So origins of these problems should be explored.
The case scope is as follows:

- We study on logistics sub-system and we don't investigate other sub-systems like "human resource" and "information systems".
- Process modeling is done to analysis transportation between warehouse and ADs. To achieve this purpose, first geographical scope is defined. See figure 1.

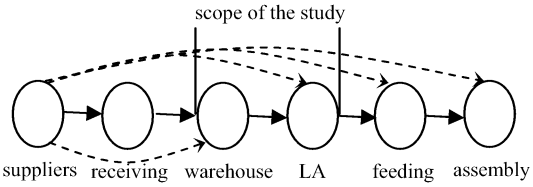

Figure1: Geographical Scope of the Case Study

- As fig. 1 shows, the scope is between warehouses and logistics areas (LA).
- A kind of automobile and nine of its parts are selected as a sample.

METHODOLOGY

In this paper, we want to predict the problems which will be resulted of our future expansions in production rate. After that we find the causes of the problem. Solving the problem with respect to the causes and their precedence relations, we define some projects to prevent consequences of this development. However, we face to a diagnostic and improvement problem in the area of internal logistics including layout and material handling system design.

Some famous procedures have been designed and proposed to improve layout and material handling systems. Among them, Apple (1977), Reed (1961), SLP (Muther, 1973), Nadler (1961) and Immer (1950) are most popular. There are to overviews in these procedures:

- Designing from scratch, and
- Improving current situation.

In this case we face to improving current situation. However, we can use form scratch procedures as a checklist in order to diagnostic and finally improve the current situation or future outcomes.

Simply, if we model the scope of our problem as a graph, we can divide our investigations into to categories:

- Diagnostics in nodes including spaces like warehouses and assembly lines: in these areas we have used some standard indices in order to check efficiency of space utilization in current space. So, first we should know whether we use these space correctly. Second, will we have any problem in future? If yes, is it related to a problem our warehouse layout or space shortage? As an instance, for one of the warehouse in the scope of the case study we have:
  - Total warehouse space: 5184 m^2
  - Total aisles space: 2836 m^2
  - Percent of spaces used as aisles: 2836/5184= %54.7
  - Dimensions of the largest pallet which move in the aisles: 220 cm×120 cm = 2.64 m^2 dimensions. Regarding to Tompkins et al. (2003), %30-%40 allowance for this area is acceptable. Therefore, first of all, our problem is in wrong warehouse layout not in space shortage!

- Diagnostics in edges including problems like traffic jam or transportation problems: In these areas, we use simulation modeling. For example, we gather transportation system data in current situation and simulate the system using the data. Next, having a forecast in future situation, we update current data to future data. Then we generate another model. After running these two models and having comparison as a result of a simulation package, we can see the future problems visually. As an instance, assuming Greenshields' traffic flow model, we will have following formulas (1) (Khisty and Lall, 1998):

$$\left.\begin{aligned} V_1 &= V_f * (1-\frac{k_1}{k_j}) \\ V_2 &= V_f * (1-\frac{k_2}{k_j}) \end{aligned}\right\} \Rightarrow \frac{t_1}{t_2} = \frac{k_j - k_2}{k_j - k_1} \qquad (1)$$

V_1: mean speed in current situation;
V_2: mean speed in future situation;
V_f: mean free speed;
k_j: jam density;
k_1: Average density of vehicles in current situation;
k_2: Average density of vehicles in future situation;
t_1: needed time to travel in current situation;
t_2: needed time to travel in future situation;

We use the formula to have a well prediction of future events. As we see in the formula this relation is not always linear. Based on these equations we can change current data to future data. In this case we have used ARENA (simulation software manufactured by Systems Modeling Corp.) as a computer simulation tool with a graphical user interface (Kelton et al., 1998). Using Arena, users can model complex systems using the available modules, blocks and elements available in the ARENA templates using simple click-and-drop operations into the model window. Examples of systems that can be modeled are (Vamanan et al., 2004):

- manufacturing plants with people, machines and transport devices,
- bank teller windows, ATMs, and deposit boxes, and
- a computer network with servers, clients and networking capabilities.

However, after running the models and having a comparison between output results based on some attributes like waiting times and queue lengths, we can visualize the future problems and their intensity quantitatively.

DATA GATHERING

First the warehouses and ADs- that are related to sample parts- were marked on a layout map. Second transportation routs of each part were drawn. Then parts transportation features were investigated. Results of this study are from-to charts, flow frequency of parts between sources and destinations, and parts transportation data. Some of these results are shown in table 1 and 2.

Parts transportation data are (loading, unloading, waiting and moving) times, distances, kind of equipment and kind of container. The percentage of times – that is assigned to different activities- for each transportation cycle is calculated. For example, see table 3.

Other data that we need to analysis the case are: traffic volume in crosses and routes that is presented in table 4 and 5 for nine sample parts.

Table 1: Distance From-to Chart between Warehouses and ADs

to / from	ware. D	Ware. A	ware. B	ware. C	ware. E	L.A. of dep. D	dep. E	buffer of dep. A	dep. B	dep. A
ware. D									1770	1600
ware. A			125					1350	1340	1450
ware. B		125							970	1080
ware. C										1050
ware. E							360			
L.A. of dep. D							2130		125	
dep. E					360	2130				
buffer of dep. A		1350								100
dep. B	1770	1340	970			125				
dep. A	1600	1450	1080	1050				100		

Table 2: Time and Distance Data

transportation container	transportation equipment	Distance (m)	times (min)				destination	source	No.
			waiting	Unload.	Trans.	Load.			
F1 type Pallet	Truck	360	21	2	4	5	dep. E	ware. E	1
F1 type Pallet	Truck	2130	6	2	6	5	L.A. of dep. D	dep. E	2
trolley	towing vehicle	125	1	3	3	7	dep. B	L.A. of dep. D	3
trolley	towing vehicle	1050	1	6	8	10	dep. A	ware. C	4
RE2 type Pallet	Truck	1600	11	2	6	12	dep. A	ware. D	5
RE2 type Pallet	Truck	1770	2	2	8	5	dep. B	ware. D	6
RE8 type Pallet	Truck	1350	8	15	7	9	buffer of dep. A	ware. A	7
RE8 type Pallet	towing vehicle	100	1	1	7	2	dep. A	buffer of dep. A	8
RE8 type Pallet	Truck	1340	2	8	7	9	dep. B	ware. A	9
RE8 & RE4 type Pallet	Truck	1080	1	4	8	7	dep. A	ware. B	10
RE8 & RE4 type Pallet	Truck	970	2	4	6	7	dep. B	ware. B	11

Table 3: The Percentage of Times that Is Assigned to Different Activities

part name	route		Distance (m)	flow amount (week)	Cycle time (min)	percentage of time		
	sou.	des.				mov.	load &unl.	waiting
A B	ware. E	dep. B	2615	2000 2000	65	20%	37%	43%

Table 4: Statistical Parameters for Vehicles Entrance to Crosses

	Entr.	dist. of entr. time	car perc.	Car percent enter to cross	probability of continuing the route				dist. of passing time	vehicle type
					N	S	W	E		
cross 1	N		0.94	0.87		0.41	0.35	0.24	TRIA(.04, .068, .08)	passenger car
	S		0.77		0.41		0.34	0.25		
	W		0.89		0.15	0.54		0.31	.06+LOGN(.0372, .0309)	truck
	E	0.71+0.831* BETA(0.19,0.236)	0.88			0.25	0.75			
cross 2	N		0.73	0.62			0.33	0.67	TRIA(.04, .068, .08)	passenger car
	S		0.42		0.52		0.26	0.22		
	W								.06+LOGN(.0372, .0309)	truck
	E		0.70		0.64	0.00	0.36			
	S	0.06+LOGN(0.357, 0.263)	0.30		0.85			0.15		
	W		0.71		0.50			0.50	.06+LOGN(.0372, .0309)	truck
	E									

Table 5: Statistical Parameters for Vehicles Movement in Routes

Routs	vehicle type	Distr. Of movement time (min)
route 1	passenger car	Normal(0.7,0.1)
	truck	Normal(1.4,0.1)
route 2	passenger car	Normal(0.3,0.1)
	truck	Normal(0.6,0.1)
route 3	passenger car	Normal(0.4,0.1)
	truck	Normal(0.8,0.1)

ANALYSIS AND RESULTS

Using ARENA as a simulation software, the models run on a PC. Figure 2 shows an example of ARENA output for current situation of the case problem.

Table 6 shows output results of a comparison between current and future situation based on some attributes like average waiting time (minutes), average number of waiting vehicles and percent of time when vehicles pass cross.

ARENA Simulation Results

Project: Run execution date : 4/ 4/2005
Analyst: Model revision date: 4/ 4/2005

TALLY VARIABLES

Identifier	Average	Half Width	Minimum	Maximum	Observations
Server 2_R_Q Queue Tim	.03529	.00163	.00000	.66824	19087
Server 12_R_Q Queue Ti	.08634	.00543	.00000	1.2799	27847
Server 7_R_Q Queue Tim	.00000	(Insuf)	.00000	.00000	82
Server 3_R_Q Queue Tim	.06317	.00315	.00000	.58578	30533
Server 13_R_Q Queue Ti	.00000	.00000	.00000	.00000	18320
Server 4_R_Q Queue Tim	.06348	.00255	.00000	.58105	26949
Server 14_R_Q Queue Ti	.00000	(Insuf)	.00000	.00000	94
Server 10_R_Q Queue Ti	1.2349	(Insuf)	.00000	7.8823	200
Server 9_R_Q Queue Tim	.00000	(Insuf)	.00000	.00000	150

Server 5_R_Q Queue Tim	2.3552	(Insuf)	.00000	17.711	68
Server 15_R_Q Queue Ti	.00000	.00000	.00000	.00000	1152
Server 1_R_Q Queue Tim	.01498	9.3790E-04	.00000	.36012	10073
Server 6_R_Q Queue Tim	13.116	2.7523	.00000	39.349	380

Figure2: An Example of ARENA Output for Current Situation of the Case Problem.

Table 6: Output Results of a Comparison between Current and Future Situation.

Cross no.	waiting time (minutes) (traffic volume in time)		Increasing percentage	average waiting time (minutes) (traffic volume in # of vehicles)		Increasing percentage	percent of time when vehicles pass cross		Increasing percentage
	Current situation	Future situation		Current situation	Future situation		Current situation	Future situation	
1	0.06317	0.30046	%375.64	0.643	2.9086	%35235	0.68343	0.97422	%42.55
2	0.03529	0.19182	%433.55	0.22455	1.3806	%514.83	0.48185	0.81616	%69.38
3	0.08634	0.72709	%742.12	0.80152	6.3593	%693.41	0.70536	0.99805	%41.495
4	0.06348	0.32793	%416.59	0.57024	2.8947	%407.63	0.65615	0.96554	%47.15
5	0.01498	0.05763	%284.71	0.0503	0.23979	%376.72	0.26865	0.49922	%85.83

We want to know about our future problems in advance based on increasing the production rate in future. However, with respect to standard indices and simulation modeling we can find the problems area. After that, expert experiences show priorities, correlations and precedence between these problems. Finally, our investigations show that there are 15 original problems which are roots of all future problems. Solving these problem and with respect to their precedence we could be able to define 15 improvement project. In Figure 3 these projects and their precedence relations are shown.

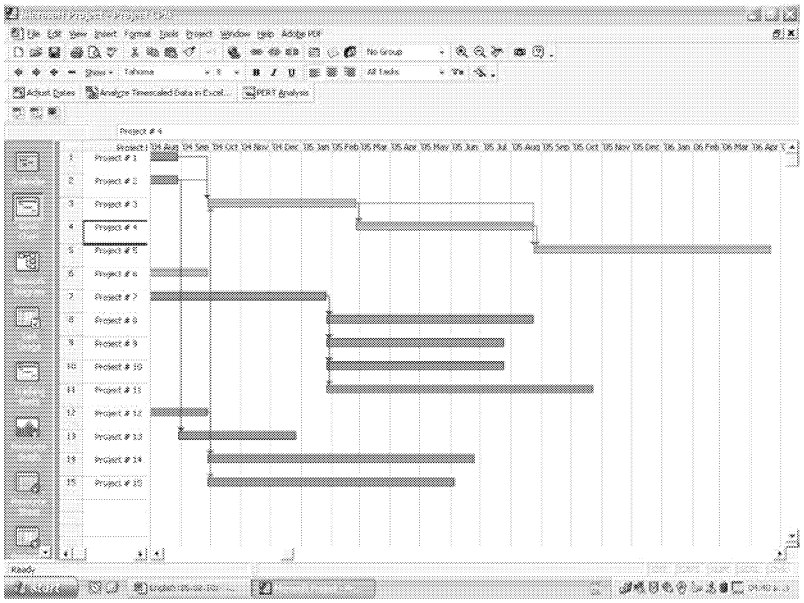

Figure 3: Projects and Their Precedence Relations.

These projects must be schedule and implement so that:

a. Precedence relations should be met,
b. Factory budgeting should be satisfied,
c. The project should be finished before starting future expansion in production rate.

CONCLUSION

At the last stage, after studying the cause-and-effect diagram and with simulation results, some projects were defined to solve current and future problems. Time and cost of the projects are different and depend on the problem that will be solved.

The problems that they don't have any precedence in the cause-and-effect diagram, lead to long time and expensive projects. But these projects will solve many problems originally in a long time. The problems that they aren't precedence for any problem in the cause-and-effect diagram, lead to short time and less expensive projects. But these projects will solve some problems temporary. Other projects are in a state between these two states. The projects are defined based on concentration in specific scopes that are inside the factory. As we told, root of some projects are beyond our study scope, defined projects are beyond our study scope too.

Last step is determining priority of projects, activities definition, and time and cost estimation that leads to projects' Gantt chart. After defining the projects and providing project mandate, priority between them are defined and required resources are estimated.

REFERENCES

Apple, J.M. 1977. *Plant Layout and Material Handling*, Wiley, New York, NY.

Immer، J.R. 1950. *Layout Planning Techniques*، McGraw-Hill Book Company, New York.

Kelton DW, Sadowski RP, Sadowski DA. 1998. *Simulation with ARENA*. Boston, MA: WCB/ McGraw-Hill.

Khisty Join C. and Lall Kent B. 1998. *Transportation Engineering*, Prentice Hall.

Mayur Vamanan, Qian Wang, Rajan Batta, Robert J. Szczerba, 2004. "Integration of COTS software products ARENA & CPLEX for an inventory/logistics problem". *Computers & Operations Research*. 31. 533–547.

Muther، R.1973. *Systematic Layout Planning*، 2nd ed.، Cahners Books، Boston.

Nadler، G. 1961. *Work Design: A Systematic Concept*, Richard D. Irwin، Inc., Homewood, IL.

Reed، R. Jr. 1961. *Plant Layout Factors، Principles and Techniques*، Richard D.Irwin، IL.

Tompkins, J.A. White, Y.A. Bozer, J.M.A. Tanchoco. 2003. *Facilities Planning*, 3rd edition, Wiley, Chichester.

MODELING THE DISPERSION OF DEMAND WHEN SIMULATING THE NEWSBOY PROBLEM

P. Douillet, B. Rabenasolo
Ecole Nationale des Arts et Industries Textiles
Laboratoire Genie et Materiaux Textiles – GEMTEX
9, rue de l'Ermitage 59056 Roubaix, France
E-mail: {pierre.douillet, besoa.rabenasolo}@ensait.fr

KEYWORDS

Forecasting, Risks analysis, Sampling distribution, Stochastic model, Supply chain management

ABSTRACT

Supply chain planning requires some knowledge of the future demand. This knowledge is often expressed by a probability distribution or, to be more robust, by some parameters that define a family of demand models, for example the family of pdfs that share a given mean and a given measure of the dispersion.

Beside the usually used standard deviation, we have introduced another measure of the dispersion: the intermeans parameter and investigated the consequences of this choice for the well known newsboy problem.

Furthermore, we have investigated the general properties of this new intermeans parameter, especially its sampling distribution, in order to obtain intervals of confidence from limited historical sales data. Closed form expressions are given for Dirac and uniform distributions. In the general case, numerical simulations have been run to obtain a better knowledge concerning this parameter.

INTRODUCTION

The supply chain planning requires the definition of the ordered quantity and the inventory level which optimize profit. For companies which cannot build distribution processes with a make-to-order strategy, these decisions depend on the knowledge of the future demand which is mainly expressed by a probability distribution function (pdf). In many papers, for example those related to the well known newsboy problem (Scarf 1958), this pdf is assumed to be exactly defined. In that case, the optimal order quantity has a simple and elegant expression which can be extended to various situations such as multi products environment with multiple discounts (Khouja 1995), multi period sales and ordering, capacity constraints (Voros and Szidarovszky 2001), or random procurement delays.

However, this assumption can hardly be verified since the demand forecasting model cannot be easily validated especially for turbulent and wildly changing markets: high competition between companies, customer volatility, unpredictable fashion trends, high degree of diversity, and short product life cycle. This situation mainly has three consequences (Douillet and Rabenasolo 2005a).

Firstly, it is difficult to conduct a real experiment for the verification of the demand models. This experiment would need a repeatable context. Secondly, the complexity of the market or the economic context may lead to the impossibility to verify various modeling hypotheses such as ergodicity, independence, ...

Lastly, especially for make-to-stock industry and commerce, it is also impossible to quantify the actual demand even afterwards. One can only observe the satisfied demand materialized by a receipt or an invoice, or observe that a stock-out has occured. When the inventory becomes empty, a common situation is that one cannot guess anything about the unobserved demand.

The impossibility to identify exactly this demand distribution function from the actual knowledge requires more robust optimization methods which are addressed by a min-max search in the expected gain.

In the min-max optimization, the primary hypothesis on the knowledge of the demand probability distribution function is reduced to the knowledge of fewer parameters that define a family of demand models. As a prerequisite, we assume that the mean demand is reasonably detected and identified by the statistical analysis of past sales data. Then, the min-max method looks for the decision which maximizes the minimum given criterion for a family of models $\mathcal{F}$, defining the "least bad" decisions. Following the method introduced by (Scarf 1958), many papers (Gallego and Moon 1993, Yue, Chen, and Wang 2006) have studied the optimal order for the family $\mathcal{F}(\mu, \sigma)$ of pdfs that share the same mean μ standard deviation σ.

Recently, from the consideration of a new expression of the cost of uncertainties, we have introduced (Douillet and Rabenasolo 2005b) a new measure of the dispersion, the intermeans parameter δ (cf. (7) and Section 4 in the present paper). And we have shown that the optimal decision differs from "the Scarf's rule" when the min-max method is applied to the family $\mathcal{F}(\mu, \delta)$ of

pdfs that share the same mean μ and intermeans parameter δ.

In this context, we have undertaken a comparative study of the properties of both this new measure of the dispersion (δ) and the usual one (σ). Among the properties investigated, the sampling distribution of δ has been studied, in order to provide some confidence levels from limited historical sales data.

Closed form expressions have been obtained for the "two Dirac's" and uniform distributions. For the general case, we have conducted numerical simulations in order to compare the behaviors of the estimators of both σ and δ. Interesting directions for future research have been obtained.

ORGANIZATION OF THIS PAPER

The rest of this paper is divided in two Sections and a Conclusion. In Section "Min-max and newsboy model" the reasons to study the intermeans parameter are given. The first subsection describes the newsboy problem and introduce our notations. A new formula for the cost of uncertainties will be given that introduces the parameter δ. The second subsection recalls the (Scarf 1958) results concerning the family $\mathcal{F}(\mu, \sigma)$. The last subsection shows that considering the family $\mathcal{F}(\mu, \delta)$ leads to very different conclusions.

In Section "intermeans parameter properties" , this parameter is studied *per se*. The first subsection shows that δ is another measure of the dispersion. The second subsection compares δ with the usual measure, namely the standard deviation σ. The last subsection deals with the sampling distribution of δ. This is a key result since it must be shown that δ can be extracted from historical data at least as well as the usual σ.

The paper ends by a concluding Section, that summarize our results, followed by a short bibliography.

MIN-MAX AND NEWSBOY MODEL

The purchasing problem is stated as follows: assuming a given knowledge of the future demand, the decision maker has to buy now a certain quantity of products in order to maximize his revenue during a future sales period. Because of the short life-cycle of most of the textile products, we suppose that there is no opportunity to correct any error that he may have made on this order quantity. As an illustration, the procurement delay for a fabric may be about three months, while the logistic and transportation delay may range from one to three weeks or more for relocated industries. In that case, the purchase decision should be taken about four months before any sale. Any error cannot be corrected if this sales period is of three months (one season). In order to get a higher comprehension of the phenomena, we will simplify the problem and illustrate it by the very simple newsboy model.

Description of the newsboy problem

Let us consider what is known as "the newsboy problem" and use the notations of (Scarf 1958). We have the opportunity to purchase now an amount y of some good, at unitary cost c (regardless of the quantity purchased). It is assumed that the future demand distribution is exactly known by its cumulative density function $\Phi(\xi)$, that the future unit selling price r is known and independent of the number sold and that non sold units are discarded. We have not considered the possibility of a salvation value s, because the only modification is to transform c, r into $c - s$, $r - s$.

When the actual ξ has occurred, the gain is given by $G(y, \xi) = r \min(y, \xi) - c\,y$. At ordering time, we have to consider its expected value: $G(y, \Phi) \doteq \mathrm{E}(G(y, \xi))$. Defining, for a given y, the overflow probability θ_y, the "lower mean" ξ_y^o and the "upper mean" ξ_y^u by:

$$\theta_y \doteq Pr\ (\xi > y)$$
$$\xi_y^u \doteq \mathrm{E}(\xi \mid \xi > y) \quad ; \quad \xi_y^o \doteq \mathrm{E}(\xi \mid \xi < y)$$

and comparing with the naive value $\widehat{G} \doteq G(\mu, \mu)$, where $\mu = \mathrm{E}(\xi)$, we obtain:

$$\widehat{G} - G(y, \Phi) = (1 - \theta_y)\left(y - \xi_y^o\right)\ c + \theta_y\ \left(\xi_y^u - y\right)\ (r - c) \qquad (1)$$

Since everything in this formula is positive, the quantity $\widehat{G}$ is an upper bound for $G(y, \Phi)$ and $\widehat{G} - G(y, \Phi)$ appears to be the cost associated with the choice y.

The usual criterion used to determine the optimal value y^* is to minimize this cost. Derivating $G(y, \Phi)$, we obtain the condition $r \int_y^\infty \mathrm{d}\Phi(\xi) - c = 0$, i.e. the well known:

$$\Phi(y^*) = 1 - \frac{c}{r} \qquad (2)$$

In other words: when Φ is known, the best quantity you can buy depends on the profitability of the product and is not the expectation of the demand. Reporting (2) into (1) leads to the following expression (where $*$ is used as index instead of y^*):

$$\widehat{G} - G(y^*, \Phi) = \theta_* (1 - \theta_*) (\xi_*^u - \xi_*^o)\ r. \qquad (3)$$

This expression gives the cost of uncertainty, i.e. the cost that remains even when we adopt the best decision.

Min-max solution for $\mathcal{F}(\mu, \sigma)$

The best order decision must be analyzed under various weaker hypotheses than an exact knowledge of the distribution Φ. For example, it can be assumed that the mean demand is identifiable with enough precision, and that, additionally, some measure of the dispersion of the demand is also identifiable. In such a condition, various families of demand pdfs need to be investigated.

The determination of the optimal decision becomes a min-then-max problem, where the objective is to optimize the gain for the worst case over a family of demand models, in order to guarantee a lower bound for the expected performance. In other words, we solve:

$$G^* \doteq G(y^*, \mathcal{F}) \doteq \max_y \min_{\Phi \in \mathcal{F}} G(y, \Phi) \tag{4}$$

The founding result given in (Scarf 1958) addresses the case where the standard deviation σ is known (together with the mean μ). The key fact is that, over all distributions Φ sharing the given values of μ, σ, the worse case for a given y is ever a "two Dirac's" distribution. Therefore the best decision against the whole family $\mathcal{F}(\mu, \sigma)$ can be obtained by taking into account only these distributions, leading to the solution:

$$\begin{array}{l} \text{if } c/r > \left(1 + \sigma^2/\mu^2\right)^{-1} \\ \text{then do nothing} : y^* = 0, \quad G^* = 0 \\ \text{else} \left\{ \begin{array}{rcl} y^* & = & \mu + \sigma\,(r/2 - c)\,/\sqrt{c\,(r-c)} \\ G^* & = & \mu\,(r-c) - \sigma\sqrt{c\,(r-c)} \end{array} \right. \end{array} \tag{5}$$

It can be noticed that, in the "two Dirac's" case, either $\xi = \xi^o$ or $\xi = \xi^u$, while the condition on c/r is needed to ensure $\xi^o > 0$.

A graphical proof of this result against the $\mathcal{F}(\mu, \sigma, \mathit{Dirac})$ family is summarized in Fig. 1 (drawn using $\mu = 1000$, $\sigma = 600$, $(r - c) = 10$ and $c/r = 5/9$). All the curves $\theta \mapsto G(y, \Phi_\theta)$ corresponding to the different values of the ordered quantity y are going through the same point, whose abscissa is $\theta = c/r$. More precisely, all these curves are made of rectilinear and "parabolic" pieces and all the complete "parabolas" are going through this same point. Therefore, the best decision is the y whose curve admits this special point as its minimum.

Min-max solution for $\mathcal{F}(\mu, \delta)$

Knowing that $\mu = \mathrm{E}(\xi)$ is not the optimal decision, we can nevertheless examine what happens when this choice is taken. By the definition of the mean, we have $\forall y : \theta_y\,\xi_y^u + (1 - \theta_y)\,\xi_y^o = \mu$. Using this expression in (1), we obtain the "cost of mean" formula:

$$\widehat{G} - G(\mu, \Phi) = r \times \theta_\mu\,(1 - \theta_\mu)\left(\xi_\mu^u - \xi_\mu^o\right) \tag{6}$$

It can be seen that μ and y^* are the only two values of y for which the "cost of choice" (1) can be written this way. Obviously, the "cost of mean" is an upper bound for (3). Being independent of the cost to price ratio, this bound is of interest and places the focus onto the quantity δ, later referred as the "intermeans parameter" and defined by:

$$\delta \doteq \theta_\mu\,(1 - \theta_\mu)\left(\xi_\mu^u - \xi_\mu^o\right) \tag{7}$$

A strange result is as follows. Fig. 2 shows what happens when playing against the family $\mathcal{F}(\mu, \delta, \mathit{Dirac})$ of all the "two Dirac's" sharing the same values of the mean and the intermeans parameter. When drawing the curves $\theta \mapsto G(y, \Phi_\theta)$, the "parabolic" parts are now straight lines but, here again, all of them are going through the same point whose abscissa is $\theta = c/r$. Therefore, the robust decision is no more given by (5) but by:

$$\left\{ \begin{array}{ll} \text{if } 1 - \dfrac{\delta}{\mu} < \dfrac{c}{r} & \text{do nothing} : y^* = 0 \\ \text{if } \dfrac{c}{r} < 1 - \dfrac{\delta}{\mu} & y^* = \mu \end{array} \right. \tag{8}$$

In other words: if you consider that (μ, δ) is the right way to summarize your knowledge of the demand, then the robust order against all the two Dirac's distributions is nothing but the mean (unless the product is so few profitable that doing nothing becomes better).

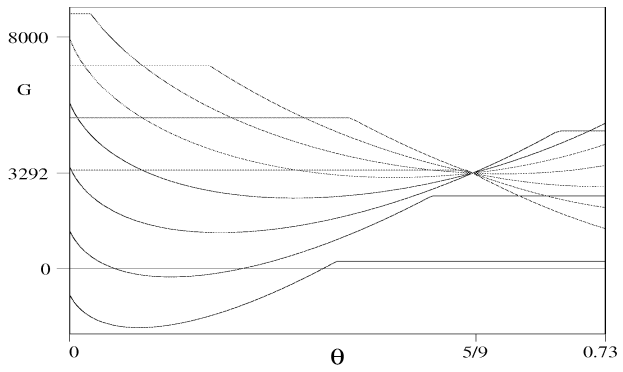

Fig. 1: Playing against $\mathcal{F}(\mu, \sigma, \mathit{Dirac})$

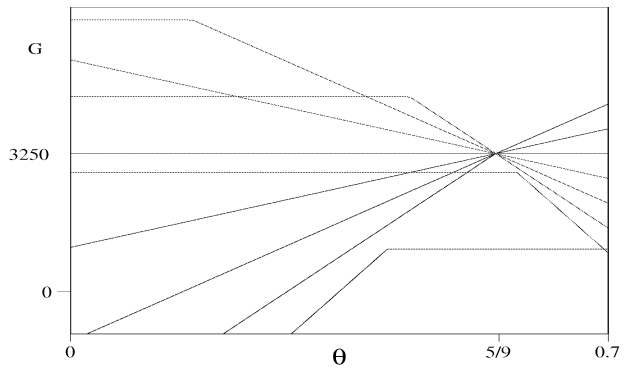

Fig. 2: Playing against $\mathcal{F}(\mu, \delta, \mathit{Dirac})$

INTERMEANS PARAMETER PROPERTIES

A measure of the dispersion

The intermeans parameter has some similarity with the interquartile range, where one subtracts the median of the left hand part from the median of the right hand part, both parts being separated by the median of the population. Here we use the means and subtract the mean of the left part from the mean of the right part, both parts being separated by the mean of the population, the result being afterwards multiplied by $\theta_\mu (1-\theta_\mu)$. Therefore δ appears to be a measure of the dispersion of the distribution.

From now on, all θ, ξ^o, ξ^u are relative to the mean, and subscripts will be omitted. It can be seen that $\mu - \xi^o - \delta = \delta\theta/(1-\theta)$ and $-\mu + \xi^u - \delta = \delta(1-\theta)/\theta$. Therefore, the points $\mu \pm \delta$ are ever situated as in Fig. 3 and the relation $x\,y = \delta^2$ holds.

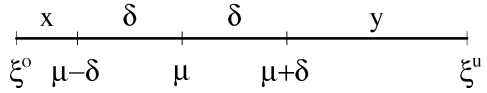

Fig. 3: Meaning of δ : the $x\,y = \delta^2$ property

Relations with the usual standard deviation

Since using δ to describe the dispersion seems to be new, we have undertaken a comparison between this parameter and the usual one, namely the standard deviation σ. For any distribution, we have:

$$\delta \leq \sqrt{\theta(1-\theta)}\,\sigma$$

equality occurring only for the two Dirac's distributions, i.e. those defined by $Pr\ (\xi = \xi^o) + Pr\ (\xi = \xi^u) = 1$. In Tab. 1, the ratio δ/σ is given for various distributions.

distribution Φ	δ/σ (exact)	δ/σ (approx)
two Dirac's	$\sqrt{\theta(1-\theta)}$	$0 \cdots 0.5$
lognormal	$\leq 1/\sqrt{2\,\pi}$	$0 \cdots 0.399$
uniform	$\sqrt{3}/4$	≈ 0.433
triangular	$1/\sqrt{6} \cdots 8\sqrt{2}/27$	$0.408 \cdots 0.419$
normal	$1/\sqrt{2\,\pi}$	≈ 0.399
exponential	1/e	≈ 0.368

Tab. 1: Comparison between δ and σ

It could be noticed that the ratio δ/σ is quite the same for all triangular distributions, whatever their skewness. For the lognormal distribution, the ratio δ/σ varies. For the wildest ones, i.e. for $\sigma \to \infty$, one has $\delta/\sigma \to 0$. But, in the practical cases, i.e. when the demand has only one chance over thousand to go outside the interval $[\mu/10,\ \mu \times 10]$, the relation $0.333 \leq \delta/\sigma \leq 0.399$ holds.

Sampling properties

In order to extract δ from historical data, the sampling distribution of this parameter must be described, and compared with the sampling distribution of the variance. Let ω be a n-sized sample, obtained by n independent random drawings from the distribution Φ.

It is well-known that $s^2 \doteq \mathrm{var}(\omega)$ is biased, while $S^2 \doteq s^2 \times n/(n-1)$ verifies:

$$\mathrm{E}\left(S^2\right) = \sigma^2 \quad ; \quad \mathrm{var}\left(S^2\right) = \frac{1}{n}\left(M_4 - \frac{n-3}{n-1}\,\sigma^4\right)$$

where M_4 is the fourth centered moment. Defining $\mathrm{nscv}\left(S^2\right)$ as n times the squared coefficient of variation of the estimator S^2, we obtain:

$$\mathrm{nscv}\left(S^2\right) = \frac{M_4}{\sigma^4} - 1 + \frac{2}{n-1} \tag{9}$$

We haven't yet obtained such general formulae when estimating the intermeans parameter. Let us now describe our partial results.

The first point is that the quantity $d \doteq \delta(\omega)$ is well defined, even if some points of the sample are near or equal to the sample mean m. If it happens that $x_n = m$, you can split at will x_n into a "left part" and a "right part" according to $x_n = \alpha(m+0) + (1-\alpha)(m-0)$ and ever obtain: $d(\omega) = d(\omega \setminus \{x_n\}) \times (n-1)/n$.

Exact results have been obtained for the "two Dirac's" and the uniform distributions. They are given in Tab. 2. The first relation $\mathrm{E}(d) < \delta$ was expected since a limited sample is unlikely to catch all the dispersion of the population (for the same reason, $\mathrm{E}\left(s^2\right) < \sigma^2$). But now, the bias depends on Φ and an unbiased estimator D cannot be obtained in a "distribution free" manner.

Φ	D/d	nscv (D)	nscv $\left(S^2\right)$
Dirac's	$\frac{n}{n-1}$	$\frac{1}{\theta(1-\theta)} - 4 + \frac{2}{n-1}$	idem
unif.	$\frac{n}{n-2/3}$	$\frac{1}{3} + \frac{2/3}{n-26/45} + \cdots$	$\frac{4}{5} + \frac{2}{n-1}$

Tab. 2: Exact Sampling Properties

The second relation shows that the uncertainty around δ decrease in $1/\sqrt{n}$ since $\mathrm{var}(D) = Cte/n + O\left(1/n^2\right)$. This mimics the well known behavior of the sample estimators for both the mean and the variance. For others distributions, direct computations aren't so easy and, at the present moment, only results obtained by simulations are available.

For each Φ of Tab. 3 and each of the four sample size $n = 4, 7, 10, 13$, we have drawn $N = 1600$ random samples. For each sample, the quantities d and S have been determined. Then $\mathrm{E}(d)$ and $\mathrm{var}(d)$ have been estimated from the N obtained values, leading to an estimation of $n \times \mathrm{var}(d) / \mathrm{E}(d)^2$. For the Gaussian, we have obtained respectively 0.739, 0.662, 0.606, 0.593 and have summarized the results as ≈ 0.6. The same has been done with S, while the values given (in the last column) for $\mathrm{nscv}\left(S^2\right)$ are proven results. For the log-normal distributions, the results depends on the shape parameter K (here $K = \sqrt{2}$ has been used).

Φ	$\mathrm{nscv}(d)$	$\mathrm{nscv}(S)$	$\mathrm{nscv}\left(S^2\right)$
unif.	≈ 0.4	≈ 0.3	$\frac{4}{5} + \frac{2}{n-1}$
gauss	≈ 0.6	≈ 0.5	$2 + \frac{2}{n-1}$
exp	≈ 1.5	≈ 1.7	$8 + \frac{2}{n-1}$
log	≈ 1.5	≈ 1.7	≈ 10

Tab. 3: Properties Obtained by Simulation

In any case, it appears that bias is $O(1/n)$ i.e. is a second order effect compared to the $O\left(\sqrt{1/n}\right)$ uncertainty and that d doesn't behave worse than S.

CONCLUSION

In this paper, we have shown that the best decision for the newsboy problem depends heavily on the choice of the dispersion measure. The "Scarf's rule" follows when assuming an exact knowledge of the variance, while another strategy follows when assuming an exact knowledge of the intermeans parameter δ.

Thereafter, we have studied the relations between δ and σ and have shown that $0.3 \leq \delta/\sigma \leq 0.5$ for all the distributions of relevance when modeling the supply chain. Moreover, we have studied how this new measure of the dispersion can be extracted from historical data and have shown that the estimator d doesn't behave worse than the estimator S.

Further work must be done in order to obtain more exact results concerning the sampling distribution of δ. In particular, obtaining distribution free bounds for the bias and the dispersion of d would be useful.

In any case, the exact identification of reduced parameters concerning the demand models seems to be questionable, and a description using larger families of pdf with confidence intervals such as $\mathcal{F}(\mu \pm \Delta\mu, \sigma \pm \Delta\sigma)$ or $\mathcal{F}(\mu \pm \Delta\mu, \delta \pm \Delta\delta)$ seems to be the way of a robust description of the problems to solve concerning the supply chain.

REFERENCES

Douillet, P., and B. Rabenasolo. 2005a. How robust is a newsboy model ? In *Proceedings of IMACS05, the 17th IMACS World Congress Scientific Computation, Applied Mathematics and Simulation*, T1–I–45–0168. July 11-15 2005, Paris (France): IMACS.

Douillet, P., and B. Rabenasolo. 2005b. Robustness analysis of the newsboy problem. In *Proceedings of IESM05, the 2005 International Conference on Industrial Engineering and Systems Management*. May 16-19 2005, Marrakesh (Morocco): IESM.

Gallego, G., and I. Moon. 1993. The distribution free newsboy problem: review and extensions. *Oper. Res. Soc.* 44:825–834.

Khouja, M. 1995. The newsboy problem under progressive multiple discounts. *EJOR* 84:458–466.

Scarf, H. E. 1958. A min-max solution of an inventory problem. In *Studies in the Mathematical Theory of Inventory and Production*, ed. K. Arrow, S. Karlin, and H. Scarf, 201–209. Stanford University Press.

Voros, J., and F. Szidarovszky. 2001. Determining the production order of two seasonal products under capacity constraint. *Int. J. Production Economics* 73:117–122.

Yue, J., B. Chen, and M.-C. Wang. 2006. Expected value of distribution information for the newsvendor problem. *To be published in Op. Res.*.

AUTHORS BIOGRAPHY

PIERRE L. DOUILLET is an assistant professor in the Department of Mathematics at Ecole Nationale Supérieure des Arts et Industries Textiles (ENSAIT). His research interests include modeling, operations research, formal computing, network performances evaluation and computers' security. His e-mail address is <douillet@ensait.fr> and his Web address is <http://www.douillet.info>.

BESOA RABENASOLO is a professor in the Department of Supply Chain Management at Ecole Nationale Supérieure des Arts et Industries Textiles (ENSAIT). His research interests include sales forecasting, economic evaluation of products design, operations research and supply chain management. He is a member of INFORMS Society. His e-mail address is <besoa.rabenasolo@ensait.fr>.

LINKING E-COMMERCE TO LOGISTICS SIMULATION: VISIONèS, THE MISSING CHAIN

Naoufel Cheikhrouhou
Luca Canetta
Rémy Glardon
Ecole Polytechnique Fédérale de Lausanne
Laboratory for Production Management and Processes
CH-1015 Lausanne, Switzerland
naoufel.cheikhrouhou@epfl.ch

Roland Fischbach
Ahmed El Mimouni

Adelante Consulting SA
Chante Merle 91
CH-2502 Bienne, Switzerland
roland.fischbach@adelante-tm.com

KEYWORDS

Simulation, e-commerce, Manufacturing systems

ABSTRACT

This paper presents the design, development and application of a simulation-based methodology dedicated to the assessment of B2B e-commerce introduction within manufacturing systems. A two-stage approach is presented: the first stage aims at predicting the evolution of the e-commerce activities through the identification of electronic market characteristics and their possible evolution scenarios. The second stage is dedicated to the evaluation of logistic performances of industrial systems by means of discrete event modelling and simulation. The proposed approach has been developed, tested and integrated in a commercial software named VISIONèS. In this paper, the methodology is pointed out, highlighting the benefits of the approach supported by the VISIONèS decision support software. The model structure and the features of the latter are presented with brief implementation results.

INTRODUCTION

The e-commerce share is still growing at a fast pace, proving that it cannot yet be considered as a mature activity and that it is thus far from having reached its steady state potential. Moreover, predicting e-commerce potential is difficult as proved by the large differences characterising the e-commerce diffusion predictions provided by the organizations in charge of monitoring its evolution (Gurunlian and Zhongzhou 2001). Business-to-Business (B2B) e-commerce accounts nowadays for more than 80% of the overall transacted e-commerce monetary value and it is expected to grow faster than Business-to-Customer (B2C) e-commerce even in the next future (Scupola 2002). The magnitude and the criticality of the potential changes faced by companies dealing with the introduction of a B2B e-commerce strategy require a clear understanding of the market demand modifications induced by e-commerce adoption. The choice of a multi-channel sales strategy, where electronic-enabled sales channels (e-sales channels) are used to support or partially replace the traditional sales channels, seems promising both in terms of sales and revenue increase. According to Roland at al. (Roland et al. 2000), an integration of traditional and e-sales channels can increase sales up to 30% to 40%, while lowering cost per revenue by up to 10% to 15%. However, the modifications of the value adding chain required by e-commerce introduction should be carefully estimated because they can critically impact on the company performances. Furthermore, the choice of an adequate e-sales strategy is a complex problem due to the wide variety of possible solutions and to the difficulty of correctly assessing customer choices. A high degree of uncertainty and heterogeneity characterises the reactions of customers faced to e-commerce. This is illustrated by the uneven utilization of online purchasing across different industrial sectors (Selhofer 2004). The complexity and uncertainty characterising the e-commerce landscape require the development of decision support systems that can help to quantitatively predict the e-sales evolution; they must simultaneously take into account the characteristics of the chosen e-strategy, the targeted customers and the offered products. Actually, the demand pattern faced by a traditional seller can be heavily modified by e-commerce introduction, both considering the overall sales turnover, as well as the characteristics of the customer order flow. Tarn (Tarn et al. 2003) states that, dealing with a broad customer base composed of highly volatile and exigent customers, increases the demand uncertainty and the complexity of the fulfilment processes. E-commerce introduction tends to increase the number of transactions while reducing the order size. Furthermore, the variability and unpredictability of the demand parameters also increase. The “convenience and asynchronous shopping” provided by e-commerce utilisation can also modify the short term distribution of the transaction arrivals, with many orders concentrated at the end of the day, endangering the performances of the traditional fulfilment practices (Iliev et al. 2004).

The weak point of many e-commerce enterprises is constituted by the poor performance of the processes needed to produce and deliver goods and/or services purchased on the web. Unfortunately, neither the consequences of marketing practices on the demand function nor the effects of customer requirements on the supply side have been sufficiently taken into account in the analysis of e-commerce introduction and deployment. Thus, the main e-commerce challenges are linked to the business processes and supply chain modifications required to ensure a satisfactory customer service and order fulfilment.

In this paper, we develop a global approach that provides, on the one hand, a quantitative predictions of the potential e-commerce demand evolution and, on the other hand, an evaluation of the potential consequences of e-commerce introduction on the value adding chain performances.

EVALUATION SYSTEMS OF B2B E-COMMERCE

Several studies have been dedicated to the analysis of B2B e-commerce. Often, they are mainly qualitative or limited to the description of benchmark case studies and/or to the overall ICT monitoring. The transaction costs reduction experienced by e-customers is considered as one of the main drivers of e-commerce adoption (Evans and Wurster 1999). The literature contains several descriptions of innovative e-commerce business models, but neither the variables to take into accounts nor the procedure to follow in order to choose the most appropriate e-business models are clearly identified and described. The existence of well-known e-commerce benchmarks (O'Sullivan et al. 1998) has focused a lot of interest to case studies. The results of these case study analysis allow to establish a first draft of the e-commerce success factors. Moreover, they provide some qualitative elements for evaluating the impact of the various innovative business models on company performances. However, the solutions developed on the basis of case studies could be useless for future applications because they are specific to a given market environment and a specific point in time.

The necessity to identify all e-commerce success factors with their relative importance, ensuring that they can be applied in a general manner over a broad range of market environments, has motivated several works. The characteristics of products and services proposed via the Web significantly influence the success/failure of e-commerce initiatives (Hunter et al. 2004; Kyang et al. 2000; Liu et al. 2004). The relationships between customer characteristics and e-commerce adoption have also been pointed out in various works concerning B2B e-commerce (Liu et al. 2004; Selhofer 2004). This is confirmed by the particular attention with which customer-oriented indicators are gathered and analysed with the aim of assessing customer e-commerce readiness (Gurunlian and Zhongzhou 2001; Selhofer 2004). These works constitute another important field of e-commerce research. They provide an estimation of the ICT infrastructure development and of the e-commerce evolution (quantitative description and prediction).

So far, another important factor of B2B e-commerce success has retained less consideration in the scientific literature, namely the characteristics of the implemented electronic sales channel and their performance in terms of customer utility. For this reason, evaluation of the importance of various e-sales channel characteristics, such as purchasing process modifications, available e-services and customer adoption efforts has been made (Canetta et al. 2004). These authors propose a method to integrate the e-sales channels functionalities and features into a global evaluation system, based on the conjoint analysis technique. Other interesting results come from the comparison of the cost structure for traditional and e-commerce sales channels. Strader and Shaw (Strader and Shaw 1999) identify the costs that buyers and sellers should take into account and they compare their entity with respect to the nature of the served markets. This allows sellers to select the most appropriate channel to compete in different markets. Their empirical results show that there are economic incentives, for all the entities of the demand & supply chain (consumers, product/service provider and commercial transactions intermediaries) to be engaged in e-commerce. More recently, Iliev (2004) evaluated the transaction cost saving potentials of different electronic enabled sales and procurement channels in a B2B environment. The evaluation is made taking into account the uncertainties about the degree of online adoption (defined as ratio between the number of online transactions divided by the total number of transactions) which are introduced considering various e-commerce adoption scenarios. However, the works on cost structure modifications have been mainly focused on the administrative and, to a lesser extend, on the logistic processes. A more comprehensive evaluation taking also into account the potential disruptions suffered by the production activities is still missing.

All of these works focus on specific aspects of e-commerce and thus, even if they point out useful information, they do not provide an overall evaluation of its impact on company performances. A first answer, taking into account the complex interdependencies and causal relationships among the different business factors influenced by e-commerce introduction, is given in (Komiya et al. 1998). Komiya et al. apply a qualitative simulation approach to assess causal relationships in intra-organisational problems. The research focuses only on costs reduction and return on investments and allows a preliminary evaluation of B2B e-commerce impact by means of qualitative simulation and scenario generation. However, this approach should be further deepened in order to embrace a more quantitative evaluation and to integrate the value adding chain performances with cost assessment.

The previous results provide many interesting findings about the e-commerce specificities that are integrated in the proposed approach. Its objective is to provide a framework and to develop a method allowing a more detailed analysis of the e-commerce demand modifications and the estimation by simulation of its impact on company performances, with a particular attention devoted to the production system and its management rules.

PROPOSED APPROACH

The proposed approach for investigating the impact of e-commerce adoption on industrial performances is

structured in two parts (Figure 1). The first stage, the market analysis module, consists of a prediction model for the estimation of the market demand through the new electronic channels. The second stage is a simulation module for industrial production systems, which estimates the performance changes due to e-commerce adoption.

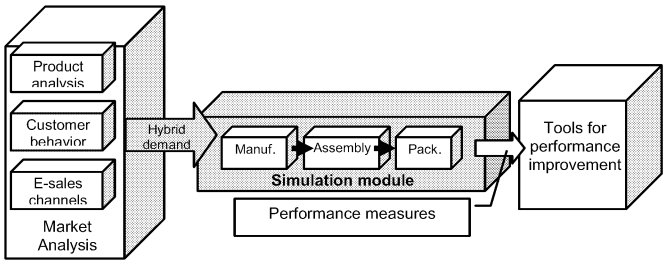

Figure 1: Adopted approach for measuring e-commerce impact on industrial performances

The market analysis module: e-marketing

The market analysis module is based on a three-phase process. In the first phase, a detailed analysis of B2B e-commerce activities is undertaken in order to identify the factors having a significant impact on e-purchasing adoption. The identified factors, called in the following sections e-commerce success factors, comprise:

- the product analysis: nature of the transacted products or services via the electronic sales channels,
- the customer behaviour: characteristics of the targeted customers for a given company,
- the e-sales channels: characteristics of the available e-sales channels,
- the features of the selling company in terms of its brand perception.

A detailed explanation of the magnitude and the direction of the influence of each of these factors is provided relying upon various established theories, such as Transaction Cost Analysis (TCA), Technology Acceptance Model (TAM) and Diffusion Of Innovation (DOI). The results of this step provide a qualitative understanding of the reasons for the large differences observed in the willingness to adopt e-purchasing by industrial customers.

The second phase aims at complementing the previous qualitative information with the analysis of quantitative data related to e-commerce adoption. B2B e-commerce adoption, for various industrial sectors, is then modelled relying upon the Bass innovation diffusion model. The application of the Bass model allows to estimate the values of three innovation diffusion parameters: the potential/saturation level, the coefficient of innovation and the coefficient of imitation for each industrial sector. As a result, the salient differences among industrial sectors in terms of e-commerce saturation level and speed of adoption are pointed out.

The third phase consists of a rule-based Decision Support System (DSS) that can predict e-sales evolutions for companies adopting e-commerce; it takes into account the targeted customers, the offered products and the provided e-sales channels. The identified e-commerce success factors are the input values of the DSS. The estimated parameters of the best fitting model, calculated on the basis of the data about B2B e-purchasing adoption, constitute the output of the DSS. In this way, a relationship is created between the description of a specific case, in terms of e-commerce success factor values, and the e-purchasing adoption behaviour, represented by the values of the innovation diffusion parameters. The e-marketing module allows then to:

- elicit the interactions between the different e-commerce success factors;
- link a specific configuration of e-commerce success factors to the correspondent e-purchasing adoption profile;
- model, relying upon innovation diffusions models, the e-purchasing adoption profile and specify the set of quantitative values that better describe e-purchasing patterns.

The logistics simulation module: SimFab

The information on the e-commerce potentials, prediction of the future electronic market demand, is combined with the demand stemming from traditional sales channels, taking into account the cannibalisation phenomenon, in order to calculate the so-called hybrid demand. The latter is the input to the logistic simulation program, which consists of a modelling and simulation software for discrete supply networks. Indeed, the simulator SimFab, designed, developed and coded in Java language allows a flexible modelling of production systems, considering different possible performance indicators such as the inventory levels, stocks and production costs and service levels with respect to customer demands. A simplified UML-class diagram of the module is shown in Figure 2. It highlights the dynamics of the software when applied to the evaluation of performance indicators of production systems. The motivations for the creation of SimFab are related to the observation made on the existing simulation tools. In fact, in most simulation programming packages, the models are designed with the help of a graphical user interface (ProModel, Arena, etc.). This approach is optimal for small and simple models but not appropriate for more complex systems often found in manufacturing environments. Therefore, most of the model logic has to be implemented in the programming language that supports the simulation package. Unfortunately, most of these programming languages are characterized by proprietary language features and poor support of modern object-oriented programming practices. Simulators without graphical user interfaces are based either on general purpose programming languages like C++ (Sim++) or JAVA (PSim/Java) or on proprietary programming

languages (QNAP). These simulators are more suitable for complex models but their major drawback is that their logic is often based on a queueing-network concept. These characteristics of existing simulator packages increase considerably the coupling between the different subsystems (Production Planning and control method and production system) of the modelled manufacturing system, leading to a rigid simulator. This problem is solved in SimFab by implementing a communication protocol between the different subsystems, based on the current states of the objects rather than on concrete messages sent between them. Compared to conventional simulation software, the simulation module SimFab, integrated in VISIONèS presents several advantages:

- integration of the different templates of production planning and control strategies: Material Resource Planning (MRP), Kanban techniques, Inventory Control and Double Speed Single Production Line (DSSPL) (Stagno et al. 2000) on the same modelled production system. This can lead to a realistic modelling of supply networks with heterogeneous production planning and control strategies,
- direct integration of design of experiments in the models, considering two possibilities: Monte Carlo simulation and factorial plans,
- open source development based on free and standard platforms; Java for the core code and XML for interfaces, external information exchanges and for configuration of supply networks and production systems,
- direct communication (Input/Output) with Excel files, thus automatically building report files and plotting corresponding graphs when desired.

With these features, linking the e-marketing module to the simulation one is simple. The hybrid demand (including different success or failure scenarios) resulting from the e-demand prediction is considered as the input to SimFab and the performance indicators of the considered supply network are evaluated for the different hybrid demand scenarios.

DEVELOPMENT AND FEEDBACK

The overall approach for the evaluation of e-commerce impact on industrial performance is developed in C-sharp (ISO/CEI 23270), which is an object-oriented programming language, compatible with the Java-based SimFab simulator and supporting XML as file exchange standards. In addition, C-sharp can support graphical user interfaces with respect to requirements from marketing and logistic users (Figure 3). As the information needed are gathered from different company departments (marketing, sales, production, purchase…), a database has been designed and developed around MySQL database to host these informations and those stemming from the simulation results. In addition, a web-based questionnaire, aiming at retrieving the real objective information from the customers and using the conjoint analysis technique, is integrated into the e-marketing module (Canetta et al. 2004). This interface, accessible from the web for identified customers, allows via proposed scenarios, taking into account the B2B e-commerce key factors, the identification of customer wishes and constraints that are used to elaborate the B2B e-commerce adoption scenarios.

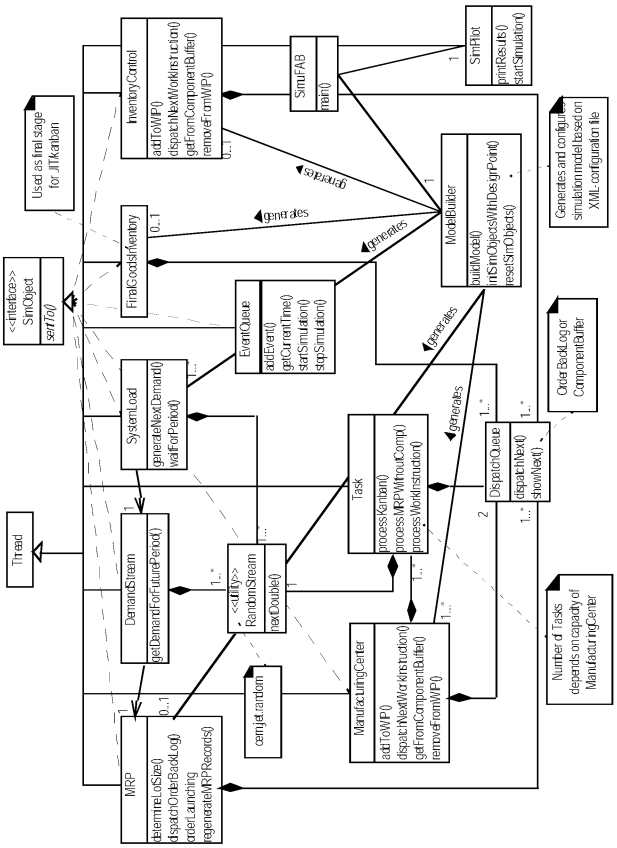

Figure 2: Design of the simulation module using UML

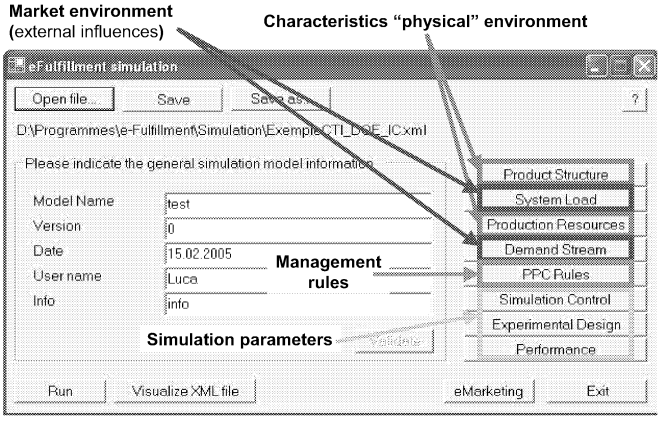

Figure 3: Some aspects of the graphical user interface of VISIONèS

The software in the early status of prototype has been installed and tested in two Swiss manufacturing companies. These companies have different management and information systems. Feedback from the implementation is

twofold. It has been observed firstly, that people in these companies have some difficulties to grasp the goals of the software, as this latter is horizontally integrated in various company departments. Secondly, for the enterprise that uses the e-marketing module, customers, that should use the proposed web-based conjoint analysis tool, are reticent to the use of internet to communicate sensitive information such as the importance of the relationship or the purchased volume of products, thus leading to trust problems between suppliers and customers.

CONCLUSION AND PERSPECTIVES

The achieved work on the development of an approach linking e-commerce to logistics has lead to the design, development and commercialisation of the VISIONèS software. Compared to some existing, market-oriented or information-oriented software, the presented work highlights modelling and simulation concepts as the major contributions to answer the question of the influence of e-commerce adoption on industrial performances. The approach, supported by the software, can be used for different purposes:

- supporting the choice and deployment of a coherent e-commerce sales channel strategy,
- modelling and predicting the hybrid market demand,
- identifying the potential effect of demand pattern modifications on enterprise and supply network performances,
- developing risk analysis and alarm tools for decision support in the design, management and parameterisation of supply networks.

As the approach presented in this paper has only covered discrete manufacturing market segments, it needs to be extended and validated to other industrial and service sectors, such as the process industry and warehousing. On the technical side, the software has to be further improved regarding its security level, insuring a more secure transmission of information from customers to suppliers. This can avoid serious trust problems.

ACKNOWLEDGEMENT

The authors wish to thank the Swiss Agency of Promotion and Innovation for supporting this work under grant CTI. 6066.1

REFERENCES

Canetta, L.; N. Cheikhrouhou; R. Glardon; and N. Iliev. 2004. "Supporting electronic sales channels deployment through the analysis of customer preferences." In *Proceedings of the IEEE International Conference on Systems, Man and Cybernetics*, (Den Haag, NL, Oct.10-13), 4123-4128.

Evans P. and T.S. Wurster. 1999. *Blown to bits: how the New Economics of Information Transforms Strategy.* Harvard Business School Press, Boston.

Gurunlian, J.; and L. Zhongzhou. 2001. *E-commerce and Development Report.* United Nations, New York and Geneva.

Hunter, L.M.; C.J. Kasouf; K.J. Celuch; and K.A. Curry. 2004. "A classification of business-to-business buying decisions: risk importance and probability as a framework for e-business benefits." *Industrial Marketing Management,* 33, No.2, 145-154.

Iliev, N.; R. Alard; L. Canetta; and N. Cheikhrouhou. 2004. "Evaluating Electronic Enabled Transaction Costs′ Efficiency." In *Proceedings of the International Conference on Global Production Management* (Bandung, Indonesia, September), 21-31.

Kiang, M.Y.; T.S. Raghu; and K.H.M. Shang. 2000. "Marketing on the Internet - who can benefit from an online marketing approach." *Decision Support Systems,* 27, 383-393.

Komiya, F.; T. Kusuzaki; S. Soga; K. Ohtani; I. Tsushima; and A. Hiramatsu. 1998. "Preliminary Evaluation of Business to Business Electronic Commerce by Using Qualitative Simulation and Scenario Generation." In *Proceeding of the IEEE International Conference on Systems, Man and Cybernetics* (San Diego, CA, Oct.11-14), 4763-4768.

Liu, J.Y.; J.M. Tarn; and H.J Wen. 2004. "Adopting e-commerce web site operation modes - the current stage of large US firms." Information Management and Computer Security, 12, No.1, 73-90.

O'Sullivan, D.; C. Richmond; and T. Power. 1998. "E-business in the supply chain, creating value in a networked marketplace." *IBM Consulting Financial Times Business Ltd.*

Roland, J.; T. Lawver; and T. Randery. 2000. "E-Sales: the Web is not enough – How to realize profitable growth from your Multi-Channel go-to-market approach." *McKinsey Marketing Practice*.

Scupola, A. 2002. "Adoption issues of business-to-business Internet commerce in European SMEs." In *Proceedings of the 35th Hawaii International Conference on System Sciences* (Big Island, Hawaii, Jan. 7-10), 2119-2128.

Selhofer, H. 2004. *The European e-Business Report - 2004 Edition.* European Commission Enterprise Directorate General, Bonn.

Stagno, A.; R. Glardon and M. Pouly. 2000. "Double Speed Single Production Line." *Journal of Intelligent Manufacturing,* 11, 169-182.

Strader, T.J. and M.J. Shaw. 1999. "Consumer cost differences for traditional and Internet markets." Internet Research: Electronic Networking *Applications and Policy,* 9, No.2, 82-92.

Tarn, M.; M. Razi; J. Wen; and A. Perez. 2003. "E-fulfillment: the strategy and operational requirements." *Logistics Information Management,* 16, No.5, 350-362.

AUTHOR BIOGRAPHY

NAOUFEL CHEIKHROUHOU is Senior Scientist at the Swiss Federal Institute of Technology at Lausanne, where he is leading the group of Operations Management. He received his PhD in industrial engineering from the Institut National Polytechnique de Grenoble. His main research interests are in the area of modelling, simulation and optimisation of production networks, the integration of human factors in production management and the reduction of management complexity in logistics and services.

ELECTRONIC NETWORKS SIMULATION

A NEW MODELING AND ANALYSIS OF ETHERNET NETWORK SYSTEM

Y. Jayanta Singh
Department of Computer Studies
Skyline College, P.O.Box. 1797
Sharjah, UAE
y_jayanta@yahoo.com

S.C. Mehrotra
Department of Computer Science and I.T.
Dr. B. Ambedkar Marathwada University.
Aurangabad - 431004. (M.S). India .
mehrotrasc@rediffmail.com

KEYWORDS:
Ethernet parameters, utilization, correlation factors

ABSTRACT

Achieving high performance depends not only on using faster hardware device but also on improvements in architecture and processing techniques. With the large growing numbers of applications and users, the exchange of the information is also increasing. Existing Ethernet systems have been investigated to see the effective utilization of the system to obtain higher performance with setting minimum changes. This study presents a detailed simulation study of an Ethernet system under different types of statistical distribution methods such as Exponential, Poisson etc. The experiment is mainly concentrated on maximum utilization of the system in a minimum delay time with a less number of collisions. The experimental results show the most effective and less effective parameters to the performance. A Correlation factor is introduced to understand the interdependence of the different parameters of the Ethernet. The study compares the different traffic outputs under different statistical distribution methods.

1. INTRODUCTION

One of the most widely used implemented LAN standards is an Ethernet system which is connecting computers within a building using hardware [E.J Coyle, B. Liu, 1983,1985]. It has the ability to support a wide variety of distributed computing environment and typical applications. Today with the efficient communication protocols, it is capable of high loads giving a high speed. Analytical studies have not been able to model the function of Ethernet's truncated binary exponential backoff algorithm, which also determines the protocol behavior in a high network demand regime. Therefore, the only feasible way to study the characteristics on a Local Ethernet in an accurate fashion is by simulation [Speros A. 1992, IEEE 1985, Guy T.A and Edward D.L.May 1979, Edward D. John Z, Willt Z,1986].

A detailed simulation model has been developed which follows the details of the Ethernet protocol on the Equidistant-Star topology [Speros A. Feb 1992, GPSS 2001]. The study performed simulation for the low cost and simple 10Mbps Ethernet system. Other advance Ethernet can also be done simulation in this same fashion. In order to verify the accuracy of this model, the simulator is set up to represent a real time system for which sufficient details are available in the literature and compared the simulation output to previous published results. The model is based on original Ethernet papers of Boggs [Robert M.M and D.R Boggs, 1976, D R. Boggs, J.C. Mogul 1988] and simulation model of GPSS world [GPSS 2001]. Different sets of simulation have performed using this model and reported the effective parameters with their optimized values.

The section 2 describes the Ethernet Simulation model and its parameters. In section 3, detail reports of the simulation system under exponential distribution method are given. In section 4 another detail of simulation of Ethernet under Poisson distribution method is given.

2. ETHERNET MODEL AND ITS PARAMETERS

This simulation focused on Maximum Utilization percent, in less average delay time with less numbers of collision or errors. The objective of the work is to report simulation results of a network system considering all performing parameters together under different statistical distribution methods. Interdependence of these parameters is also established by defining an interdependence factor between parameter values. The major system components are the workstations and the network. The workstations are responsible for providing the necessary processing to the data units and for organizing them into frames for transmission over the network. The frames or messages are processed under some distributed statistical methods. One of the Primary concerns in the network design is its topology which plays an important role to the system performance. This model follows a star topology where each node is equidistance from each other.

2.1 Simulation Model

The study is based on initial Ethernet study of Boggs [Robert M.M and D.R Boggs, 1976, D R. Boggs, J.C. Mogul, 1988] and simulation model of GPSS world [GPSS 2001]. In this, the messages are arrived exponentially as short or long. Each Node on the Ethernet is busy with a single message until it is sent. A Node is selected and held for the duration of message transmission and for any collision. A node gets free either in two ways: a) after sending the assigned message on it, and b) after declaration of a permanent error. Time is taken in units of milliseconds (ms). Nodes are presumed to be 2.5 m apart. The node ID numbers are used to determine the separation distance while calculating the collision window. The propagation delay to an adjacent node is 0.01 μs(microseconds). The signal propagation delay prevents nodes from having simultaneous knowledge of each other. Each bit is

transmitted in 0.1 μs. The interframe gap is modeled by having the sender hold the Ethernet for an additional delay after it has sent its message. The messages are represented by GPSS Transactions. The study has taken 1000 transactions. Nodes and the Ethernet are represented by GPSS Facilities. An additional Facility is used during jamming to prevent the startup of any new messages. The collisions are represented by removing the transmitting transaction from ownership of the Ethernet and sending it to a back off routine. The new owner jams the Ethernet briefly and then goes through the back off, itself. When a transaction's message is being sent, the transaction has ownership of the Ethernet Facility at priority 0, and can be preempted by transactions that are at priority 1. When a Transaction is jamming, it has ownership of the Ethernet Facility at priority 1, and is never itself is preempted.

2.2 Ethernet simulation model parameters

The values of typical Ethernet model parameters are given in table 1. The 'node count' is number of workstations used in an Ethernet system and initial value is set to 100. Inter message time is the average global time between arrival of two immediate messages and is set to 1 (milliseconds). Minimum (short) messages and Maximum (long) messages are the two different messages that are produced by the applied distribution rules. The value of Minimum messages is 512 bits and the Maximum message is 12144 bits. Fractional short messages are the short message arrived in parts per thousand messages and set to 600.

Parameter	Mean Value	Description
1.Node count	100	Total Ethernet nodes
2.Intermessage time	1.0	Avg. Global arrival every milliseconds
3.Minimum message	512	Shortestmessage (bit)
4.Maximum message	12144	Longestmessage (bit)
5.Fractionalshort message	600	Short message in parts per thousand
6. Slot time	0.0512	512 bit times
7. Jam time	0.0032	32 bit times
8. Back off limit	10	Max. back off limit
9.Interframe time	0.0096	96 bit times

Table 1. Ethernet Parameters (the mean avg values.)

Slot times are the slots for number of the nodes of the Ethernet system. The nodes are first divided groups. Only the members of group 0 are permitted to complete in slot 0. If one of them succeeds, it acquires the channel and transmits its message. If there is a collision, the members of group 1 contend for slot 1 etc. By making appropriate division of nodes into groups, the amount of contention for each slot can be reduced. As more and more nodes are assigned to same slot, the probability of a collision grows [A.S. Tanenbaum, 1994]. The slot time is also known as worst case time delay and a DTE (Data transmission equipment) must wait before it can reliably know a collision has occurred [H. Fred, 1997]. Any node detecting a collision aborts its transmission, generates a noise burst to warn all other nodes and then waits a random time before repeating the entire cycle. After a collision the time is divided up into discrete slots. To accommodate the longest path, the slot time has been normally set to 512 bits times and is managed by the BRAP (broadcast recognition with alternating priorities). After the first collision, each node waits either 0 or 1-slot times before trying again. In general after ***i*** collision, a random number between 0 and 2^{i-1} is chosen. However after 10 collisions have been reached the randomization interval is frozen at a maximum of 1023 slots. But after 16 collisions the controller reports failure back to computer. Jam times are taken as 32 bit times. The back off limit is fixed to 10. Interframe times are the time taken in between two immediate frames. Probability of a collision is higher with the smaller in frame size. Simulation result with these normal values, gives 47% utilization, 0.97 ms mean time and 3 collisions.

3. STUDY 1: EXPONENTIAL DISTRIBUTION LAW

Under exponential distribution method, a 10 Mbps Ethernet network is running satisfactory and giving highest 47% utilization [GPSS 2001]. To start the simulation study, the values of all the parameters have been changed one after another, for example, the value of Node count changed to 200, 300 so on, keeping other parameter values constant. From the simulated results, percent of Ethernet Utilization, Average delay time, and number of collisions are recorded and plotted graphs to analyze the most effective result. Thus study continued for remaining different parameters. The execution procedures are done similarly for the other distribution methods. The best values of the effective parameters are also plotted. Finally the interdependence values between the different parameters are calculated.

Ethernet Parameters (values)	% of utilization	Avg. Delay (ms)	No. of Collision
1.Fractional short (300)	80	3.2	22
2.Intermessagetime(0.7)	67	1.6	22
3.Interframetime(0.2048)	65	1.78	16
4.Max. message (16384)	61	1.7	15
5. Min. message (2048)	56	1.2	7
6. Jam time (0.0032)	48	0.97	3
7. Node Count (250)	48	0.98	0
8. Slot time (0.0128)	48	0.98	5
9. Back off limit (10)	47	0.97	3

Table.2. Optimum results for Parameters (values)

3.1 Optimum results under Exponential distribution

The most effective values of the each of the parameter are selected. Selection of such effective parameter and its value is made under such a condition that, the parameter should have maximum utilization percent, in less average delay with less number of collisions. An interdependence factors is also introduced in next section to see the interdependent characteristics of the parameters upon one another. The optimum values of each of the parameters of the system are given in table 2. The most optimum values of parameters are given in the bracket.

The study shows that the most efficient performance is dependent on fractional short message. When the systems have fractional (normal) value 600, the system gives only

47% utilization. By changing this value to 300, the utilization can be increased up to 80%. This type of system gives 3.2 ms average delay with total of 22 collisions. If it gives such utilization %, the average delay of 3.2 ms is tolerable as compared to result of Intermessage time. The total of 22 collisions comes to 0.022 collisions per messages. According to literature [A.S. Tanenbaum, 1994], if a node experienced 16 collisions continuously, the node is failed to do further work. There are 100 or more nodes in a system, so the possibility of occurring all 22 collisions to a specific node is rare. The dependent parameters are Inter message time, Inter frame message and so on. The Optimum percent of utilization, average delay time and number of collisions versus performing parameter are shown in figure 1 (A), (B) and (C) respectively.

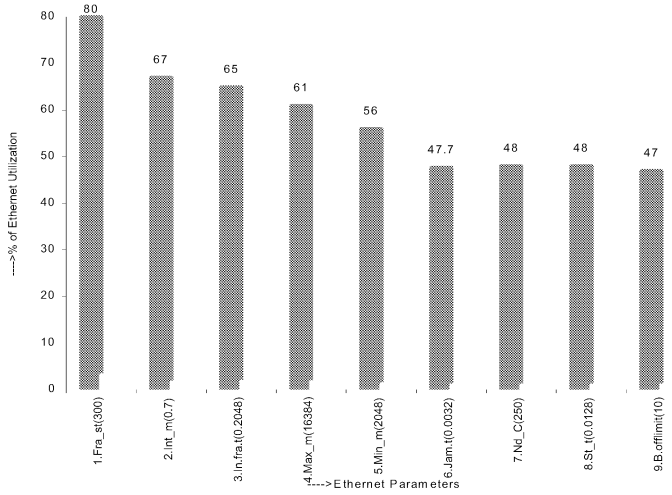

Figure 1 (A). Exponential: Optimum % of Utilization

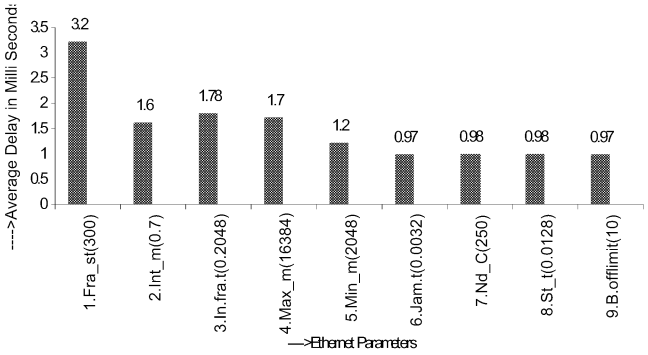

Figure 1 (B). Exponential: Optimum average delay time

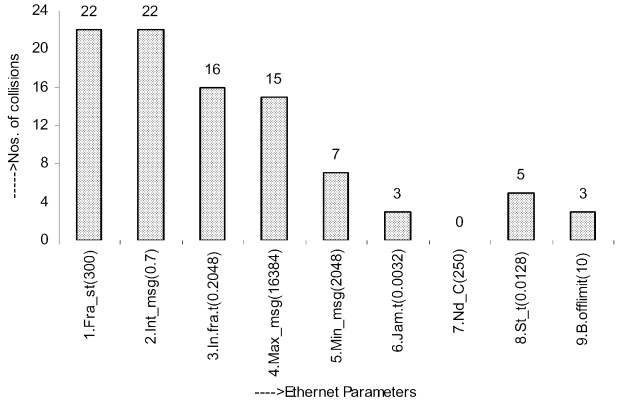

Figure 1 (C) Exponential: Optimum number of Collisions

3.2 Interdependence Parameters

To measure interdependence between any two parameters *a* and *b* with respect to any performance parameters, we define interdependence factor as follows. The *u* is one of the performance parameters, such as utilization%, average delay time and number of collisions in equation 1.

$$I(a,b) = \frac{(\delta u / \delta b) / b}{(\delta u / \delta a) / a} = (\delta u / \delta b) / (\delta u / \delta a) * b / a \quad \text{.....(1)}$$

Large values of *I(a,b)* indicate that change in one parameter will lead to large change in second parameter in relation to the performance parameter. The interdependence between Inter message time and Maximum message gives a largest interdependence value of 366.7 (not shown here). And next largest value is 333.3 given by Fractional short message and Maximum message. This large in interdependence values indicate that, value changed in one of these parameter leads to large change in the performance of the other parameter. On other side the interdependence value of Node count and Fractional short message is 0.1. Another value of Slot time and Inter message time is 0.2. These minor interdependence values indicate that change in one of this parameter will not give much effect on another parameter. They are just like independent from each other. The interdependence between Minimum message and Slot time gives a large interdependence value of 23000. And next largest value is 25600 given by Maximum message and slot time, indicating dependency on each other. The interdependence between Minimum message and Interframe time gives a large interdependence value of 250 and this indicating the dependency of values on each other. Another interdependence value between Jam time and Minimum message, Slot time and Jam time are all zeroes. These show that they are independent to each other. So in designing such a new system, concentration should be given to these inter dependent parameters to have a optimized performance.

3.3 Conclusion: Exponential distribution

The study mainly considered three performance factor utilization, delay time, and collisions. Here a maximum of 80% is possible by reducing the values of average delay time and also setting less number of collisions. If the performance is bring up to half, the values of average delay time and number of collisions becomes almost zero. The performance parameter gives maximum of optimized utilization percent in range of 47% to 80%, in average delay of 0.97ms to 3.2ms with of collisions in range of 0 to 22. So the nature of traffic and setting of performing parameter to appropriate values are important for optimum utilization of a system.

4. STUDY 2: POISSON DISTRIBUTION LAW

As the simulation of an Ethernet under Exponential distribution method is given in section 3, this section is explaining the simulation results of Ethernet under Poisson distribution method. Any message entered inside the Ethernet is processed under the Poisson distribution. Only the distribution method is changed and rests of simulation fashion are same as the previous simulation. It also plotted

graphs the best value of the effective parameters. The interdependent values between the different parameters can be calculated as done in previous simulation process. The comparisons of the most effective parameters along with their values are given in table 3. The comparisons of the performance of the different parameters are shown in following figures 2. The interdependent factors can be calculated as done in section 3.2 to see the interdependent relation of the parameters one upon another.

4.1. Optimum results under Poisson distribution method

The most effective values are given inside the bracket. The individual graphs of each of the outputs are also given.

Ethernet Parameters	% of Utilization	Avg. Delay in m s	No. of Collision
1. Fractional short message (400)	74.3	2.68	113
2.Min.message (4096)	73.3	2.11	130
3.Interframetime(0.2048)	70.5	2.16	144
4. Jam time (0.4096)	67.1	2.80	426
5.Max.message(16384)	66.8	2.34	155
6.Intermessagetime (0.8)	65.4	1.98	206
7.Slot time (0.1024)	52.5	1.23	190
8.Node count (100)	50.8	1.30	197
9.Back off limit (10)	50.8	1.30	197

Table 3. Optimum results for Parameters with their values

In this study the most effective performance is given by the fractional short message. By changing the value of this parameter to 400 from its original value 600, the utilization can be increased up to 74.3%. This type of system gives 2.68 ms average delay with total of 113 collisions. When the system has fractional short message value 600, the system gives only 47% utilization. Comparing the two cases of system utilization, the existing value of parameter is recommended to change to 400 or other to get a better performance condition.

Most of the results of the Poisson distribution always give a large number of collisions. For the Ethernet system, which is used to traffic pass flows under the Poisson distribution need to be compromised between either of the Optimized utilization percent or large collisions. Other changeable parameters are Minimum message, Inter frame message and so on. The detail is shown in table 3. The Optimum percent of utilization, average delay time and number of collisions versus performing parameter (its effective value) is given in figure 2 (A), (B) and (C) respectively.

4.2 Conclusion: Simulation under Poisson distribution:

The performance of the system can be bring at maximum of 74.3% utilization with setting the system at a possible less average delay time and less number of collisions condition. If we bring the performance to half, the values of average delay time and number of collisions become almost zero. The performance parameter gives maximum of optimized utilization percent in range of 50.8% to 74.3%, in average delay of 1.30ms to 2.68ms with number collisions in range of 100s to 200s. To know specific number of collisions per message, these total numbers of collisions should divide by the number of total messages (1000 in our case), which are grouped to form a single transaction. Although, it always gives a large number of collisions; still gives a good utilization percent. Under this Poisson distribution, the system need to be compromise between either of optimizes utilization or large collisions values.

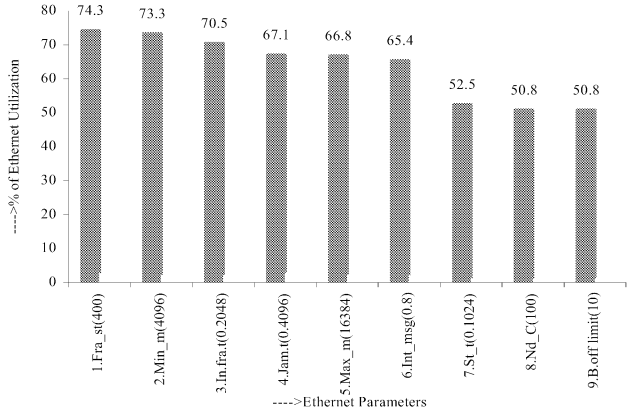

Figure 2. (A). Poisson: Optimum % of Utilization

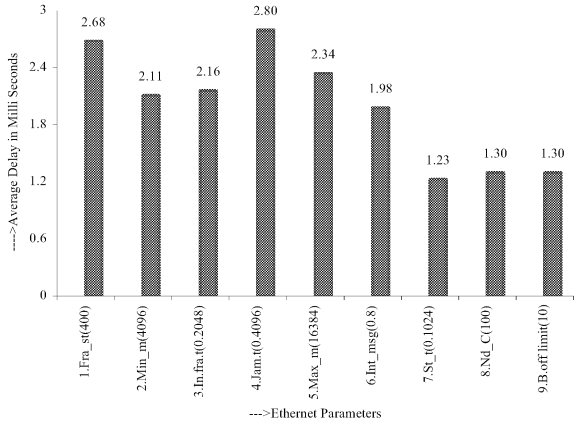

Figure 2 (B). Poisson: Optimum Minimum Delay time

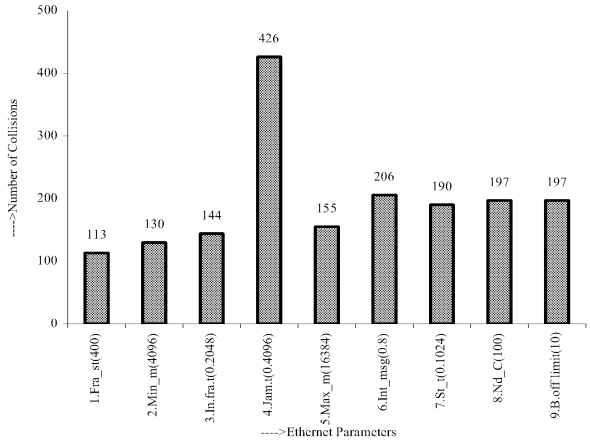

Figure 2 (C) Poisson: Optimum number of Collisions

5. CONCLUSION OF THE STUDY

A network system is said to be in normal and good working condition if it has a better utilization% with less delay time and less numbers of collisions. The 10Mbps Ethernet networks can be brought to nearly 100% utilization with minimum numbers of collision and less delay time. This can be done by changing the set values of the parameters individually. For overall performance of the systems, the correlation values give detail ideas about what value a parameter is required to set to get better performances. Firstly in results of the Exponential distribution, normally by setting the system at a possible less delay mean time and less collision condition, the system can bring at a maximum 80% utilization. If the performance has brought to half, the values of mean time and collisions will becomes almost zero. Secondly, in results of Poisson distribution it can't set the system to best normal state as it always gives a large numbers of collisions. If it is required to apply this distribution, there should be compromise and overlook the effect gives by collisions and need to concentrate on the mean time and Utilization % only. It can be noted that Poisson distribution can not give a quantitative performance to the system in normal condition. To design a system to have optimum utilizations, it is very important to know the types of the traffic in the network. The traffic with Poisson distribution is likely to be more inefficient as compare with the exponential distribution. Thus any study can be done for a new or an existing system by modifying the set parameters values for further development through Simulations. The parameters of any system and method of traffic flows are directly related to performance of any network system.

ACKNOWLEDGEMENT

It is gratefully acknowledge Minuteman Software, P.O. Box 131, Holly Springs, North Carolina, 27540-0131, USA for providing free Study materials in their site http://www.minutemansoftware.com

REFERENCES

Andrew S. Tanenbaum (1994). 'The medium access sub layers". **Computer Networks** (2E), 143-3. Prentice Hall.

D. R. Boggs, J.C. Mogul, and C.A. Kent.(1998). "Measured Capacity of an Ethernet: Myths and Reality", In Proc.of the SIGCOMM'88 Symposium on Communication Architectures & Protocols, **ACM SIGCOMM**, California, Aug.1988. Also as Tech. Report .by DEC **Western Research Laboratory** (WRL). 1988.

E. D. Lazowska, J.Zahorian, D.R. Cheriton, and Willt Z. (Aug.1998) "File Access Performance of Diskless Workstations." **ACM Transactions on Computer Systems**, 4(3): 238-268.

Edward J. Coyle and Bede Liu.(Nov. 1983)"Finite Population CSMA/CD Networks", **IEEE Transactions on Communications**, 31(11): 1247-1253.

Edward J. Coyle and Bede Liu.(Jan 1985) "A Matrix Representation of CSMA/CD Networks". **IEEE Transactions on Communications**, 33(1): 53-64.

GPSS 2001, Simulation on Ethernet, **GPSS World Tutorial Manual** NC US, *Minutes software,* (4E). Web site: www.minutemansoftware.com

Guy T. Almes and Edward D. Lazowska.(May 1979) "The Behavior of Ethernet- Like Computer Communications Networks". In Proc. of the **Local Area Communication Networks Symposium**, Boston,

Halsall Fred.(1997). **Local Area Networks**, *Data Communications, Computer Networks & Open System* (4E), 285, 290.

IEEE Standard 802.3-1985(1985). "Carrier Sense Multiple Access with Collision Detection CSMA/CD".

Robert M. M & D R. Boggs.(July 1976) "Ethernet: Distributed Packet Switching for Local Computer Networks." **Communication of the ACM**, 19(7):395-404.

Speros Armyros, (1992). "On the Behavior of Ethernet: Are Existing Analytic Models Adequate", Technical Report, **CSRI**-259.

BIOGRAPHY

Dr Y. Jayanta Singh is working as a Lecturer in department of Computer Studies in Skyline College, Sharjah, UAE. He obtained his M.Sc and Ph.D in Computer Science from Dr. Babasaheb Ambedkar Marathwada University, (India) in 2000 and 2004 respectively. He had worked with Mahindra British Telecom (MBT). His research papers are published in International and National Journals and in conference proceedings. His areas of interest are Networking, DBMS, ISO Process, Software Engineering and Simulation etc.

Dr. S. C Mehrotra, F.N.A,Sc., FIETE is working as a professor in Dr. Babasaheb Ambedkar Marathwada University, Aurangabad (India). He received his master degree in Physics from Allahabad University (India) in 1970 and Ph.D. in Physics from Austin (USA) in 1975. He is recipient of Welch Foundation Fellowship (1975), Alexander Von Humboldt Foundation Fellowship (1983-85), FOM (Neitherland). He has published more than 150 papers in areas of Time Domain Reflectometery, Speech Processing, and Network Simulation.

SWITCHED ETHERNET RESPONSE TIME EVALUATION VIA COLORED PETRI NET MODEL

Dmitry A. Zaitsev[1] and Tatiana R. Shmeleva[2]

Department of Communication Networks,
Odessa National Telecommunication Academy,
Kuznechnaya, 1, Odessa 65029, Ukraine
Web[1]: http://www.geocities.com/zsoftua, E-mail[2]: tishtri@rambler.ru

KEYWORDS

Ethernet, Switch, Response time, Colored Petri net, Evaluation

ABSTRACT

The enterprise class model of switched LAN in the form of a colored Petri net is represented. The components of the model are submodels of switch, server and workstation. For the evaluation of network response time a special measuring workstation model is proposed. It counts response times for each request and calculates the average response time. For the simulation of network behavior and accumulation of statistical information, CPN Tools was applied. Hierarchical nets usage allows the convenient representation of an arbitrary given structure of LAN. The influence of such features as limitations of switch's buffer size and dynamic maintenance of switching table were estimated.

INTRODUCTION

The technology of switching (Hunt 1999) is prospective for bandwidth increase in local and global computer networks. But it is hard enough to create an adequate analytical model of a switched network (Elsaadany et al. 1995). Petri net models (Peterson 1981) contain facilities for precise description of network architecture and traffic peculiarities and allow the representation of interaction within the client-server systems.

Early represented model (Zaitsev 2004a) has been refined up to enterprise quality. CSMA (Carrier Sense Multiple Access) procedures are implemented. Complete full-duplex mode is simulated with separate input and output frames' buffers. The model of switch is arranged for technological convenience with fusion places allowing an easy description of an arbitrary number of ports. Moreover, the general model is supplied with a special measuring workstation model that calculates network response time. Further to (Zaitsev 2004d) the influence of such features as limitations of switch's buffer size and dynamic maintenance of switching table are estimated.

It should be noticed that the model is represented with hierarchical colored (Jensen 1997) timed (Zaitsev and Sleptsov 1997; Zaitsev 2004b) Petri nets. For automated composition (Zaitsev 2005) of model and accumulation of statistical information during network behavior simulation, CPN Tools (Beaudouin-Lafon at al. 2001) is used.

At simulation, two major problems arise: to construct an adequate model and to evaluate its characteristics. Several simulating systems provide basic facilities for measurement of average storage capacity and frequencies of actions. But from the practical point of view more complicated characteristics are significant. For example, network response time and number of collisions for Ethernet. To solve this problem special facilities for measurement of models' characteristics are required. Colored Petri net is universal algorithmic system (Jensen 1997). We propose to represent algorithms of measurement as special measuring fragments of model implemented in the same language of colored Petri nets.

Results obtained may be used in real-time applications sensitive to delays, as well as at communication equipment, for instance, switches, development.

SWITCHED ETHERNET LAN

Recently the Ethernet has become the most widespread LAN. With gigabit technology it started a new stage of popularity. And this is not the limit yet. Hubs are dumb passive equipment aimed only at the connection of devices as wires. The base element of the Local Area Network (LAN) Ethernet (IEEE 802.3) is a switch of frames. Logically a switch is constituted of a set of ports (Rahul V. 2002). LAN segment (for example, made up via hub) or terminal equipment such as workstation or server may be attached to each port. The task of a switch is the forwarding of incoming frame to the port that the target device is connected to. The usage of a switch allows for a decrease in quantity of collisions so each frame is transmitted only to the target port and results in an increased bandwidth. Moreover the quality of information protection rises with a reduction of ability to overhear traffic.

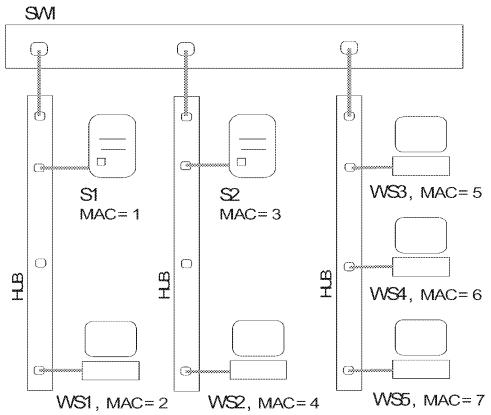

Figure 1: Scheme of railway dispatch center LAN

As a rule, the Ethernet works in a full-duplex mode now, which allows simultaneous transmission in both directions. To determine the target port number for the incoming frame a static or dynamic switching table is used. This table contains the port number for each known Media Access Control (MAC) address.

The scheme shown in Fig. 1 represents a fragment of a railway dispatch center LAN supplied with special railway CAM software GID Ural (Zyabirov at al. 2003). The core of the system constitutes a pair of mirror servers S1 and S2. The workstations WS1-WS5 are situated in the workplaces of railway dispatchers.

The right choice of time unit for model time measurement is a key question for an adequate model construction as well as the calculation of timed delays for elements of the model. It requires an accurate consideration of the real network hardware and software characteristics. We have to consider the performance of the concrete LAN switch and LAN adapters to calculate the timed delays (further represented with model's transitions **In***, **Out***, **Send**, **Receive)**. Moreover, the peculiarities of client-server interaction of GID Ural software ought to be considered for the estimation of such parameters as delay between the requests (**Delta)** and the time of request execution (**dex)**. Since the unit of information transmitting through net is represented with a frame, we have to express the lengths of messages in numbers of frames. For these purposes the maximal length of an Ethernet frame equaling 1.5 Kb was chosen. The types of LAN hardware used are represented in Table 1.

Table 1: Types of hardware

Device	Type
LAN adapter	Intel EtherExpress 10/100
LAN switch	Intel SS101TX8EU
Server	HP Brio BA600
Workstation	HP Brio BA200

In Table 2 the parameters of the model described are represented. LAN switch and adapter operations are modeled with fixed delays so they are small enough in the comparison with client-server interaction times. Moreover, in reliable Ethernet frames of maximal length are transmitted mainly, since the time of frame's processing is a fixed value. Stochastic variables are represented with uniform distribution, which corresponds to Ural GID software behavior. The smallest timed value is the LAN switch time of read/write frame operation. But for the purposes of future representation of faster equipment we choose the unit of model time (MTU) equaling 10 mcs.

Table 2: Parameters of model

Parameter	Real value	Model value	Variable/ Element
LAN switch read frame delay	50 mcs	5	In*
LAN switch write frame delay	50 mcs	5	Out*
LAN adapter read frame delay	100 mcs	10	Receive
LAN adapter write frame delay	100 mcs	10	Send
Server's time of request processing	1-2 ms	100-200	Dex
Client's delay between requests	10-20 ms	1000-2000	Delta
Length of request	1.2 Kb	1	
Length of response	15-30 Kb	10-20	Nse

MODEL OF LAN

A model of sample LAN with topology, shown in Fig. 1, is represented in Fig. 2. Let us describe the model constructed. It should be noticed that the model is represented with colored Petri net (Jensen 1997) and consists of places, drawn as circles (ellipses), transitions, drawn as bars, and arcs. Dynamic elements of the model, represented by tokens, are situated in places and move as a result of the transitions' firing. Tokens of a colored Petri net are objects of abstract data types (colors). Transition's firebility rules in colored Petri net involve inscriptions of input arcs, which chose input tokens, and a guard of transition, which constitutes a predicate defined on input tokens. Inscriptions of transition's output arcs constitute constructors of output tokens.

The elements of the model are sub models of: Switch (**SWI**), Server (**S**), Workstation (**WS**) and Measuring Workstation (**MWS**). Workstations **WS1-WS4** are the same type exactly **WS**, whereas workstation **WS5** is the type **MWS**. It implements the measuring of network response time. Servers **S1** and **S2** are the same type exactly **S**. Hubs are a passive equipment and have not an independent model representation. The function of hubs is modeled by common use of the corresponding places **p*in** and **p*out** by all the attached devices. The model does not represent the collisions. Problems of the Collision Detection (CD) were studied in (Zaitsev 2004c).

Each server and workstation has it's own MAC address represented in places **aS***, **aWS***. A switch has separate places for input (**p*in**) and output (**p*out**) frames for each port. It represents the full-duplex mode of work. Bidirected arcs are used to model the carrier detection procedures. One of the arcs checks the state of the channel, while another implements the transmission.

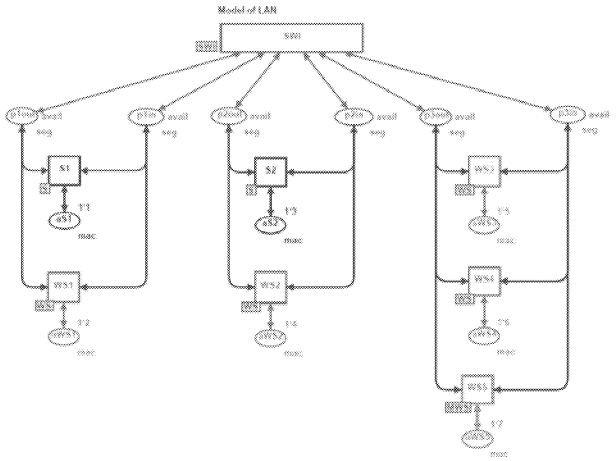

Figure 2: Model of sample LAN

```
color mac = INT timed;
color portnum = INT;
color nfrm = INT;
color sfrm = product nfrm * INT timed;
color frm = product mac * mac * nfrm timed;
color seg = union f:frm + avail timed;
color swi = product mac * portnum;
color swf = product mac * mac * nfrm * portnum timed;
color remsv = product mac * nfrm timed;
var src, dst, target: mac;
var port: portnum;
var nf, rnf: nfrm;
var t1, t2, s, q, r: INT;
color Delta = int with 1000..2000;
fun Delay() = Delta.ran();
color dex = int with 100..200;
fun Dexec() = dex.ran();
color nse = int with 10..20;
fun Nsend() = nse.ran();
fun cT()=IntInf.toInt(!CPN'Time.model_time)
```

Figure 3: Declarations

All the declarations of colors (**color**), variables (**var**) and functions (**fun**) used in the model are represented in Fig. 3. The Ethernet MAC address is modeled with integer number (color **mac**). The frame is represented by a triple **frm**, which contains source (**src**) and destination (**dst**) addresses, and also a special field **nfrm** to enumerate the frames for the calculation of response time. We abstract of other fields of frame stipulated by standard of Ethernet. The color **seg** represents unidirectional channel and may be either available for transmission (**avail**), or busy with transmission of a frame (**f.frm**). It is represented with a **union** type of color. It should be noticed that the descriptor **timed** is used for tokens, which take part in timed operations such as delays or timestamps.

The marking of places is represented with multisets (Jensen 1997) in CPN Tools. Each element belongs to a multiset with defined multiplicity, in other words – in a few copies. For instance, the initial marking of the place **aWS2** is **1`4**. It means that place **aWS2** contains 1 token with the value of 4. The union of tokens is represented by the double plus sign (++). Tokens of timed color have the form **x @ t** which means that token **x** may be involved only after a moment of time **t**. So, notation **@+d** is used to represent the delay with the interval **d**.

MODEL OF SWITCH

Let us construct a model for a given static switching table. We consider the separate input and output buffers of frames for each port and common buffer of the switched frames. The model of switch (**SWI**) is presented in Fig. 4. The hosts' disposition according to Fig. 1 was used for the initial marking of a switching table.

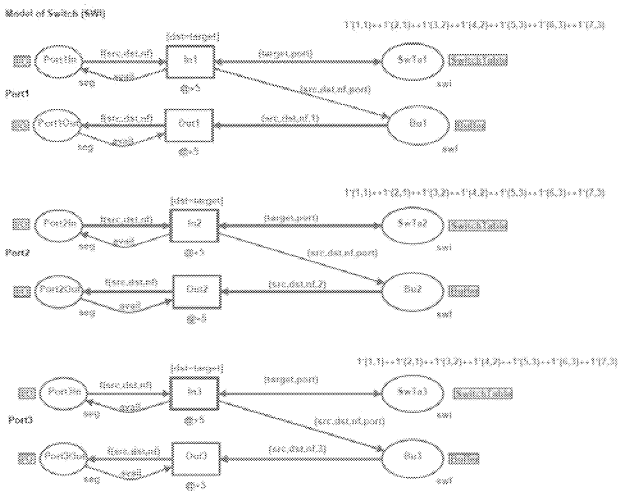

Figure 4: Model of switch

The color **swi** represents records of switching table. It maps each known MAC address (**mac**) to the number of port (**nport**). The color **swf** describes the switched frames, waiting for output buffer allocation. The field **portnum** stores the number of the target port. The places **Port*In** and **Port*Out** represent input and output buffers of the ports correspondingly. The fusion place **SwitchTable** models the switching table; each token in this place represents the record of the switching table. For instance, token **1`(4,2)** of the initial marking means that the host with MAC address 4 is attached to port 2. The fusion place **Buffer** corresponds to the switched frames' buffer. It should be noticed that a fusion place (such as **SwitchTable** or **Buffer)** represents a set of places. The fusion place **SwitchTable** is represented with places **SwTa1, SwTa2, SwTa3**. The fusion place **Buffer** is represented with places **Bu1, Bu2, Bu3**. It allows the convenient modeling of switches with an arbitrary number of ports avoiding numerous cross lines.

The transitions **In*** model the processing of input frames. The frame is extracted from the input buffer only in cases where the switching table contains a record with an address that equals to the destination address of the frame (**dst=target**); during the frame displacement the target port number (**port**) is stored in the buffer. The transitions **Out*** model the displacement of switched frames to the output ports' buffers. The inscriptions of input arcs check the number of the port. The fixed time delays (@+5) are assigned to the operations of the switching and the writing of the frame to the output buffer.

It is necessary to explain the CSMA procedures of LAN access in more detail. When a frame is extracted from the input buffer by transition **In*,** it is replaced with the label **avail**. The label **avail** indicates that the channel is free and available for transmission. Before the transition **Out*** sends a frame into a port, it analyses if the channel is available by checking the token **avail**.

It should be noticed that places **Port*In** and **Port*Out** are contact ones. They are pointed out with an **I/O** label. Contact places are used for the construction of hierarchical nets with substitution of transition. For example, the transition **SWI** in the top-level page of model (Fig. 2) is substituted by a whole net **SWI** represented in Fig. 3. Places **Port*In** and **Port*Out** are mapped into places **p*in** and **p*out** correspondingly.

MODELS OF WORKSTATION AND SERVER

To investigate the frames' flow transmitting through LAN and to estimate the network response time it is necessary to construct the models of terminal devices attached to the network. Regarding the peculiarity of the traffic's form we shall separate workstations and servers. For an accepted degree of elaboration we consider periodically repeated requests of workstations to servers with random uniformly distributed delays. On reply to an accepted request a server sends a few packets to the address of the requested workstation. The number of packets sent and the time delays are uniformly distributed random values.

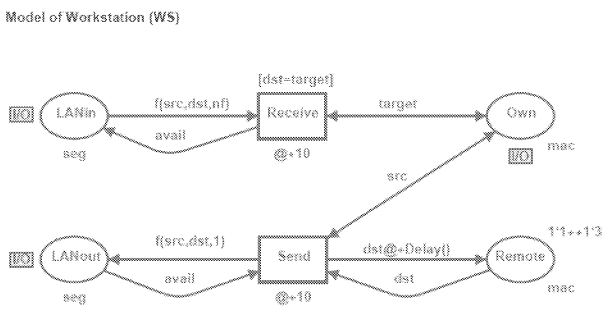

Figure 5: Model of workstation

A model of workstation (**WS**) is represented in Fig. 5. The places **LANin** and **LANout** model the input and output channels of the local area network correspondingly. The workstation listens to the network by means of transition **Receive** that receives frames with the destination address, which is equal to the own address of the workstation (**dst=target**) saved in the place **Own**. The processing of received frames is represented by the simple absorption of them. The workstation sends periodic requests to servers by means of transition **Send**. The servers' addresses are held in the place **Remote**. After the sending of a request the usage of the server's address is locked by the random time delay given by the function **Delay()**. The sending of the frame is implemented only if the LAN segment is free. It operates by checking place **LANout** for a token **avail**. In such a manner the workstation interacts with a few servers holding their addresses in the place **Remote**.

It should be noticed that the third field of frame, named **nfrm,** is not used by the ordinary workstation **WS**. The workstation only assigns the value of a unit to it. This field is used by a special measuring workstation **MWS**. The copies of the described model **WS** represent workstations **WS1-WS4**. To identify each workstation uniquely, the contact place **Own** is used. This place is shown also in the top-level page (Fig. 2) and contains the MAC address of a host.

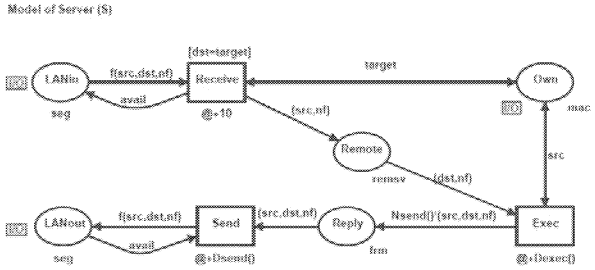

Figure 6: Model of server

A model of server (**S**) is represented in Fig. 6. The listening of the network is similar to the model of the workstation but it is distinct in that the frame's source address is held in the place **Remote**. The transition **Exec** models the execution of the workstation's request by a server. As a result of the request execution the server generates a random number **Nsend()** of the response frames, which are held in the place **Reply**. Then these frames are transmitted into the network by the transition **Send**. It should be noticed that the request number **nf** is stored in the place **Remote** also. It allows us to identify the response with the same number as the request.

MODEL OF MEASURING WORKSTATION

A model of the measuring workstation (**MWS**) is represented in Fig. 7. In essence, it is an early considered model of workstation **WS**, supplied with the measuring elements (the measuring elements are drawn in magenta).

Let us consider the measuring elements in more detail. Each frame of a workstation's request is enumerated with a unique number contained in the place **num**. The time, when the request was sent, is stored in the place **nSnd**. The function **cT()** calculates the current value of the model's time. The place **nSnd** stores a pair: the frame's number **nf** and the time of request **cT()**.

The place **return** stores the timestamps of all the returned frames. As the network response time we consider the interval of time between the sending of the request and receiving the first frame of the response. This value is stored in place **NRTs** for each responded request. The transition **IsFirst** determines the first frame of response. The inscription of the arc, connecting the transition **IsFirst** with the place **NRTs**, calculates the response time (t2-t1).

A residuary part of the measuring elements calculates the average response time. The places **sum** and **quant** accumulate the sum of response times and the quantity of accepted responses correspondingly. The arrival of a new response is sensed by the place **new** and initiates the recalculation of average response time with the transition **Culc**. The result is stored in the place **NRTime**.

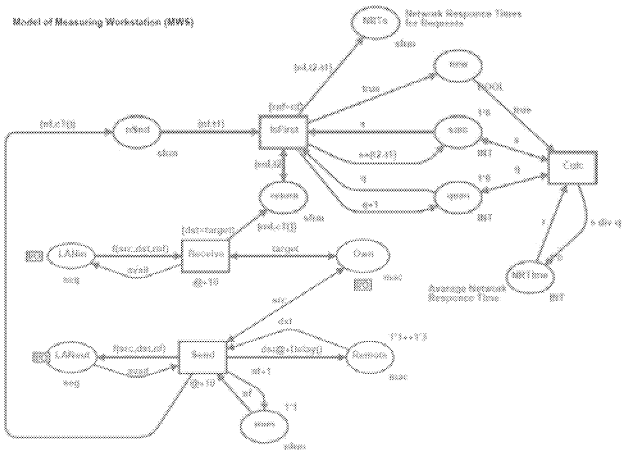

Figure 7: Model of measuring workstation

EVALUATION TECHNIQUE

The model constructed was debugged and tested in a step-by-step mode of simulation. For these purposes the frame generated by the workstation was traced through the network to the server and backwards. Also we observed the behavior of the model in the process of automated simulation with a display of net's dynamics – in the mode of the so-called game of tokens. It allows us to estimate the model with a glance at the top-level page and at sub pages during simulation.

To estimate the network response time precisely, rather huge intervals of model time are required. It is convenient for such purposes to use the simulation mode without displaying intermediate marking aimed at the accumulation of statistics.

A snapshot of the measuring workstation model is represented in Fig. 8. The rectangular labels (drawn in bright green) describe the current marking of the simulation system; the circular labels contain the number of tokens. The place **LANin** contains frame (1,5,1). The place **LANout** represents the available state of the channel **avail**. The number of the next request, according to the marking of place **num**, is 7. The place **return** indicates that 83 frames of responses have arrived. The place **NRTs** contains the response times for each of the 6 responded requests. For instance, the network response time for request 5 equals to 235. It should be calculated easily, that the average network response time 389 in the place **NRTime** equals to 2337/6 according to the markings of the places **sum** and **quant**.

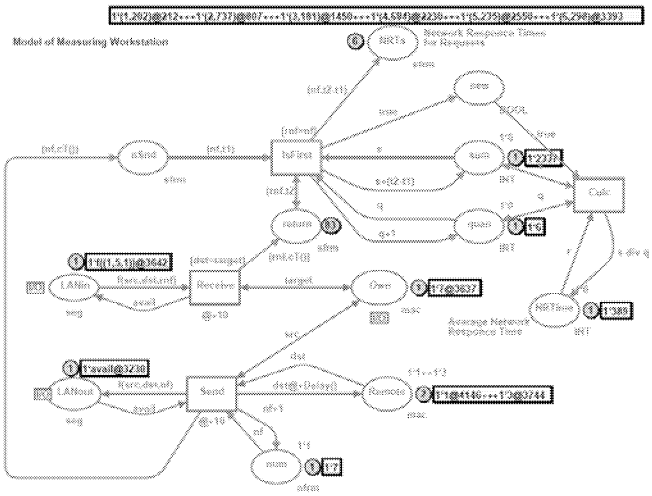

Figure 8: Evaluation of network response time

To estimate the response time precisely we have to observe huge enough intervals of model time to accumulate statistical information. It should be noticed that one second of real time corresponds to 10^5 MTU. At first we interested in existence of steady-state mode. For example, model with parameters described has a steady-state mode with the value of response time represented in Table 3. The increasing of the observation interval does not change the value of response time. In spite of this example twice-slower switch or twice slower network adapters usage leads to unstable network with constantly increasing response time (Tables 4, 5). Consequently, the first question is about existence of a steady-state mode and the second one consists in concrete values of parameters.

Thus, the average network response time obtained (Table 3) equals 304 MTU or about 3 ms. This delay satisfies the requirements of train traffic control (Zyabirov at al. 2003).

Table 3: Steady-state conditions for network response time

Step	1000	11000	111000	1111000	2111000	3111000
Model time, MTU	2831	24488	245973	3124656	5340611	7547756
Response time, MTU	318	316	307	304	304	304

Table 4: Response time for twice slower switch (In*, Out*: @+10)

Step	1000	11000	21000	121000	221000
Model time, MTU	3306	26978	50536	285136	521713
Response time, MTU	336	800	1284	4477	7692
Queue size, frames	43	96	102	357	498

Table 5: Response time for twice slower network adapters (Receive, Send: @+20)

Step	1000	11000	21000	121000	221000
Model time, MTU	3306	26978	50536	352956	644517
Response time, MTU	336	800	1284	14665	27803
Queue size, frames	43	43	102	3462	6305

BUFFER SIZE LIMITATIONS INFLUENCE

Though model constructed represents a lot of characteristic features of real-life Ethernet, such, for instance, as full-duplex mode, switching table, CSMA procedures, it is simplified enough. There are a few additional peculiarities of switched LAN, which influent more or less essentially on the bandwidth of network. Let us enumerate them. The model of switch does not take into accounting real size of internal buffer of frames and does not implement mechanism of jam messages to avoid overload. Switching table is static whereas the majority of real-life hardware provide dynamic switching table. Random extraction from switching table is implemented. Moreover, we do not consider the timed characteristics of frame transmission through segment of LAN. It is adequate in the case we do not consider broadcasting and multicasting. In model constructed we put frame into the place, modeling the segment, and we are assured that there is a target device in this segment, which will get the frame. For representing of multicasting we have to remove the frame from segment after the elapsing of transmission time.

As for technology of client-server interaction, we consider two-way handshake only. The model may be refined for more complicated algorithms of interaction reflecting the behavior of concrete software. But for algorithm of interaction implemented we use random discipline of extraction for places representing the queues of requests and responses. Moreover, execution of request does not take into accounting the number of server's processors and issue on unlimited number of processors.

But the complete detailed model of Ethernet LAN is too sophisticated. Therefore, we not go beyond to consider the influence of most significant items of real-life network on response time obtained. At first we modify the model for limited switch's buffer and estimate the network response time under different values of buffer's size. The model of switch's port for limited buffer's capacity is represented in Fig. 9.

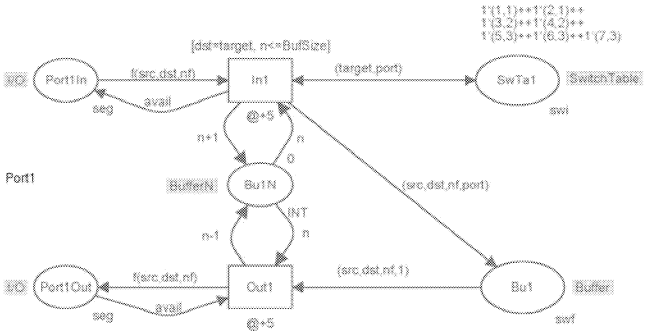

Figure 9: Model of port for limited capacity of buffer

In the comparison with the base model of switch represented in Fig. 2 we added new fusion place **BufferN** represented for Port 1 with place **Bu1N**. This place contains the number of frames in buffer. Transition **In1**, which puts frame into buffer increments the value of **BufferN** and transition Out1, which gets frame from buffer - decrements the value of **BufferN**. The guard of transition **In1** checks the size of **Buffer** represented with the constant **BufSize**. The models of another ports are analogous.

The results of network response time estimation under various values of switch's buffer size are represented in Table 6. We may conclude that small buffer sizes influence on response time essentially but more volumetric buffers than of 100 frames usage has no effect and does not decreases the network response time.

Table 6: Influence of buffer size on network response time

Buffer size, frames	2	10	20	100	1000	2000
Response time, MTU	803	312	308	305	304	304

DYNAMIC SWITCHING TABLE INFLUENCE

Static switching tables are used in the networks with the extreme requirements to security. But the administration of static switching table for large networks is laborious enormously. Dynamic maintenance of switching tables is usual practice for the majority of networks. In this case the bandwidth of network is decreased because the broadcast

and multicast traffic but network became more flexible and self-adjusting to variable structure.

The task to model dynamic switching table is complicated enough. Let us remind the general technique of dynamic switching stipulated by standards. We pay our attention only to peculiar properties:

1) At arrival of frame with unknown source MAC-address switch adds new record corresponding to this address to switching table.

2) At arrival of frame with unknown destination MAC-address switch executes multicasting forwarding frame to all the ports. In this case it works like a hub.

3) Periodically switch clears its switching table.

First item provides the passive recognition of network structure. Second item allows the avoidance of special active recognition. Periodical reset of switching table provides the adjusting to current structure of network and the set of devices alive.

Implementation of dynamic switching requires not only modification of switch's model but also the total revision of the entire model. Now we have to represent the timed characteristics of frame's transmission at least for channel of segment in the direction from switch. If frame of multicasting will not been removed by destination device we have to remove it at the elapsing of transmitting time. The implementation of the absence checking for token with specific properties requires the usage of list data type (color) of CPN Tools. The model of switch's port for dynamic switching and the model's fragment for periodic cleaning of switching table are represented in Fig. 10.

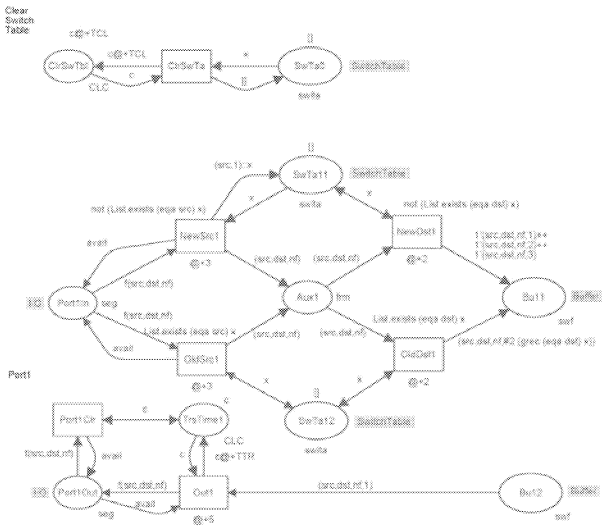


```
color swita=list swi; var x:swita;
fun eqa a (rr:swi)=((#1 rr)=a);
fun grec prd [] = (0,0) | grec prd (q::r) =if prd(q) then q else grec prd r;
color CLC=unit with c timed;
```

Fig. 10: Model of dynamic switching

Let us consider the additional declarations used. Color **swita** is the list of **swi** and models the switching table. List structure is applied to provide the checking of absence of records in switching table with specified MAC-address. Color **CLC** represents a timer. It consists of one timed element **cl**. Function **eqa** provides the comparison of MAC-addresses. Function **grec** gets the record of switching table for which the value of function **eqa** is true.

At arrival frame in **Port1In** one of transitions **NewSrc1**, **OldSrc1** fires and puts frame to auxiliary place **Aux1**. The difference of these transitions' actions consists in that transition **NewSrc1** adds new record to switching table corresponding to source MAC-address. Standard function **List.exists** checks the existence of record with MAC-address equaling to **src**. Function **eqa** provides the comparison of address with first field of record. Then one of transitions **NewDst1**, **OldDst1** fires. The checking of address is implemented in the same way but **dst** field of frame is used. If the destination address is known (**OldDst1**) then frame is moved to buffer and the number of target port is calculated according to switching table. Function **grec** provides the usage of required record; as the number of destination port the second field of record is taken. If the destination address is unknown (**NewDst1**) then multicasting is implemented. The frame arrived is forwarded to all the ports of switch. To avoid a cross influence of modification we save the total time of input frame processing distributing the time amongst two sequential transitions.

At the transmission of output frames to **Port1Out** we set the timer in place **TrsTime1** with value **TTR**. And if the frame will not been removed by terminal device then transition **Port1Clr** removes it after elapsing of transmission time. For simulation the value of **TTR** is chosen equaling to 10 MTU that correspond to 100Mbps speed: $(1{,}5 \cdot 10^3 \cdot 8)/\ 10^8$ c.

The models of other ports are analogous. Moreover, model of switch has one common fragment representing the cleaning of switching table. Place **ClrSwTbl** contains a timer token, which starts the cleaning with the aid of transition **ClrSwTa**. Period of cleaning is determined by value of constant **TCL**. Table 7 represents estimations of network response time under various values of cleaning period **TCL**. Frequent cleaning leads to increase of response time, whereas infrequent cleaning with period more than 10^5 practically does not influent on response time. It should be noticed that at **TCL** about 1000 MTU or less the state-stable mode is not approached.

Table 7: Influence of dynamic switching on network response time

TCL, MTU	1000	2000	4000	10000	100000	200000
Response time, MTU	-	512	362	320	304	304

REAL-LIFE LAN MEASUREMENTS

The measurements of response time in the environment of the real-life network of the railway dispatcher center were implemented using sniffer of packets WinDump, which is MS Windows version of well-known Unix sniffer TCPDump. The results have been acknowledged also with the aid of SoftPerfect Network Protocol Analyzer.

WinDump is a command-line tool, which provides writing of Ethernet frames into a file together with time stamps. Then the content of the file may be displayed and analyzed. The following command line provides the writing of frames into file SavedFrames:

WinDump -w SavedFrames

For analysis of frames' transmission and calculation of response time the following command line was used:

WinDump -ttt -r SavedFrames

Option -ttt is used for automatically calculation of time interval between frames; option -r provides reading of early saved information from the file SavedFrames. An example of the obtained listing is represented in Fig. 11.

```
000252 IP 192.168.0.158.1172 > 192.168.0.130.139: P 854:917(63) ack 840 win 64957
000854 IP 192.168.0.130.139 > 192.168.0.158.1172: . 840:2300(1460) ack 917 win 64502
000141 IP 192.168.0.130.139 > 192.168.0.158.1172: . 2300:3760(1460) ack 917 win 64502
000029 IP 192.168.0.158.1172 > 192.168.0.130.139: . ack 3760 win 65535
000107 IP 192.168.0.130.139 > 192.168.0.158.1172: . 3760:5220(1460) ack 917 win 64502
000138 IP 192.168.0.130.139 > 192.168.0.158.1172: . 5220:6680(1460) ack 917 win 64502
000024 IP 192.168.0.158.1172 > 192.168.0.130.139: . ack 6680 win 65535
000114 IP 192.168.0.130.139 > 192.168.0.158.1172: . 6680:8140(1460) ack 917 win 64502
000086 IP 192.168.0.130.139 > 192.168.0.158.1172: P 8140:9095(955) ack 917 win 64502
000287 IP 192.168.0.158.1172 > 192.168.0.130.139: . ack 9095 win 65535
000606 IP 192.168.0.158.1172 > 192.168.0.130.139: P 917:980(63) ack 9095 win 65535
000729 IP 192.168.0.130.139 > 192.168.0.158.1172: . 9095:10555(1460) ack 980 win 64439
```

Fig. 11. Dump of frames

Let us consider the information of the dump. The first column contains delays between frames in microseconds, then IP-addresses and port numbers of sender and receiver are printed. After semicolon the details of packet header are printed such as start and finish numbers of transmitting bytes, the length of frame in brackets, acknowledged byte number and the length of window. In above example 192.168.0.158 is the IP-address of workstation and 192.168.0.130 is the IP-address of the server. The port number 139 corresponds to MS NetBIOS TCP service, the port number 1172 is a random port number of client software. In this example the response time for the first request is equal to 854 mcs, for second - 107 mcs, for third 114 mcs.

WinDump was started on the operating GID Ural Workstation. We calculated an average value of response times of individual requests collected on the period of observation about one shift of work, which is equal to 12 hours. Obtained real-life average NRT is equal to 2,83 ms. The error of NRT measurement via Petri net model constitutes about 6% that is good enough result, which proves the applicability of the described technique.

CONCLUSION

In the present work the technology of switched local area networks' models development was studied. The usage of colored Petri nets allows the peculiarity of interaction within the client-server systems to be taken into account. The model reflects the major features of real-life network. CSMA procedures, full-duplex mode and switching tables were modeled. A special measuring model of workstation was suggested and implemented to estimate the network response time.

The model developed is of enterprise class, so it allows easy and convenient adequate representation of LAN with an arbitrary given topology. Moreover, the influence of such features as switch's buffers limitations and dynamic switching were studied. The technique described is aimed at real-time applications, requiring the precise estimation of timed delays before implementation.

REFERENCES

Beaudouin-Lafon M., Mackay W.E., Jensen M. et al. 2001. "CPN Tools: A Tool for Editing and Simulating Coloured Petri Nets". In *LNCS 2031: Tools and Algorithms for the Construction and Analysis of Systems*, 574-580. (http://www.daimi.au.dk/CPNTools)

Elsaadany M., Singhal T., Lui Ming. 1995. "Performance study of buffering within switches in local area networks". In *Proc. of 4th International Conference on Computer Communications and Networks*, 451-452.

Jensen K. 1997. *Colored Petri Nets – Basic Concepts, Analysis Methods and Practical Use.* Springer-Verlag, Vol. 1-3.

Hunt R. 1999. "Evolving Technologies for New Internet Applications". *IEEE Internet Computing*, 5, 16-26.

Peterson J. 1981. *Petri Net Theory and the Modelling of Systems.* Prentice Hall.

Rahul V. 2002. *LAN Switching.* OHIO.

Zaitsev D.A. and Sleptsov A.I. 1997. "State Equations and Equivalent Transformations of Timed Petri Nets". *Cybernetics and System Analysis*, no. 5, 659-672.

Zaitsev D.A. 2004a. "Switched LAN simulation by colored Petri nets". *Mathematics and Computers in Simulation*, 65, no. 3, 245-249.

Zaitsev D.A. 2004b. "Invariants of timed Petri nets". *Cybernetics and Systems Analysis*, no. 2, 92-106.

Zaitsev D.A. 2004c. "Verification of Ethernet protocols". *Proceedings of Odessa National Telecommunication Academy*, no. 1, 42-48.

Zaitsev D.A. 2004d. "An Evaluation of Network Response Time using a Coloured Petri Net Model of Switched LAN". In *Proceedings of Fifth Workshop and Tutorial on Practical Use of Coloured Petri Nets and the CPN Tools*, October 8-11, Aarhus, Denmark, 157-167. 14

Zaitsev D.A. 2005. *Functional Petri Nets.* Universite Paris-Dauphine, Cahier du Lamsade 224, Avril, 62p. (http://www.lamsade.dauphine.fr/cahiers.html).

Zyabirov H.S., Kuznetsov G.A., Shevelev F.A., et al. 2003. "Automated system for operative control of exploitation work GID Ural-VNIIZT". *Railway transport*, no. 2, 36-45.

MOBILITY-BASED ROUTING FOR MOBILE AD HOC NETWORKS

M. Alchaita ,M. Al-Akaidi, J. Ivins

School of Engineering & Technology
De Montfort University
Leicester, UK
E-mail: mma@dmu.ac.uk

KEYWORDS
Mobile Ad hoc Networks, Routing Protocols, Heading Directional Angle, On-demand, Mobility

ABSTRACT

Mobility is a prominent characteristic of Mobile Ad hoc Networks (MANETs), and the main factor affecting topology change and route invalidation. Several routing problems are posed by mobility, such as frequent breaking of the wireless link, short life time of the established routes, and asymmetric communication links. These problems increase the signalling overhead required to establish routes, and thus affecting the performance of the protocol. As mobility is inevitable, we need to take advantage of one positive aspect of this phenomenon as much as possible, which is the heading direction of the node. In order to exploit mobility of nodes to provide a robust and long-lived route to destination and reduce flooding and overhead in the network, three novel routing schemes are proposed in this paper. In these schemes, only a small number of nodes are selected based on its Heading Direction Angle (HDA), to form a route. Our results show how these schemes reduced the overhead and flooding and increased the life of the route in comparison with the conventional Ad hoc On-demand Distance Vector (AODV) protocol. These schemes could be applied to other routing protocols in order to improve the performance of these protocols.

INTRODUCTION

A mobile ad hoc network, unlike a static network, has no infrastructure (e.g. Base stations). It is a collection of mobile nodes where communication is established in the absence of any fixed infrastructure. The only possible direct communication is between neighbouring nodes; therefore communication between remote nodes is based on multi hop. These nodes are dynamically and arbitrarily located in such a manner that the interconnections between nodes are capable of changing on a continual basis, and each mobile host acts as a host and a router, relaying information from one neighbour to others. As host mobility can cause frequent unpredictable topology changes, and establishing a route between end-points requires routing over multiple-hop paths whose end-points are likely to be in motion, the task of finding and maintaining routes in MANET is nontrivial (Young-Bae Ko et al. 2000; Elizabeth M. Royer, 1999).

Another obstacle of mobility in ad hoc networks is the increased rate of link failure and the activation of broken links with increasing mobility of nodes that increases both the congestion due to traffic backlogs and the volume of control traffic required to maintain routes. Thus in order to achieve adaptive routing responsiveness and efficiency, a decisive protocol design goal has to be the diminution of reaction to mobility (A. Bruce McDonald and Taieb Znati 1999). Hence, mobility is a very important factor affecting the performance of the routing protocol. Many protocols have been proposed for mobile ad hoc networks, with the aim of achieving efficient routing (S. Basagni et al. 2001, W. Su, et al. 2000). These protocols differ in the approach used for searching a new route and/or modifying a known route, when hosts move.

From previous discussion, mobility in ad hoc networks is an obstacle that cannot be avoided. The mobility causes the expiration of the information used by traditional routing protocols in establishing a route. Therefore, dealing with mobility by exploiting the positive aspect of this phenomenon as much as possible is less demanding than if the positive aspect was ignored completely.

In this paper, we propose three on-demand schemes that could be adopted by most of the existing routing protocols. These schemes exploit the mobility of nodes to establish routes from sources to destinations using the heading direction information for mobile hosts. Hence, these routes are selected based on the longest duration of their existence. We also show in this paper how to utilize axis-mapping technique, and Heading Direction Angle (HDA) of a mobile node to propagate a message between nodes in the network in order to establish and maintain a robust and long-lived route to destination, as well as limiting the scope of route requests to reduce the overhead in the network.

The remainder of this paper is organized as follows. Section II discusses some related work. Section III describes the main idea of our schemes of using HDA information for route discovery in MANET, and presents the three designed schemes that utilize different ways to select the proper neighbour(s) to forward packets to. In section IV, we evaluate the effectiveness of the three schemes by simulation using the Network Simulator NS-2. In addition, we have studied the impact of overhead and the cost of data delivery on routing protocol performance. Conclusion and suggestions for future work are made in Section V.

NODES HEADING DIRECTION ANGLES

Since GPS (Peter H. Dana, 2000) may not work properly in certain situations; routing protocols that uses geographical information may not always be able to work properly for such situations. Therefore, another new method should be used to derive the required information. In our scheme we have utilized a digital advanced compass with magneto resistive (MR) technology (Solid State Electronics Center), which delivers the heading direction angle of the mobile device hosting it.

In this section we explore the possibility of using heading information to improve performance of routing protocols for MANET. As an illustration, we show how a route discovery protocol based on mobility information can be improved. Consider two mobile hosts and are within the transmission range R of each other (assume that the transmission range of n_1 and n_2 are the same). (x_{n1}, y_{n1}), v_{n1} and (x_{n2}, y_{n2}) , v_{n2} are the coordinate and velocity of n_1 and n_2 respectively. Let us assume that n_1 and n_2 move in direction θ_{n1} and θ_{n2} from the north respectively.

The amount of time that two mobile hosts will stay connected D_t (changeable with the time) remains within the coverage distance, depends on the difference between θ_{n1} and θ_{n2} as denoted by the equation:

$$D_t = \frac{-(pl+qd)+\sqrt{(p^2+q^2)R^2-(pd-lq)^2}}{p^2+q^2}$$

Where

$$p = v_{n1}\sin\theta_{n1} - v_{n2}\sin\theta_{n2},\ l = x_{n1} - x_{n2},$$
$$q = v_{n1}\cos\theta_{n1} - v_{n2}\cos\theta_{n2},\ d = y_{n1} - y_{n2}.$$

Note that θ_{n1} and θ_{n2} are with the north, and the link between n_1 and n_2 stays longer when the two nodes move in similar direction. Fig. 1 depicts the relation between D_t and the difference between θ_{n1} and θ_{n2}. It is clear from Fig. 1 that the probability of a path breaks increases as the difference between the direction angles of the end nodes increases. Hence, when the next node in the link is selected based on its direction to be near to the upstream nod heading direction, the link will last longer, and when $\theta_{n2} - \theta_{n1} = 0$, the time of path break increases to infinity.

The expected lifetime of a link is examined in (D. Turgut et al. 2001), and the relation between the life time of a link and the difference between the motion angles of two communicating nodes is derived.

MECHANISMS OF PROPOSED SCHEMES

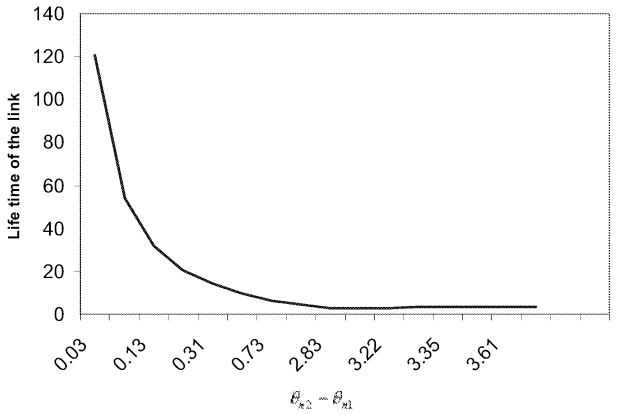

Figure 1

The life time of the link vs. the difference between the heading angles of end nodes, with $v_{n1} = v_{n2} = 10$, R = 50, $x_{n1} = y_{n1} = 10$ and $x_{n2} = y_{n2} = 20$

The core of the proposed schemes is termed Heading-direction Angles Routing Protocol (HARP), as it makes use of direction information of nodes in the network to reduce routing overhead and elongate the lifetime of links between communicated nodes. The information of the node's direction used in HARP protocol may be provided by digital advanced compass. It has been assumed that each mobile node in the network is equipped with a digital advanced compass with magneto resistive (MR) technology, which delivers the heading direction angle of the mobile device hosting it. Most navigation systems today use some type of compass to determine heading direction. Electronic compasses based on magneto resistive (MR) sensors can electrically determine the change in direction up to 0.1-degree. It can easily be integrated into systems via a simple communication interface, which makes it ready for use in applications like automobile GPS systems, cars, and mobile nodes (Solid State Electronics Center). It has been assumed that all hosts wishing to communicate with other hosts in the network are willing to participate fully in the protocols of the network, and each node is willing to receive and forward packets for other nodes in the network. Moreover, each node will exchange heading direction information with its neighbours in periodic manner. The information received from another node (neighbour) will be stored in one of the eight zone ranges in the cache regardless of the actual position of that neighbour.

In HARP, each mobile node in the network will classify its neighbour's nodes into eight different zone range areas (d1… d8) according to the heading direction of those neighbours; theoretically, the nodes are categorized within at least one of the eight zone ranges, regardless of their actual relevant positions to the node.

Our schemes are based on on-demand routing technique; this means that when a source node *S* has data packets to send to a destination *D*, and in order to find a route to *D*, *S* will send route request packet to one of its neighbours (not flooding) from its cache. The selected neighbour (next hop) has an angular heading direction similar or near to the heading direction angle of *S*, where is the value to expand the search around the source heading direction angle. Using the eight heading direction will ensure that route request

will be well distributed over a wider area. This will result in less computational overheads and minimized bandwidth use, since not all neighbouring nodes need to react to a route request. If the node did not find a neighbour that fulfils the heading angle condition, expanding the search will be applied. To widen the search, the angular value represented by δ is added or subtracted from the θ_s being considered such that more heading direction are taken into account when a route request message is being propagated or a reply message is being sent along already established route. Similarly, when an intermediate node receives a route request and needs to forward it to another node, it follows the same technique of selecting the neighbour and forwards the packet to that neighbour.

HARP Scheme 1

Our first scheme considers that the source *S* does not know the location of the destination *D*, and all the mobile nodes in the networks do not have location information about each other. At the source node, when a source *S* requests route to a destination *D*, it will look into its cache for the destination node, and if the destination node is found in its cache, *S* will start forwarding the data packets to *D*. If *D* is not found in the source cache, a time T_d will be initiated by *S*, where T_d is the time required to find the destination. Then, *S* starts looking into its cache for a neighbour that has a reference or near reference angle, matching with or close to the heading direction angle of *S*, (in order to elongate the life time of the route). This protocol performs well in a network where nodes form groups, and each group moves together in one direction such as in military, vehicles on highway, and so on). Here we have two possibilities: 1) If *S* did not find a neighbour in its cache; axis mapping will be applied with increment an angle value ±δ around the heading angle of *S*, to widen the search in a new direction. If no neighbour found in the time T_d, a route request *RREQ* will be initiated again (*S* will repeat the route request for a limited number of times, e.g. 5 times to avoid the search-to-infinity), while excluding neighbours that have been selected in previous tries of finding *D*. *S* will otherwise proceed as next. 2) If *S* found a neighbour in its cache (in case more than one neighbour is found, the nearest to *S* direction will be selected and the first neighbour met in the search); a List of Route Records *LRR* is initiated and adds its information record to that list. Each *LRR* record has the fields *Node IP* address, Node heading angle and Zone range area. The route request message will be propagated along chosen heading angle of a neighbour node to that neighbour. Fig. 2 presents the algorithm executed at the source S that has data packets to send to node *D*, where *Max RREQ* Count is the maximum number of *RREQ* allowed to be sent in searching for particular *D*, *S_Dir* is the heading direction angle of the source *S*, *S_Zone* is the zone of *S* (Zone1 between 0o and 45°, Zone2 between 45° and 90°, and so on). In this work we have divided the directions to eight zones, but it could be divided to different number of zones if necessary, for example in high density network the possibility of finding a neighbour in small direction zone is high, hence grouping the nodes in a greater number of zones allows for greater efficiency in finding the proper neighbour. *Nb_Dir* is the heading direction angle of the neighbour *Nb*, and Max acceptable *HDA* is the maximum accepted angle around the *HDA* axis of node that the node uses to search for a

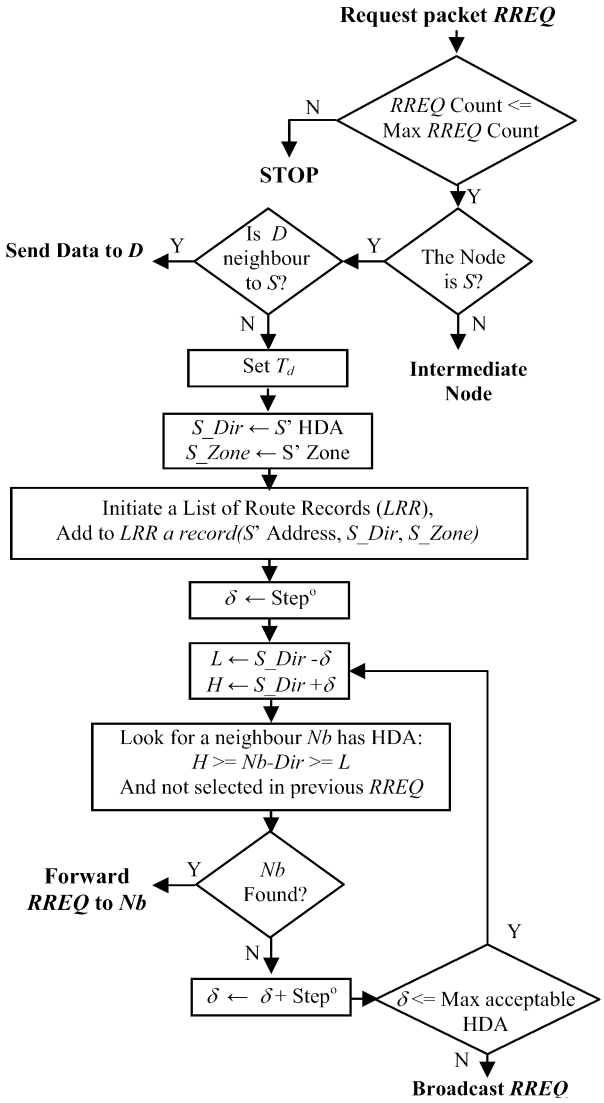

Figure 2: Route Request Message at the node *S*

neighbour.

At any intermediate node *i,* the intermediate node is the node between the source and the destination), all the nodes that receive the route request, will update their route cache entries by updating the information of the node (neighbour) which the message was received from, and only the intermediate node that the message is addressed to will deal with the message. Other nodes will silently drop it. Then *i* will search in its cache of neighbours for the destination *D*. If *D* is found in the cache, the intermediate node will update LRR by adding a record to the route list containing information about the node itself, then propagate a reply message along the nodes that have records in *LRR* that is backtracked to the initiating source *S*. if *D* is not found in the cache, the same technique of finding a neighbour that has near heading direction to the node *i* will be followed.

Before forwarding the request packet, *i* will add a record to *LRR* contains information about *i*.
Route reply message would be initiated in two cases: (1) By the destination itself, when the destination *D* receives the route request packet, *D* will piggyback the LRR, that is included in the route request, in the replied message and send the message along the reversed path determined by the nodes recorded in *LRR*. (2) By an intermediate node which has received the route request message and has the destination information in its cache. The intermediate node will update *LRR* by adding the next node *IP address* and its heading direction piggyback the list of route records in the replied message and send the message along the reversed path determined by the nodes recorded in the list *LRR*. All the nodes, along the route that receives the route reply, will update their route cache by updating the information of the node (neighbour) from which the message was forwarded.

HARP Scheme 2

In first scheme, the chance of finding the destination from first try of route discovery is low, particularly if the nodes in the network do not move as a group. Thus, first protocol scheme is efficient in such situations where nodes form one or more groups or the nodes' decisions on movement depend upon the other nodes in the group, or where nodes are uniformly moving forward in a particular direction such as vehicles in the highway. To increase the efficiency of the protocol by increasing the probability of finding the destination, scheme 2 is proposed.
In this scheme each node knows only the heading direction angles of its neighbours, each of which is classified in eight zones according to its *HDA* regardless of their locations. By this scheme, at the source node S, when S requests route to a destination *D*, it will look into its cache for the destination, and if *D* is found in its cache, *S* will start forwarding the data packets to the destination. If *D* is not found in the source cache, a time Td will be initiated by S, where T_d is the time required to find *D*. Then S will select only one neighbour from each zone from the eight zones of neighbours, therefore at most eight neighbours will be selected in the same time. An *LRR* is then initiated (as described in scheme1), and the route request message that includes the *LRR* will be propagated to selected neighbours. If a neighbour in one zone of S direction zones is not available, the number of selected neighbours will be less than eight. All the nodes that receive the route request, will update their route cache entries by updating the information of the node (neighbour) from which the message was received, and only the intermediate node that the message is addressed to will accept the message, other nodes will silently drop it. Fig. 3 shows the pseudo-code algorithm that is run at the source node.
The intermediate node (*i*), that the packet is addressed to, will search in its cache of neighbours for *D*, if *D* is found in the cache, i will update the LRR by adding a record to it; this record containing information about the node itself. It then propagates a reply message along the nodes that have records in *LRR*; the list of route records is backtracked to the initiating source *S*. if *D* is not found in the cache, the same technique of finding a neighbour that has near heading direction to this node will be followed. Before forwarding the request packet, the node will add a record to *LRR* containing information about itself. If no neighbour is found for the time T_d, *RREQ* will be initiated again (*S* will repeat the route request a limited time e.g. 5 times for avoiding the search-to-infinity). For avoiding loops in the search, all schemes use a sequence number, and check the availability of the selected neighbour node in *LRR* before sending the packet to that neighbour. If the neighbour is found in the list, another neighbour will be selected.
In this scheme, the route is established without knowing the geographical information of nodes, and the path life

```
If RREQ_Count <= Max_RREQ_Count then
 {
    If the node is S then
    {
     If IPAddr_D ∈ NbCache_S then       // if D is neighbour to S
     {
                Send (data packets toIPAddr_D);
     }
     Else
     {
       Init (T_d); // initiate T_d
                S_Dir = HDA of S;
       S_Zone = Zone number of S;
       Init (LRR); // initiate a List of Route Records
       //Add to LRR: S' Address, HDA of S, Zone number of S
       LRR_Add (IPAddr_S, S_Dir, S_Zone);
       For (ZoneNo = 1; ZoneNo<= MaxZoneNo; ZoneNo++)
                {
            // Find a neighbour in ZoneNo and skip the selected
          //neighbour in previous RREQ
                IPAddr_Nb = Find_Nb (ZoneNo);
                If IPAddr_Nb <> 0 then   // Neighbour is found
                {
                    // Forward RREQ to a neighbour Nb
              Forward_RREQ (IPAddr_Nb)
                }
       }
    }
   }
 }
Else STOP // do not initiate RREQ
```

Figure3: Pseudo code for scheme2.

between *S* and *D* will be longer because the intermediate nodes will be selected to be in near heading direction to each other. It is most likely that the route will be found from the first try due to forwarding the *RREQ* to eight neighbours in parallel. This scheme is efficient in high density networks, where the possibility of finding a neighbour in each zone is higher than in a low density network. We have reduced the number of nodes that share in route discovery to the number of direction zones (number of direction zones can be optimized according to the environment of the network and application, to reduce the required time of finding the destination.

HARP Scheme 3

In scheme2, the number of packets propagated by the source to its neighbours is equal to the number of direction

zones (eight zones in our case), and only one neighbour from each zone is selected. In order to reduce the number of selected nodes without reducing the performance of the protocol, we need more information about the geographical locations of nodes and destination. Hence, scheme3 is assisted by the location information that could be provided by the Global Positioning System (GPS) (Peter H. Dana, 2000).

Scheme3 assumes that each node knows:

- Its geographical location and its *HDA*.
- Its neighbours' geographical locations and their HDA.

The neighbours' *HDA* at each node are grouped in eight zones according to their *HDA* and regardless to their locations. It is also assumed that the source node *S* knows the location (X_d, Y_d) of node *D* at the time at which route discovery is initiated by node *S*. The coordinates (X_d, Y_d) are included in the route request.

At the source node, when S requests route to a destination *D*, it will look into its cache for *D*, and if *D* is found in its cache, S will start forwarding the data packets to *D*. Whilst if *D* is not found in S cache, a time T_d will be initiated by S, where T_d is the time required to find the destination. Then, *S* starts looking into its cache for a neighbour that satisfies the two conditions:

- Its location is the nearest to the destination location among all neighbours.
- Has a near *HDA* to *S*.

If the neighbour is found, a LRR is initiated (as described in scheme1), and then the route request message that include the *LRR* will be propagated by *S* to that neighbour. If no neighbour has satisfied the two conditions together, then *S* will select the neighbour that satisfies the first condition with the most near *HDA* to *S*.

All the nodes that receive the route request, will update their route cache entries by updating the information of the node which the message was received from, and only the intermediate node i that the message is propagated to, and has a record in the list of route records, will accept the message and will follow the same rule followed by *S* to select its next neighbour until *D* is reached, other nodes will silently drop it.

In this scheme, we use more information (Heading direction information, GPS system for geographical location), but this scheme guarantees:

- To find the destination quickly from the first try (if the destination is available).
- To find the route between *S* and *D* that is likely to last longer, by selecting the nodes that contribute in the route according to the heading directions.

RESULTS AND DISCUSSION

In this section, we have evaluated the performance of our three novel routing protocols by simulation. The Network Simulator NS-2 was used to perform extensive simulations and to evaluate our Protocols. However, table I provides a summary of the rest of our simulation parameters. The results presented are mean values of ten simulation runs. For fair comparisons, all simulated routing protocols use the same set of mobility and traffic scenarios. The following performance metrics are used for comparisons:

The Route discovery packets (the Overhead) are defined as the number of all control packets generated by all nodes in the network in order to establish routes between sources and destinations.

The Cost of data packet delivery is defined as the measured ratio of the number of data packets delivered to the destinations to the number of all packets generated in the networks. Note that each time a packet is forwarded is counted as one packet transmission. This metric is used to investigate how efficiently control packets and selecting long-lived routes are utilized in delivering data packets.

TABLE I
PARAMETERS OF MOBILITY SCENARIOS
USED WITH NS-2 AND RANDOM WAYPOINT

Scenario Name	Pause Time Scenario	Max Node Speed Scenario	Network Size Scenario
Pause time (s)	0,50,100,200, 300,500	10	10
Max Node Speed (m/s)	10	10,20,30,40, 50,60	10
Number of mobile nodes	50	50	10,30,50,60,7 0
Simulation Time (s)	500	500	500
Network Space	1kmX1km	1kmX1km	1kmX1km
Radio range.	250m	250m	250m
MAC Protocol	IEEE 802.11	IEEE 802.11	IEEE 802.11
Radio propagation model	Free space/ two-ray	Free space/ two-ray	Free space/ two-ray
antenna model	Omni Antenna	Omni Antenna	Omni Antenna
Traffic pattern	CBR	CBR	CBR
Maximum number of connections	10	10	10

The Average end-to-end delay of transferred data packets includes all possible delays caused by buffering during route discovery, queuing at the interface-queue, retransmission delays at the medium access control layer, propagation and transfer times, and ARP delay that has a considerable value especially in second scheme where eight packets need to be sent and need some delay between them.

We have simulated each metric parameter mentioned above in three different scenarios:

1) **Mobility scenario**: with different pause time values,
2) **Speed scenario**: with different node speeds,
3) **Network sizes scenario**: with different number of nodes.

We have compared our schemes with AODV which is a fully On-demand and flooding protocol since the schemes we present in this paper are entirely based on On-demand.

Figures 4 and 5 show the route discovery packets as a function of mobility with different pause time, and network size respectively. We can see in our novel three schemes

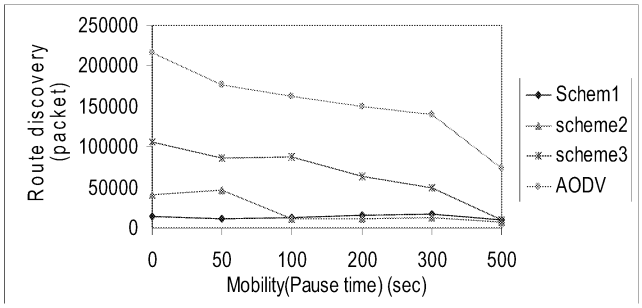

Figure 4: Route discovery vs. mobility

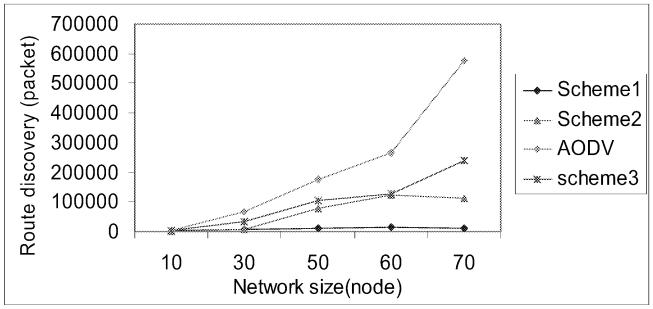

Figure 5: Route discovery vs. number of nodes

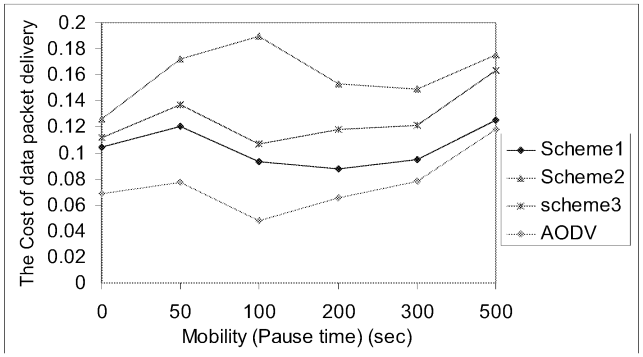

Figure 6: The cost of data packet delivery vs. mobility

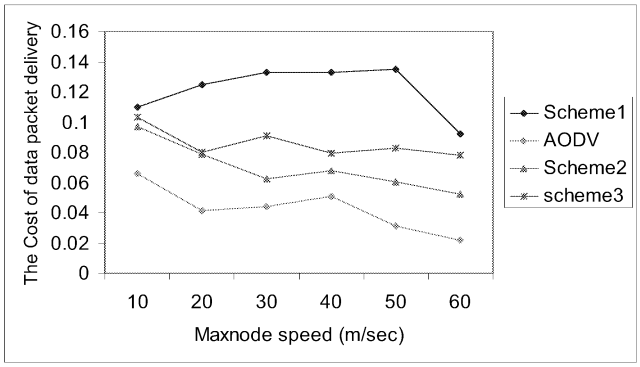

Figure 7: The cost of data packet delivery vs. speed

that the route discovery packets needed to find the path are much less than the packets needed in AODV protocol. As can be seen in Fig. 5, that as the number of nodes increases, the number of route discovery packets slightly increases. This means that our schemes scale well with the network size.

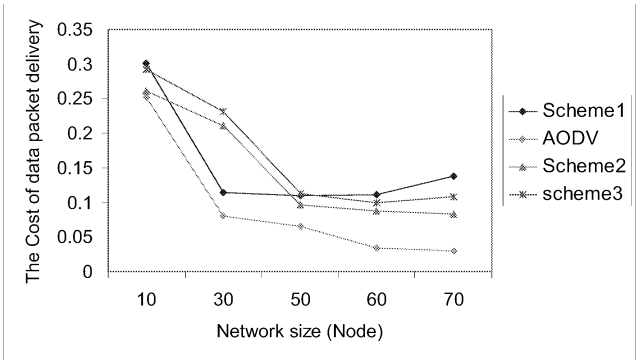

Figure 8:The cost of data packet delivery vs. nodes' number

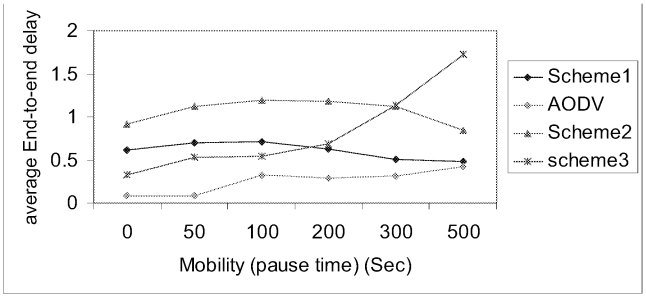

Figure 9: Average End-to-end delay vs. mobility

Figures 6, 7, and 8 show the Cost Ratio of Data Packet delivery (CRDP) as a function of mobility with different pause time, maxima of node speeds, and network size. Higher CRDP means better performance. As can be seen in these figures, that CRDP in the three schemes is better than the CRDP of AODV, which means that less control packets are needed to deliver data packets from sources to destinations, as a result of long-lived route established by using HDA.

In fact, by applying flooding technique, it is most likely to find the required path in short time with some acceptable delay, on the expense of significant overhead and more collisions, but with no guarantee to select the path that lasts for acceptable period of time. In most of the applications, it is important to find the path that lasts longest with reduced overhead and collision, with an acceptable level of delay. Figure 9 shows the average end-to-end delay of transferred data packets as a function of mobility with different pause time. In these figure, we can see that our novel schemes increase delay compared to the fully flooding technique protocol AODV, and further scheme 3 is shown to perform better than other schemes, particularly when the mobility increases. The delay degrades due to the selection of the node heading to the destination direction and that is also closer to it. The delay is mostly steady in all schemes in the network that has greater mobility.

CONCLUSION

Effectively delivering data packets and minimizing connection breakdown and control packets overheads, beside routes stay connected longest with some accepted delay are crucial in ad hoc networks. In this paper, we have presented three new schemes for mobile ad hoc networks.

In these schemes we examined the use of heading direction angle of nodes to choose routes that stay connected longest and to overcome the effect of flooding technique and overhead in the network by doing selective forwarding, and to elongate the life time of the route. These schemes utilize Axis-Mapping techniques to propagate a message in the network, and exploit the mobility patterns of nodes to provide a robust and long-lived route to destination. These schemes could be an answer to some of the questions in ad hoc networks, for example, providing mechanisms to handle the frequent changes in the network topology due to mobility; and maintaining the long-lived multi-hop paths between two communicating nodes. Other routing protocols for mobile ad hoc networks could apply these schemes in order to improve the performance or QoS of these protocols in term of protracting the life time of the communications. Results show improvement in reduction of the effect of flooding in terms of routing discovery packets needed to deliver data packets with different mobility, speeds of nodes and different network size. In addition, results show that the ratio of the number of data packets delivered to the destinations to the number of all packets generated in the networks is higher in all schemes compared to AODV, which gives hint of choosing the longest path to the destination. As future work, the investigation of choosing the number of zones that the node' neighbours are grouped into according to the density and mobility of the network is required to improve the performance of these protocols. In addition, investigating the number of selected neighbours to forward the packet to will be further step to enhance the performance too. Furthermore, applying these schemes on other existing protocols to improve their performance is our main aim for future work.

REFERENCES

A. Bruce McDonald and Taieb Znati 1999, "A Mobility-Based Framework for Adaptive Clustering in Wireless Ad-Hoc Networks", IEEE Journal on Selected Areas in Communication, Vol. 17, No. 8, August 1999.

Charles E. Perkins, Elizabeth M. Belding-Royer, Samir R. Das, 2003, "Ad hoc On-Demand Distance Vector (AODV) Routing", (Internet-draft), in: Mobile Ad-hoc Network (MANET) Working Group, IETF, 17 February 2003.

C. Siva Ram Murthy and B.S. Manoj, 2004, "Ad Hoc Wireless Networks: Architectures and Protocols", book, ISBN 0-13-147023-X, first printing, 2004, pg.275.

D. Turgut, S.K. Das, M. Chatterjee, 2001, "Longevity of Routes in Mobile Ad hoc Networks", Proc. IEEE VTC, Rhodes, Greece, spring 2001.

Elizabeth M. Royer, 1999, "A Review of Current Routing Protocols for Ad Hoc Mobile Wireless Networks", IEEE Personal Communication April 1999.

Guolong Lin, Guevara Noubir, and Rajmohan Rajamaran, 2004, "Mobility models for ad-hoc network simulation", In Proceedings of IEEE Infocom 2004.

IEEE Computer Society LAN MAN Standards Committee, 1997, "Wireless LAN Medium Access Protocol (MAC) and Physical Layer (PHY) Specification", IEEE Std 802.11-1997. The Institute of Electrical and Electronics Engineers, New York, NY, 1997

J. Broch, D. A. Maltz, D. B. Johnson, Y.-C. Hu, and J. Jetcheva, 1998, "A performance comparison of multi-hop wireless ad hoc network routing protocols", in Mobile Computing and Networking (MobiCom), 1998, pp.85– 97.

Kumar Banka, R. Guoliang Xue, 2002, " Angle routing protocol: location aided routing for mobile ad-hoc networks using dynamic angle selection.", IEEE Milcom'2002 Conference, (2002), pages: 501- 506 vol.1.

M. Musolesi , S. Hailes , C. Mascolo, 2004, "An ad hoc mobility model founded on social network theory", In Proceedings of the 7th ACM/IEEE International Symposium on Modeling, Analysis and Simulation of Wireless and Mobile Systems (MSWiM 2004). October 2004.

Peter H. Dana, 2000, "Global Positioning System Overview", URL: http://www.colorado.edu/geography/gcraft/notes/gps/gps_f.html, 2000.

R. Chellappa Doss, A. Jennings, N. Shenoy, 2004, "A REVIEW OF CURRENT MOBILITY PREDICTION TECHNIQUES FOR AD HOC NETWORKS", Proceeding of the 4th IASTED International Multi-Conference on Wireless and Optical Communications (WOC), July 8 – 10, 2004, Canada.

Solid State Electronics Center, home page, http://www.ssec.honeywell.com/magnetic/.

S. Basagni, D. Turgut and S. K. Das. 2001, "Mobility-adaptive protocols for managing large ad hoc networks", Proceedings of IEEE International Conference on Communications (ICC)}, Jun, 2001, pp. 1539-1543.

Samarth H., and Klara Nahrstedt, 2002, "Predictive Location-Based QoS Routing in Mobile Ad Hoc Networks", In Proceedings of IEEE International Conference on Communications, (2002).

The network simulator—NS-2 Notes and documentation and source code. [Online]. Available: http://www.isi.edu/nsnam/ns/

T. Camp, J. Boleng, and V. Davies. 2002, "A survey of mobility models for ad hoc network research", Wireless Communications and Mobile Computing (WCMC): Special issue on Mobile Ad Hoc Networking, 2(5):483— 502, 2002.

W. Su, S-J. Lee and M. Gerla, 2000, "Mobility Prediction in Wireless Networks", In Proceedings of IEEE MILCOM 2000, Vol. 1, Los Angelas, CA, October 2000, pp. 491- 495.

W. Su, S-J. Lee and M. Gerla, 2000, "Mobility Prediction and Routing in Ad Hoc Wireless Networks", International Journal of Network Management, Wiley and Sons, 2000.

Xinwei Luo; Camp, T.; Navidi, W., 2005, "Predictive Methods for Location Services in Mobile Ad Hoc Networks", 19th IEEE International, Parallel and Distributed Processing Symposium, 2005. Proceedings 04-08 April 2005, Page(s):246b - 246b [1]Young-Bae Ko and Nitin H. Vaidya 2000, "Location-Aided Routing (LAR) in mobile ad hoc networks", Wireless Networks 6 (2000) 307–321.

Yu J.Y., Chong P.H.J., 2005, "A survey of clustering schemes for mobile ad hoc networks", Communications Surveys & Tutorials, IEEE, Volume 7, Issue 1, First Qtr. 2005, Page(s):32 - 48 .

Simulation of Broadband Flattening Optical Communication System using Raman Amplifier

Sawsan Abdul Karim Abdul Majid[1], Abeer Dahfir Al_Rikabi [2]
1 College of Information technology/University of Koya / Iraq_ email:acape@yahoo.com
2 Ministry of Constructions & Housing-National Consultancy of Engineering Centre-Baghdad-Iraq_ email:abeeralrukabi@gmail.com

Abstract
In an industry where cost effectiveness and productivity are imperative for success, the award winning CAD for photonics can minimize time requirements and decrease cost related to the design of optical systems, links, and components.
This paper presents a design of 64 Dense Wave Length Division Multiplexing DWDM to support the existing Optical Fiber Communication System currently available south of Iraq. It introduces a theoretical analysis of the needs of using Raman Amplifiers for such DWDM systems, analyses the problems related to un-flattened band. Proposes are specific techniques to flatten the broad bandwidth gain. The proposed design is simulated and tested using Optisystem4.0 a License product of Optiwave Corporation, a Canadian based company. The design uses real fiber data, which are provided by the Iraqi Ministry of Communication. The test results are very good, which will support the Iraqi industry to improve the usage of already installed fiber optic bone in Iraq

1. CAD for Photonics
The design of a fiber-optic communication system involves optimization of a large number of parameters associated with transmitters, optical fibers, in-line amplifiers, and receivers. The power and the rise-time budgets are only useful for obtaining a conservative estimate of the transmission distance and the bit rate. Simple approach fails for modern high-capacity systems designed to operate over long distances using optical amplifiers. An alleviative approach uses computer simulations and provides a much more realistic modeling of fiber-optic communication systems. The computer aided design-CAD techniques are capable of optimizing the whole system and can provide the optimum values of various system parameters such that the design objectives met at a minimum. [1]

2. Optisystem
OptiSystem is an innovative, rapidly evolving, and powerful software design tool that enables users to plan, test, and simulate almost every type of optical link in the transmission layer of a broad spectrum of optical networks from LAN, WAN, and MAN to ultra-long-haul. It offers transmission layer optical communication system design and planning from component to system level, and visually presents analysis and scenarios. OptiSystem4.0 enables users to plan, test, and simulate: [2]

- WDM/TDM or CATV network design
- SONET/SDH ring design
- Transmitter, channel, amplifier, and receiver design
- Amplified System BER and link budget calculations

2.1 Key Features and Functionality
2.1.1. Component Library
The OptiSystem Component Library includes hundreds of components that enable you to enter parameters that can be measured from real devices. It integrates with test & measurement equipment from different vendors. Users can incorporate new components based on subsystems and user-defined libraries.

2.1.2. Quality and performance algorithms
In order to predict the system performance, OptiSystem calculates parameters such as BER and Q-Factor using numerical analysis or semi-analytical techniques for systems limited by inter symbol interference and noise.

2.1.3. Advanced visualization tools
Advanced visualization tools produce WDM analysis tools listing signal power, gain, noise figure, and OSNR per channel.

2.1.4. Hierarchical simulation with subsystems
To make a simulation tool flexible and efficient, it is essential to provide models at different abstraction levels, including the system, subsystem, and component levels. OptiSystem features a truly hierarchical definition of components and systems, enabling you to employ specific software tools for integrated and fiber optics at the component level. [2]

3. Existing Optical Fiber in Iraq
The optical fiber network in Iraq first where tested during November-2004 by Nortel/Acterna Company. An existing network fiber was installed in Iraq around year 2000 without completed the over all design for the optical communication network (the design of transmitter, receiver active components, ect.). Recently the Ministry of Communications in Iraq decided to integrate these fibers with a network after testing these existing fiber links. As Nortal Networks tests on the existing fiber shows that it can be used as DWDM communication network. This type of DWDM will need to use an Optical Amplifier(s) with Broadband Flattening gain. Therefore the gain characteristics of Raman Amplifier will be demonstrated using multichannel system, also the techniques using to flatten the broad bandwidth gain will be proposed. [3]

4. Optical Amplifier
4.1. Raman Amplifier-Significance of Calculation and Measurement of Fiber Raman Amplifier (FRA)
FRA is to amplify optical signals in optical fibers, based on transferring the power from the pump beam to the signal via Raman interaction between the light and vibration modes of the glass. Typically, the Raman gain coefficient in fused silica peaks at a Stokes shift of about 13.2THz with a 3dB bandwidth of about 6THz, as shown in figure (1). FRAs exhibit several attractive features for applications in transmission systems, which are listed as follows:

1. Simplicity of amplifier architecture: Raman gain is obtainable in any conventional transmission fiber. Only high pump lasers are required to be launched with the signals, and there is no excess loss in the absence of pump power. [4]
2. Low noise: Distributed Raman amplifiers may deliver negative noise figures [5], while the Erbium Doped Fiber Amplifiers (EDFA) have at least 3dB noise figure.

3. Broad gain spectrum: The Raman gain bandwidth is very broad, around 60nm in terms of Full Width at Half Maximum (FWHM), which is of significance to the wavelength division multiplexed system. One unique technique applicable for RFA is that a broader gain spectrum may be obtained by the use of multi-wavelength pump sources [6] [7].
4. Flexibility of transmission window: The pump wavelength determines the gain spectrum of a Raman amplifier, which means the operation window, is adjustable. Furthermore, the multi-wavelength pump technique increases and flattens the bandwidth by pumping simultaneously at different wavelengths.

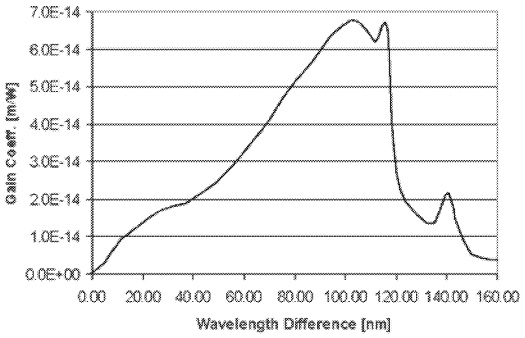

Figure (1) Typical Raman gain coefficient in fused silica

5. WDM Light-wave System

5.1 Introduction

WDM *corresponds to the scheme in which multiple optical carriers at different wavelengths are modulated by using independent electrical bit streams (which may themselves use TDM and FDM techniques in the electrical domain) and are then transmitted over the same fiber.*

The optical signal at the receiver demultiplexed into separate channels by using an optical technique. WDM has the potential for exploiting the large bandwidth offered by optical fibers. For example, hundreds of 10-Gbps channels can be transmitted over the same fiber when channel spacing is reduced to below 100 GHz. Figure (2) shows the low-loss transmission windows of optical fibers centered near (1.3 and 1.55) μm.

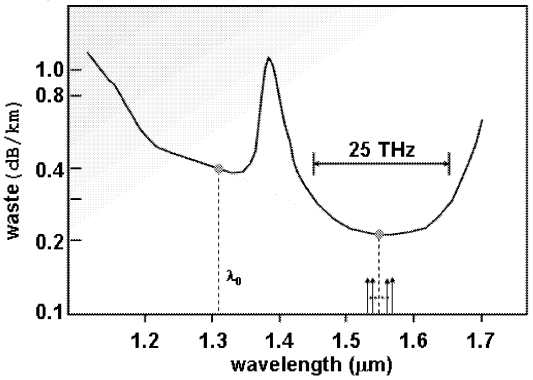

Figure (2): Low-loss transmission windows of silica fibers in the wavelength regions near 1.31 and 1.55 μm.

For example, an existing 1.3-μm lightwave system can upgrade in capacity by adding another channel near 1.55 μm, resulting in a channel spacing of 250 nm. Clearly, the advent of WDM has led to a virtual revolution in designing lightwave systems. WDM systems can be classified into three broad categories: Point - to - Point Links, Distribution Networks, and Local Area Networks

Figure (3) shows two WDM's allowing unidirectional streams of data to carry on a single fiber. The type of data streams does not matter. One could be a video signal, the other data stream. Alternatively, both signals could be video signals or high-speed data signals at 2.5 Gbps. [8]

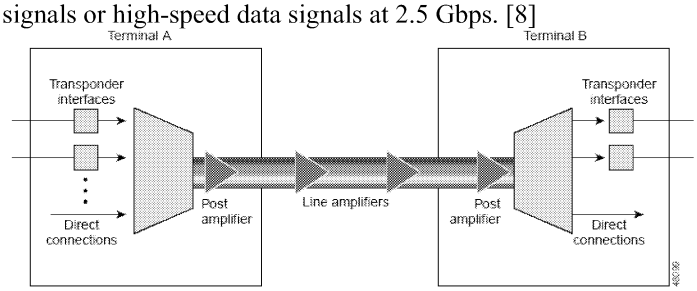

Figure (3) shows two WDM's allowing unidirectional streams of data

Theoretically, fiber has extremely high bandwidth (about 25 THz), i.e., 25 million MHz in the 1.55 low-attenuation band and this is 1,000 times the total bandwidth of radio on the planet Earth. However, only data rates of a few gigabits per second achieved because the rate at which an end user can access the network limited by electronic speed, which is a few gigabits per second. Hence, it is extremely difficult to exploit all of the huge bandwidth of a single fiber using a single high-capacity wavelength channel due to optical-electronic bandwidth mismatch or "electronic bottleneck." The recent breakthroughs (Tb/s) are the result of two major developments:

First: Wavelength division multiplexing (WDM), which is a method of sending many light beams of different wavelengths simultaneously down the core of an optical fiber. Second: Optical Amplifier which amplifies signals at many different wavelengths simultaneously, regardless of their modulation scheme or speed. [1]

The advent of Optical Amplifiers (OAs) has enabled commercial development of WDM systems by providing a way to amplify all the wavelengths at the same time, regardless of their individual bit rates, modulation scheme, or power levels. Before the invention of OAs, the effects of optical loss compensated every few tens of kilometers by an electronic regenerator, which require that the optical signals be converted to electrical signals and then back again to optical ones. Most important, electronic regenerators work only for the designated bit rate at only one wavelength.

5.2 DWDM

The demand for Internet bandwidth grows as new applications, new technologies, and increased reliance on the Internet continue to rise. Dense wavelength division multiplexing-DWDM is one technology that allows networks to gain significant amounts of bandwidth to handle this growing need. Dense wavelength-division multiplexing involves sending a large number of closely spaced optical signals over a single fiber.

Standards developed by the ITU-International Telecommunications Union [10] define the exact optical wavelengths used for DWDM applications. The center of the

DWDM band lies at 193.1 THz with standard channel spacing of 200 GHz and 100 GHz. [9]

5.2.1 DWDM Advantages

1. The ability to carry signals of different speeds and types simultaneously and transparently over the fiber.
2. Single optical amplifier can re-amplify all the channels on a DWDM fiber without demultiplexing and processing them individually, with a cost approaching that of a single regenerator.
3. DWDM as WDM carries each input signal independently of the other; this means that each channel has its own dedicated bandwidth.
4. DWDM systems greatly simplify the expansion of network capacity.
5. The only requirement is to install additional or higher bit-rate interfaces in the DWDM systems at either end of the fiber. In some cases, it will only be necessary to increase the number of lambdas on the fiber by deploying existing interfaces, as shown in figure (4-a). In the case of adding higher bit-rate interfaces, as shown in figure (4-b), fiber type can become a consideration. [11]

(a)

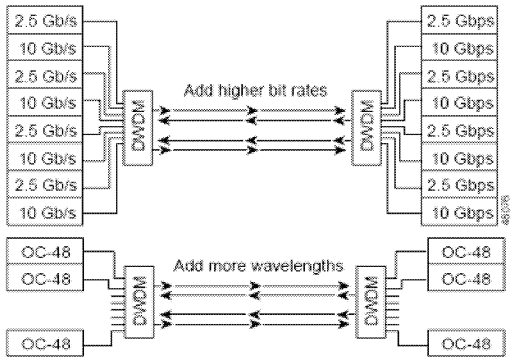

(b) Figure (4) Upgrading with DWDM

6. Simulation Example on Existing Fiber in Iraq

6.1 Important Notes

Optical interface parameter values (such as, Launched Power, Channel Spacing, Channel Output Power, Attenuation, Dispersion, receiver Sensitivity), those are required at various interfaces within an optical communication system, identifies as in ITU-T G692. [12]

1. The value of each channel power is than (0 dBm) to avoid the threshold levels of nonlinearity effects in multi channels.
2. Layout Parameters: choosing proper global parameters is very crucial when trying to obtain accurate results. For WDM systems, the best suggestion would be to use 128 for both the length Sequence and samples per bit.
3. Choosing channel central frequency with G.652 fiber at 193.1 THz, [13].
4. SMF type NDSF fiber is used as in fiber characterization test in final report [3].
5. NRZ modulation format is used [14].

6.2. Broadband Flattening Gain Using Raman Optical Amplifier

The designed simulation system is shown in figure (5) with sixty-four DWDM wavelengths and (-17.44 dBm) transmitted power, ~100 GHz channel spacing using the fiber type non-dispersive shifted fiber (NDSF), Raman Amplifier-average power model [10] using group of 4 backward pumps. The 64 channels operate within C-band (1530 - 1565) nm. The expectation is 64 channels to be used in the center of Iraqi fiber network between Jadria_Mamon [3].

6.2.1. Before optimization

The simulation design shown in figure (5) has been calculated. The results are measured by Optical spectrum analyzers, connected at different points of the system. The 64 channels along the optical fiber system are shown in figure (6). It can be seen clearly that using the fiber, will cause attenuation, which was improved by using Raman Amplifier. Unfortunately the Raman Amplifier created a problem of un-flattened gain.

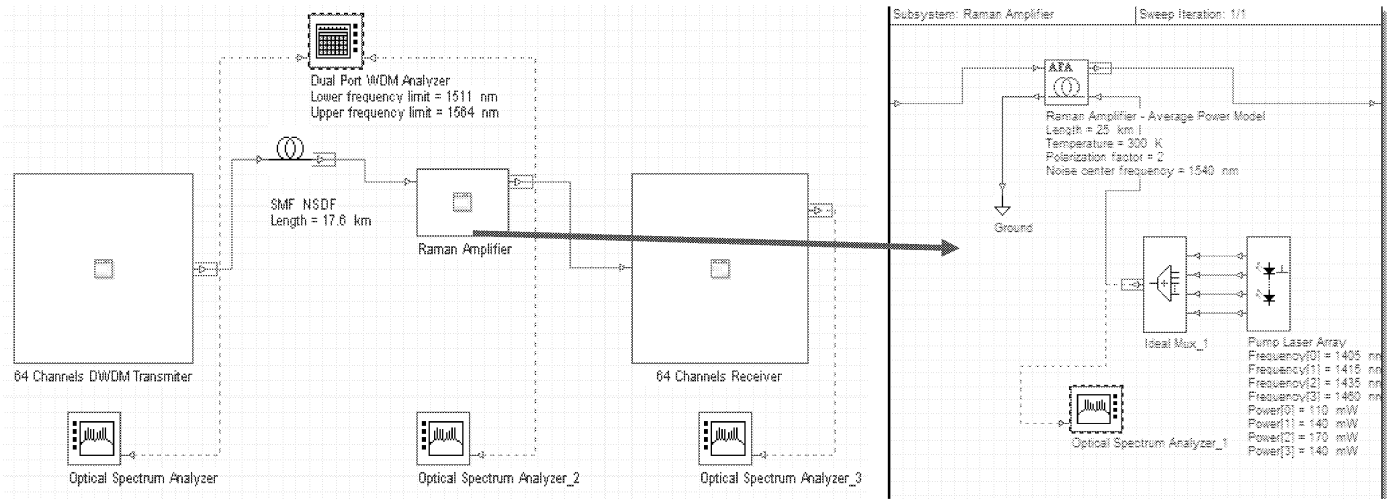

(a) (b)

Figure (5): (a) Layout of 64 channels Between Centers from Jadria _ Mamon using Raman Amplifier. (b) Inside the Raman Amplifier sub-system where average power amplifier shown with the group of pumps.

6.2.2 Raman Amplifier Pumps Optimization

Figure (6, b and c) show that using Raman Amplifier caused big problem related to the max/min gain ratio (un-flattened gain). In order to solve the problem with the un-flattened gain, the optimization technique is applied in this design.

The pumps power and wavelength of Raman Amplifier are optimized in order to get good flattening to its broadband equal to 1.5dB, so we have added Gain Flatness (Ratio Max/Min Gain) as a constraint which is measured by the Dual Port WDM Analyzer. The steps of optimization are:

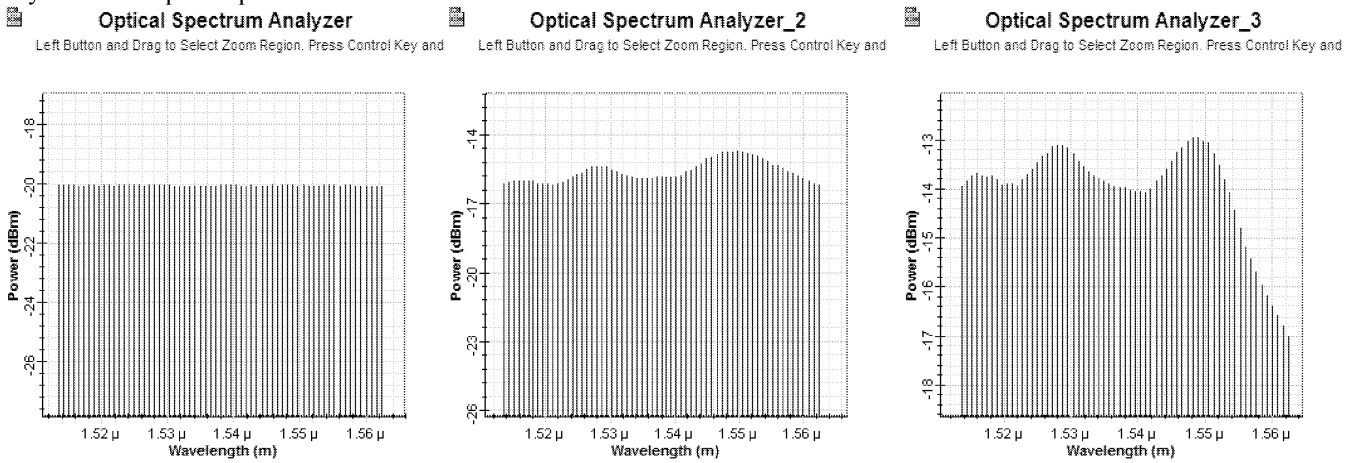

(a) (b) (c)

Figure (6): (a) 64 channels just after the multiplexer, (b) 64 channels after Raman Amplifier with high ratio of max/min gain. (c) 64 after the demultiplexer.

1. In the optimization setup, the Gain Flattening type of optimization has been selected in the main tab.
2. In the Parameters tab, pump powers and frequencies are added to the table. Minimum and maximum pump powers are selected to be 0 and 300 mW, respectively. Minimum and maximum pump wavelengths are selected to be 1400 nm and 1500 nm, respectively.
3. In the Results tab, we selected the Gains for all channels from dual port WDM analyzer to be add the table. Target gain is 10.0 dB as inserted in Target Value of this tab.
4. In the Constraints tab, we have added Gain Flatness (Ratio Max/Min Gain) as a constraint. Gain flatness is measured by the Dual Port WDM Analyzer. As a constraint, gain flatness less than 1.5 dB is required. Note that no unit for parameters and results is indicated in the optimization tool. The units of parameters and results in optimization tool are taken to be same as the ones that are given in project layout for the corresponding parameter or result.

6.2.3 After Optimization

The output results calculated with optimization are shown in figure (7). The ratios of max/min gain before the optimization were 4.01 dB as shown in figure (8-a), and after optimization the broadband gain flattened leading to minimizing the ratio to 1.5 dB, as shown in figure (8-b).

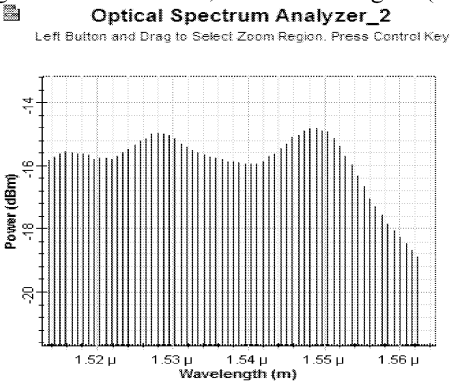

(a)

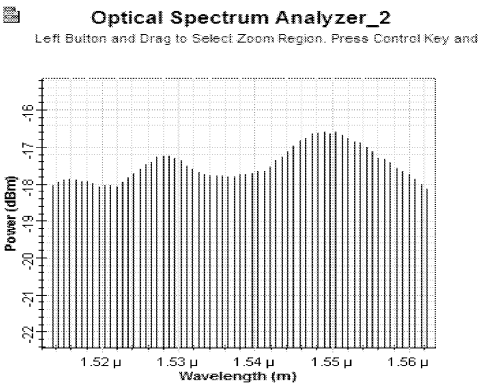

(b)

Figure (7): (a) Before optimization (b) After optimization

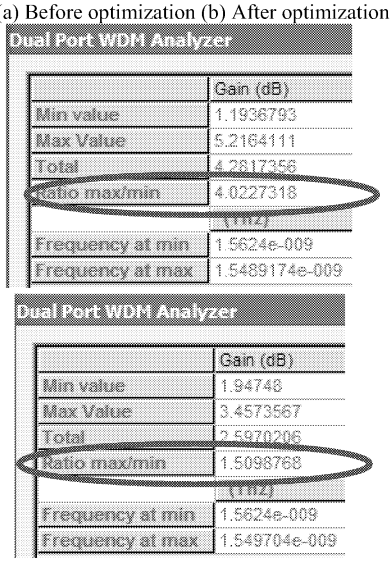

(a)

(b)

Figure (8): (a) Before optimization (b) After optimization

7. Evaluation test of the results

1. Optisystem4.0 software simulator is built on visual C++ which is advanced object oriented programming language (OOP). That makes it flexible and robust to integrate layouts, components with all their features and with minimum errors. The objects (Optical Components) sending messages to each other and to their classes to perform their jobs and the goals of the projects. Optisystem4.0 offers high flexibility for the user to create a new component based on Matlab or to change any property of any component using iteration. It has a special configuration steps for optimization.

2. WDM transmitter optical component is used to generate channels in simulation design. WDM transmitter (Tx) is used to simulate a new manufacturing component which provides easiest way when changing any of its properties window, such as number of output ports, frequency, frequency spacing, power, and line width. It provides small size component for large WDM systems. Using Tx facilitated the design of 32 channels with many changes for different tests (4 components / channel * 32 channels = 128 components) where this large number of components emphases more (losses, layout space, errors, time for more number of properties changing), figure (9).

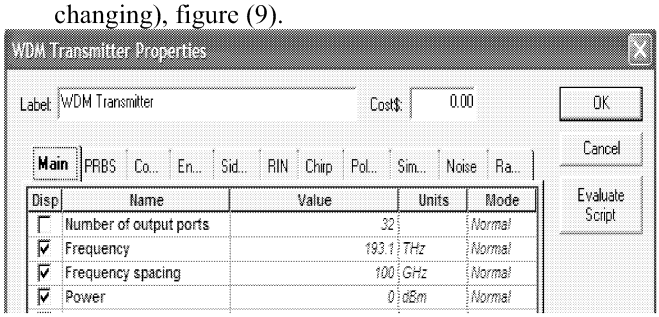

Figure (9) WDM transmitter component properties

3. WDM Mux is used where the input signals are filtered by an optical filter and combined in one output signal that will minimize the child frequencies around a specific wavelength. It is preferred from using Ideal WDM Max (without filters). Figure (10) is illustrated the technical subsystems design of the two types. The optical filter of WDM Max type chooses to be a Bessel optical filter. The same point for WDM Demux.

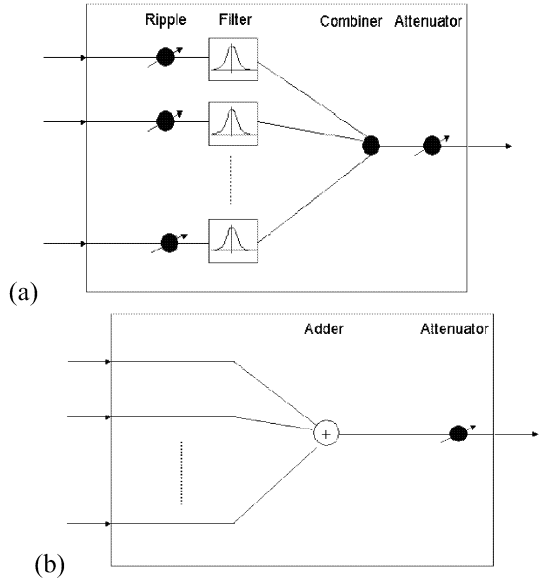

Figure (10): Technical design for (a) WDM mux (b) Ideal mux

4. SMF_NDSF type is used for all simulation design with all nonlinear effects, as shown in figure (11), to make the design more practical and reliable.
5. Using sub-system simplifies the overall system design and testing for each component or layout. The tested optical component(s) or layout(s) could be used for the same file design or another file designs.
6. The 64 channel system that includes the Raman amplifier has been tested. The results show that the Raman gain is good, but is associated with a problem related to un flattened gain profile.(the ratio is 4.1 dB).
7. The paper proposes specific solution to improve the ratio, where the value of pumps power and the wavelength of each pump are important issue in order to have good and correct amplification within Raman Amplifier. Before optimization the wavelengths were selected such as each one is less than a specific transmitted wavelength by ~100nm [4]. The optimization technique was used to optimize the pumps power and wavelength in order to achieve the ratio max/min gain equal to 1.5 dB.

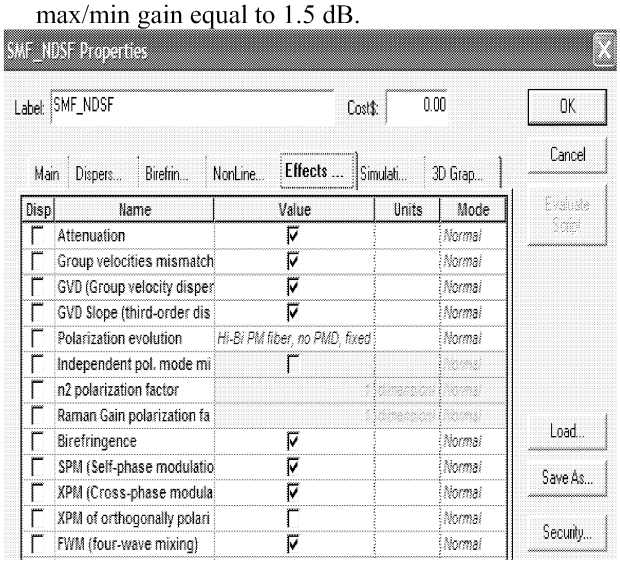

Figure (11): Nonlinear effects in SMF_NDSF

8. *Conclusion*

Broadband Flattening Gain is an important feature in new DWDM communication system with Raman Fiber Amplifier, its complex technique in design required time, cost, experiences on how to choose pump power, wavelength and what rang of group pump to activate Raman Effect to achieve amplification for wide range of frequencies. This paper proposes successful technique to flatten the gain of 64 channels using the optimization technique. The gain ripple has been minimizing from 4.1 dBm to 1.5 dB.

9. *References*

1. Mohan Gurusamy, C. Murthy "WDM Technology and Issues in WDM Optical Networks" 2002.
2. Optical Communication System and Amplifier Design Software – 2006.
3. Iraq FC project "Fiber Characterization Final Report ACTERNA" from (15th July 2004 to 3rd September 2004).
4. Dr. Sawsan Abdul-Majid/ P.Eng./ University Professor, Eng. Abeer Dahfir/High Diploma, "Raman Amplification Measurement Method", AT IIPS (Informatics Institute of Post Graduate Studies) - University of Technology / Baghdad / Iraq, 2005.
5. P.B. Hansen, et al., "Rayleigh scattering limitations in distributed Raman preamplifiers", IEEE Photonics Technology Letters, Vol.10, No.1, pp.159-161, 1998.
6. Howard Kidorf, Karsten Prottwitt, Morten Nissov, Matthew Ma, and Eric Rabarijana, "Pump Interactions in 100-nm Bandwidth Raman Amplifier," IEEE Photonics Technology Letters, Vol.11, No.5, pp. 530-532, May 1999.
7. Victor E. Perlin, Herbert.
8. G. Winful, "On distributed Raman amplification for Ultrabroad-band Long-Haul WDM systems", Journal of Lightwave Technology, Vol. 20, No. 3, pp.409-416, March 2002.
9. GOVIND P.AGRAWAL "Fiber Optic communication systems"_3rd Edition, 2002.
10. Ashwin Gumaste, Tony Antony "DWDM Network Designs and Engineering Solutions" Published by Cisco Press, Series: Networking Technology, 2004.
11. Eng. ABEER DAHFIR AL_RIKABI Julay/2005 "Software Simulation of Optical Amplifier Systems" University of Technology as Master of Science in Network and Telecommunication.
12. USA-Cisco System, Inc _ Corporate Headquarters "Introduction to DWDM technology", http://www.cisco.com, 2000.
13. Recommendation ITU-T G.692 (10/98) / TELECOMMUNICATION STANDARDIZATION SECTOR OF ITU "Optical interfaces for multichannel systems with optical amplifiers", updated 1/2005.
14. ITU-T G.652 "Characteristics of a single-mode fiber and cable".
15. Optiwave Corporation "OptiAmplifier 4.0 Tutorials", 2004.

ANALYTICAL MODEL FOR RESOURCE ALLOCATION IN MULTIMEDIA COMMUNICATION NETWORKS

O. Alani, M. Al-Akaidi and J. Ivins
School of Engineering & Technology
De Montfort University
Leicester, UK
E-mail: oalani@dmu.ac.uk

KEYWORDS
Multimedia communication, Queuing system, Markov chain, Blocking probability

ABSTRACT

In current communication systems we have a number of different resources being used exclusively and simultaneously to satisfy the requirements of an arriving subscriber. This requires the occupation and release of these resources to be managed. In this article we propose a mathematical model for resource allocation to investigate the performance of a multimedia mobile network in terms of call blocking probability. The model assigns resources from the available classes of resources to each multimedia user. The occupation of these resources occurs concurrently, however the release could occur either concurrently or independently. The resulting queuing model has no product form solution. We derive the state probabilities and related performance measures by numerically solving a multi-dimensional Markov chain.

INTRODUCTION

Multimedia applications incorporate different media information, which includes voice, audio, video and data. A major issue in designing current and future wireless networks is to support all these service categories simultaneously, using the same system architecture.

Multimedia applications capture, generate, store, retrieve, process, transmit and present time dependent and time independent data streams. Multimedia applications have a wide variety of real-time requirements, which consists of synchronization, on-time delivery, minimum end-to-end delay bounds and minimum data loss rates. In addition to their timing requirements, multimedia applications are data intensive. They require large storage, high processing and large amount of network bandwidth. Therefore one multimedia call may consist of traffic from more than one service class called *components*. Each component call in a multimedia call requires its own quality of service (QoS) and has its own arrival rate λ and call holding time μ. A subscriber entering the multimedia system needs some of these resources for his treatment on account of their special properties. The occupation and release of the resources (call components) can occur *concurrently* or *non-concurrently*. This consideration needs a special treatment such as queuing theory to handle this problem.

QUEING MODEL

Each arriving multimedia call would require resources from each class of service in the system to complete its job. Let's assume that we have two classes of service in the system, with class-1 has C_1 resources and class-2 has C_2 resources. If a call arrives and there is no available resources at either or both classes of service the call is blocked. An active call will occupy resources from each of the two services for a negative exponentially distributed amount of time. We consider calls to arrive as a Poisson process with rate λ. The resources are released independently from each other and there holding time can be different for both classes. The queuing model can be described as an $M/M/C_1,C_2$ system as shown in Figure 1. The state of this model is given by the number of the occupied resources of both classes. Since we have negative exponentially distributed interarrival and service times we end up with a two dimensional Markov chain.

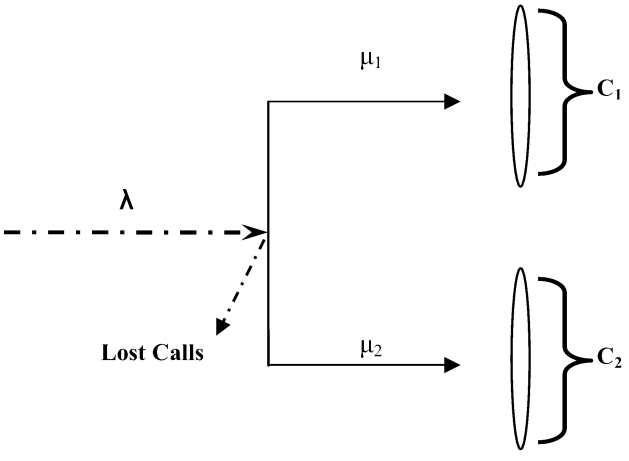

Figure 1 Call service pattern

ANALYZING QUEING MODEL

To derive the steady-state probabilities and related performance measures we have to investigate this Markov chain by using the balance condition for the steady-state behaviour of the queuing system, that entering and leaving a certain state occurs with equal probabilities.

The state transition diagram of the system for $C_1 = 4$, $C_2 = 3$ is shown in Figure 2 with all possible transitions between the states denoted by arrows and the corresponding transition-rates. It is not possible to obtain a closed form solution for this model as a result of the complexity of the transition diagram. Also the iterative derivation of the state probabilities by setting one state probability to an arbitrary positive real value, computing the rest of the state probabilities in dependence on this set probability and normalization of the state probabilities by dividing through their sum is not feasible. Another way to derive the state-probabilities would be to solve a system of (C_1 + 1). (C_2 + 1) -1 linear equations. This can result in numerical as well as in computing-time problems for larger values of C_1 and C_2. In (Robertazzi, 1990; Wang, and Robertazzi, 1990) the same state-space has been investigated for another problem. It is stated that the derivation of the steady-state probabilities is only feasible when one dimension of the state-space is bounded by two. In the notation used here this means $C_2 \leq 2$.

A more sophisticated algorithm which was already used in (Tran-Gia, 1982) reduces the dimension of the system of linear equations that must be solved and allows for an arbitrary number $C_1 \leq C_2$. This dimension-reduction algorithm avoids the solution of a system of linear equations which grows with O(C_1 .C_2). However the expense for that advantage is the storage of a C_2 + 1-vector for each state.

We have used a numerical example to show the performance of the model in Figure 2. The state of the system is given by *P(i,j)* denotes that *i* resources of class-1 and *j* resources of class-2 are occupied. The steady state balance equations are:

$$[\lambda\delta_{i+1,j+1} + i\mu_1\delta_{i-1,j} + j\mu_2\delta_{i,j-1} + i\mu_3\delta_{i-1,j-1}]P(i,j) = (\lambda + i\mu_3)\delta_{i-1,j-1}P(i-1,j-1) + (i+1)\mu_1\delta_{i+1,j}P(i+1,j) + (j+1)\mu_2\delta_{i,j+1}P(i,j+1) \quad (1)$$

and

$$\sum_{(i,j)\in A} P(i,j) = 1 \quad (2)$$

$$\delta_{k_1,k_2} = \begin{cases} 1 & if\ (k_1,k_2) \in A \\ 0 & if\ (k_1,k_2) \notin A \end{cases}$$

Where *A* is the space of acceptable states.

The blocking probability for an arriving multimedia call is therefore given by:

$$P_B = \sum_{i=0}^{C_1} P(i,C_2) + \sum_{j=0}^{C_2-1} P(C_1,j) \quad (3)$$

The above equation is the sum of two independent probabilities; the first term of (8) represents the blocking probability P_{b1} of calss-1 service, while the second term represents blocking probability P_{b2} of class-2 service when there are no available resources, whereas P_{b1}, and P_{b2} are given by:

$$P_{b1} = \sum_{j_2=0}^{C_2} P(C_1,j_2) \quad (4)$$

$$P_{b2} = \sum_{j_1=0}^{C_1} P(j_1,C_2) \quad (5)$$

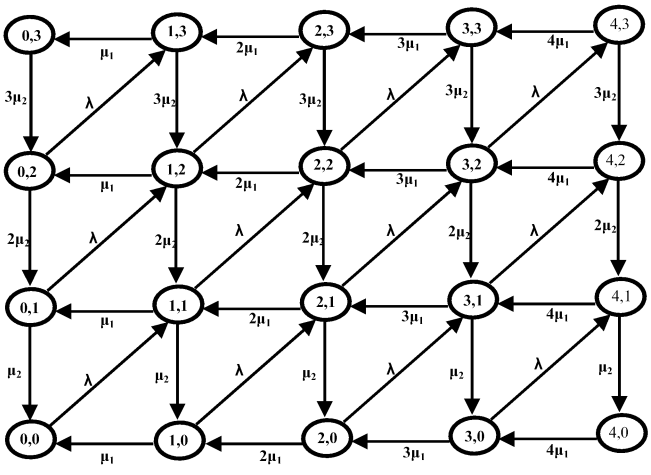

Figure 2 State space with C_1=4, C_2=3

NUMERICAL RESULTS AND DISCUSSION

Numerical results for the model shows that when there is a difference in the number of available resources of the different classes, and when the service rate per class are equal, the loss of calls depends mainly on the class with fewer resources.

Next we deal with the product of the number of resources and holding time (C_n*μ_n) in the. If C_1=¬C_2 then equality of blocking probabilities can be reached provided both services have equal service rate. But if C_1≠¬C_2 then, the blocking probabilities will be different. Figure3 and Figure 4 show the performance of the proposed scheme when the product of the number of resources and holding time are equal for two cases; case A, when C_1=24 and C_2=12, with μ_1 =1, μ_2 = 2, and case B, when C_1=24 and C_2=6, with μ_1 =1, μ_2 =4. For the first case there were C_2=12 slow components (long channel holding time) with μ_2 =2, whereas in the queuing system of the second case there were C_2=6 fast components (short channel holding time) with μ_2 =4. It could be noticed that call blocking probability is greater when there are less but faster users in service-2. Hence we can conclude that from QoS perspective its better

to have more slow components than few fast components when using the proposed scheme.

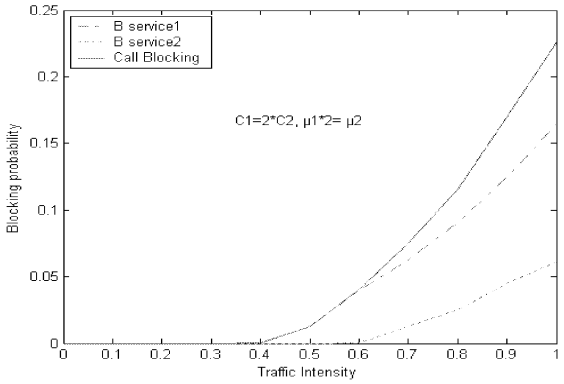

Figure 3 Blocking probability proposed scheme with equal (c*μ) product; $C_1=2C_2$, $2\mu_1 = \mu_2$

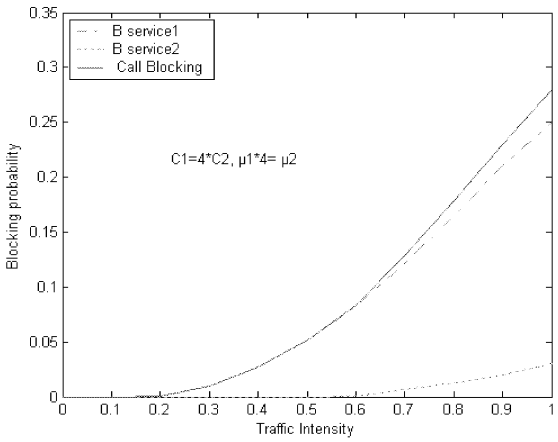

Figure 4 Blocking probability proposed scheme with equal (C*μ) product; $C_1=4C_2$, $4\mu_1 = \mu_2$

In the case of *concurrent* occupation and *concurrent* release, a subscriber needs one resource from each of the resource-classes at the beginning of its treatment. Each resource is occupied for a negative exponentially distributed amount of time (which can be different for each resource) but no one is released until the longest of the service periods is over. This means that if there is an n-class service in the system, n-1 resources are kept by a subscriber for a more or less amount of time although they are not any longer needed to satisfy the user requirements.

Therefore, the state probabilities and the related performance measures like the blocking probability depend on the minimum of the numbers of resources in the classes, this leads to an $M/G/C_{min}$ queuing system as a model for the *concurrent occupation/ non-concurrent* release case operating in pure loss mode.

The transition diagram for this case is shown in Figure 5. In this figure two types of services were assumed, multimedia traffic and voice traffic, the total number of channels C=6, *j* represent the number of multimedia users in the system while *i* represent the number of voice users. Each multimedia call requires 3 channels, while a voice call requires a single channel, i.e. (*j*=3**i*). It is clear that blocking probability of this case is given by Erlang-B formula with the accessible number of channels is determined by the minimum number of resources available to any service in the system, as in the following equation:

$$P_b = \frac{\rho^{C_{\min}} / C_{\min}!}{\sum_{k=0}^{C_{\min}} \rho^{k} / k!} \qquad C_{min}= \min \{C_1, C2,.....,C_n\} \quad (6)$$

Where *n* is the maximum number of services in the system and $\rho_n = \frac{\lambda_n}{\mu_n}$ for *n*=1, 2.

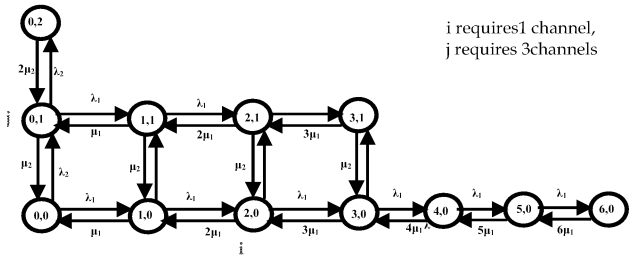

Figure 5 State space for the concurrent occupation/concurrent release case

CONCLUSION

An analytical model is developed in this paper to measure the performance of a proposed bandwidth access control scheme for wireless communication systems. The scheme realises the problem of allocating resources in systems that support multimedia applications, hence requires different types of channels to be assigned to a single subscriber. The problem arises when a call arrival is distinguished as a multimedia call; in this case a simultaneous occupation of a number of resources that have different attributes occurs. This would lead the system to be loaded in a certain manner which requires the implementation of the Queuing theory In order to solve the problem. Despite that we have only considered two types of service a closed form solution for the resulting queuing model cannot be obtained.

We have also considered the non-concurrent release of resource. There is a possibility for the user to keep all resource occupied till the subscriber finishes the call, even when some of these resources are not in use. The transition state is determined by the minimum number of resources available to the services in the system. The blocking probability of such system is given by Erlang-B formula.

REFERENCES

Tran-Gia P. " Modeling Overload Control in SPC Switching Systems", *36th Report on Studies in Congestion Theory, Institute of Switching and data Techniques, University of Stuttgart,1982.*

Robertazzi T.G, "Computer Networks and systems: Queuing Theory and Performance Evaluation", *Springer, 1990.*

Wang I.Y.and Robertazzi T.G, "Recursive Computation of Steady-State Probabilities of Nonproduct Form Queuing Networks Associated with Computer Network Models", *IEEE Transaction on Communications, Vol.38, No.1, January 1990.*

MIMO-OFDM CHANNEL MODELING AND PERFORMANCE

Omar Daoud, Marwan Al-Akaidi and Jonathan Ivins
School of Engineering & Technology
De Montfort University
Leicester, UK
mma@dmu.ac.uk

KEYWORDS
Orthogonal Frequency Division Multiplexing, Multiple-Input Multiple-Output, capacity, SDM, and STC.

ABSTRACT

This paper presents a systematic derivation of the channel capacity of MIMO-OFDM systems. In addition, we model a new MIMO channel to help in understanding the effect of spatial multiplexing on the MIMO channel, such as reducing the capacity and the BER, if spatial correlation is high. This effect will be found for some of the Space Division Multiplexing (SDM) algorithms, namely, Zero Forcing (ZF) and Minimum Mean-Square Error (MMSE).

INTRODUCTION

Due to its several significant advantages, such as the ability to support a high data rate for wide area coverage, robustness to multipath fading and simplification of channel equalisation, Orthogonal Frequency Division Multiplex (OFDM) has been adopted in both wireless and wired applications in recent years. These advantages render the employment of OFDM attractive for different applications such as IEEE 802.11, WLAN, ETSI terrestrial video broadcasting and Broadband Radio Access Network (BRAN). While the main advantages behind using the multiple antennas technology are to increase the system capacity and to improve the communication reliability via the diversity gain. The capacity of Multiple-Input Multiple-Output (MIMO) channels scale linearly with respect to the minimum available transmitter and receiver antennas (Juntti *et al*., 2005). These advantages have led to combine these two systems in B3G systems.

There are many issues that must be taken into consideration while using MIMO technology. Such as the MIMO channel model and the structure of the transmitted and received signals.

The received signal(s) has/have a very important effect on the maximum data rate in a given bandwidth. However, our concern is about improving the overall system capacity (i.e. the BER must be reduced, since the capacity is the received useful data), thus it is an important to have a rigid and proper MIMO channel model. The structure of the transmitted signal has a major impact on the achievable performance and capacity of the MIMO systems. In addition, the design of the signal directly influences the complexity of the transmitter and the receiver. The above issues have led to numerous research activities to achieve appropriate MIMO techniques, such as the useful transmitter structure and a MIMO channel modelling. Basically, the proposed schemes can be divided into two groups Space Time Coding (STC) and Space Division Multiplexing (SDM). These concepts have been the basis for various types of transmission schemes; respectively, they increase the robustness/ performance for the communications systems and improve the overall system data rate. These techniques will offer a variety of trade-offs between capacity capabilities and the BER when they are combined with corresponding receiver techniques.

Moreover, it is an important to have a correct MIMO channel model to improve the overall system performance. This model should cover the best and worst cases of the channel be however the effect of the spatial fading correlation.

In this work, we will concentrate on the SDM algorithm, because we are studying the effects of the MIMO channel behaviour on the capacity. Therefore, this work will present a capacity formula for MIMO channel; linking the BER with the SNR for some of the SDM algorithms, namely ZF and MMSE; and modelling a simple MIMO channel to cover the best and worst cases of the channel capacity.

MIMO–OFDM SYSTEM CAPACITY

The main factor that makes the MIMO systems preferable over the SISO system is the capacity. The capacity here is defined as the maximum rate of information sent without any losses at the receiver. It must be mentioned here that the capacity for the MIMO systems is based not only on the fading statistics, as for SISO systems, but also on the spatial correlations coefficient. Nevertheless, a proper coding and modulation techniques design will help in improving the channel capacity, such as the Forward Error Correcting codes.

Starting from (J. Andersen, 2000), the equivalence of the MIMO channel, **H,** consist of N_k parallel spatial subchannels with the k-th eigenvalue, λ_k, as gain for the k-th subchannel is shown as

$$b_k = \lambda_k^{1/2} a_k + n'_k . \quad (1)$$

where b_k , a_k and n'_k are the received signal, transmitted signal and the noise for the k-th subchannel, respectively. The equivalence representation of (1) can be shown in

Figure 1. From this figure we can measure the capacity according the spatial subchannels, since they are the parallel baths that are allocated to send the data in the same allocated bandwidth. Making use of the Shannon's capacity formula (C. Shannon, 1948), capacity depends on the power allocated per channel, we can define the common two types of capacities, namely *open-loop* and *closed-loop* capacities.

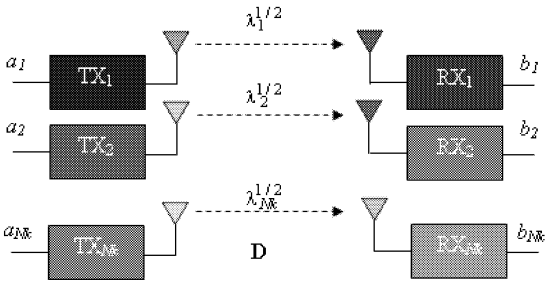

Figure 1: the equivalence representation of the MIMO system.

Let us first calculate the capacity formula starting from the information theory definition. Since the capacity is the maximum mutual information, then let us express the mutual information between transmitted vector **a** and received vector **b**. This mutual information is given by:

$$I(\mathbf{a};\mathbf{b}) = H(\mathbf{b}) - H(\mathbf{b}/\mathbf{a}) = H(\mathbf{b}) - H(\mathbf{n}), \quad (2)$$

where $H(.)$ denotes the entropy. Maximising (2) results if we maximising $H(\mathbf{b})$. According to (I. Telatar, 1999), the Gaussian distribution of a complex multivariate **y** has the largest entropy. The entropy of this complex multivariate normal distribution is given by:

$$H(\mathbf{y}) = -\int p(\mathbf{y}) \log_2 (p(\mathbf{y}))\, d\mathbf{y} \quad (3)$$

where $p(\mathbf{y})$ is the pdf of a complex multivariate normal distribution **y** with covariance matrix $\mathbf{Q}_y$ and mean μ_y, and it is given by

$$p(z) = \det(\pi \mathbf{Q}_z)^{-1} e^{(-(z-\mu_z))^H \mathbf{Q}_z^{-1} (z-\mu_z))}. \quad (4)$$

Thus, the capacity can be expressed as

$$C = \max(I(\mathbf{a};\mathbf{b})) = \max(H(\mathbf{b}) - H(\mathbf{n})) \quad (5)$$

From (3) and (4), and making use of that $\mathbf{a}^H\mathbf{b} = \mathrm{tr}(\mathbf{b}\mathbf{a}^H)$, where tr (.) stands for the *trace* of a matrix, *i.e.*, the sum of diagonal elements of the matrix, the entropy of **y** will be as

$$H(\mathbf{y}) = -\int p(\mathbf{y}) \log_2 (\det(\pi \mathbf{Q}_y)^{-1} e^{(-(y-\mu_y)^H \mathbf{Q}_y^{-1} (y-\mu_y))})\, d\mathbf{y}$$

$$= -\int p(\mathbf{y}) \log_2 (\det(\pi \mathbf{Q}_y)^{-1}) d\mathbf{y} - \int p(\mathbf{y}) ((-(\mathbf{y}-\mu_y)^H \mathbf{Q}_y^{-1} (\mathbf{y}-\mu_y))) \log_2 (e)\, d\mathbf{y}$$

$$= \log_2 (\det(\pi \mathbf{Q}_y)) + (\log_2 e)\, E[(\mathbf{y}-\mu_y)^H \mathbf{Q}_y^{-1} (\mathbf{y}-\mu_y)]$$

$$= \log_2 (\det(\pi e \mathbf{Q}_y)) \quad (6)$$

From (6), the capacity can be written as

$$C = \log_2 (\det(\pi e \mathbf{Q}_b)) - \log_2 (\det(\pi e \mathbf{Q}_n))$$

$$C = \log_2 (\det(\mathbf{I}_M + \frac{1}{\sigma_n^2} \mathbf{H}\mathbf{Q}_a\mathbf{H}^H)) \text{ bits/s/Hz} \quad (7)$$

(Foschini and M. Gans, 1998; A. Goldsmith, *et. al.*, 2003) also derived a capacity formula similar to what we derived in (7). To achieve the closed-loop capacity from (7), $\mathrm{tr}(\mathbf{Q}_a)$ must be smaller or equal to P_t (I. Telatar, 1999). Thus,

$$C_{cl} = \log_2 (\det(\mathbf{I}_M + \frac{1}{\sigma_n^2} \mathbf{D}\mathbf{V}^H\mathbf{Q}_a\mathbf{V}\mathbf{D}^H)) \text{ bits/s/Hz} \quad (8)$$

If the channel state information is not known at the transmitter (*i.e.*, the open-loop) thus, the available transmitted power will be distributed uniformly over the transmitting antennas (Foschini and Gans, 1998). Thus, $\mathbf{Q}_a = \frac{P_t}{N} \mathbf{I}_N$, which leads to

$$C_{ol} = \log_2 (\det(\mathbf{I}_M + \frac{P_t}{N \cdot \sigma_n^2} \mathbf{H}\mathbf{H}^H)) \text{ bits/s/Hz} \quad (9)$$

In this work, we will concentrate on the open-loop capacity formula, since it is more convenient classify for mobile communication systems.

PROPOSING A MIMO CHANNEL MODEL

As a designer, the main concern is to cover a wide range of scenarios in modelling the MIMO channel (including the worst-case scenarios for the correlation matrices, the capacity, BER, etc.). However, this will raise difficulties in determining which parameter has the greatest impact on performance. Therefore, in this section we will focus on deriving the capacity formula including the maximum value of spatial correlation as the worst case.

Spatial correlation is a key factor in the performance calculations of the MIMO system. Thus, to keep the spatial correlation to a minimum, the antenna spacing must be chosen to be equal or greater than λ/two, while λ is the carrier wave length (G. Foschini and M. Gans, 1998). However, if the space is limited then the spatial correlation must be taken into consideration. The modelling will start from the definition of the MIMO channel spatial correlation matrix, as in (D.-S. Shiu *et al.,* 2000; J. Li and E. Zhang, 2005)

$$\mathbf{R}_H = E[\mathrm{vec}(\mathbf{H})\, \mathrm{vec}(\mathbf{H})^H], \quad (10)$$

where **H** is the channel matrix with zero mean and variance one elements, $(.)^H$ denotes the Hermitian transpose[1], and vec(.) denotes the vec-operations of a matrix, defined as an MN X 1 dimensional vector composed by stacking the column of **H**. Furthermore, based on the assumption that the correlation among receiver antennas is independent from the correlation between transmit antennas the nonnegative definite correlation matrix can be defined as (K. Yu *et. al.*, 2004)

$$\mathbf{R}_H = \mathbf{R}_{TX} \otimes \mathbf{R}_{RX} \quad (11)$$

[1] The Hermitian transpose is the conjugate transpose of a matrix.

where $\otimes$ represents the Kronecker product, $\mathbf{R}_{TX}$ is an N X N dimensional nonnegative definite matrix, denotes the transmitter side correlation matrix, while $\mathbf{R}_{RX}$ is an M X M dimensional nonnegative definite matrix, denotes the receiver side correlation matrix. From (11), the correlation between different MIMO channel elements results from the Kronecker product of the correlation seen from the transmitter side with the one at the receiver side. After defining the correlation matrices, we want to generate the independent narrowband flat-fading MIMO channel with spatial correlation. (K. Pederson *et al.*, 2000) will be used to achieve the definition of **H** as:

$$\mathbf{H} = \text{unvec}\,(\mathbf{R}_H^{1/2}\ \mathbf{h}_{iid}), \tag{12}$$

The i.i.d. matrix contains i.i.d. zero-mean unit variance complex Gaussian elements, while **h** is an NM X 1 stochastic vector, and the unvec (.) is the reverse of the vec-operation. The channel correlation matrix can be resolved into its basic components (i.e., the eigenvalues and eigenvectors) as follows:

$$\mathbf{R}_H = \mathbf{U}\,\Lambda_H^{1/2}(\mathbf{U}\,\Lambda_H^{1/2})^H = \mathbf{R}_H^{1/2}(\mathbf{R}_H^{1/2})^H \tag{13}$$

where Λ_H is a diagonal matrix with eigenvalues of $\mathbf{R}_H$ and **U** contains the $\mathbf{R}_H$ orthonormal eigenvectors in it is columns. In the same way in (12), $\mathbf{R}_{TX}$ will be reformulated to be equal to $\{\mathbf{R}_{TX}^{1/2}(\mathbf{R}_{TX}^{1/2})^H\}$and $\mathbf{R}_{RX}$ equal to $\{\mathbf{R}_{RX}^{1/2}(\mathbf{R}_{RX}^{1/2})^H\}$. By making use of the property for any matrices with proper dimensions, namely, **A**, **B**, and **C,** {vec (**ABC**) = ($\mathbf{C}^T \otimes \mathbf{A}$) vec (**B**)}, (12) will be reformulated to be

$$\mathbf{H} = \mathbf{R}_{RX}^{1/2}\ \mathbf{H}_{iid}\,(\mathbf{R}_{TX}^{1/2})^T \tag{14}$$

The same result of the introduced spatial correlation model was obtained in (K. Yu *et. al.*, 2004).

Applying the achieved result from (14) to (9)

$$C = \log_2(\det(\mathbf{I}_N + \frac{\rho}{N}\mathbf{R}_{RX}^{1/2}\mathbf{H}_{iid}(\mathbf{R}_{TX}^{1/2})^T ((\mathbf{R}_{TX}^{1/2})^T)^H(\mathbf{H}_{iid})^H(\mathbf{R}_{RX}^{1/2})^H)\ \text{bit/s/Hz}. \tag{15}$$

For more simplification, reformulate (15) under the assumption of high SNRs

$$C \approx \log_2\det(\frac{\rho}{N}\mathbf{R}_{RX}^{1/2}\mathbf{H}_{iid}(\mathbf{R}_{TX}^{1/2})^T((\mathbf{R}_{TX}^{1/2})^T)^H(\mathbf{H}_{iid})^H(\mathbf{R}_{RX}^{1/2})^H)$$

$$= \log_2(\det(\frac{\rho}{N}\mathbf{I}_M)) + \log_2(\det(\mathbf{H}_{iid})\det((\mathbf{R}_{TX})^T)\det((\mathbf{H}_{iid})^H)\det(\mathbf{R}_{RX}))) \tag{16}$$

The capacity achieved from (16) is consists of two components; the first part is the capacity of parallel independent subchannel, while the second is from the correlation between the subchannels. Thus, in a correlated channel the MIMO capacity can be calculated by evaluating the determinant of the correlation matrices. Assume that we have a similar correlation matrices (*i.e.*, $\mathbf{R}_{TX} = \mathbf{R}_{RX}$). As we mentioned earlier, the correlation matrices are nonnegative definite matrices, therefore, the zero is a lower bound of the determinant. Furthermore, from our assumption, that $\mathbf{R}_{TX} = \mathbf{R}_{RX}$, then the diagonal elements for the correlation matrices are ones. ***As a conclusion, the determinant is bounded by one as a maximum and by zero as a minimum.***

As we mentioned earlier in this subsection, the correlation between two antennas will be neglected if the spacing is greater or equal to half the wavelength. In our model, the spatial correlation will be taken into our account, thus let us assume that the maximum spacing between the first and the last antenna is equal to half the wavelength, then the limits of the correlation between each two antennas will be described in Figure 2. Let us build our model based on four antennas. Explicitly, this model figures the effect of spatial correlation on the MIMO capacity. Moreover, it is quite a reasonable model from the physical representation point of view; this is obvious since the correlation will be decreased if the distance is increased.

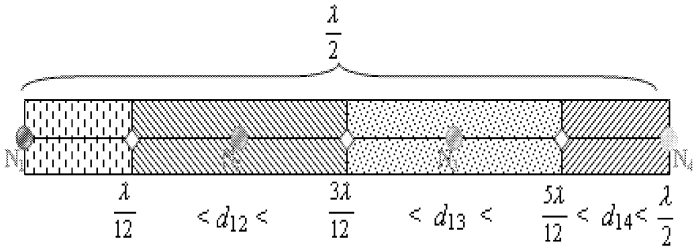

Figure 2: The proposed model N =4.

Figure 2 show that our model, ***Marwan-Omar Model (MOM)***, is a distance-based. In addition, a reference correlation coefficient must be assumed to be at the middle of d_{12} and equal to r. As an example, $\mathbf{N_3}$ is placed in the distance-range d_{13}, $\lambda/4 < d_{13} < 5\lambda/12$. Thus the correlation coefficient range is in between $(r/\left[(\frac{(N-3)+(N-2)}{2})2\right]$, $r/\left[(\frac{(N-2)+(N-1)}{2})2\right])$, where r is the correlation coefficient. Also, when $\mathbf{N_2}$ is placed at the middle of d_{12} range, the correlation coefficient will be equal to $\lambda/6$. Where, $\mathbf{N_3}$ and $\mathbf{N_2}$ are the antennas number 3 and 2 respectively. Assuming that r_{tx} is the reference correlation coefficient, and then the transmitter correlation matrix for N XN model is

$$\mathbf{R}_{TX} = \begin{pmatrix} 1 & (a_1,a_2) & (b_1,b_2) & \cdots & (c_1,c_2) \\ (a_1,a_2) & 1 & (a_1,a_2) & \ddots & \vdots \\ (b_1,b_2) & (a_1,a_2) & 1 & \ddots & (b_1,b_2) \\ \vdots & \ddots & \ddots & \ddots & (a_1,a_2) \\ (c_1,c_2) & \cdots & (b_1,b_2) & (a_1,a_2) & 1 \end{pmatrix} \tag{17}$$

where, $(a_1, a_2) = (\frac{1-r_{tx}}{2}, \frac{r_{tx}}{(3/2)^2})$, $(b_1, b_2) = (\frac{r_{tx}}{(3/2)^2}, \frac{r_{tx}}{(5/2)^2})$, and $(c_1, c_2) = (\frac{r_{tx}}{(\frac{(N-2)+(N-1)}{2})^2}, \frac{r_{tx}}{(N-1)^2})$.

From (17), Replacing N, $\mathbf{R}_{TX}$ and r_{tx} by M, $\mathbf{R}_{RX}$ and r_{rx} respectively will define the receiver correlation matrix for M X M.

To simplify our model, let us assume that each antenna is placed at the middle of its range area. Then $\mathbf{R}_{TX}$ and $\mathbf{R}_{RX}$ will be defined as

$$\mathbf{R}_{TX}=\begin{pmatrix} 1 & r_{tx} & \frac{r_{tx}}{4} & \cdots & \frac{r_{tx}}{(N-1)^2} \\ r_{tx} & 1 & r_{tx} & \ddots & \vdots \\ \frac{r_{tx}}{4} & r_{tx} & 1 & \ddots & \frac{r_{tx}}{4} \\ \vdots & \ddots & \ddots & \ddots & r_{tx} \\ \frac{r_{tx}}{(N-1)^2} & \cdots & \frac{r_{tx}}{4} & r_{tx} & 1 \end{pmatrix} \quad (18)$$

$$\mathbf{R}_{RX}=\begin{pmatrix} 1 & r_{rx} & \frac{r_{rx}}{4} & \cdots & \frac{r_{rx}}{(M-1)^2} \\ r_{rx} & 1 & r_{rx} & \ddots & \vdots \\ \frac{r_{rx}}{4} & r_{rx} & 1 & \ddots & \frac{r_{rx}}{4} \\ \vdots & \ddots & \ddots & \ddots & r_{rx} \\ \frac{r_{rx}}{(M-1)^2} & \cdots & \frac{r_{rx}}{4} & r_{rx} & 1 \end{pmatrix} \quad (19)$$

where r_{tx} and r_{rx} are real-reference correlation coefficients for the $\mathbf{R}_{TX}$ and $\mathbf{R}_{RX}$, N and M are the total number of antennas at the transmitter and receiver, respectively.

SIMULATION RESULTS AND DISCUSSION

MIMO Channel Capacity

Figures 3 and 4 depict the ergodic capacity as a function of the SNR. The ergodic capacity is determined for 10,000 realisations of **H** to cover most cases of the real life channel. The realisations of **H** are assumed to be i.i.d. circularly-symmetric complex Gaussian distributed. The number of nonzero eigenvalues of $\mathbf{HH}^H$ or $\mathbf{H}^H\mathbf{H}$ for this type of channels equal $N_k = \min(N,M)$.

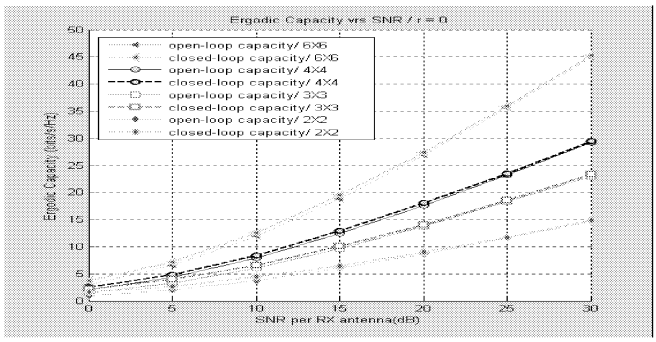

Figure 3: Ergodic channel capacity for different MIMO configuration and a correlation coefficient equal to 0.

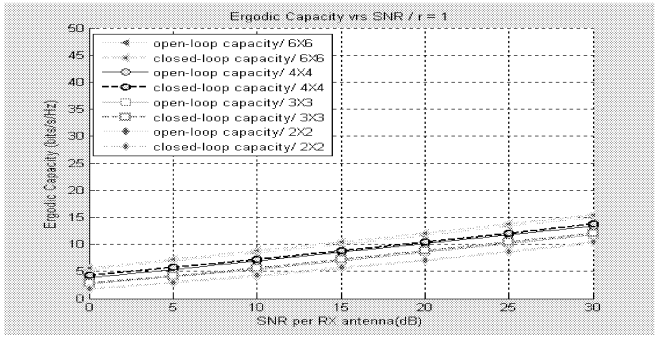

Figure 4: Ergodic channel capacity for different MIMO configuration and a correlation coefficient equal to one.

From these figures, we have to conclude, that a closed-loop scheme is only providing significant capacity enhancements over an open-loop scheme for scenarios in which spatial multiplexing is not performing correctly. Besides, the ergodic capacity has a direct relationship with the number of antennas and an inverse relationship with the correlation coefficient. This means that in the closed-loop scenario, the optimal transmitter will use more power on the stronger subchannel and enhance the capacity, whereas the transmitter that applies equal power on all subchannels wastes energy in the null modes and loses capacity.

MOM Channel Model

Figure 5 shows the determinant of $\mathbf{R}_{TX}$ as a function of r_{tx}. From this figure, the determinant for the *modelled* matrix is monotonically decreasing in the range of interest, *i.e.*, $0 \leq r_{tx} \leq 1$.

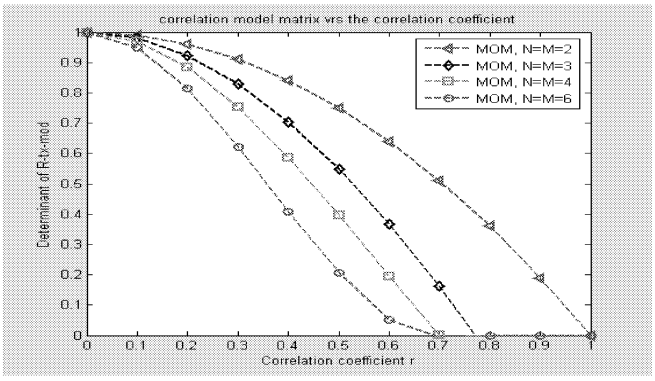

Figure 5: The determinant of $\mathbf{R}_{TX}$, versus r_{tx} for a various number of TX antennas.

In order to compare our model with a validated practical work, (J. Kermoal *et. al.*, 2002) afford a measured correlation matrices given for both $\mathbf{R}_{TX}$ and $\mathbf{R}_{RX}$ in (21) and (22), respectively. Applying (21) and (22) to our achieved result in (15), with 10000 realisation of $\mathbf{H}_{iid}$ we achieved the ergodic capacity as a function of the SNR depicted in Figure 6.

$$\mathbf{R}_{TX,mod}=\begin{pmatrix} 1 & -0.61+0.77i & 0.14-0.94i & 0.24+0.89i \\ -0.61-0.77i & 1 & -0.85+0.5i & 0.57-0.78i \\ 0.14+0.94i & -0.85-0.5i & 1 & -0.91+0.4i \\ 0.24-0.89i & 0.57+0.78i & -0.91-0.4i & 1 \end{pmatrix} \quad (21)$$

$$\mathbf{R}_{RX,mod}=\begin{pmatrix} 1 & -0.12-0.18i & 0.08+0.05i & -0.02-0.13i \\ -0.12+0.18i & 1 & -0.17-0.16i & 0.11+0.04i \\ 0.08-0.05i & -0.17+0.16i & 1 & -0.17-0.16i \\ -0.02+0.13i & 0.11-0.04i & -0.17+0.16i & 1 \end{pmatrix} \quad (22)$$

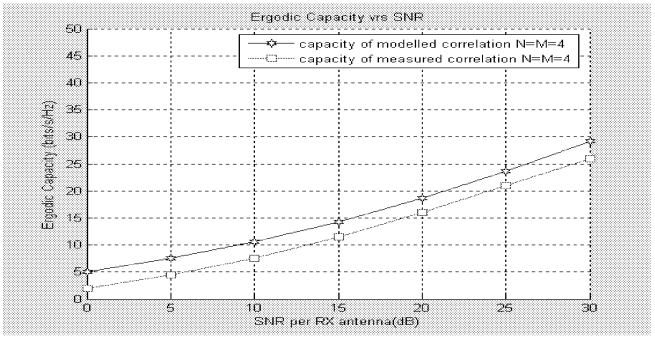

Figure 6: The effect of the measured and modelled spatial multiplexing on the ergodic capacity vs. SNR per RX antenna for a various number of TX antennas.

Linking BER and SNR for Different SDM techniques

Different MATLAB programme were run to model and obtain the performance characteristics of the ZF and the MMSE. The BER performance is obtained by averaging over 10000 realisation of the channel to cover all choices of the real life MIMO channel in our simulation.. Figure 7 depicts the BER *vs*. the SNR of the ZF and the MMSE techniques for the configuration of 2X2 MIMO systems.

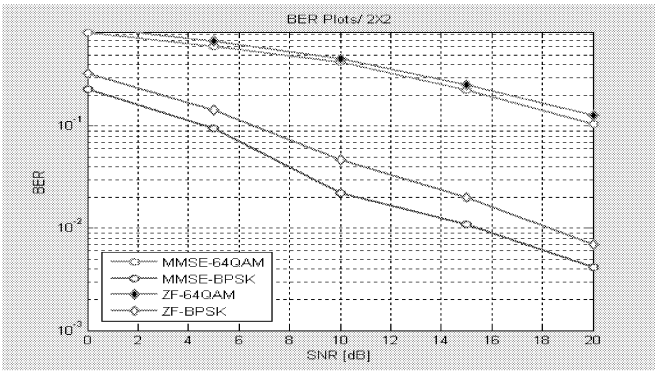

Figure 7: BER vs. the SNR for a 2X2 MIMO system with BPSK and 64QAM modulation techniques.

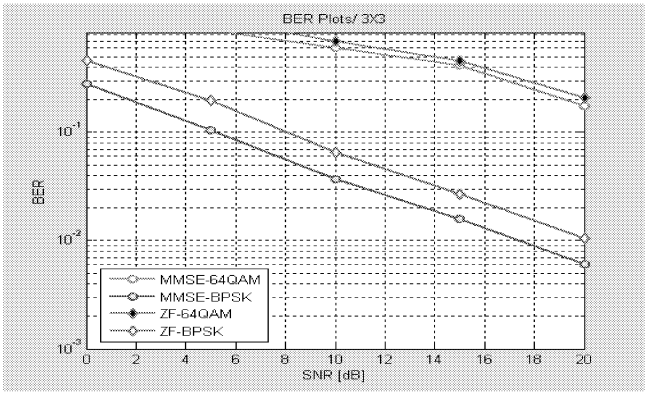

Figure 8: BER vs. the SNR for a 3X3 MIMO system with BPSK and 64QAM modulation techniques

From Figure 7, the MMSE gives better performance to the ZF technique. It can be concluded that a low constellation order is better than a high one. Figure 8 presents the result of 3X3 configuration. Comparing to the performance achieved from Figure 8, increasing the system configuration from 2X2 to 3X3 antennas will reduce the system performance for both of the SDM techniques.

CONCLUSION

In this paper, we have presented our new MIMO channel model (MOM) and derived the MIMO channel capacity formula. It is clear from the results that spatial multiplexing has an important effect on the system capacity, thus for a better system performance it should be reduced. MOM has been validated practically. Figure 6 shows that MOM improves the capacity by, at least, 2 bits/s/Hz.

Also, from Figures 7 and 8, increasing the system configuration will reduce the system performance for both of the SDM techniques, and it can be concluded that a low constellation order is better than a high constellation order.

REFERENCES

J. Andersen, "Array gain and capacity for known random channels with multiple element arrays at both ends", *IEEE Journal on selected areas in Communs*, vol. 18, no. 11, pp. 2172-2178, Nov. 2000.

G. Foschini and M. Gans, "On limits of wireless communications in a fading environment when using multiple antennas", *AT&T-Bell Labs Internal Tech. Memo*, Sept. 1995. *Journal of Wireless Personal Comms*, vol. 6, no. 3, pp. 311-335, March 1998.

A . Goldsmith, S. Jafar, N. Jindal and S. Vishwanath, " Capacity Limits of MIMO Channels", *IEEE Journal on selected areas in Comms,* vol. 21, no. 5, pp. 684-701, Jun. 2003.

M. Juntti, M. Vehkapera, J. Leinonen, V. Zexian,, D. Tujkovic, S. Tsumura., and S. Hara, ", MIMO MC-CDMA Communications for Future Cellular Systems", *IEEE Commun. Mag.*, pp. 118-124, Feb. 2005.

J. Kermoal, L. Schumacher, K. Pedersen, P. Mogensen and F. Frederiksen, "A stochastic MIMO radio channel model with experimental validation", *IEEE Journal on Selected Areas in Comms,* vol. 20, no. 6, pp. 1211-1226, Aug. 2002.

S. Loyka, "Channel capacity of MIMO architecture using the exponential correlation matrix", *IEEE Comms Letters,* vol. 5, no. 9, pp. 369-371, Sept. 2001.

K. Pederson, J. Andersen, J. Kermoal, and P. Mogensen, "A stochastic multiple-input-multiple-output radio channel model for evaluation", in *Proc. Of the 52nd IEEE VTC 2000 Fall,* vol. 2, pp. 893-897.

C. Shannon, " A mathematical theory of communications", *Bell Systems Technical Journal,* vol. 27, 379-423, 623-656, 1948.

D.-S. Shiu, G. Foschini, M. Gans and J. Kahn, "Fading correlation and its effect on the capacity of multielement antenna systems", *IEEE Transactions on Comms,* vol. 48, no. 3, pp. 502-513, March 2000.

I. Telatar, "Capacity of multi-antenna gaussian channels", Rm. 2C-174, Lucent Technology, CiteSeer.IST , 1999.

K. Yu and B. Ottersten, "Models for MIMO propagation channels: a review", *Wireless Comms and Mobile Comp. 2002,* John Wiley & Sons, no. 2, pp. 653-666.

L. Zheng and D. N. Tse, " Diversity and multiplexing: a fundamental tradeoff in multiple-antenna channels" *IEEE Tran on Info Theory,* vol. 49, no. 5, pp. 1073-1096 May 2003,.

ELECTRONIC APPLICATIONS SIMULATION

Evaluation Textile Fabrics Color Difference by Digital Camera

A. Shams-Nateri
Assistant Professor
Textile Engineering Department, Guilan University, Rasht, Iran
E-mail: a_shams@guilan.ac.ir

KEYWORDS: Camera, Color Difference, Fabric, Textile, Color Control

ABSTRACT
This technical report describes new method for prediction color differences of textile fabrics. Initially, polyester fabrics dyed in variety color. The color specification of colored fabrics have been measured by spectrophotometers. The color differences have been calculated by several formula as actual color differences between colored fabrics. In next section, their pictures have been taken by digital camera and RGB values of image were converted to CIEXYZ by SRGB formula and polynomial regression method. Then, color difference has been calculated by several formula as predicted color difference between colored fabrics. As the result show, the best prediction and correlation between actual and predicted and prediction is achieved by BFD color difference formula and polynomial regression method.

INTRODUCTION

A color space is a method by which we can specify, create and visualize color. As humans, we may define a color by its attributes of brightness, hue and colorfulness. A computer may describe a color using the amounts of red, green and blue phosphor emission required to match a color. A printing press may produce a specific color in terms of the reflectance and absorbance of cyan, magenta, yellow and black inks on the printing paper. A color is thus usually specified using three co-ordinates, or parameters. These parameters describe the position of the color within the color space was used. They do not tell us what the color is, that depends on what color space is being used (Ford et al. ; MacdDonald et al. ; Gary et al.).

A device dependent color space is a color space where the color produced depends both the parameters used and on the equipment used for display. For example, try specifying the same RGB values on two different workstations, the color produced will be visually different if viewed on side-by-side screens (Ford et al. ; MacdDonald et al. ; Gary et al.).

Some device dependent color spaces are well characterized so that the user can translate between them and some other, device independent, color space. Typically, this characterization takes the form of specifying the chromaticities of the three primaries as well as the transfer functions for each channel. Such color spaces are known as device calibrated color spaces and are a kind of half way house between dependent and independent color spaces. A color gamut is the area enclosed by a color space in three dimensions. It is usual to represent the gamut of a color reproduction system graphically as the range of colors available in some device independent color space. Often the gamut will be represented in only two dimensions, for example on a CIE Yxy chromaticity diagram (Ford et al. ; MacdDonald et al. ; Gary et al.).

Due to the increase of low-cost color devices (digital color scanners, cameras, printers etc.) during the last few years, color calibration has become an important issue. Such devices should truly reproduce color images, but experience shows they don't. Among the main reasons, we note the diversity of acquisition, display and printing technologies, which makes standardization difficult. Each device has a different gamut, i.e. a different set of colors that it can acquire or reproduce. Furthermore, the characteristics of the devices often vary with time. Hence, a calibration procedure is unavoidable for high quality color reproduction. Each device has its own color space, defined by the relationship between the input colors and the corresponding RGB codes used to represent them. Consequently, waiving device calibration, which converts the native color space into a standard device-independent one, will often result in unmatched colors throughout the system. Moreover, images acquired with different devices cannot be reliably compared and stored. In some cases, experimental results might not be reproduced with different digitizing equipment. A simple method of converting camera RGB responses to estimates of object tristimulus XYZ coordinates is to apply a linear transformation to the RGB values. The transformation parameters are selected subject to minimization of some significant error measure. The basic idea of color target-based characterization is to use a reference target that contains a certain number of color samples. These colors are then imaged by a digital camera and measured by a spectrophotometer to obtain the RGB values and their corresponding XYZ values. Typical methods like three-dimensional lookup tables with interpolation and extrapolation, least squares polynomial modeling and neural networks can be used to derive a transformation between camera RGB values and XYZ values (Hong et al. ; Cheung et al. ; Izadan et al. ; MacDonald et al. ; Vrhel et al.) .

Color Difference: The most widely used color difference equations in the last decades are CIELAB color difference equations recommended in 1976 by the

CIE. In CIELAB color spaces, the color difference between two arbitrary colors is defined as Euclidian distance in a uniform space comprising a lightness L* axis and red-green (a*), yellow-blue (b*) opponent color axes using rectangular coordinates. The CIELAB color difference is given by Equations 1:

$$\Delta E_{CIELAB} = (\Delta L^{*2} + \Delta a^{*2} + \Delta b^{*2})^{1/2} \quad (1)$$

Where a* and b* are the redness-greenness and yellowness-blueness scales in CIELAB color space. The color difference formula CIE1976 is in many cases not adapted to human perception. Work in area color differences has concentrated on collecting reliable data and developing equations that describe the perceived color - difference results. Newer equations have been developed on base of the CIELAB (CIELCH) color space with application weighting difference components such as DL*, DC* and DH*. Weighting functions S_L, S_C, S_H are computed from regression analysis used linear (CIE1994) or hyperbolic model (CMC(l:c)). During the development of a new color – difference formulas (CIE1994) was considerable discussion about possible hue dependencies, as exemplified by the CMC1 and BFD2 equations. The CMC (l:c) color – difference formula was a refinement of the JPC79 equation developed by Dr. McDonald. Simplicity is not always a good thing. Sometimes complexity is necessary for obtaining higher accuracy. Compared to the CIE94 formula, the CIE2000 formula is much more complex. However, the latter gave more accurate prediction than the former did when being tested on both the old and the new experimental data sets(Gary et al.; CIE Technical Report).

METHOD

The Nikon COOLPIX 4500 digital camera has been used for scanning colored fabrics. The RGB values of images were converted to CIEXYZ by sRGB Equation. The colorimetric data of dyed fabrics measured by using Texflash spectrophotometer of Datacolor Corporation under condition of 2 degree standard observer and D65 illuminant. Polyester fabrics dyed with disperse dyestuff in varieties of colors. The chromaticities of 182 colored fabrics are shown in figure1. The color difference between pairs colored fabrics was calculated to form a combined data set, which contains about 16656 pairs.

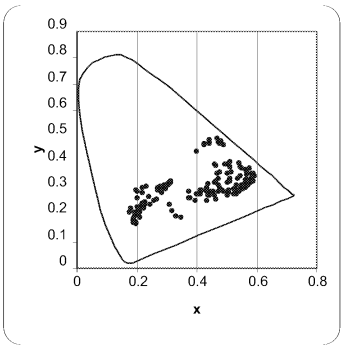

Figure 1. Chromaticity distribution of colored fabrics

Conversion by SRGB Method: In this method RGB value of camera was converted to CIEXYZ by follow:

$$\begin{cases} R = R/255 \\ G = G/255 \\ B = B/255 \end{cases} \quad (2)$$

$$r = \begin{cases} \dfrac{R}{12.92} & R \le 0.04045 \\ \left(\dfrac{R+0.055}{1.055}\right)^{2.4} & R > 0.04045 \end{cases} \quad (3)$$

$$g = \begin{cases} \dfrac{G}{12.92} & G \le 0.04045 \\ \left(\dfrac{G+0.055}{1.055}\right)^{2.4} & G > 0.04045 \end{cases} \quad (4)$$

$$b = \begin{cases} \dfrac{B}{12.92} & B \le 0.04045 \\ \left(\dfrac{B+0.055}{1.055}\right)^{2.4} & B > 0.04045 \end{cases} \quad (5)$$

$$\begin{cases} \overline{R} = 100 \times r \\ \overline{G} = 100 \times g \\ \overline{B} = 100 \times b \end{cases} \quad (6)$$

$$\begin{cases} X = 0.4124 \times \overline{R} + 0.3576 \times \overline{G} + 0.1805 \times \overline{B} \\ Y = 0.2126 \times \overline{R} + 0.7152 \times \overline{G} + 0.0722 \times \overline{B} \\ Z = 0.0193 \times \overline{R} + 0.1192 \times \overline{G} + 0.9505 \times \overline{B} \end{cases} \quad (7)$$

Then, The XYZ has been converted to CIELAB (L*, a* and b*) by follow:

$$\begin{cases} L^* = 116 \times F\left(\dfrac{Y}{Y_n}\right) - 16 \\ a^* = 500 \times \left[F\left(\dfrac{X}{X_n}\right) - F\left(\dfrac{Y}{Y_n}\right) \right] \\ b^* = 200 \times \left[F\left(\dfrac{Y}{Y_n}\right) - F\left(\dfrac{Z}{Z_n}\right) \right] \end{cases} \quad (8)$$

Where

$$F(I) = I^{1/3} \quad for \quad I > 0.008856$$

Otherwise, $F(I) = 7.7871 \times I + \dfrac{16}{116}$

Where X, Y, Z and Xn, Yn, Zn are the tristimulus values of the sample and a specific reference white. It is common to use the tristimulus values of the perfect diffuser illuminated by a CIE illuminant or a light source as the Xn, Yn, Zn values.

Calibration by Polynomial Regression Method: In this work, some methods for the colorimetric calibration digital cameras are proposed. The goal of our characterization is to establish the relationship between the device dependent color space of the camera and the device independent CIELAB and CIEXYZ color spaces. The camera characterization is based on polynomial regression techniques. Several regression schemes have been tested. The first proposed method consisting of applying a non-linear correction to the camera RGB values followed by polynomial regression function directly to CIELAB color space. The experimental procedure is outlined below:

1. Scan fabrics by camera and obtain the camera RGB responses from colored fabrics images.

2. Measure the CIEXYZ and CIELAB values of colored fabrics by spectrophotometer.
3. Derive a transfer matrix that matches camera RGB to their CIE specification of color fabrics by multiple polynomial regressions.
4. Transform camera RGB to CIE color space via the derived matrix.
5. Calculate both the individual color difference for each patch and find the mean of these differences for each model.

The characterization model can be represented in a simple form as follows:

$$XYZ = M \times RGB \tag{9}$$

In the above, XYZ is a vector of color tristimulus $\left[X_i\ Y_i\ Z_i\right]$ with i = 1, 2, … n, n is the number of samples, M is a 3 x m matrix of coefficients , m is the number of terms in a polynomial. RGB is a vector of camera output signals $\left[R_i^j G_i^j B_i^j\right]$, i = 1, 2, … n and j = 1, 2, … m, where m is the number of terms in a polynomial. By the well-known method for solving a least-squares problem, the M is:

$$M = XYZ \times RGB^T \times (RGB \times RGB^T)^{-1} \tag{10}$$

This can be expanded as fallow:

$$XYZ = M \times RGB \tag{11}$$

or

$$\begin{bmatrix} X \\ Y \\ Z \end{bmatrix}_{3\times 1} = \begin{bmatrix} a_{1,1} & a_{1,2} & \cdots & a_{1,m} \\ a_{2,1} & a_{2,2} & \cdots & a_{2,m} \\ a_{3,1} & a_{3,2} & \cdots & a_{3,m} \end{bmatrix}_{3\times m} \times \begin{bmatrix} R \\ G \\ B \\ R^2 \\ G^2 \\ B^2 \\ \cdot \\ \cdot \\ \cdot \\ \cdot \end{bmatrix}_{m\times 1} \tag{12}$$

Where m=31 and

RGB = [R G B R×G×B R×G R×B G×B R^2 G^2 B^2 R^3 G^3 B^3 $G\times R^2$ $B\times G^2$ $R\times B^2$ $B\times R^2$ $R\times G^2$ $G\times B^2$ $G\times B\times R^2$ $B\times R\times G^2$ $R\times G\times B^2$ R^4 G^4 B^4 R^5 G^5 B^5 $R^2\times G^3$ $G^2\times B^{\wedge 3}$ $B^2\times R^3$].

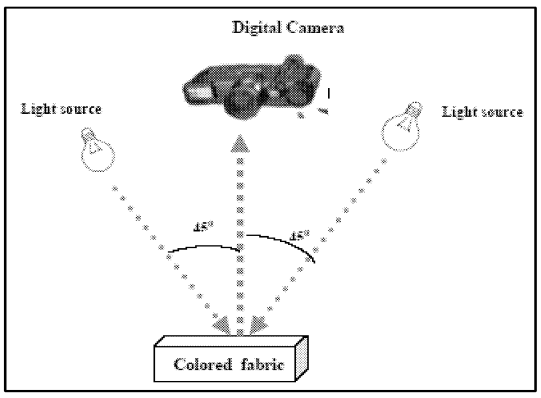

Figure 2. Take picture by digital camera

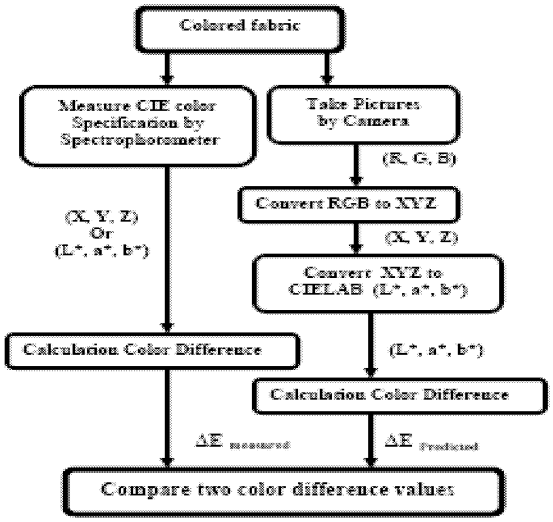

Figure 3. Algorithm of color difference calculation

Result and Discussion

In SRGB method, the actual and predicted color differences of 16656 pairs for all color difference formula have been calculated. For evaluation and comparison relationship between measured and predicted color difference, the correlation between them are shown in figures 4, 5, 6, 7 and 8 respective for CIELAB, CMC, CIE94, BFD and CIE2000 color difference formula. The correlation coefficients of predicted and actual color difference are shown in table 1. As results are shown, the best color difference prediction has been obtained BFD formula.

In next section, the prediction error has been calculated by Equation 13 and the results were summarized in table 2. The less error has been achieved by BFD formula.

$$Error = \left|\Delta E_{measured} - \Delta E_{caculated}\right| \tag{13}$$

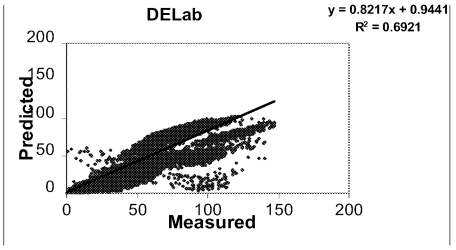

Figure 4. Relationship between actual and predicted color difference by CIELAB (sRGB)

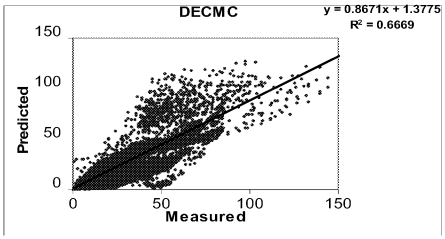

Figure 5. . Relationship between actual and predicted color difference by CMC formula (sRGB)

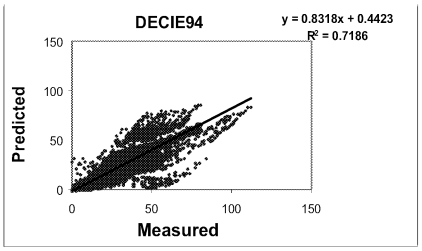

Figure 6. . Relationship between actual and predicted color difference by CIE94 formula (sRGB)

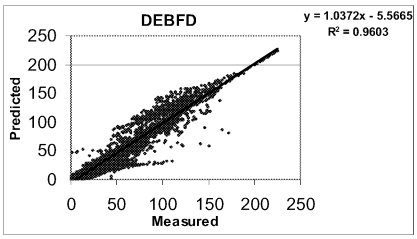

Figure 7. . Relationship between actual and predicted color difference by BFD formula (sRGB)

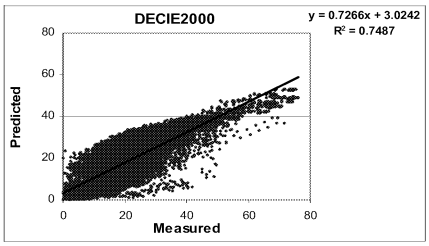

Figure 8. Relationship between actual and predicted color difference by CIE2000 formula (sRGB)

Table 2. The correlation coefficients between actual and predicted color difference (sRGB)

No.	Color difference formula	Correlation coefficients
1	CIELAB	0.846
2	CMC	0.858
3	CIE94	0.869
4	BFD	0.981
5	CIE2000	0.869

Table 1. The error of color difference prediction (sRGB)

No.	color difference Formula	average	Max.	Min.	SD
1	CIELAB	13.32	106.29	0	14.08
2	CMC	9.05	102.59	0	9.40
3	CIE94	7.98	56.49	0	7.55
4	BFD	5.61	93.19	0	7.79
5	CIE2000	6.24	39.57	0	5.50

In Polynomial Regression Method, the actual and predicted color differences of 16656 pairs for all color difference formula have been calculated. The correlation between measured and predicted color difference are shown in figures 9, 10, 11, 12 and 13 respective for CIELAB, CMC, CIE94, BFD and CIE2000 color difference formula. The correlation coefficients of predicted and actual color difference are shown in table 3. As results are shown, the best prediction has been obtained BFD formula.

In next section, the prediction error was calculated by Equation 13 and the results were shown in table 4. The less error was obtained by BFD formula.

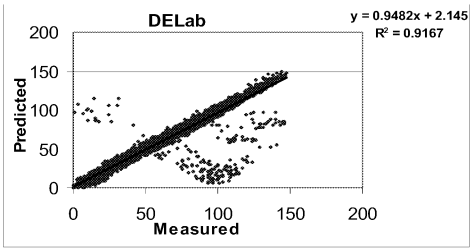

Figure 9. . Relationship between actual and predicted color difference by CIELAB (Calibration)

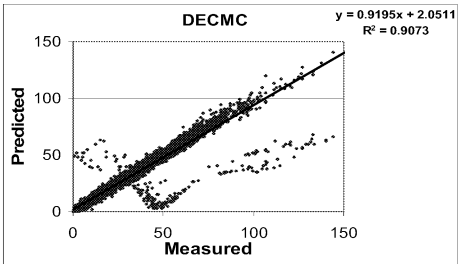

Figure 10. . Relationship between actual and predicted color difference by CMC formula (Calibration)

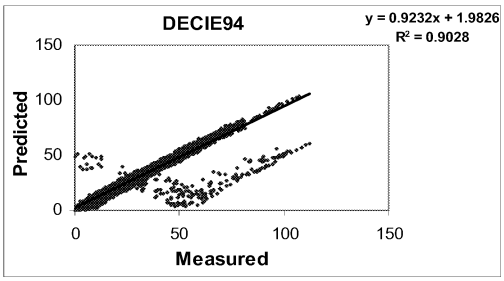

Figure 11. . Relationship between actual and predicted color difference by CIE94 formula (Calibration)

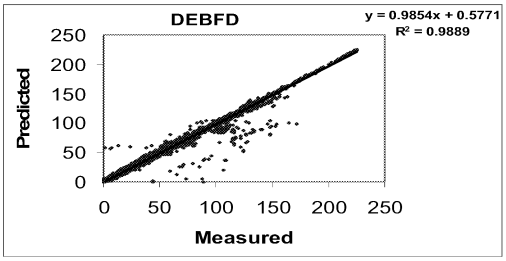

Figure 12. . Relationship between actual and predicted color difference by BFD formula (Calibration)

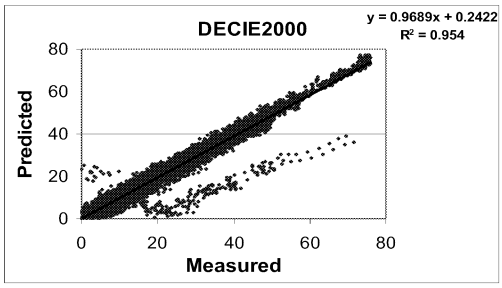

Figure 13. . Relationship between actual and predicted color difference by CIE2000 formula (Calibration)

Table 3. The correlation coefficients between actual and predicted color difference (Calibration)

No.	Color difference formula	Correlation coefficients
1	CIELAB	0.954
2	CMC	0.948
3	CIE94	0.948
4	BFD	0.993
5	CIE2000	0.967

Table 4. The error of color difference prediction (Calibration)

No.	color difference Formula	average	Max.	Min.	SD
1	CIELAB	3.67	104.13	0	8.76
2	CMC	2.57	123.82	0	6.99
3	CIE94	2.31	54.75	0	5.73
4	BFD	1.61	90.64	0	4.93
5	CIE2000	2.01	36.63	0	3.40

Conclusion

In this work, it has been tried to evaluate color difference of colored fabrics by digital camera. Initially, the color specification has been measured by spectrophotometers. The actual color difference between colored fabrics has been calculated by several formula such as CIELAB, CMC, CIE94, BFD, and CIE2000. In next section, their picture has been taken by camera. The RGB values of picture have been converted to CIEXYZ by sRGB formula and polynomial regression method. Predicted color difference between colored fabrics has been calculated by several formula. The correlation between measured and predicted color difference have been calculated for various color difference formula.

In SRGB method, the best correlation between measured and predicted color difference has been obtained BFD formula. The less error has been achieved by BFD formula.

In polynomial regression method, the best prediction has been obtained BFD. formula. The less error was achieved by BFD formula.

Reference

Ford, A. and A. Roberts, "Color Space Conversions"; http://www.poynton.com/Poynton-color.html; 1998.

MacdDonald, W. and M. Ronnier Luo;" Color Imaging: Vision and Technology"; John Wiley &Sons Ltd, 1999.

Gary, N. M, Modern Concepts of Color and Appearance, Science Publishers Inc. U.S.A, (2000).

Hong, G.; R. M, Luo, and P.A., Rhodes, "A study of digital camera colorimetric characterization based on polynomial modelling", Color Research and Application, Vol. 26, No.1, 76-84 (2001).

Cheung T.L.V.; and S. Westland, " Color Camera Characterisation Using Artificial Neural Networks", IS&SID Tenth Color Imaging Conference, 2002.

Izadan , H. and J. H. Nobbs; " The effect of different linearisation methods on scanner characterization" AIC Colour 05 - 10th Congress of the International Colour Association, PP. 1251-1254;2005.

MacDonald, L.; T. Song, G. Hong, K. Findlater ; " Characterising a digital camera for stained glass"; AIC Colour 05 - 10th Congress of the International Colour Association;PP. 279-283; 2005.

Vrhel, M.J.; H.J. Trussell, "Color Device Calibration: A Mathematical Formulation", IEEE Transactions on Image Processing, 1999.

CIE Technical Report; " Methods to derive color differences for images " ;Draft Version 0.4; October, 2000.

A VERSATILE SONAR SIMULATION PLATFORM FOR TESTING SEABED ESTIMATION ALGORITHMS

Ghedhban Swadi
School of Product and Engineering Design
University of Wales Institute, Cardiff
Western Avenue, Llandaff
Cardiff CF5 2YB, UK

Tahseen Rafik
School of Product and Engineering Design
University of Wales Institute, Cardiff
Western Avenue, Llandaff
Cardiff CF5 2YB, UK
E-mail: trafik@uwic.ac.uk

Ivan Jordanov
Computer Science and Software Engineering Department
University of Portsmouth, UK

KEYWORDS

Seabed Mapping, High Resolution Sonar, Estimation Algorithms.

ABSTRACT

This paper describes a simulation model of a sonar seabed mapping system based on echo sounder. The purpose of this simulation is to study the performance of linear predictors of different orders in estimating the future values of seabed depths. The simulated system consists of random seabed generator, echo sounder simulated signal generator and a predictor. The beam width of the echo sounder and the order of the estimator can be selected by the user. Labview and Matlab were used to build the simulation model. Results showed that a second order predictor gives the best results.

INTRODUCTION

Seabed mapping and imaging represents one of the main activities in sonar research. The earliest technique of depth measurement in water (bathymetry) involved lowering a weight-down rope or cable over the side of a ship, then measuring the length of the wet end when it reached the bottom. Todays, the seabed and related features such as wrecks, pipelines, navigation obstructions and general topography can be imaged or detected by several different techniques, each with their own merits. These include Single Beam Echo Sounder, Multi-beam Echo Sounder, Side Scan Sonar and Synthetic Aperture Sonar.

The single-beam echo sounder has been around for many years and is now a common sight on even very small craft. Basically, a short but powerful pulse of electrical energy is converted to sound/acoustic energy and is transmitted from the bottom of the vessel directly at the seabed. The frequency of these small boat sounders is usually in the region of 150 kHz. The pulse is in the form of a narrow beam, which is defined by the way in which the sounder transducer fitted to the bottom of the boat is designed. The sound travels through the water at approximately 1500 m/second, which is about 5 times the speed of sound in air. When the sound pulse hits the seabed, some of the energy will be absorbed by the seabed material and some will be reflected back up the way it came down. However a proportion will also be scattered in all directions as the seabed is not a flat perfect surface. Another important factor is that the sound will spread as it travels through the water and thus the pulse energy will also be weakened as it travels.

A typical echo sounder might operate at 150 kHz and, for a depth scale of 200 m, transmit a pulse four times per second. The standard display presentation is known as an echogram. Depth is on the vertical axis, and time, or distance traveled over the seabed is on the horizontal axis (Waite 2002).

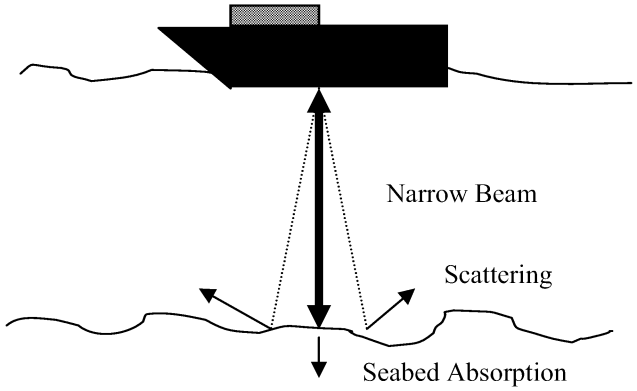

Figure 1: Single Beam Echo Sounder

The inherent problem in trying to survey the seabed with a single beam echo sounder is that only a set of readings along a narrow line will be produced. Unless the boat is run up and down a very narrowly spaced survey grid it could easily miss features. Thus the multi-beam echo sounder was developed which have several sounders arranged as a fan and cover a wide swath of seabed with each transmit ping (Figure 2).

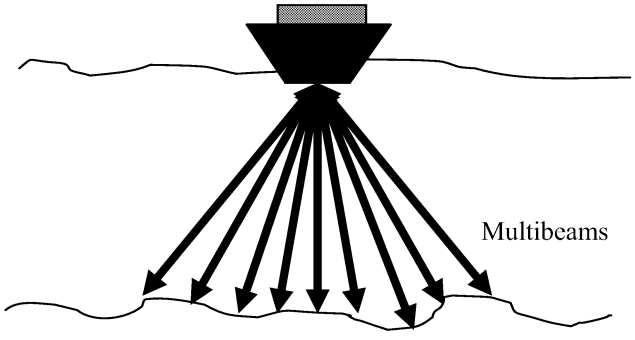

Figure 2: Multi Beam Echo Sounder

The fan of the beam is again narrow in the along track view, but spreads out either side of the vessel and is made up of lots of overlapping single beams. Thus for every transmission "ping" a large number of depth readings are obtained. There may be 90 or more narrow beams of about 1° wide giving a fan of 90° width. With this fixed fan shape, the deeper the water the wider the "swath" covered at the seabed. However the same number of beams to give a depth sounding is still the same. Therefore the number of soundings per metre of seabed reduces with depth. This obviously reduces the ability to decipher accurately what the seabed topography is and features could be missed. Also because the swath width changes with depth, the width of survey tracks have to be varied to cover all the area adequately.

As with single beam echo sounders all the acoustic problems remain, but are multiplied by the number of beams. Huge amounts of soundings are created over a short period of time and inevitably incorrect sounding will be taken due to acoustic problems. The outer beams, because of their steep angle, are more susceptible to errors.

During the 1960's, side scan sonars evolved and made it possible get large-scale images of the seabed. A side scan sonar builds up a two-dimensional picture of the seabed using a combination of an asymmetrical transducer and the motion of the sonar platform through the water (Figure 3). The transducer may be mounted on the keel of the ship or located in a towed body. A towed body will have the advantage of depth capability. Modern side scan sonar devices produce very high-resolution images of the seabed that can detect objects in the order of tens of centimeters.

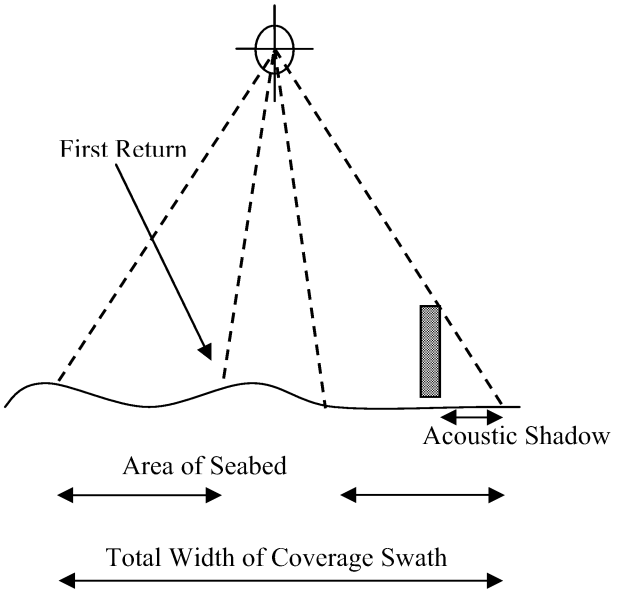

Figure 3: Side Scan Sonar

Side scan sonars are now a widely accepted and important tool of ocean technology. Broadly, they fall into one of two classes: the short-range high-resolution systems working at a relatively high frequency (e.g., about 100kHz), and the long-range low-resolution systems working at 10kHz or less. The former has a wide range of applications in surveying of oil wells, pipelines and shipwrecks, and in defense in mine hunting. The longer range systems such as GLORIA have contributed significantly to the study of the deep ocean floor.
Echo sounder and side scan sonar are very complementary but the fusion of both information is difficult because the side scan is mounted on a tow fish and the echo sounder on boat so the scene is observed from two different point of view with their own navigation and distortion. More over the two information to merge are different image and bathymetry (Sintes 2002).

THE SIMULATION PLATFORM

The main blocks of the sonar platform are shown in the Figure 4.

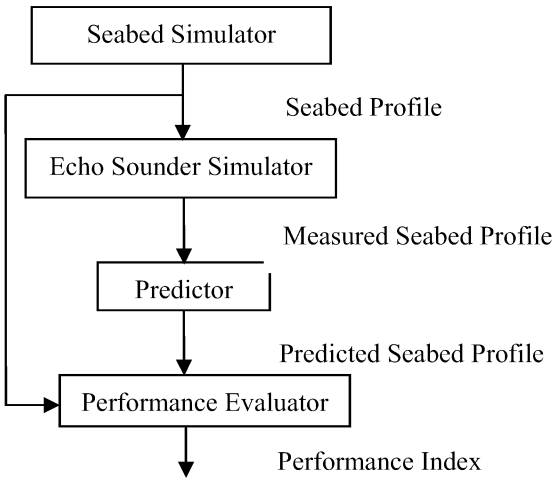

Figure 4: The Simulation Platform

The platform consists of two simulators, predictor and performance evaluator. The output of the seabed simulator is considered as the real values of the seabed profile which are fed to the echo sounder. The output of the echo sounder is considered the measured values (measured seabed). The predictor will process the measured values and find a one step ahead predicted value. The performance evaluator will compare the predicted value with the original real value and generate a performance index.

SEABED SIMULATION

A seabed simulator is essential to evaluate the performance of an echo sounder. The simulator should generate a suitable seabed profile. Seabed profile can vary from one area to another, and can be classified as follows:

- Muddy seabed: this sort of profile may have little variation with depth.
- Sandy seabed: which may appear wavy and have a near periodic structure.
- Rocky seabed: this has very rapid and abrupt changes.

Rocky profile has been chosen for this study.

The rocky irregular shaped seabed can be considered as consisting of two components. One, which represents the average depth, which is very slowly changing and can be considered as constant equal to the average value. The other component is the roughness, which can be modeled as follows:

1. A gaussian random generator whose mean value is zero and its standard deviation is proportional to the seabed roughness. The standard deviation value is determined after investigating and analysing the seabed area under study.
2. The output of the random generator is fed to a low pass filter that will reject some of the higher frequencies to get a more realistic seabed profile.
3. The third part is adding a constant offset value equal to the average depth of the seabed.

Figure 5 shows the main blocks, which constitute the seabed simulator.

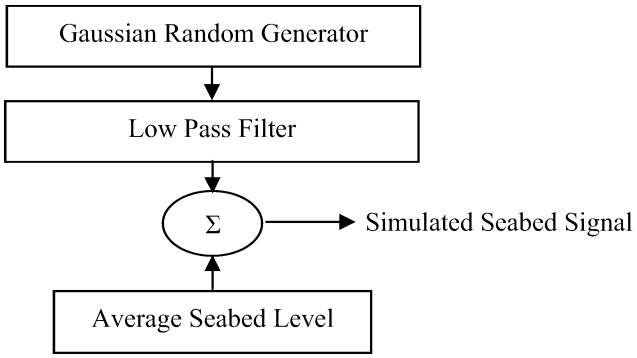

Figure 5: The Basic Blocks of The Seabed Simulator

The chosen low pass filter is a simple second order filter whose transfer function is:

$$H(Z) = 1/(1+ C_1Z^{-1}+ C_2Z^{-2})$$

Typical values which give reasonable seabed profile are C_1 = -1.72 and C_2 = 0.722. Those values are chosen to give stable filter output with acceptable characteristics. Other values can be chosen since the simulator lets the user set the proper values. The output of a seabed simulator for an average value depth of 100 units is shown in Figure 6.

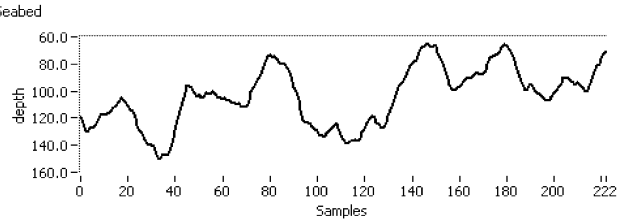

Figure 6: The Output of The Seabed Simulator

THE ECHO SOUNDER EQUATIONS

The echo sounder is a simple sonar system, which determines the elapsed (travel) time from sending the signal till receiving it back. By knowing the acoustic signal speed through water, the elapsed time can be converted to depth.

The signal sent by the echo sounder has the form of a beam of width θ, a circular area of radius Rad meters will be illuminated:

$$Rad = D \tan(\theta/2)$$

where: Rad radius of the illuminated area
D depth under the ship in meters

A signal transmitted from an echo sounder can be expressed as follows:

$$g(t) = p(t) \cos \omega_c$$

where: p(t) represents the pulse shape
ω_c carrier frequency

The received signal has the following form:

$$v(t) = p(t - 2R/C) \cos(\omega_c t - 2R/C)$$

where: R target distance
C sound velocity under water (1500 meter/sec)

The last equation could be expressed using the convolution notation:

$$v(t) = g(t)*\delta(t-2R/C)$$

In Figure 7, a signal measured by the echo sounder simulator is shown, which is reflected from the seabed shown in Figure 6. It shows the behaviour of the echo sounder which seems to be similar to a low pass filter.

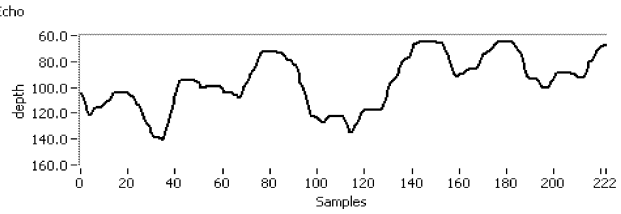

Figure 7: The Output of The Echo Sounder Simulator

SEABED PREDICTION

For the navigation and instruments design, the measurement of the seabed in advance is necessary. The measured seabed, in general, is smoother than that generated by the seabed simulator, and that is due to the beam width effect. Accordingly, the measured seabed can be considered as the sum of a fluctuating component and the average depth.

In our work, a predictor can be built to estimate the fluctuating component. In order to extract the fluctuating component, the average depth should be found which is the expected value of the measured seabed.

Let b(n) be the measured seabed, then the average seabed will be E[b(n)]. The fluctuation component y(n) will be:

$$y(n) = b(n) - E[b(n)]$$

The fluctuation component can be fed to the predictor and the output will be the estimated fluctuation component. Adding the estimated value to the average seabed, we get the estimated measured seabed value. The predictor is a linear one. It predicts the next value on the basis of the measured past values. The predicted value $y_p[n]$ can be made in terms of m of the weighted past measured values as shown below:

$$y_p[n] = a_1\ y[n-1] + a_2\ y[n-2] + \ldots + a_m\ y[n-m]$$

where: y_p predicted value
y actual measured values
m order of the predictor
a predictor coefficiets

Let e be the error between the predicted value $y_p[n]$ and the measured y[n].

$$e = y_p[n] - y[n]$$

Minimizing the mean square error, the optimal coefficients values can be obtained. The minmization is based on Levinson-Durbin recursion (Jackson 1989). This recursion is a fast algorithm for solving a system of symmetric Toeplitz linear equations. The predictor will calculate the coefficients of a FIR (Finite Impulse Response) filter that predicts the current value from the historical input data. The number of those coefficients is dependent on the predictor order. The coefficients are found by minimizing the predictor error in the least squares sense.

A snapshot of the front panel of the simulator system is shown in Figure 8.

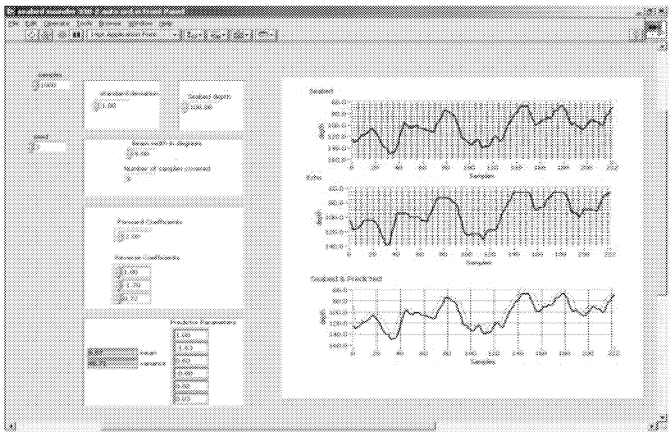

Figure 8: The Front Panel of the Sonar Simulator

The sonar simulator allows the user to experiment with different values of seabed profiles and orders of the predictor. One of the parameters displayed is the variance of the difference between the generated seabed profile values and the estimated values, which is considered as a performance index. The less value, the better prediction. The predictor coefficients are displayed as well, to allow the study of the trend of these values.

RESULTS

In order to evaluate the prediction algorithm, selected data were fed to the simulator. The standard deviation of the Gaussian random generator was 1 to generate a realistic rough seabed profile. The number of samples generated by the Gaussian generated could be set to any value. Feeding a seed value to the generator will let the generator start with a definite random signal pattern, this will allow using the same random pattern with different parameters. For example, the same pattern with different echo sounder beam width and depth. The two parameters, beam width and depth can be set. Increasing any of these two parameters will increase the illuminated area and in turn increasing the radius of the illuminated spot which is displayed on the front panel. The simulator can accept a range of values for the predictor order. The performance index (the variance) is plotted against the predictor order. The less performance index value indicates a better predictor quality (Jones 1982).
Figures 9 – 15 show the plots of the seabed, the predicted values and the performance index for different predictor orders. The solid line is the seabed while the dotted one for the predicted values. In Figures 9 – 12 beam width is incremented by 2° starting from 0.5°, while the depth is kept constant and equal to 100 distance units. In Figures 13 – 15, the same for the beam width while the depth is set to 150 distance units. It seems the prediction is getting worse while increasing both beam width and depth.

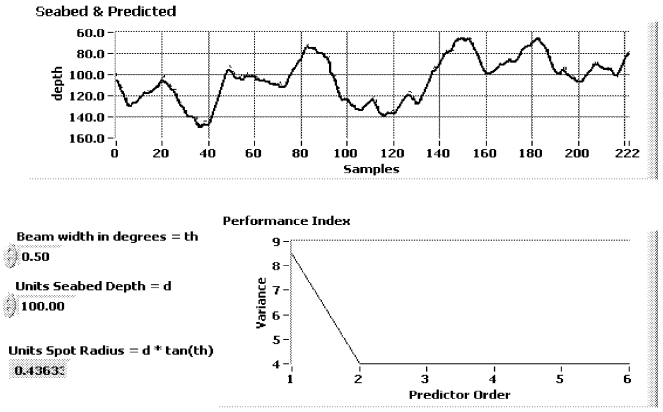

Figure 9: Beam Width = 0.5°, Depth = 100

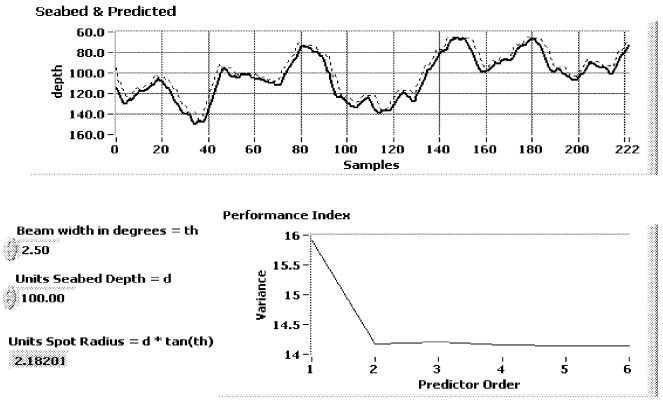

Figure 10: Beam Width = 2.5°, Depth = 100

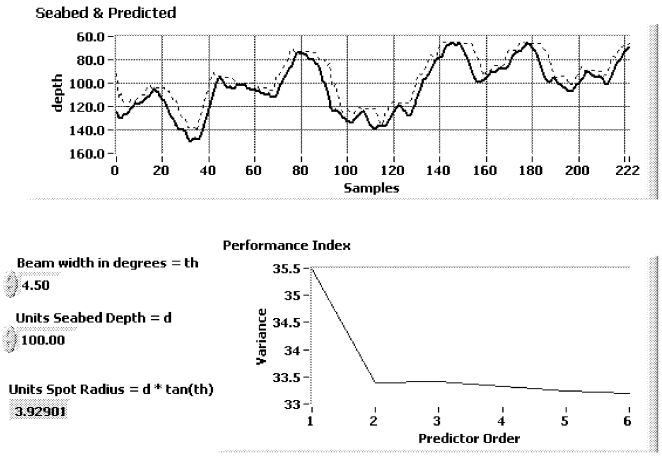

Figure11: Beam Width = 4.5°, Depth = 100

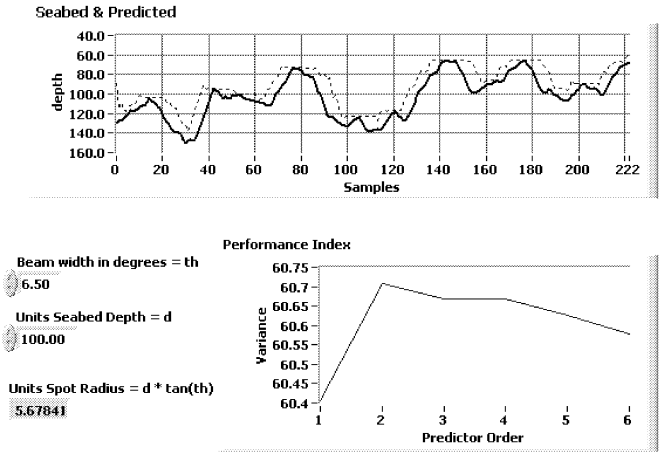

Figure 12: Beam Width = 6.5°, Depth = 100

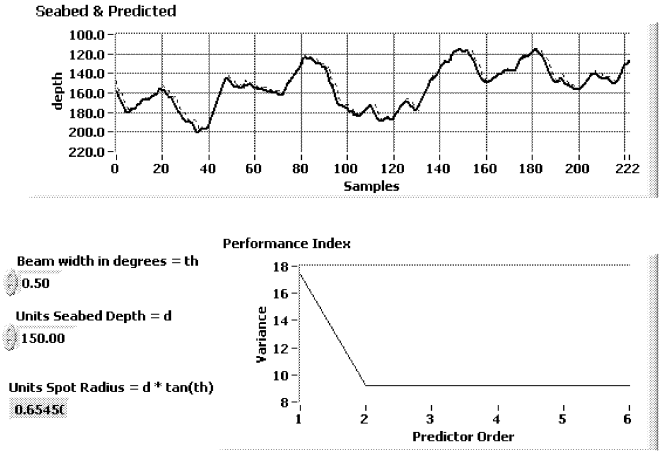

Figure 13: Beam Width = 0.5°, Depth = 150

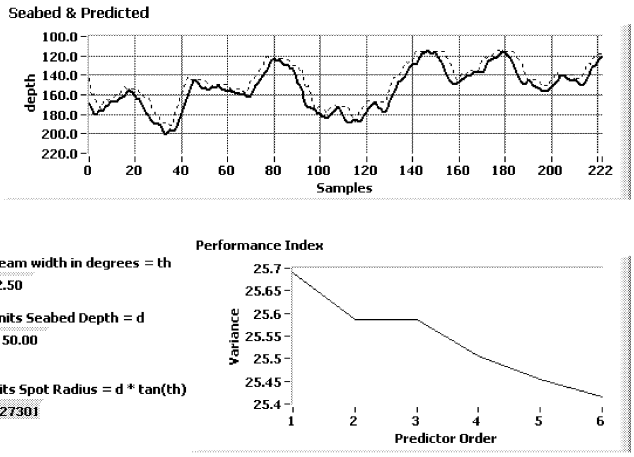

Figure 14: Beam Width = 2.5°, Depth = 150

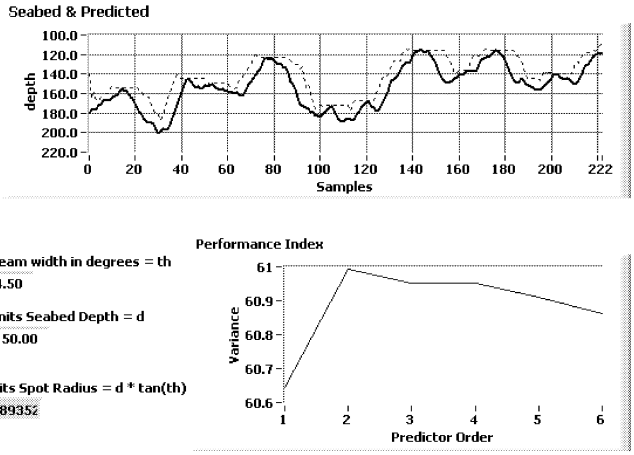

Figure 15: Beam Width = 4.5°, Depth = 150

CONCLUSIONS

A simulation model for testing seabed estimation algorithm was developed based on echo sounder. The model includes random seabed generator, echo sounder simulator, predictor and evaluator. Matlab and Labview software were used to develop the simulation model.

The model was tested for different beam widths and estimator orders. Results show that a second order predictor gives the best estimation (Performance Indicator). The predictor is no longer effective when the radius of the illuminated spot by the echo sounder exceeds three units. The research team intends to continue researching in this area and test other estimation algorithms.

REFERENCES

Jackson, L.B.: 'Digital Filters and Signal Processing'. Second Edition, Kluwer Academic Publishers, 1989. pp. 255-257.

Jones, N. B.: 'Digital Signal Processing'. Peter Peregrinus LTD., England, 1982

Sintes, C.: 'Interferometric Side Scan Sonar: A tool for High Resolution Sea Floor Exploration'. UDET Journées Acoustiques Brest 17 Juin, 2002.

Waite, A. D.: 'Sonar for Practicing Engineers'. Wiley, England, 2002, pp. 221-228

Simulation and Experimental Calculations of Short Circuit Current of In-Doped Silicon Solar Cells

Dr. Wagah F. Mohamad
Electrical Engineering Dept.,
Al-Isra private University
Amman-Jordan

Dr. Omar Radaideh
Electrical Engineering Dept.,
Mu'tah University,
Karak, Jordan.

ABSTRACT

Theoretical and practical calculations of short circuit currents of In-doped Silicon (n) structure have been calculated. Theoretically maximum value of generated current was 5.25 mA at $0.5x10^{17}$ cm^{-3} indium concentrations. Practically the ideal I-V characteristic of the structure is obtained with indium thickness of 1500 °A annealed at 1100 °C for an hour. This structure has a knee voltage at 0.8 V with very small value of reverse saturation current and 1.6 ideality factor. The maximum photogenerated current about 2.3 mA is obtained at $0.396x10^{17}$ cm^{-3} of indium concentration. Theoretical & practical results agree that the maximum photogenerated current occurs at zero cell output voltage.

INTRODUCTION

Silicon solar cells have different design and material requirements from most other silicon electronic devices. Not only ideal passivation of silicon surfaces is required, but the bulk properties must also be free defects and uniformly high quality for high energy conversion efficiency. This is because some wavelengths of light have to pass several microns through the silicon before absorption that producing carrier to be collected by the cell [1]. Improved techniques for crystal growth producing single crystal wafers of silicon used boron diffusion with the efficiency of about 6% led to the first report of modern silicon cell in 1954 by person, Fuller and Chapping of Bell labs [2]. M. J. Keevers [3] showed that the impurity photovoltaic effect (IPV) can indeed improve theoretical efficiency limits. In order to improve and extend the sub-band gap response, the indium should be added to an n-type layer of silicon cell. In fact indium acts as an electrical dopant responsible of changing the surface layer (10.2-0.5 um) of n-type wafer to a p-type, as well as the optical dopant [4].

THE NET RECOMBINATION (U)

In the standard SRH model [5], electrons and holes be captured by impurity level and thermally excited from it. The six impurities related transition included in the modified SRH model is shown in figure 1.

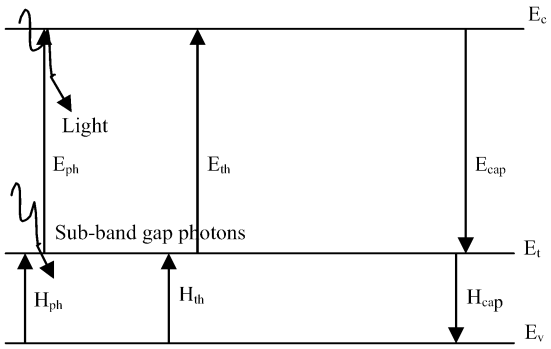

Fig. 1: Modified Shockley-Read-Hall (SRH) transition model.

Under steady state condition the impurity level occupancy does not change with time, so that the net rate for electron capture (E_{cap}) by the impurity is balanced by the net rate of hole capture (H_{cap}), the net recombination rate via an impurity level is found to be [6].

$$U = \frac{np - n_1^* p_1^*}{\tau_{no}\left[p + p_1^*\right] + \tau_{po}\left[n + n_1^*\right]} \qquad (1)$$

Where n and p are the electron and hole concentrations, τ_{no} and τ_{po} are SRH low injection lifetime for electrons and holes and they can be expressed as follow:

$$\left.\begin{aligned}\tau_{no} &= 1/C_n N_t \\ \tau_{po} &= 1/C_p N_t\end{aligned}\right\} \quad (2)$$

$$\left.\begin{aligned}n_1^* &= n_1 + \tau_{no} g_{n\,max} \\ p_1^* &= p_1 + \tau_{po} g_{p\,max}\end{aligned}\right\} \quad (3)$$

Where n_1 and p_1 are the impurity electron and hole concentration, N_t is the impurity concentration. C_n and C_p are the electron and hole capture coefficients; finally g_{namx} is the optical emission rate of electrons from the impurity level which is fully occupied, while g_{pmax} is the optical emission rate of holes from the impurity level which is completely empty. The basic idea of equation 1 is that for some impurities incorporated into a solar cell, the recombination rate (U) may be positive or negative. As far as SRH recombination mechanism is concerned, the impurity acts either to increase recombination (U is positive), in other words, decrease the carrier lifetime, consequently decreasing current generation, or to increase current generation in the cell (U is negative). In order to increase the current generation (makes U negative), this requires:

$$n_p - n_1^* p_1^* < 0 \quad (4)$$

So $n_1^* p_1^*$ must be as large as possible. Using equation 3, equation 4 can be written as:

$$np - (n_1 + \tau_{no} g_{n\,max})(p_1 + \tau_{po} g_{p\,max}) < 0 \quad (5) \qquad (5)$$

For midgap impurity levels $n_1 \cong p_1 \cong n_i$, therefore place a strong requirements on both photoemission terms in equation 5. A shallow impurity level gives rise to an asymmetry between n_1 and p_1. For the case here of shallow acceptor $p_1 >> n_1$ which means that only one of the photo excitation process is crucial for $\mathbf{n_1^* p_1^*}$ to be large i.e. τ_{no} $g_{n\,max}$.

Due to the large values of p_1 ($\cong 1.8 \times 10^{16}$ cm^{-3}) compared with small value of n_1 ($\cong 6.4 \times 10^3$ cm^{-3}) [7] for indium doped silicon structures, hole emission from the indium level is generally thermal and not optical. Here indium is considered as a shallow-level impurity which provides both reasonable access to the sub-band gap spectrum and depends only on one of the weak impurity optical processes. The smallness of n_1 indicates that the electron photoemission term g_{nmax} is crucial if the recombination rate to be negative thus;

$$n_1^* p_1^* \cong p_1 \tau_{no} g_{n\,max} \quad (6)$$

PHOTOGENERATED CURRENT SIMULATION

The photo generated current (J_{in}) in side the cell due to indium doping is given by [8]:

$$J_{in} = q \int_o^{xj} [-U(x)]dx \quad (7)$$

Where q is the electronic charge and x_j is the junction depth.

Substituting equation 1 in equation 7 yields:

$$J_{in} = q \int_o^{x_j} \frac{np - n_1^* p_1^*}{\tau_{no}(p + p_1^*) + \tau_{po}(n + p_1^*)} dx \quad (8)$$

Substituting τ_{no}, τ_{po}, n_1^* and p_1^* from equation 2 and 3 in equation 8 and knowing that:

$$n_1 = g_t N_c e^{-\frac{E_c - E_t}{KT}} \quad (9)$$

$$p_1 = \frac{1}{g_t} N_v e^{-\frac{E_t - E_v}{KT}}$$

Where g_t is the impurity level degeneracy, N_c and N_v are the effective density of states in the conduction and valance band respectively, E_c and E_v are the conduction and valance band edges, E_t is the effective impurity level, k is Boltzman constant and T the temperature in ^oK gives:

$$J_{in} = q\int_o^{x_j} \frac{np - \left[\left(g_t N_c e^{-\frac{E_c - E_t}{KT}} + \frac{g_{nmax}}{C_n N_t}\right)\left(\frac{N_v e^{-\frac{E_t - E_v}{KT}}}{g_t} + \frac{g_{pmax}}{C_p N_t}\right)\right]}{\frac{1}{C_n N_t}\left[p + \left(\frac{N_v e^{-\frac{E_t - E_v}{KT}}}{g_t} + \frac{g_{pmax}}{C_p N_t}\right)\right] + \frac{1}{C_p N_t}\left[n + \left(g_t N_c e^{-\frac{E_c - E_t}{KT}} + \frac{g_{nmax}}{C_n N_t}\right)\right]} dx \qquad (10)$$

Knowing the values of g_t, N_c, N_v, p, C_n, C_p and x_j = 0.3 μm, equation 10 can be solved numerically using the Mat lab program and the values of the photo generated current can be calculated. The photo generated currents depends on the photon flux density which is a function of spectrum wavelength, impurity concentration, depth inside the cell and the cell reflectivity.

Figure 2 shows the calculated short circuit current from the model as a function of indium concentration for two values of rear cell reflectivity (R_b). It is clear from the figure that the short circuit current is significantly generated when indium concentration was higher than 10^{14} cm^{-3} and less them 10^{18} cm^{-3}. The maximum current (5.75mA) is obtained at 0.5 $\times 10^{17}$ cm^{-3} of indium concentration which is completely compensate the background dopant of the wafer. When indium overcompensates the n-type dopant, then indium level is not fully occupied which reduces the photon flux available for the crucial electron process. Also it is obvious that we can make use of rear cell reflectivity to enhance the generated current.

Figure 3 shows the calculated photo generated current as a function of indium concentration with different cell output voltage. Usually the maximum generated current is occurs at zero cell output voltage. Increasing the cell voltage to a value of 0.7 V will result in a rapid decreasing of the photo generated current. As the cell operating voltage increase the carrier concentration increase (exponentially depends on applied voltage). Recombinations in the cell therefore, increase in the same manner, until eventually the recombination current dominates the cell.

ELECTRICAL & SPECTRAL RESPONSE OF LAB. PREPARED SAMPLES

Few samples of In-doped Si (p)/Si (n) structures were prepared. A thin layer of indium was deposited on the top of an n-type single crystal silicon wafer, using thermal vacuum deposited technique. In order to form a pn junction the indium must

be diffused into the silicon wafer for depth between 0.2-0.5 μm by annealing. The wafer is placed inside an evacuated silicon quartz tube and heated up to the required temperature (450 – 1100 ^{o}C) for an hour. For more details about the samples (S) preparation and fabrication see reference [9]. The effect of different annealing temperatures on the dark I-V characteristics is shown in figure 4. S1 and S2 seem to have comparable forward and reverse characteristics. The difference between S1 and S2 in one hand and S3 in the other hand is that the reverse dark current is much smaller in S3 than that in the others. It is concluded that the annealing temperature of S1 and S2 is not enough to form the required pn junction at the right depth with good ideality factor. The junction depth is expected to be very shallow for the previous two samples, while in S3 it is thought that indium is diffused deeply into the silicon wafer, but the forward and reverse I-V characteristics of S3 seems to be the same and the ideality factor still high.

To have a better idea about the junction formation, I-V characteristics of other samples with difference indium thickness (different concentrations) at high annealing temperature (1100 ^{o}C) are shown in figure 5. S6 (500 ^{o}A indium thickness) given high leakage current, since the depletion region is narrow (low carrier concentration) and junction depth is still very small (shallow). It is clear from S3 (2000 ^{o}A indium thickness) that the indium is diffused deeply into the silicon wafer, which prevents the junction formation under these conditions. Therefore the I-V characteristics more or less are a resistive one (Same characteristics in the forward and reverse bias). S4 and S5 (1000 ^{o}A and 1500 ^{o}A indium thickness, respectively) have a knee voltage a round 0.85 V and very small reverse current which starts to build up at –4 Volt of reverse voltage. S4 gives an optimum characteristic and will be used in the following discussion. The ideality factor around 1.6, which indicates a reduction in the recombination process inside the structure

C-V characteristics of the different samples (S3, S4, S5 and S6) are measured and the values of indium concentrations, ideality factors, and short circuit currents of the samples are calculated and tabulated in table 1.

Table 1. The calculated parameters of the prepared samples annealed at 1100 ^{o}C and under AM 1.5 illumination and 300 ^{o}C.

Sample No.	Indium thickness (^{o}A)	Barrier Voltage (V)	Ideality Factor	Indium Concen. (cm^{-3})	I_{SC} (mA/cm^{2})
S3	2000	0.85	2.5	1.37x10	0.5
S4	1500	0.75	1.6	3.96x10	2.3
S5	1000	0.62	1.92	2.65x10	0.6
S6	500	0.35	3.2	5.36x10	0.1

Figure 6 shows the variation of the short circuit currents of the prepared samples (S3, S4, S5, and S6) versus the incident light wavelength for different indium thickness. It is clear that S4 produce a maximum short circuit current at 0.9 μm wavelength. This means that an optimum junction depth is formed so that the electron-hole pairs are almost collected inside the junction yielding a maximum current generation. Indium concentration for S4 was calculated from C-V characteristics to be equal to 3.96×10^{16} cm^{-3} and it seems to compensate all the background n-type dopant which is equal to 2×10^{16} cm^{-3}.

Looking back at figure 6 it is obvious that there is no photo response of these

samples at wavelength less than 0.45 μm. This is a thought to be the formation of surface layer which acts as a filter for the generation and recombination phenomena to take place at the layer. The current starts increasing at $\lambda > 0.5$ μm and the maximum current obtained at $\lambda = 0.9$ μm. As λ increases about 0.9 μm the current starts decreasing gradually and still have a significant value of 34% at $\lambda = 1.1$ μm. At this range of wavelength most of the photo generated currents is due to the sub-band gap absorption mechanism (IPV effect) which extend the sample photo response to near infrared (1.1 μm) or more [10].

The photon energies absorbed by emitter and base regions of the pn junction varies with junction depth. Since at low photon energies, most of the cattier are generated in the base because of the low absorption coefficients. But as the photon energy increases, the diffused side of the junction takes place [11]. The effect of the junction depth and indium concentration on the short circuit current is shown in figure 7. When the junction depth is shallow the probability of collecting the carriers generated at the top (near the surface) decreases which in turn causes the photocurrent to decrease. Also a very shallow junction will be produced at low indium concentration (N_t) consequently small current will be generated. This result agreed with that obtained from the simulation. At lower values of N_t, the generation factor (g_{nmax}) will be small giving a small product of $n_1^* p_1^*$ (See equations 2 & 3) which gives positive recombination.

In the other hand increasing the junction depth, decreases the sheet resistance of the diffused layer (12), thus enabling the use of larger grid line spacing, and utilizing relatively of the light flux. This causes the current collection efficiency to be increased.

Also as the indium concentration increased to a large value > 10^{17} cm^{-3} the junction is deeply diffused and he carrier lifetime will be decreased, consequently small photo generated current is collected at very high concentration. Comparing the practical results with the simulation results shows similarity. Large indium concentration will result in a lower value of carrier lifetime (equation 2**)**. So at lower value of carrier lifetime the recombination will be positive and the recombination current will dominant.

CONCLUSIONS

On the basis of experimental results obtained and compared with the computer simulation results of In-doped Si(p)/Si(n) structure, it can be concluded that; a significant photo generated current is only obtained when indium is at least close to compensating the front n-type dopant. In fact indium acts as an electrical dopant responsible of changing the surface layer of n-type wafer to a p-type as well as the optical dopant. A maximum photo generated current occur at zero applied voltage, photo generation is dominant. Increasing the applied voltage will result in rapid decreasing of the photo generated current. This is due to the exponential increase of the carrier concentration, until eventually current dominants the cell.The current collection efficiency will be increased if the junction depth of mid distance. Shallow junction will form a dead layer that reduces that carrier collection. While a very deep junction reduces the relative lifetime consequently the recombination rate will be positive and the recombination current will dominant.

REFERENCES

1. M. A. Green, “Silicon Solar Cells: Advanced principles and practice”, Center to Photovoltaic Devices & Systems, Sydney, (1995).
2. D. M. Chapin, C. S. Fuller and G. E. Fuller J. Appl. Phys. 25, PP. 676 (1954).
3. M. J. Keevers and M. A. Green "Efficiency Improvements of Silicon Solar Cells by the Impurity Photovoltaic Effect" J. Appl. Phys. 75, PP. 80 (1995).
4. M. J. Keevers and M. A. Green, "Extended Infrared Response of Silicon Solar Cells and the Impurity Photovoltaic Effect", First ECPEC, Hawaii, PP. 1433, (1994).
5. W. Shockly and H. J. Queissey, "Detailed Balance Limit of Efficiency of pn Junction Solar Cells", J. App. Phys. 33, PP. 510 (1961).
6. W. Shockly and W. T. read, JR, "Statistics of the Recombination of Holes and Electrons", Bell Tel. Lab., Murray Hill, New Jersey, (1952).
7. M. A. Green and M. J. Keevers, "Optical Properties of Intrinsic Silicon at 300 ^{o}K", Process in Photovoltaic Research & Applications, Vol. 3, PP. 189, (1995). J. J. Loferski, "Photovoltaic Advanced Material" IEEE Spectrum, February (1980).
8. Y. M. Aboush, "Theoretical Investigation of the Efficiency of Silicon Solar Cell", M. Sc. Thesis Mosul University, (1985).
9. K. Khalell, "Fabrication and Characterization of In-doped Silicon Solar Cells", Ph. D. Thesis, Mosul University (2000).
10. W. F. Mohamad, and Kh. Khalell, "Infrared Response and Quantum Efficiency of In-doped Silicon (n) Structure", Renewable Energy Journal, V. 3-4, PP. 1, (2000).
11. S. Wenham et al., "Limits to the Efficiency of Silicon Multilayer Thin Film Solar Cells", First WCPEC; Hawaii, PP. 1430 (1994).
12. W. F. Mohamad & M. A. Shahatha, "The Effect of the Series Resistance on the Photovoltaic Properties of In-doped CdTe (P) Thin Film Homojunction Structured", Renewable Energy Journal, Vol. 21, P. 141, (2001).

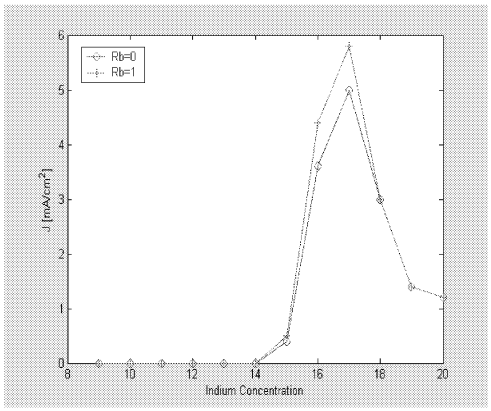

Fig.2: Simulated short circuit current versus indium concentration for two values of reflectivity.

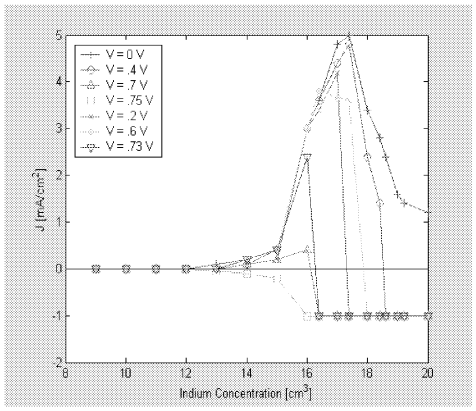

Fig. 3: Simulated generated current versus indium concentration with different cell output voltages.

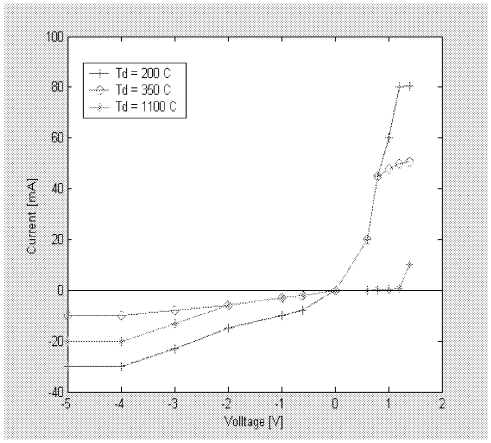

Fig. 4: I-V characteristics of the samples of 2000 °A indium thickness with different annealing temperatures.

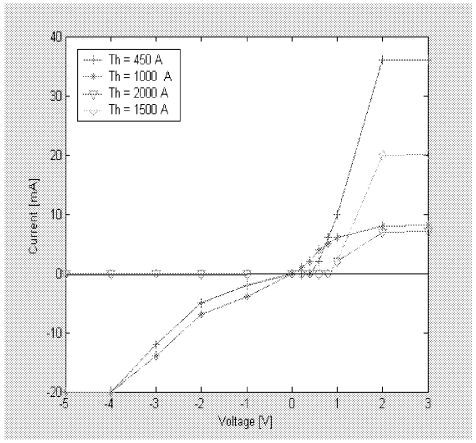

Fig. 5: I-V characteristics of the samples at constant annealing temperature and different indium thickness.

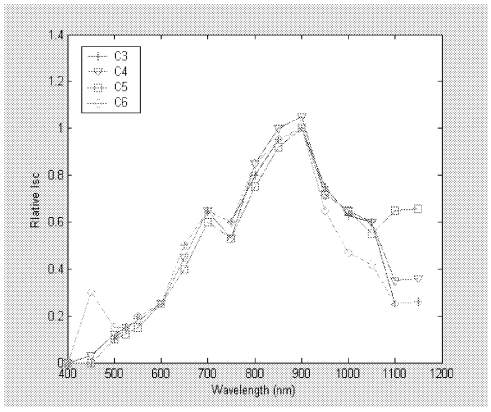

Fig. 6: Relative current VS incident light Wavelength for the fabricated cells C3, C4, C5, C6 at P=10E-2 mbar.

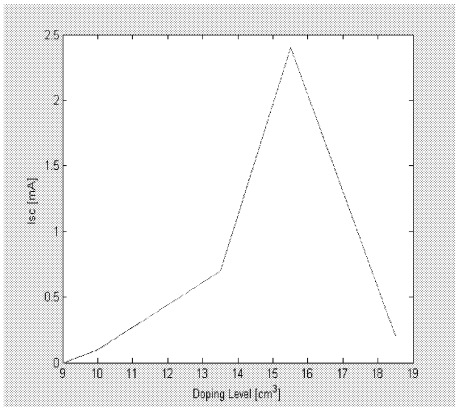

Fig. 7: The short circuit current Versus indium concentration characteristics

FAST ENERGY LOSS COMPUTATION AND FUZZY-BASED SHUNT CAPACITOR INSERTION

Dr. W. F. Mohammad, Dr. N. Tawalbeh

Electrical Engineering Dept.
Al-Isra Private University, Jordan
wagah_aljubori@yahoo.com
nabiltawalbeh@yahoo.conm

Dr. K. M. Al-Aubidy

Computer Engineering Dept.
Philadelphia University ,Jordan
kma@philadelphia.edu.jo

ABSTRACT

Fast energy loss computation is implemented using supervisory control and data acquisition system (SCADA) with personal computer. Logic Control Array (LCA) and EPROM circuits are used to implement SCADA system and to facilitate the measurement of the active and reactive power, then plot the daily load curve for residential and commercial customers. LCA, EPROM and PC are used to simplify the electronic circuits, reduce the cost and speed up the computation time.
An illustrative example had been considered to measure, store and show the active power, reactive power, load voltage, load current, power factor, and the shunt capacitors current. It is found that when 2.7 MVAR bank capacitor is inserted in the network the load current is decreased from 740.8A to 688.4A and the power factor improved from 0.80 up to 0.93 and led to add more loads on the network and release the feeder capacitor.
A rule-based fuzzy decision maker has been designed and tested with the real data collected from Jordan using SCADA system. The calculated output is almost similar to that obtained from the first approach presented in this paper. The advantage of using fuzzy decision maker is its simplicity that can be implemented on a programmable logic device and can be programmed to improve the power factor.

KEYWORDS
Energy loss computation, Power factor improvement, Intelligent systems, Fuzzy logic, Fuzzy decision maker, Rule-based system.

INTRODUCTION

Capacitors are widely used in distribution system to achieve power and energy loss reduction, and to maintain the voltage profile with impermissible limits and to minimize the voltage flicker in power distribution networks. The extent of these benefits depends on the location, size, type, and number of capacitors and the fast method of capacitor insertion [Granger and Lee 1981, Eawzi et al. 1983, Ponnavaikko and Prakasa 1983]. The power factor depends on the electrical loads type; it is usually that the current lagging voltage and the angle of lagging are varied as the load varied and the daily time elapse. Increasing the lagging will cause more energy loss in the distribution network. This problem has been treated by inserting shunt capacitors in the distribution network which is essentially reduces the current flow.

If the daily energy losses are evaluated the different load patterns of daily local current (DLC) of different customers should be taken into account. The customers are divided into three groups: Urban residential, commercial and industrial. Each type of load has its typical DLC set for twenty four hours at working days. The fast method of total energy loss calculation can be manipulated using supervisory control and data acquisition system (SCADA), with personal computer [Kaplan 1984, Batur and Guven 1994]. Data acquisition operation includes measurements of voltages, load currents, power factors and power capacitor currents, also estimate power and reactive power for main transformer. An electronic circuit based on Logic Control Array (LCA) has been designed and build to do all the measurements and insert the required shunt capacitors at the right time and allocation.

To find the optimal solution of the above formulated complicated combinational problem, the fuzzy logic is used which imitates the process of natural evolution. This optimization tool proved to be very successful for capacitors evaluation and insertion [Raid 2002, Kuo and Hso 1993, Nazarko and Zalewski 1999]. A special feature of the fuzzy set approach is capable of dealing with uncertain and linguistic terms such as “heavy load” to describe system loading condition. It is also suitable as a decision maker.

POWER FACTOR CORRECTION

As mentioned earlier, the fundamental function of shunt capacitors to regulate the voltage and reactive power flows at the point where they are inserted, in other words they are changing the power factor of load. In typical distribution loads, the current lags the voltage; the cosine of the angle between current and voltage is known as the power factor of the circuit. Figure 1 illustrates the power factor correction for a given system. Capacitors draw leading reactive power from the source; i.e. they supply lagging reactive power to the load:

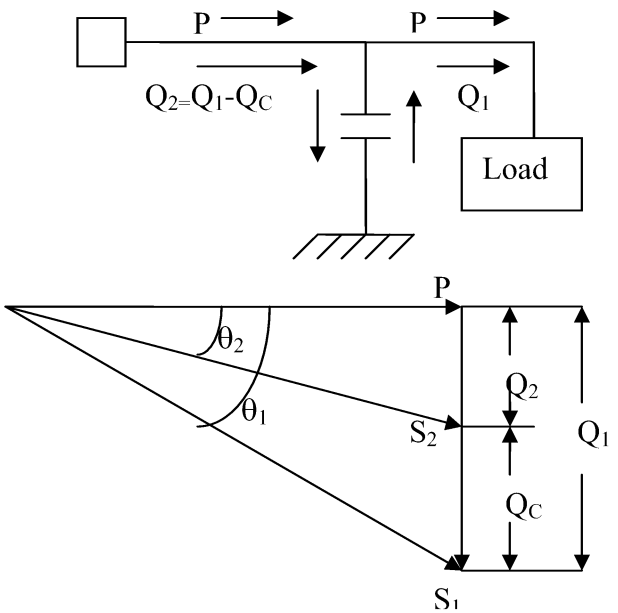

Figure 1: Illustration of power factor correction

Assume that a load is supplied with a real power P, lagging reactive power Q_1, and apparent power S_1 at a lagging power factor of:

$$Cos\theta_1 = \frac{P}{S_1} = \frac{P}{\left[P^2 + Q_1{}^2\right]^{1/2}} \quad \text{.....(1)}$$

When a shunt capacitor of Q_c KVA is installed, the power factor can be improved from $Cos\theta_1$ to $Cos\theta_2$ when:

$$Cos\theta_2 = \frac{P}{S_2} = \frac{P}{\left[P^2 + (Q_1 - Q_C)^2\right]^{1/2}} \quad \text{.....(2)}$$

Therefore, as can be observed from the above figure, the apparent power and the reactive power are decreased from S_1 KVA to S_2 KVA and from Q_1 KVAR to Q_2 KVAR (by providing a reactive power of Q_c) respectively.

The economic power factor is the point at which the economic benefits of adding shunt capacitors just equals the cost of capacitors. Today's high plant and fuel costs have pushed the economic power factor toward unity. Here you need to be careful that as a lagging system power factor is detrimental to the system on various counts, a leading system power factor is also undesirable. It tends to result in overvoltages, higher losses and lesser capacity utilization. For the above reasons fast energy loss computation and efficient method of inserting and removing the shunt capacitors must be implemented.

Many power-factor-correction tables can be tabulated [Levitin et al. 2000] using personal computers to simplify the calculations involved in determining the capacitor size necessary to improve the power factor of a given load from original to desired value. The capacitor size (Q_c in KVAR) is:

$$Q_C = P_L \text{ (Correction factor) } \text{..... (3)}$$

where P_L is the real power load. A load flow digital computer program (will be discussed and explained later) can be employed to determine the KVolt-Ampere, KVolt and KVAR at annual peak level for the distribution substation. As a result of local flows program runs, the system's lagging reactive loads (i.e. power demands) can be determined and the results can be plotted on curve as shown in figure 2. This curve is called the reactive load duration curve, once the daily reactive load duration curve is obtained, then by visual inspection of the curve the size of the fixed capacitor can be determined to meet the minimum reactive load, the high and variable remaining demands of the loads are met by the switched capacitors.

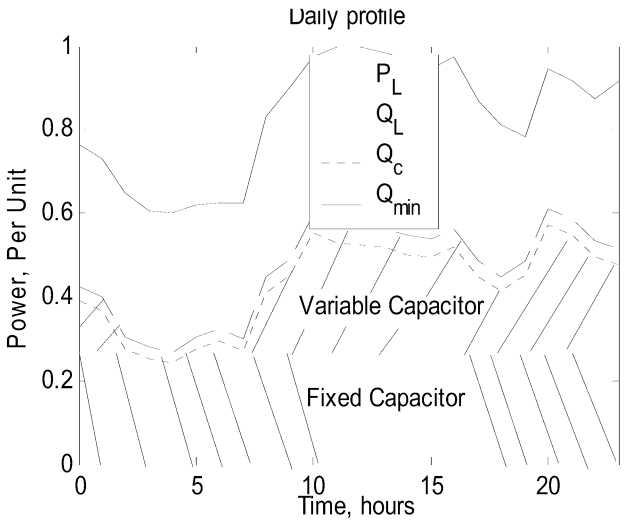

Figure 2: Sizing of the fixed and switched capacitors

To meet the daily reactive power and switched capacitors many utilities apply the rule of thumb to determine the size of the switched capacitor. In this research a very fast computation system based on SCADA system is used to find the reactive load duration curve for residential, commercial and industrial customers at weekdays. Then a fuzzy logic is used to determine the size of switched capacitors.

Power Factor Measurement Using SCADA System

Supervisory control and data acquisition (SCADA) system could be considered as one of the most recent technologies used on data collection and control for distribution power system. Figure 3 shows the block diagram of data acquisition system to measure the kilovolt-amperes, kilovolts and kilovars at daily reactive load curve. Logic control Array (LCA) is used to control the input and output circuit of the

personal computer (PC). For more details see reference [Gonen 1986]. LCA type XC3030 is used to reduce the electronic circuits, the cost and speed up the measurements operation. LCA (XC3030) consists of more than 100 configurable logic blocks and can capacitate more than 22 kilobyte, and it is connected to 27C64 EPROM that capacity of 8 Kbytes which store the data, perform and allocate the logic circuits inside LCA. This operation called LCA programming used the ready software supplied with the device.

The final circuits which consist of set of power transistors (BC337-40) are controlled by the LCA output signal to drive the relays which insert or disconnect the shunt capacitors.

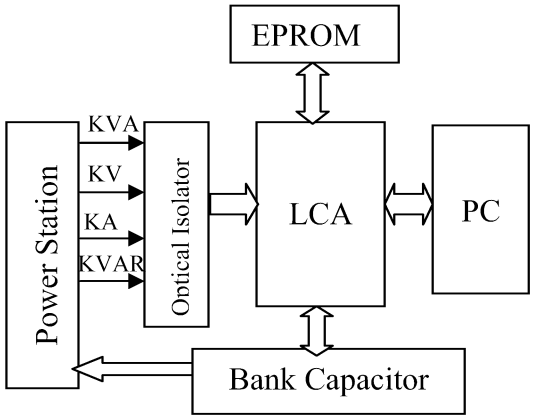

Figure 3: block diagram of data acquisition system.

As start, shunt capacitors are applied to each substation bus for correcting to an initial power factor, for example, 90 percent. Then, a load flow run is performed to determine the total system Kilovolt-amperes, and kilowatt losses at this level and capacitors kilovars are noted. Later additional capacitors are applied to substation bus under test to increase the power factor by 1 percent, and another load flow run is made. This process of iteration is repeated until the power factor becomes unity. The additional capacitor size required can be calculated as:

$$\Delta Q_C = P_{PK}\,(\tan\phi - \tan\theta) \quad \text{.....(4)}$$

Where $\Delta\ Q_C$ is the required capacitor size in KVAR P_{PK} is the system demand at annual peak in KW, tanϕ is the tangent of original power factor angle and tan θ is the required power factor angle.

Illustrative Example:

To verify the proposed method of shunt capacitor insertion the measurements of daily peak load P_{dp} at single feeder fed by 33 / 11KV, 16 MVA substation transformers were made from August to July. The program has the ability to measure, store and show the active power, reactive power, load voltage, load current, power factor, and the shunt capacitor current, every ten seconds [Al-Abdaly 2003]. For this reason capacitor can be inserted in the power network in no time, and the power loss can be reduced to minimum.

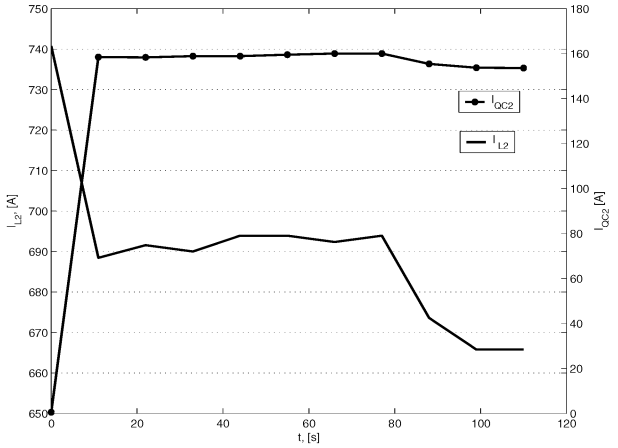

Figure 4: Variation of I_L and I_{QC} with time before and after capacitor insertion.

Figure 4 represents variation of load current (I_L) and shunt capacitor current (I_{QC}) after 10 second when a bank capacitor of 2.7 MVAR inserted in the network.. If you inspect the figure carefully, you can noticed that at time=0, I_{QC}=0A and I_L= 740.8A. When the bank capacitor of 2.7 MVAR is inserted at time t=10 seconds the currents IQ_C = 158.47A and I_L = 688.44A. It is very interesting to notice that when shunt capacitors are inserted in the network will draw a lead current from the (substation) transformer and supply a lagging current to the load. The load current will decrease consequently; the total substation transformer current will be decreased. The power factor is improved from 80% up to 93.6%, and this leads to add more loads on the network and release the feeder capacity.

Figure 5 represents the daily peak loads for different customers (residential, commercial, and industrial) for working days. The measurements were taken at substation transformer of 132/33 KV, 40 MVA power, during April-June. It is very interesting to notice that there is a lot of differences between the customers. In residential the fixed reactive power is around 37% of the maximum reactive power and it occurs around seven o'clock at the morning. On the other hand there is no fixed reactive power for the commercial and becomes minimum for long time of the day namely between 00:00 and eight o'clock at the morning and it is maximum on the other times of the day.

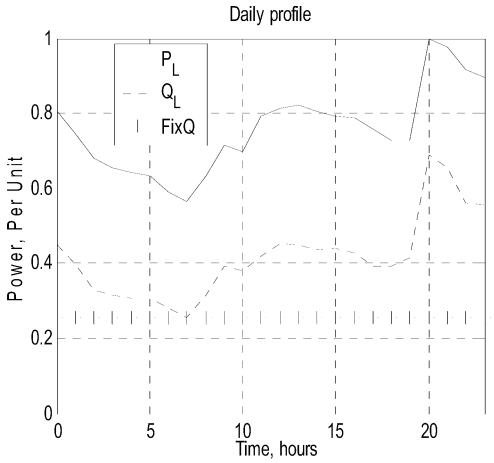

(a) Residential.

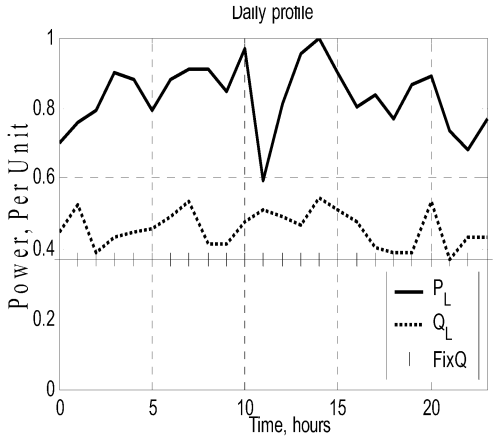

(b) Commercial.

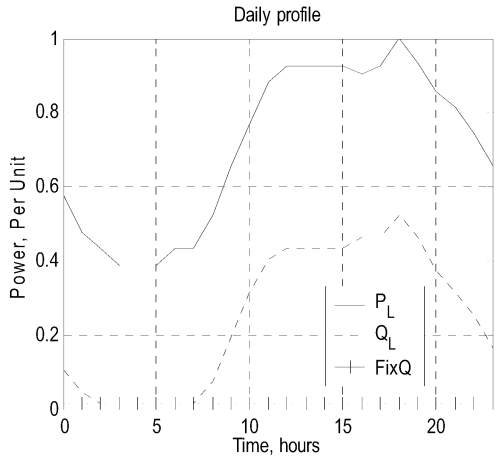

(c) Industrial.

Figure 5: Active and reactive power of the transformer for twenty four hours for different customers; (a) Residential, (b) Commercial, (c) Industrial

The story from the industrial daily load profile is quite different. At first the constant reactive power is quite high around 67% of the maximum reactive power. Also the variable reactive power is quite changeable. These changeable events occur during all the hours' day and nights. From the above inspection, it is understandable that different feeders must be used for different type of customers in order to insert the right values of the shunt capacitors in the networks, rather than putting identical units of bank capacitors at all networks, which will be never used sometime or could be more than what is needed and that will the power factor leading , which result in over-voltages and higher losses.

FUZZY-BASED DECISION MAKER

One year after the electronic circuit designed and used for test in last section and the draft of this paper was under preparation, some researcher on fuzzy logic suggested to add a section here applying fuzzy regression of shunt capacitor insertion to improve the power factor. The answer was going on because that will simplify the electronic circuits, reducing its cost with very simple software. It is also found that the fuzzy regression do all the uncertainty measurements and replaces all the huge measurements that must be included to draw the daily load curves for different customers and identify the approximate values of shunt capacitors.

A fuzzy-based decision maker (FDM) has been proposed to compute the required shunt capacitor to improve the power factor according to the measured power factor (A) and measured active power (B), as shown in Fig.(6).

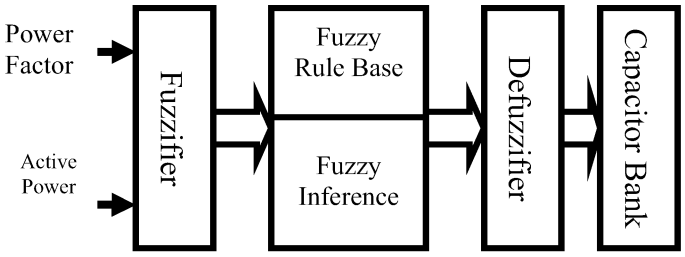

Figure 6: Fuzzy Decision Maker Layout.

The measured variables are inverted into suitable linguistic variables. In this application, the following linguistic variables are used for measured power factor (A) and calculated variable (C); Very Small (VS), Small (Sb), Medium (M), Large (L), and Very Large (VL). The fuzzy sets definition for measured active power (B) are; Very Small (VS), Small (S), Rather Small (RS), Medium (M), Rather Large (RL), Large (L), and Very Large (VL). Figure (7) shows the universe of discourse and fuzzy sets of these variables. Fuzzy sets can have a variety of shapes. However, a triangular or a trapezoid can often provide an adequate representation of the knowledge.

The proposed fuzzy decision maker is a collection of linguistic rules which describe the relationships between measured variables (A & B), and calculated output (C). Table (1) contains 35 rules, since we have five fuzzy sets for first input variable, and seven fuzzy sets for the second input variable. Each rule is represented by IF and THEN statement such as;

IF A is S and B is RS THEN C is M

This means that if the measured power factor is Small and the active power is Rather Small, then the fuzzy calculated output is Medium.

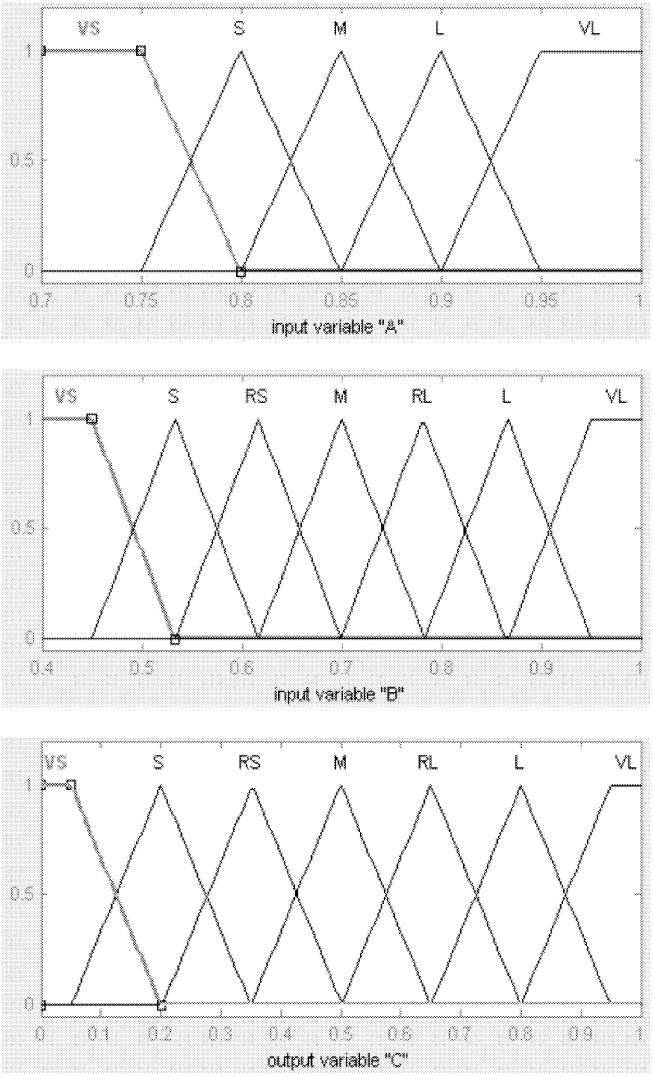

Figure 7: Universe of discourse of the variables.

The Mamdani-style inference process is used [Negnevitsky 2005], and the center of gravity defuzzification method is applied to convert the fuzzy output into a crisp value, Fig.(9), which is used as an index to select the suitable shunt capacitor.

Table 1: Fuzzy Rules.

A / B	VS	S	M	L	VL
VS	S	S	S	VS	VS
S	M	S	S	S	VS
RS	M	M	S	S	VS
M	L	M	M	S	VS
RL	L	M	M	S	VS
L	L	L	M	S	S
VL	VL	L	M	M	S

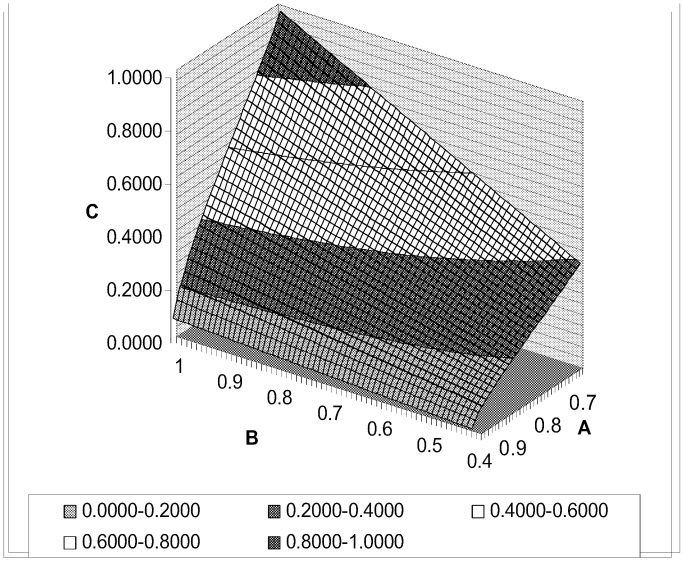

Figure 9: Control Action calculated from FDM.

CONCLUSIONS

Fast energy loss computation has been implemented using data acquisition system. Logic control array has been used to control the input and output interface of the personal computer. The electronic circuit has the ability to measure, store and monitor the active power, reactive power, load voltage, load current, power factor, and the shunt capacitor currents. The daily peak loads for residential, commercial and industrial customers has been measured and drawn. Several differences between customers were outlined, where fixed capacitor is minimum for commercial, medium for residential and maximum for industrial customers. On the other hand, the switched capacitor is minimum for industrial, medium for residential and maximum for commercial customers. Therefore, to find the optimal solution of the above complicated combinational problem, a fuzzy-based decision maker has been used to compute the suitable shunt capacitor required to improve the power factor according to the measured parameters.

The proposed fuzzy decision maker has been tested with the real data collected from Jordan, and the calculated output is almost similar to that obtained from the first approach presented in this paper. The advantage of using fuzzy decision maker is its simplicity that can be implemented on a programmable logic device and can be programmed to improve the power factor.

REFERENCES

Al-Abdaly I.S.H. 2003. "Computerized Method for Capacitor Banks Insertion to Improve Power Factor in the Distribution Substation", *M.Sc. Thesis, Mousel university, Iraq.*

Batur I. and A.N Guven. 1994. " A Proposed Application of an Industrial DOS Computer for Distribution Substation Monitoring and Central", *IEEE Trans. On Power Delivery, Vol. 9, no.2, April, PP. 729-735.*

Fawzi T.H.; S.M. El-Sobki, and M.A. Abdel-Halim. 1983. "New Approach for the Application of Shunt Capacitors to the Primary Distribution Feeders", *IEEE Trans . Power Appra. Syst. , Vol. PAS-102, no.1, PP. 10-13.*

Gonen T. 1986. "Electric Power Distribution System Engineering", *Section: Application of Capacitors Distribution systems, PP. 385-398, McGraw-Hill Inc.*

Granger I.S. and S.H. Lee. 1981. "Optimum Size and Location of Shunt Capacitors for Reduction of Losses on Distribution Feeders" *IEEE Trans. Power Appar. Syst. Vol. PAS-100, no.3, PP. 1105-1118.*

Kaplan M. 1984. "Optimization of Number, Location, Size, Central Type, and Central Settings of Shunt Capacitors on radial Distribution Feeders", *Trans . Power Appra. Syst. , Vol. PAS-103, no.9, PP. 2659-2665.*

Kuo H.C. and Y.Y Hso. 1993. "Distribution System Load Estimation and Service Restoration Using A Fuzzy Set Approach", *IEEE Trans. On Power Delivery, Vol.8, no. 4, October, PP. 1950-1957.*

Levitin G.; A. Kalyuzhny; A. Shenkman, and M. Cherktov. 2000. "Optimal Capacitor Allocation in Distribution Systems Using a Genetic Algorithm and Fast Energy Loss Computation Techniques", *IEEE Trans. On Power Delivery, Vol.15, no. 2, April.*

Nazarko J. and W. Zalewski. 1999. "The Fuzzy Regression Approach to Peak Load Estimation in Power Distribution System", *IEEE Trans. On Power Systems, Vol.4, no. 3, Aug.*

Negnevitsky M. 2005. "Artificial Intelligence; A Guide to Intelligent Systems", *Addison Wesley, USA.*

Ponnavaikko M. and K.S. Prakasa Rao. 1983. "Optimal Choice of fixed and Switched Shunt Caoacitors on Radial Distributers by the Method of Local Variations", *IEEE Trans. Power Appra. Syst. , Vol. PAS-102, no.6, PP. 1607-1615.*

Raid M.C.F. 2002. "Study and Improvement of Supervisory Control and Data Acquisition System in Distribution Station", *M.Sc. Thesis, Mousel University, Iraq.*

ELECTRONICS SIMULATION IN MEDICINE

A SCALABLE AUTHENTICATION SCHEME OF THE STORED AND TRANSMITTED MEDICAL IMAGES

Atef MASMOUDI and Mohamed Salim BOUHLEL
Research Unit: Sciences and Technologies of Image and Telecommunications
Higher Institute of Biotechnology, Sfax TUNISIA
mas_atef@yahoo.fr medsalim.bouhlel@enis.rnu.tn

Keywords
Medical imaging, JPEG2000, encryption, authentication, data integrity.

Abstract

This paper presents a new approach for ensuring authenticity and data integrity of the stored and transmitted medical images. The proposed scheme allows users to verify authenticity and data integrity of a specific resolution or quality of an image which is protected with digital signatures. We prove that the proposed scheme is fully compatible with the core part of JPEG2000 standard, very efficient and highly scalable.

1. INTRODUCTION

JPEG2000 is the latest international standard for still image compression [01-05]. JPEG2000 is developed jointly by the *International Organization for Standardization* (ISO), and the *International Electrotechnical Commission* (IEC) and also recommended by *International Telecommunications Union* (ITU).

The aim of the JPEG2000 is to develop a new algorithm for digital image compression that can be used for many applications like Internet, digital archives, e-commerce, client-server networking, satellite imagery, remote browsing, mobile multimedia communication, medical imaging, etc. Each application imposes some requirements that JPEG2000 should fulfil. Thus, the new standard should provide a set of functionalities [03].

Some of these functionalities are the following:
• Continuous-tone and bi-level compression
• Lossless and lossy compression
• Progressive transmission by quality and resolution
• Random code-stream access
• Region-Of-Interest coding
• …

JPEG2000 offered much new functionalities and advantages. Therefore, the transmission and the exchange of digital images has become a very simple task. However, the ease to manipulate digital images and to transmit them under a public network raises the issues of security.

Knowing that compression and security are a major issue in many imaging applications, especially in storage and transmission of medical images, we proposed a new framework for secure JPEG2000 image code-streams and files. Therefore, the purpose of this paper is to describe our approach for verifying authenticity and data integrity of sub-images progressively extracted from a single JPEG2000 code-stream.

This paper is structured as follow. In Sec. 2, we first give an overview of the JPEG2000. The technique for authentication and data integrity is presented in Sec. 3. Finally, we draw some conclusions in Sec. 4.

2. Overview of JPEG 2000 encoding algorithm

The block diagram of the JPEG2000 encoder is illustrated in Figure 1. The partitioning image into tiles, which are compressed independently, is first applied on the source image data. The DC level shifting is the second operation and it is followed by the multicomponent transformations. The wavelet transform coefficients are then quantised and entropy coded, before forming the output code-stream. In what follows, we provide a brief description of the JPEG2000 coding engine.

2.1. Preliminary treatment:

The first step in the JPEG2000 coding algorithm is decomposed into three functionalities called: Tiling, DC level shifting and multicomponent transforms. The term “tiling” refers to the partition of the source image into rectangular blocks called tiles [01-05]. Tiling reduces memory requirements and constitutes one of the methods for the efficient extraction of a region of the image.

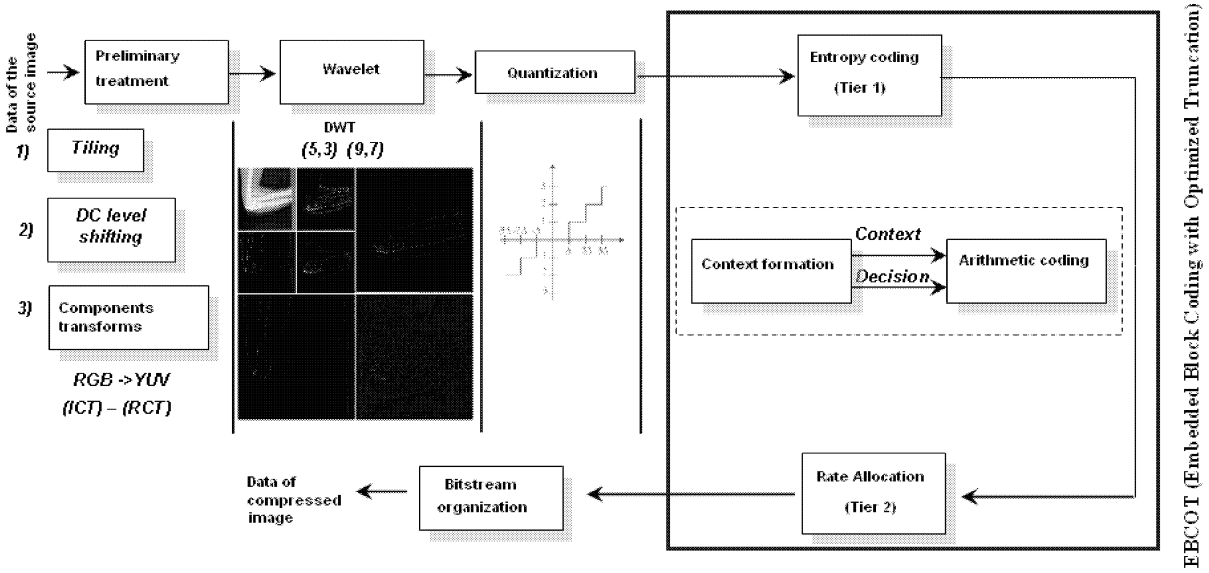

Figure1: Block diagrams of the JPEG2000 encoder.

Then, The DC level shifting is performed on image samples that are represented by unsigned integers only.

Commonly, Colour images are represented in RGB format. Thus, the image is composed of three component planes, one each for the red, green, and blue colour components. However, since Y, C*r* and C*b* colour components are less statistically dependent than R, G and B colour components, they independently compress better.

JPEG2000 part one supports two different transforms RCT and ICT for respectively reversible and irreversible components transforms, which are performed to convert RGB data into YC*r*C*b* data.

2.2. Discrete wavelet transform

During the third step, the image is decomposed into wavelet subbands, by applying a 1-D Discrete Wavelet Transform scheme [07], successively on the rows and the columns. The output of these decompositions is then organized into four new images of one half the sizes. The DWT can be irreversible or reversible. So, JPEG2000 part 1 actually supports two filter banks.

The first is the default irreversible transform based on Daubechies 9x7 wavelet filters and is used for lossy compressions. The second is based on Le Gall 5x3 wavelet filters which allow encoding and decoding of an image without any loss [07].

The output of applying two decomposition levels of an image is shown in Figure 2.

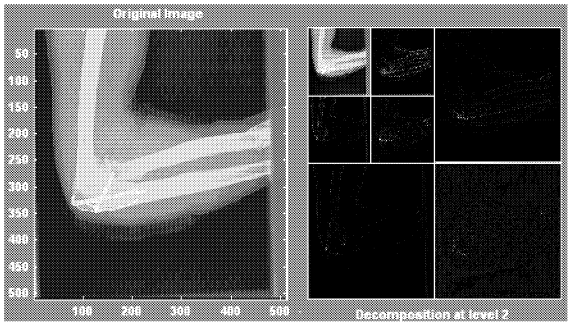

Figure 2: A two decomposition levels of a test image.

2.3. Quantization

After the wavelet transform, all wavelet coefficients are uniformly quantized according to the rule:

$$w_{m,n} = \operatorname{sign} s_{m,n} \left\lfloor \frac{|s_{m,n}|}{\delta} \right\rfloor$$

Where $s_{m;n}$ is the transform coefficient, $w_{m;n}$ is the quantization result, δ is the quantization step size, sign(x) returns the sign of coefficient x, and $\lfloor \rfloor$ is the floor function.

The main functionality of the quantization module is to reduce the coefficients precisions [06]. It should be noticed here that each subbands of each resolution level can be quantized by a different quantization step size, since they have different statistical properties.

2.4. The JPEG2000 Entropy Coding

The algorithm adopted by JPEG2000 for the entropy coding is ***EBCOT*** (embedded block coding with optimized truncation) [09,10]. This algorithm is presented by David Taubman and it is the central part on the JPEG2000 standard since it provides the following advantages:

• Excellent visual quality of the reconstructed images even at lowest bit rates
• SNR scalability
• Resolution scalability
• Region of interest coding
• Error resilience in noisy channels.

For the sake of completeness we give a short overview of the *EBCOT* algorithm. So, after quantization, each subband is divided into rectangular blocks, called "code-blocks", which form the input to the entropy coder (figure 3).

Code-blocks are then coded bit-plane by bit-plane, starting from the most significant bit-plane (***MSB***) with a non-zero element to the least significant bit-plane (***LSB***), to generate bit-stream.

The last procedure is to concatenate all code-block bit-stream for the formation of the final code-stream (figure 3).

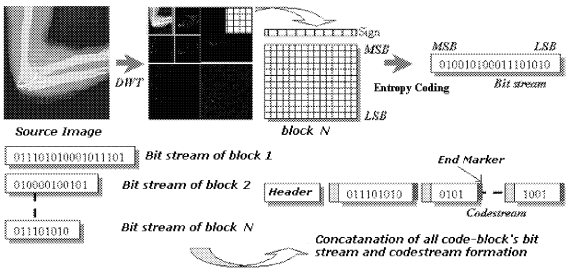

Figure 3: Embedded block coding diagram in JPEG2000 standard

It should be noted here that The JPEG2000 compression system supports scalability [10] and we can construct a code-stream with different progression order to support the need of a wide variety of applications. A key advantage of scalable compression is that the target bit rate or reconstruction resolution need not be known at the time of compression.

In addition, scalability is very important for Internet, database access applications and bandwidth scaling for robust delivery.

For example, regarding the spatial scalability, it is useful for fast database access as well as for delivering different resolutions to terminals with different display capabilities. An example of three levels progressive by resolution decoding for a test image is shown in the figure 4. Another example of a code-stream progressive by quality is shown in the figure 5.

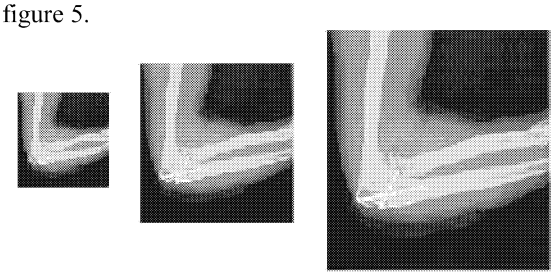

Figure 4: Example of the progressive-by-resolution decoding for a test image (the resolution grows with the decoding of the codestream).

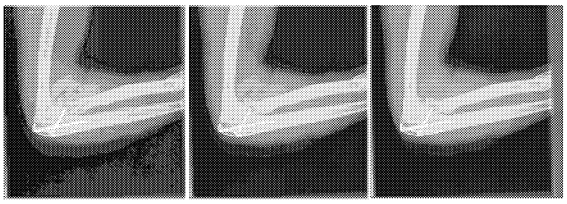

Figure 5: Example of the progressive-by- quality decoding for a test image (the visual quality become well with the decoding of the code-stream).

3. Authentication and data integrity of JPEG 2000 code-stream

The aim of data integrity and authentication is to guarantee, respectively, that data sent from one end of a network arrives unaltered to the other end and to provide information about the sender. A typical image authentication scenario is shown in figure 6.

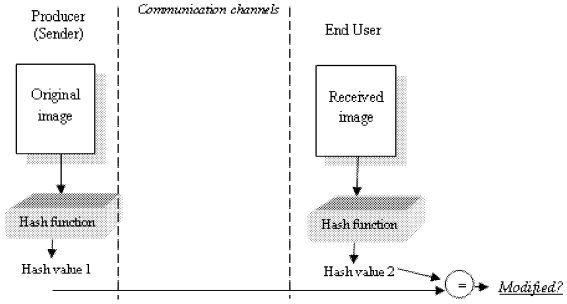

Figure 6: Typical image authentication scenario.

For these considerations, our goal is to provide a way to verify that the image has not been modified or replaced and to prove the identity of image signer.

In other way, our scheme must be compatible with the core part of JPEG2000 standard to conserve its properties, in particular, the progressive decoding.

For the sake of completeness, we first present the most popular and acceptable solutions.

Grobois [12] proposed an authentication scheme using digital signature for each code-block individually. Next, he proposed to insert the digital signature to the end of the code-block bit-stream. Hence, the scheme is compatible with JPEG2000 part 1, but it is inefficient and vulnerable to collage attacks which reorder signed code-blocks. Also, knowing that the size of each code-block is 64x64, thus for a test medical image, which it is generally very large, the hiding of information directly in the code-stream increases the size of the compressed image.

Another method [13] presents an authentication scheme for JPEG2000 image code-stream employing the use of a hash function and a digital signature algorithm. The solution consists in calculating incrementally hash values of all packets of compressed image as follows:

$$h_n=H(P_n)$$

$$h_i=H(P_i \,||\, h_{i+1}) \; i=n-1,\ldots,2,1$$

where H(.) is a one way hash function and || is the concatenation operator. Finally, with the hash value h1 we generate a signature for the code-stream using an underlying signature scheme such as RSA.

The proposed scheme is fully compatible with the core part of the JPEG2000 standard but it is inefficient. Thus, as the users had a different network bandwidth, discarding a part of a code-stream to sending a specific resolution or quality of one image, the producer must recalculate for each user request the corresponding hash value and signature that may cause a waste precious time.

Our proposed authentication and data integrity technique can be summarized in the following three steps as described below (figure 7).

3.1. Hashes generation

A hash provides a mechanism for assuring integrity of data and the authentication of its signer. We propose to use a hash function to compute a hash for each resolution or quality packets. Note that we can use any hash function like SHA, MD2, MD5... The choice of such function and message digest length depends on the application requirements, like the algorithm simplicity, or the security level, or the influence on compression performance and compression ratios because the hashes are sent to the receiver.

The difficulty here consists in specifying the way in which a hash function must be used to generate hashes without making it possible malevolent to distort the procedure checking the hashes. The solution will be analyzed in the following stage.

3.2. Encrypt all hashes

An attacker knowing the hash function used during the generation of the hashes, will be able to modify the code-stream and to generate the corresponding hashes without the receiver being conscious. Indeed, without encryption [11] of the hashes we can guarantee neither authentication nor data integrity. Thus, we proposed to encrypt all hashes. Note that an encryption hash forms a digital signature and we can use any cryptosystem algorithm like RSA, DES or AES. However, the choice of such algorithm and encryption key length depends on the application requirements like security level and algorithm simplicity. Finally, if the image is modified, the checking of signatures will fail.

3.3. Sending of signatures (encrypted hashes)

Up to now, we haven't presented the manner of sending the signatures to the receiver. It is the most delicate phase more especially as our method of authentication must be compatible with the core part of the JPEG2000 standard. Indeed, since the arithmetic decoder stops reading bytes from the bit-stream when it become at its end, we used this property in order to insert the signatures behind the end of each resolution or quality packets. Note that we can use any other means to communicate the signature such as mail, telephone, fax or any other way.

Thanks to our method, when a user wants to receive a particular resolution or quality of one image, he can check the authentication of the received resolution without needing to receive the totality of the image code-stream, which proves the originality of our approach like it's efficiently and compatibility with the JPEG2000 standard.

Another advantages of our approach is that compression as well as signature generation occur only once and when any user wants to download or see a specific resolution or quality of an image the producer doesn't need to make computations with each new request.

Finally, thanks to our approach we no longer need to make calculation signature for each code-block, since the number of signature is proportional to the number of resolutions or qualities of the image itself. So, if the signatures are directly inserted into the final code-stream, we lightly increase the size of the compressed image.

4. Conclusion

In this paper, we initially presented a fast overview of the JPEG2000 still image compression standard.

Next, in order to provide a standard as well compression as authentication of the digital images, we proposed a new method for ensuring authenticity and data integrity of JPEG2000 code-streams and files.

Our approach is based on the use of a hash function to compute a hash for each resolution or quality packets. Next, we proposed to encrypt all hashes to secure the procedure checking the hashes. Finally, we proposed to insert the signatures directly in the JPEG2000 code-stream but the producer can choose any other means to communicate the signature.

To conclude, our approach is scalable, efficient and compatible with the JPEG2000 algorithm.

5. REFERENCES

[01] Adams M. D., "The JPEG-2000 Still Image Compression Standard (Last Revised: 2002-12-25)", *ISO/IEC JTC 1/SC 29/WG1 N 2412*, December 2002.

[02] Christopoulos C., Skodras A.N. and Ebrahimi T., "The JPEG2000 still image coding system: an overview", *IEEE Transactions on Consumer Electronics, vol. 46, No. 4, pp. 1103–1127*, November 2000.

[03] Skodras A., Christopoulos C. et Ebrahimi T., "The JPEG2000 Still Image Compression Standard", *IEEE Signal Processing Magazine, vol. 18, pp. 36-58*, September 2001.

[04] ISO/IEC JTC1/SC29 WG1, Boliek M., Christopoulos C., and Majani E., "JPEG 2000 Part I Final Draft International Standard (corrected and formatted)", *ISO/IEC JTC 1/SC 29/WG1 N1890*, September 2000.

[05] http://www.jpeg.org/jpeg2000.

[06] Michael W. M., Margaret A. L., Bilgina A., Flohrc J. T., Chinend T. T., Kasnere J. H.,"An overview of quantization in JPEG 2000", *Signal Processing: Image Communication 17 (2002), pp. 73–84*, 2002.

[07] Unser M. and Blu T.,"Mathematical Properties of the JPEG2000 Wavelet Filters", *IEEE TRANSACTIONS ON IMAGE PROCESSING, Vol. 12, No. 9, pp. 1080-1090*, September 2003.

[08] Twelves S. and Wu M., "JPEG2000 Arithmetic Encoding on the StarCore SC140", *Freescale Semiconductor, Inc. Rev 1.0*, October 2001.

[09] Taubman D., "High performance scalable image compression with EBCOT", *IEEE Trans. Image Processing, vol. 9, pp. 1158-1170*, July 2000.

[10] Taubman D., Ordentlich E., Weinberger M. and Seroussi G., "Embedded Block Coding in JPEG2000", *Signal Processing: Image Communication 17, pp. 49–72*, 2002.

[11] Boneh D., "Twenty Years of Attacks on the RSA Cryptosystem", *In Notice of the AMS (American Mathematical Society), pp. 203-213*, February1999.

[12] Grosbois R., Gerbelot P. and Ebrahimi T., "***Authentication and access control in the JPEG2000 compressed domain***", In Proc. of the SPIE 46th Annual Meeting, Applications of Digital Image Processing XXIV, San Diego, July 29th - August 3rd, 2001.

[13] Robert H. Deng, Yongdong Wu and Di Ma, "Progressive protection of JPEG2000 codestreams".

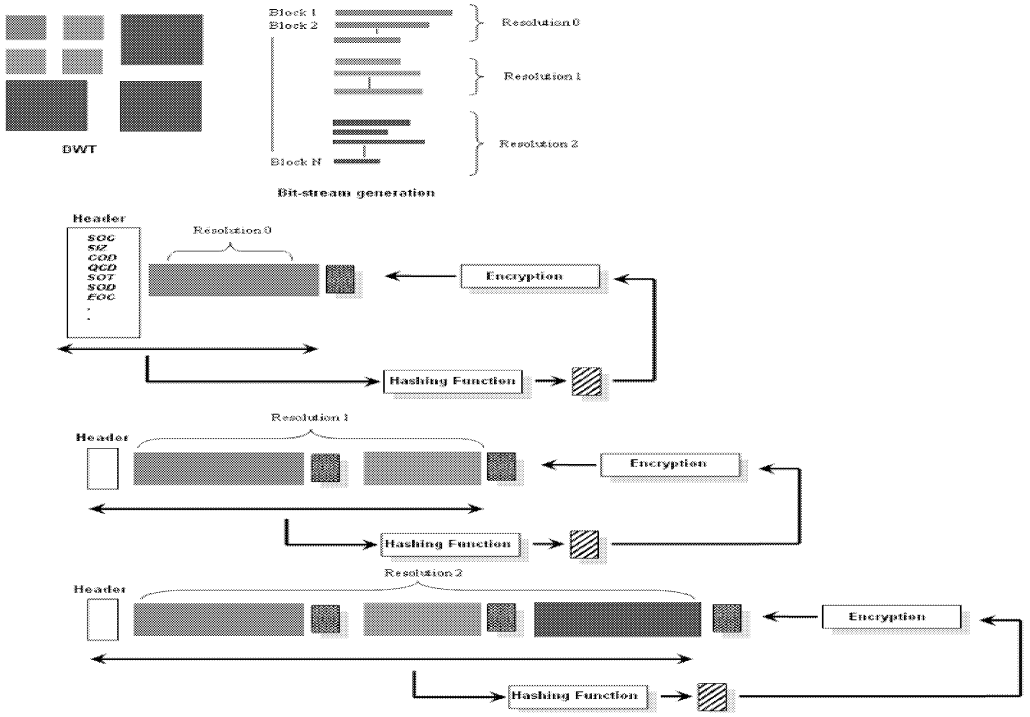

Figure 7: Progressive authentication and data integrity for PEG2000 code-stream.

Statistical and Neural Network Classification of Skin Lesion Images

Khaled Taouil
Nadra Ben Romdhane
Med Salim Bouhlel
Research Unit: Sciences and Technologies of Image and Telecommunications
Higher Institute of Biotechnology, Sfax
E-mail: khaledtaouil@yahoo.com, medsalim.bouhlel@enis.rnu.tn

ABSTRACT

The ultimate aim of this work is to provide an automatic detection of melanoma skin lesion images using a Computer-aided diagnosis (CAD) system. This work presents the different steps of such a process. We detail in this paper the segmentation step by describing the different used methods in the literature and propose a hybrid approach based on morphology functions and active contours (snakes) that can be integrated in our system. We present also several statistical methods of classification (the discriminative factorial analysis (AFD), Gaussian estimation and the projection on the direction linking the two conditional means) and the non linear classification method by the use of the neural network.

We evaluate our work on different cases of color skin lesion images from digitized slides data base selected by expert dermatologists from the hospital "CHU de Rouen" France.

KEYWORDS
Melanoma, segmentation, morphology functions, snake, classification, neural network.

1. INTRODUCTION

Melanoma is an increasing form of skin cancer in the world. The incidence is on the order of 10–12 per 100,000 in Europe, five times more than 50 years ago, 18–20 per 100,000 in the USA, and 30–40 per 100,000 in Australia, where the climate and sun exposure are especially hazardous (Schmid et al . 2003). Successful treatment of melanoma depends directly on early diagnosis (Institute of physics publishing, 2005) (Joly and Lauret 1992). The curability of this type of skin cancer (about 70%) depends on early enough recognition and surgical treatment (Popa and Aiordăchioaie 2004). The rate of accurate diagnosis is around 75% (true positives) (Schmid et al. 2003). The ABCD clinical rule was introduced for assisting the visual recognition of early melanoma(Friedman1985). Computer-aided diagnosis (CAD) systems based on image processing were introduced since 1987 (Xu et al.1999; cascinelli et al.1987; Taouil 1995; Schindewolf et al 1994). It has been proved that such CAD systems can improve the recognition rate of the nature of a suspect lesion (Ganster et al 2001; Khanfir et al 2003) particularly at centers not experienced in the field of pigmented skin lesions (Barzegari1 et al. 2005).

2. CAD SYSTEMS IN MELANOMA DETECTION

Complete integrated dermatological image analysis systems are hardly found in clinical use (Popa and Aiordăchioaie 2004, Ganster et al 2001). CAD systems in melanoma detection are usually based on image processing and data classification methods. Five steps are generally needed.

The first step is the data acquisition. The dermatologists use slides for lesion images storage and visual inspection. Different image acquisition techniques can be used such as color slides digitization and direct image acquisition. Recent studies have shown that dermatoscopic diagnosis has an accuracy of 75% to 97% while this range is 65% to 80% for macroscopic diagnosis (Schmid et al . 2003).

The pre-processing step is used to filter noise in the digitized images and to overcome different lighten conditions. In order to quantify geometric and colorimetric properties of a lesion, a segmentation step is used to label each pixel of the entire image as belonging to the lesion or to the safe skin. Image segmentation is the most critical step in the entire process. The next step is the quantification. We use a parametric classification approaches. The description of each lesion is resumed in a vector of features which dimension depends on the number of extracted primitives. The last step is the quantification. To develop a classification method a data base of malignant and benign lesions is needed. A first set of lesions are used for training and a second set is used for test. The nature of all used lesions has to be well known by dermatologists.

3. SNAKES TECHNIQUES

Snakes or active contours are curves defined within an image domain. These contours can move under the influence of internal forces coming from within the curve itself and external forces computed from the image data. Snakes are parameterized curves, $v(s) = [x(s), y(s)]$,$s \in [0,1]$, that move through the spatial domain of an image to minimize the functional

energy (Xu and Prince 1998, Zhao and Zhuang 2005, Erkol et al.2005):

$$E_{snake} = \int_0^1 E_{int}(v(s)) + E_{ext}(v(s))\ ds \quad (1)$$

$$E_{int}(v(s)) = \alpha \left| v'(s) \right|^2 + \beta \left| v''(s) \right|^2 \quad (2)$$

$$E_{ext}(x,y) = -\left| \nabla I(x,y) \right|^2 \quad (3)$$

where:

- v(s) is a set of coordinates to form a snake contour.
- v'(s) and v"(s) denote the first and second derivatives of v(s) with respect to s .
- α and β are weighting parameters that control respectively the snake's tension and rigidity.
- $\nabla I(x,y)$ is the gradient of grey-level image I.

A snake that minimizes E_{snake} must satisfy the Euler equation:

$$\alpha v''(s) - \beta v''''(s) - \nabla E_{ext} = 0 \quad (4)$$

4. SEGMENTATION ALGORITHM

We use hybrid skin lesion border determination algorithms for dermatological images that incorporate the advantages of both morphology functions and snakes. For pre-processing step, we use the combination of different morphology functions to overcome noise effects which prevent the snake from converging to the real skin lesion boundary. Then, we initialize the snake using the approximate contour of safe skin mask and the curve moves closer to the real skin lesion border as shown in Figure 1.

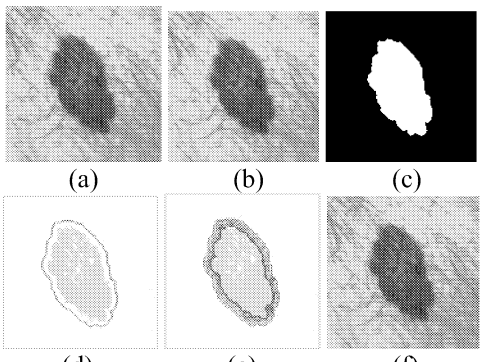

Figure 1. Hybrid Segmented Image using morphology functions and snakes. (a)Initial image, (b) gray level image, (c) Approximate skin lesion region, (d) Initial snake boundary, (e) Output of snake deformation process, (f) Final skin lesion border.

5 . CLASSIFICATION

After having summarized information contained in the different images of our database in vectors of 14 parameters we tested several methods of classification. We present in this work different statistical methods of classification (the discriminative factorial analysis (AFD), Gaussian estimation and the projection on the direction linking the two conditional means (Taouil 1995)) and the non linear classification method by the use of the neural network (Khanfir et al 2003).

5-1. Statistical Classification Methods

The observations of d variables on n individuals are gathered in a rectangular table X with n lines and d columns (Saporta 1992). In the present analysis, we have n=60 and d=14.

$$X = \begin{array}{c|ccccc} & P & .. & P & .. & P \\ \hline \ell & & & : & & \\ : & & & : & & \\ \ell & .. & .. & X_{ij} & .. & .. \\ : & & & : & & \\ \ell & & & : & & \end{array}$$

Every attribute, noted Pj, is a list of n numeric values: we will consider it like a vector of a space E with a dimension n called space of variables. Let's note $\ell(i)$ an individu whose coordinates are

$$\ell(i) = \left(X1(i), ..., Xd(i)\right)$$

In the space of dermatologic lesions we can distinguish two statistic populations: the malign lesions and the benign lesions. We used two methods of statistic classification: a geometric method, the AFD and a probabilistic method under Gaussian hypothesis. The objective of AFD is to find a linear descriptive parameter combination that minimizes variance within the classes and that maximizes the variance between classes (Saporta 1992). The individuals represented by the vector parameters are projected on this separated direction. We use the $M = \Gamma^{-1}$ metric, where Γ is the total variance matrix.

The probabilistic method consists on achieving a test between two hypotheses, which are:

The Hm hypothesis: the lesion belongs to the class of malignant lesions Cm.

The Hb hypothesis: the lesion belongs to the class of benignant lesions Cb.

This test is based on the different values of the vector $\ell(i)$ with 14 components, corresponding to the i[th] line of the statistical table X and representing the 14 parameters, previously selected, describing the lesion i.

We compute the means and the covariances of the vector ℓ under each hypothesis. We replace the mathematical expected values by statistical means under the hypothesis Hm and under the hypothesis Hb:

$$E(\ell / H_m) \approx m_m = \frac{1}{card\, C_m} \sum_{(i,j) \in C_m} \ell(i,j) \quad (7)$$

$$V(\ell / H_m) \approx \Gamma_m = \frac{1}{card C_m - 1} \sum_{(i,j) \in C_m} \left(\ell(i,j) - m_m\right)^{tr} \left(\ell(i,j) - m_m\right) \quad (8)$$

Under the hypothesis Hb, we obtain the same formula where b stands for m.

We consider that ℓ follows a Gaussian distribution such as:

$$f(\ell) = \frac{1}{(2\pi)^{\frac{n}{2}} (\det\Gamma)^{\frac{1}{2}}} \exp\left[-\frac{1}{2} (\ell - m)^{tr} \Gamma^{-1} (\ell - m) \right] \quad (9)$$

The logarithm of the likelihood $\frac{f(\ell / H_b)}{f(\ell / H_m)}$ gives:

$$Ln\frac{f(\ell/H_b)}{f(\ell/H_m)} = \frac{1}{2}Ln\left[\frac{\det\Gamma_m}{\det\Gamma_b}\right] - \frac{1}{2}\left[(\ell-m_b)^{tr}\Gamma_b^{-1}(\ell-m_b) - (\ell-m_m)^{tr}\Gamma_m^{-1}(\ell-m_m)\right] \quad (10)$$

Let U be the n-dimensional unit vector giving the direction of the centers of gravity such as:

$$U = \frac{m_b m_m}{\|m_b m_m\|}$$

(11)

Let be T the Gaussian estimator to choose between the two hypotheses H_m and H_b. It is based on the computation of the scalar product of the vector ℓ of observation and the direction of the centers of gravity, that is to say:

$$T(\ell(i,j)) = \sum_{k=1}^{n} U_k \ell_k(i,j) = \langle U, \ell(i,j)\rangle$$

(12)

Under the hypothesis Hb, T is a Gaussian estimator with the mean:

$$E(T(\ell)/H_b) \approx \sum_{k=1}^{n} U_k m_{b,k}$$

(13)

and with the variance

$$V(T(\ell)/H_b) \approx U^{tr}\Gamma_b U$$

(14)

Under the hypothesis H_m, we obtain the same formula where m stands for b. If we compute the projection of the observations on the direction's conditional means of the two classes, we define a cutt-off direction U.

5-2. Classification by Neural Network

Neural networks are used as pattern classifiers to classify skin tumours as malignant or non-malignant from colour photographic slides of the tumours (Maglogiannis et al.2005). It can learn and gain experience on its own about the melanoma diagnosis problem. A multilayered feedforward neural network trained using the backpropagation training algorithm is built to classify digital images of tumours into a small number of fixed categories. In the basic feed-forward neural network, an input layer sends signals to a hidden middle layer. One hidden layer will normally suffice for classification problems (Khanfir et al 2003, Maglogiannis et al.2005, Lepage and Solaiman 2003).

The neural network that adjusts best to our application is the multilayer network. We chose to train our network by the backpropagation algorithm. Figure 2 shows the architecture of the network that we had trained. It includes 14 nodes in its entry layer, corresponding to the 14 selected parameters, only one hidden layer of seven nudes and one node to the output layer giving the nature of the lesion. For the training and the test, we used several combinations of two sets of individuals that are statistically independent.

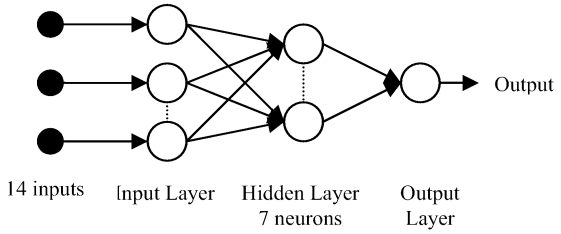

Figure2: Architecture of the used neural network.

6. EXPERIMENTAL RESULTS

The dermatologist usually uses slides for lesion image storage. Our database has been collected in France with the collaboration of PSI-INSA Rouen research laboratory and supported by the French Ligue Nationale contre le Cancer. We use 62 images of benign and malignant lesions. The images were digitized in true RGB color with a 35 mm film scanner Nikon LS-1000. The results of thresholding and classification algorithms were described in previous works (Khanfir et al 2003, Bouhlel et al.2002).

After pre-processing of images by Gaussian and median filtering, we segmented the set of images while using our automatic approach of segmentation based on morphological filters and snake as shown in figure1. The snake begins with the calculation of a field of external forces over the image domain. It starts at the approximate boundary of safe skin obtained after application of morphological functions. The forces drive it toward the boundary of the lesion. The process is iterated until it matches the contour of the lesion. We superpose the obtained contour on the original color image. Then, lesions have been summarized in vectors of 14 parameters that served like entries for training and test stages. These parameters derive from clinical features or are original features. It is possible to increase the number of primitives but only robust and efficient parameters are needed in a classification step.

The different methods of classification have been tested on a set of 60 lesions whose malign or benign nature is perfectly known after histological analysis. Every class of lesions contributes, by the same percentage of its total number, to the sample of training and test sets. Classification using the statistical methods gave a mean of 95% for the AFD, 80% for the Gaussian estimation and 90.83 % for the direction linking the two conditional means. The classification by neural network (NN) has been achieved for different combinations of lesion images for samples of training and test. We used, respectively, percentages of (60/40), (70/30) and (80/20) for training and test databases. We gave results lesion recognition during the tests in Table1.

To complete the survey of the relevant retained parameter at the classification step, we set to zero each parameter and we repeat the steps of training and test. We gave the number of wrong classified lesions following the setting to zero of every parameter. More the percentage of good recognition falls, more the efficiency of the parameter will be considered

important. The decreasing efficiency of variables is given in Table 2. We notice that the compactness of the shape (cs) is the most pertinent and that the middle level of the red colour (rmoyL) is the least pertinent.

% of lesions / samples	60/40		70/30		80/20	
	Min	Max	Min	Max	Min	Max
FP	1	1	1	0	0	0
TP	9	12	7	9	5	6
FN	3	0	2	0	1	0

Table 2 : Parameters effects on lesions classification.

TN	11	11	8	9	6	6
Recognition	83,3	95,8	83,3	100	91,6	100
Mean of % recognition	89,5		91,65		95,8	

- FP (False Positive) : wrong classified Benign Lesion.
- TP (True Positive) : correct classified Malign Lesion.
- FN (False Negative) : wrong classified Malign Lesion.
- TN (True Negative) : correct classified Benign Lesion.

Table1: Percentage of lesion recognition during the test

% of lesions/parameter	cs	rc	scR	Em	Delta	scB	bmoyL	conc	scv	er	Alpha	scG	eb	rmoyL
FP	0	2	2	1	3	2	2	2	2	0	1	1	1	1
TP	3	8	8	8	10	9	9	10	10	8	10	10	10	10
FN	7	2	2	2	0	1	1	0	0	2	0	0	0	0
TN	10	8	8	9	7	8	8	8	8	10	9	9	9	9
% of recognition	65	80	80	85	85	85	85	90	90	90	95	95	95	95

7. CONCLUSIONS

In this paper we have described the different steps used in CAD system in melanoma detection. To make this tool useful by the dermatologist community outside specialized centers, each stage of processing has to be automatic. Our hybrid approach of segmentation based on morphology functions and snakes can be integrated, with classification using the neural network, in the entire process of melanoma detection to replace supervised used methods.

References

Barzegari1 M; H Ghaninezhad1; P Mansoori and al,2005, « Computer-aided dermoscopy for diagnosis of melanoma », BMC Dermatology, 5:8

Bouhlel MS; K Taouil and L Kamoun, 2002 "Melanoma-Pattern Extraction using histogram-thresholding approach", *Official Journal of Egyptian Society for Medical Education*, "Scientufic Medical Journal" , Sci.Med J. (ESCME), Vol.14, No.3.

cascinelli N; M Ferrario; T Tonelli, and al. 1987 ,A possible new tool for clinical diagnosis of melanoma : *the computer.J AM Acad Dermatol*; 16 : 361- 7.

Friedman RJ; "Early detection of malignant melanoma: the role of the physician examination and self examination of the skin" CA Cancer J. Clin. 35 130–51, 1985.

Ganster H; A Pinz; R Röhrer; and al, March 2001, "Automated Melanoma Recognition", IEEE Transactions on Medical Imaging, vol. 20, no. 3, Institute of physics publishing, physics in medicine and biology," Automated melanoma detection with a novel multispectral imaging system : results of a prospective study ", Phys. Med. Biol. 50 (2005) 1675–1687.

Joly P ; Ph. Lauret. 1992, "Mélanome Malin, Prévention et Dépistage". Melanome Malin. M. DELAUNY, Ed MASSON. PARIS.

Khanfir.I; K.Taouil; M.S.Bouhlel; L.Kamoun,2003, « Strategie de traitement des images de lesions dermatologiques », Sciences Electronique, Technologies de l'Information et des Télécommunications, ed M.S.Bouhlel, B.Solaiman et L.Kamoun. ISBN 9973-41-685-6.

Lepage R and B Solaiman, 2003, Les réseau de neurones artificiels et leurs applications en imagerie et en vision par ordinateur, Coop.ETS Ecole de technologie supérieure.

Otsu N,1978;"A treshold selection method from gray-level histogram".IEEE Trans.Sys Man Cybernet. SMC-8, 62-66.

Maglogiannis I; S.Pavlopoulos; D.Koutsouris, March 2005, "An Integrated Computer Supported Acquisition, Handling, and Characterization System for Pigmented Skin Lesions in Dermatological Images" IEEE Trans. on Information Technology in Biomedicine, vol. 9, no. 1.

Popa.R and D Aiordăchioaie, 2004 "Genetic Recognition of Changes in Melanocytic Lesions". The 8th International Symposium on Automatic Control and Computer Science, SACCS 2004, Iasi, Romania, 22-23 October.

Saporta G, 1992, Probabilités, Analyse des données et Statistique, Editions TECHNIP.

Schindewolf T; R Schiffner; W Stolz, and al, July 1994, "Evaluation of different image acquisition techniques for a computer vision system in the diagnosis of malignant melanoma", *Journal of the American Academy of Dermatology.*

Schmid P; J Guillod; JP Thiran, 2003 "Towards a computer-aided diagnosis system for pigmented skin lesions" Computerized Medical Imaging and Graphics 27 65–78

Taouil Khaled 1995, "Faisabilité en détection des mélanomes", Thèse de doctorat, INSA de ROUEN.

Xu L; M. Jackowski; A. Goshtasby, D. Roseman, S. Bines, C. Yu, A. Dhawan, A. Huntley, 1999 "Segmentation of skin cancer images", Image and Vision Computing 17, 65–74. Zhao CG and TG Zhuang, 2005 , "A hybrid boundary detection algorithm based on watershed and snake", *Pattern Recognition Letters* 26 1256–1265.

APPENDIX

1. Geometrical parameters

- Compactness of the shape (cs) :

The compactness of the shape gives the deviation between the shape and a disk. It depends on its area S and its perimeter P:

$$c_s = 4\pi \frac{S}{P^2} \tag{1}$$

- The regularity of the contour (rc) :

A contour C is regular if it presents neither no distortion nor notch. It is characterized by:

$$r_c = \frac{\frac{1}{P}\sum_{p\in C}\left(d(p)-\overline{d}\right)^2}{\overline{d}^2} \tag{2}$$

where P is the perimeter of the lesion, $\overline{d}$ is the mean Euclidian distance to its gravity center having coordinates $(\overline{i},\overline{j})$, and where p (i, j) is a given pixel of its contour C.

$$\overline{d} = \frac{1}{P}\sum_{p\in C} d(p) \tag{3}$$

$$d^2(p) = (i-\overline{i})^2 + (j-\overline{j})^2 \tag{4}$$

- The expanse (Δd):

$$\Delta d = \frac{d_{\max} - d_{\min}}{\overline{d}} \tag{5}$$

where $d_{\max}$ and $d_{\min}$ represents respectively the maximal and the minimal of the Euclidian distance of points of the contour pixels to the gravity center of the lesion.

- The mean deviation (E_m):

$$\mathrm{E_m} = \frac{\frac{1}{P}\sum_{p\in C}\left|d(p)-\overline{d}\right|}{\overline{d}} \tag{6}$$

where P is the perimeter of the lesion. d(p) is the Euclidian distance of a given pixel p to the gravity center of the lesion.

- The index of concavity (conc): The index of concavity in surface is a measure of the distribution of the lesion on the polygon in which it is written down. For example, a disk of ray a/2 wrote down in a square (n=4), the surface of the square is $(2a)^2 = 4a^2$ and the surface of the disc is πa^2, the indication of concavity in surface is :

$$c = \pi \frac{a^2}{(2a)^2} = \frac{\pi}{4} \tag{7}$$

2. Photometric parameters

The Mean $\overline{C}$ for the distribution of a variable C (C could be R, G, B, r, g or b) inside the lesion L, is:

$$\overline{C} = \frac{1}{S}\sum_{p\in L} C(p) \tag{8}$$

The standard deviation σ_C of the distribution of C, is:

$$\sigma_C^2 = \frac{1}{S}\sum_{p\in L}\left(C(p)-\overline{C}\right)^2 \tag{9}$$

Where $\overline{C}$ is the mean of levels of C calculated on the lesion. C(p) is the value of C in L and S is the surface area of L.

- The deviation between the color mean of the lesion and the color mean of the safe skin:

We define the parameter d_C, as follows:

$$d_C = \frac{\overline{C}_S - \overline{C}_L}{\sigma_{CS}} \tag{10}$$

where $\overline{C}_L$ et $\overline{C}_S$ represent respectively the mean of the color C inside the lesion and the mean of C inside the surrounding safe skin.

σ_{CS} is the standard deviation of C calculated on the safe skin. The normalization by the standard deviation has been introduced because of the dynamics of gray levels which differs from an image to another.

- The color symmetry

The difference between the means of distances to the gravity center of the lesion, of the darkest pixels and the clearest pixels constitutes a means to measure the symmetry s_C of the color within a lesion.

$$s_c = \frac{\left|\overline{d}_s - \overline{d}_c\right|}{\overline{d}_G} \tag{11}$$

where $\overline{d}_s$ and $\overline{d}_c$ are respectively the mean distance to the gravity center of the darker and clearer pixels .

$\overline{d}_G$ is a normalized mean of the distance to the gravity center of the lesion.

- The spherical coordinate (Alpha) is expressed by :

$$\alpha = \cos^{-1}\left(\frac{B}{L}\right) \tag{12}$$

Where $L = \sqrt{R^2+G^2+B^2}$

Mammographic Microcalcifications Detection Using Discrete Wavelet Transform

Nizar Ben Hamad
Khaled Taouil
Med Salim Bouhlel

Research Unit: Sciences and Technologies of Image and Telecommunications
Higher Institute of Biotechnology Sfax
Sfax -TUNISIA

E-mail:{n_benhamad@yahoo.fr, khaledtaouil@yahoo.com, medsalim.bouhlel@enis.rnu.tn}

KEYWORDS

DDSM, Digital Mammograms, Microcalcification, Discrete Wavelet Transform, Multiresolution analysis.

ABSTRACT

Breast cancer can be diagnosed with an early training course by detecting the presence of microcalcifications in screening mammograms. The multiresolution analysis using discrete wavelet transform presents characteristics which can be exploited to develop tools for detection of microcalcifications. The objective of our work is to study the best type of wavelet and the optimal level of decomposition for a better detection.

Our approach is divided into two phases. The first phase of our algorithm consists on multiresolution analysis based on 1-D discrete wavelet transform over profiles of microcalcifications extracted from mammographic images. This analysis is carried out with several families of wavelets. The second phase of our algorithm is interested in the validation of the results of the first. In this stage, we apply 2-D discrete wavelet transform in analysis and synthesis on screening mammograms extracted from the DDSM base (DIGITAL Database for screening Mammography) in order to detect the microcalcifications.

INTRODUCTION

With more than 10 million new cases every year, cancer has became one of the most devastating diseases world-wide (Stewart et al. 2003). Early detection of breast cancer provides successful treatment. SCREEN–FILM mammography is recognized as being the best means of early detection of the breast cancer. Currently, there is a consensus on the fact that the mammography of tracking may reduce mortality by breast cancer at least 30% (Murgo 2002). Mammograms are the most difficult of radiological images to interpret since they are of low contrast. Also, features in mammograms indicative of breast disease, such as microcalcifications, are often very small. Therefore, a computer system has already been used to help the radiologists to pre-screen mammograms (Wang et al. 1998).

During the last twenty years, considerable research has been undertaken in the development of automated detection of microcalcifications. Several image processing methods were proposed (a thorough review of various methods can be found in (Thangavel et al. 2005) and (Cheng et al. 2003)).

Among these, there are many promising wavelet approaches based on the discrete wavelet transform multiresolution analysis.

Although, there are various wavelet decomposition approaches microcalcifications detection algorithms, the study of the optimal level of decomposition is of great interest to perform computer aided detection of microcalcifications based on multiresolution wavelet transform.

The remaining of the paper is organized as follows. First, an overview of some wavelet-based approaches is provided in section II. Next, we introduce the principles of wavelet transform and multiresolution approach in Section III. The proposed approach is developed in Section IV. Results and applications are presented in Section V. Finally, conclusion and some suggested directions for future work are given in Section VI.

OVERVIEW OF SOME WAVELET-BASED APPROACHES

Several types of wavelet transforms were employed in algorithms to achieve automated detection of microcalcifications. In this section, a few most important techniques for microcalcification detection are reviewed.

(Wang et al. 1998) presented an approach for detecting microcalcifications in digital mammograms employing wavelet-based subband image decomposition. Given that the microcalcifications correspond to high-frequency components of the image spectrum, microcalcifications can be extracted form the original mammograms by suppressing the subband of the wavelet-decomposed image that carries the lowest frequencies, before the reconstruction of the image.

(Sersic et al. 1998) introduce a novel approach based on redundant wavelet transform to enhance digital mammography images. The procedure consists of three steps: low-frequency tissue density component removal, noise filtering and microcalcification enhancement. The experimental results have shown good properties.

(Chan et al. 1999) developed an enhancement algorithm relying on multiscale wavelet analysis and extracted oriented information at each scale of analysis was investigated. The evolution of wavelet coefficients across scales characterized well the local shape of irregular structures.

(Zadeh et al. 2000) extracted three kinds of features from ROIs: wavelet features, multi-wavelet features, and co-occurrence based features. Using a neural network, it could classify benign and malignant microcalcification clusters. The test results on a set of 103 regions containing microcalcifications show that the multi-wavelet method has better performance, and gets an area of 0.91 under the ROC curve.

(Mata et al. 2000) proposed a multiresolution analysis by decomposing the image through a band-pass filter bank, so that in each sub-band image visible only the details at the given scale. Thereafter, all the images will be combined in a final one in order to obtain an image that contains all the interest details at the scale where microcalcifications tend to appear. Statistical analysis of the histogram is used to classify the susceptible zones containing microcalcifications.

(Sentelle et al. 2002) shows that a multiresolution FCM-based segmentation combined with wavelet processing can be employed to quickly detect and segment calcifications as a possible pre-processing step for a classifier. This algorithm exhibits difficulty with the detection of some subtle calcifications.

(Heinlein et al. 2003) presented a new algorithm for enhancement of microcalcifications in mammograms. The main novelty was the application of techniques developed for construction of filterbanks derived from the continuous wavelet transform. These discrete wavelet decompositions, called integrated wavelets, are optimally designed for enhancement of multiscale structures in images. These techniques were applied to the detection of microcalcifications.

Since microcalcifications appear as singularities in mammograms, (Lemaur et al. 2003) provide new wavelets with a higher Sobolev regularity compared the classical wavelets, assuming the same support width. The results show that the detection of clustered calcifications in digitized mammograms is improved by the use of wavelets with a high Sobolev regularity.

WAVELET TRANSFORM AND MULTIRESOLUTION APPROACH

Because of a powerful underlying mathematical theory, wavelet methods of analysis and representation are presently having a significant impact on the science of medical imaging and the diagnosis of disease and screening protocols. They offer exciting opportunities for the design of new multiresolution image processing algorithms (Unser et al. 2003).

In this section, we describe the procedure of implementing the one-dimensional wavelet transform.

Most images correspond to signals which have high-frequency components of short duration (details) and low-frequency components of long duration (approximations) (figure 1). Bearing these consi-derations, a multiresolution analysis works best with this kind of signals.

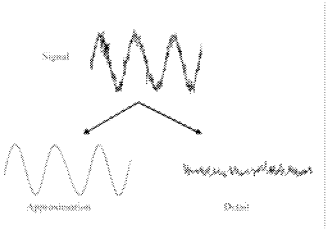

Figure 1: Details and Approximation signals

1-D Wavelet analysis filter bank:

The 1-D wavelet transform analysis is the first step in the multiresolution approach.

Consider a multiresolution hierarchy with j levels. Each level contains an approximation, Aj, and details Dj. The original data can be thought of as A0. Approximation A1 is the low frequency components of A0, and D1 is the high frequency components of A0. The detail can be thought of as the difference between A1 and A0 so that A0=A1+D1=A2+D2+D1 etc…

Two closely related basic functions are needed for the multiresolution formulation. The first basic function is the wavelet function ψ(t) and the other one is called the scaling function and denoted by φ(t) (Sajda et al. 2002). All other wavelets are obtained by simple scaling and translating of ψ(t) as follows:

$$\psi_{a,\tau} = \frac{1}{\sqrt{a}}\psi\left(\frac{t-\tau}{a}\right) \qquad (1)$$

The two-parameter wavelet expansion for signal *S(t)* is given by the following decomposition series in which the scaling and wavelet functions are utilized.

$$S(t) = \sum_{k} cA_k \varphi_{j_0,k}(t) + \sum_{k}\sum_{j=j_0}^{\infty} cD_{j,k}\psi_{j,k} \qquad (2)$$

In this expansion, ck coefficients are referred to as approximation coefficients at scale j0. The set of dj,k coefficients represents details of the signal at different scales.

The hierarchical model can be illustrated as follows (figure 2): (Erickson 2005).

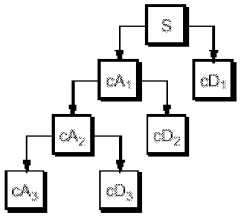

Figure2: Multiresolution Hierarchical Model. S is the original image.

Mallat demonstrates that the dyadic nature of multiresolution approximations, in orthogonal basis, is closely related to the possibility of implementing the discrete wavelet transform (DWT) using filter bank.

The implementation of the discrete wavelet transform using filter bank is shown in figure 3.

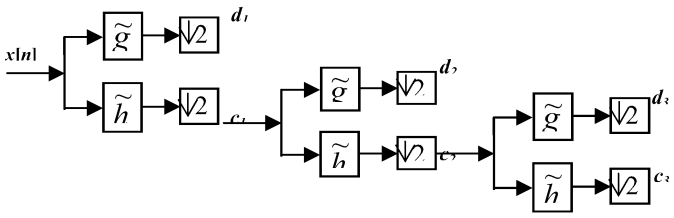

$\downarrow 2$: Down-sampling by 2.

Figure 3: 1-D DWT filter bank implementation

2-D Wavelet analysis and reconstruction filter bank:

For the processing of images, the 1-D DWT is extended to 2-D DWT. Using tensor product wavelets, one performs the 1-D decomposition process along both x (row) and y (column) axes. A total of four subband images HH, HL, LH and LL are generated (figure 4). Different subband images contain different information and they may be processed individually using different algorithms. The subband image LL corresponds to the lowest frequencies. It contains the smooth information and the background intensity of the image. The subbands HL, LH, HH contain the detail information of the image. The subband HL gives the vertical high frequencies (horizontal edges), LH gives the horizontal high frequencies (vertical edges) and HH gives the high frequencies in both directions (corners and diagonal edges).

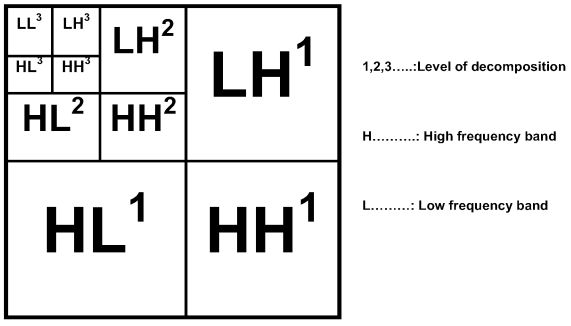

Figure 4: 3 Levels Hierarchical subbands decomposition

For reconstruction Filters, we denote the importance of choosing the right filters. In fact, the choice of filters not only determines whether perfect reconstruction is possible, it also determines the shape of the wavelet we use to perform the analysis.

The reconstruction can be performed from each level and each subimage while keeping the size of the reconstructed image the same as the original image.

PROPOSED APPROACH

One of the important symptoms of breast cancer in the mammograms is the appearance of microcalcification clusters, which have a higher X-ray attenuation than the normal breast tissue and appear as group of small localized granular bright spots in the mammograms (Yu et al. 2000).These bright spots, presented as singularities, appear in the frequency domain as high-frequency. It was denoted that high-frequency features of an image can be recovered locally using the wavelet-based subband decomposition. In each subband, the coefficients of details which have high modulus correspond to singularities in the image. In order to recognize with exactitude clustered microcalcifications regions on mammograms, we asked for the opinion of the expert radiologist who marked us manually the position of the pixels corresponding to the microcalcifications. The knowledge of the band or the frequency bands occupied by the microcalcifications makes it possible to define a level of decomposition which will constitute important information a priori for the development of computer aided detection of microcalcification based on wavelet subband decomposition. Different wavelet families are available and it is not always evident to decide the best wavelet to use for the detection of microcalcifications (Gendron et al.) We propose the use of 1-D wavelet transform to find out this level.

Our algorithm consists of two main phases.

Phase 1: based on 1-D WT and composed of four steps:

- Dimension reduction of the image to reduce the dimensions of a data set. This work is performed by a cropping matlab function to delimitate the region of interest (ROI) which contains microcalcifications and a limit background area.
- We perform a localisation of microcalcifications according to notes of an expert radiologist. Then, we extract profiles of microcalcifications in two directions (vertical and horizontal).
- 1-D WT with different families of wavelet is applied on the signal up to the sixth level.
- Comparison between details coefficients of each level is done to carry out the best wavelet and its optimal level from which the microcalcifications disappear.

Phase 2: To validate the results of the first phase, we perform 2-D wavelet decomposition up to this optimal level. Then, we put at zero the approximation coefficients

of the last level which are supposed to correspond to the background of the image (breast tissues) and finally we reconstitute the image. The reconstituted image will be then filtered to keep only the frequencies corresponding to the microcalcifications. We follow the stages of figure 5.

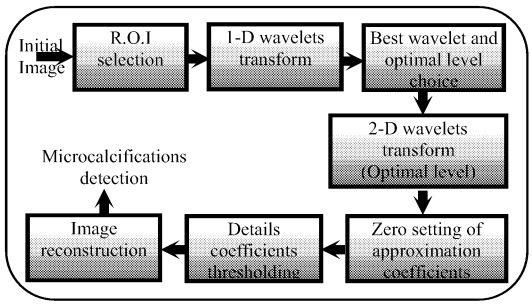

Figure 5: Computer aided detection algorithm

By applying the step described above, we noted that the number of false detections due to the noises and the nature of the breast tissues were relatively important. To reduce the number of false positives, we perform two types of operations.

First, a binary thresholding at all details subbands images. The details coefficients of all levels, which have modulus less then 50% of the maximum absolute value modulus of each level, are set to zero. This technique will decrease the rate of false detection due to noise, blood vessels, artifacts and dense breast tissue in the mammograms. Then, we reconstruct image, at the original size to preserve localization of microcalcifications.

In the second operation, we used a method of local thresholding based on moments of order one and two. The rebuilt image is divided into blocks of size 5x5. The blocks which do not present a strong variance or wide amplitude of the gray level are put at zero. We obtain a matrix of zeros and ones which we call matrix of the blocks. We carry out then a product between the matrix of blocks and the matrix of rebuilt image.

The results obtained with the two operations are presented in the following paragraph.

EXPERIMENTAL RESULTS

The first step in phase 1 is the dimension reduction of the image to reduce the dimensions of a data set. (figure 6).

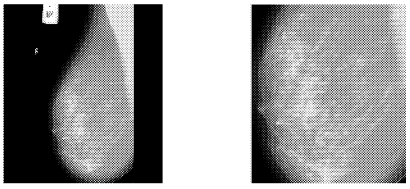

Figure 6: Original image (1024x1024) ; Cropped image (550x540)

The Second step is the extraction of microcalcification profile from digital mammograms. (figure 7 a,b).

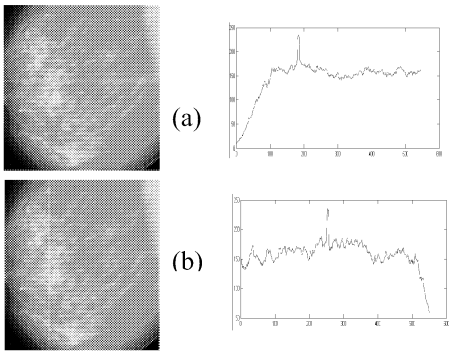

Figure 7: Microcalcification profile along; a: Horizontal direction; b: Vertical direction.

Next, 1-D multiresolution wavelet transform is applied until the sixth level. Different wavelet families with different null moments have been used. The best one, performed on mammograms would be the one which would provide very small detail coefficients when analyzing the normal areas whereas abnormal areas would give detail coefficients with high modulus.

The results show that the maximum details signal, are obtained using the biorthogonal 2.4 wavelet at the third level.

At the second phase of our approach, we perform 2-D wavelet subband decomposition up to level 4.

Figure 8 shows the different subbands images obtained.

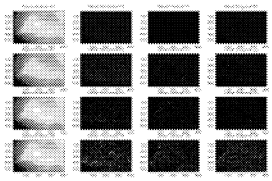

Figure 8: 4 levels decomposition

Then, we set to zero the approximation coefficients of the LL^4. Finally, we rebuild our image. The reconstituted image is given on figure 9.

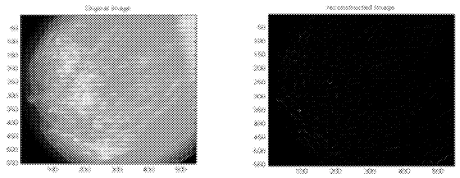

Figure 9: Original and reconstructed image

Binary thresholding is applied on the image in order to have a more readable one. The result is presented at figure 10. This image presents a certain number of false positive detections (light points which does not correspond to microcalcifications).

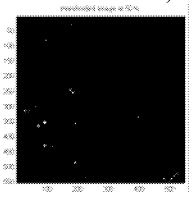

Figure 10: Thresholded reconstructed image

To reduce the number of false positive detections, we first perform a binary thresholding at all details subbands images. The result is presented at figure 11.

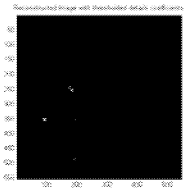

Figure 11: Reconstructed image with thresholded details

In this figure, we observe that some microcalcifications are missed with this technique. For this reason, we perform a local thresholding on the reconstructed image. The result is presented at figure 12.

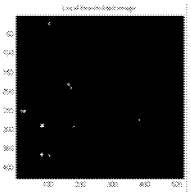

Figure 12: Local thresholded image

CONCLUSIONS

Multiresolution analysis based on 2-D discrete wavelet transform was used in our algorithm for the development of computer aided detection of microcalcifications to help radiologists in the diagnosis of breast cancer. In this paper, we studied in a first stage the optimal level of decomposition and we chose the wavelet which appears most suitable with our problems. This study showed that from a certain level of decomposition, we lose information which corresponds to the microcalcifications. In the second stage, we perform a multiresolution decomposition filter banks of the mammograms. The binarisation of the reconstituted image as well as the local thresholding gave a clear reduction in the number of false positives.

For further studies, it seems important to develop algorithms to find optimal size of blocks when using local thresholding. Also, we denote that classifier algorithms will improve the false positive rate.

REFERENCES

Bernard W.Stewart and Paul Kleihues, "World cancer Report", International Agency for research on Cancer, 2003.

Salvator MURGO "Classifications des Anomalies Mammographiques", Université libre de Bruxelles, 2002.

Ted C. Wang and Nicolaos B. Karayiannis, "Detection of Microcalcifications in Digital Mammograms Using Wavelets", IEEE Tran. on Medical Imaging, vol. 17 pp. 498-509, Aug. 1998.

K.Thangavel, M.Karnan, R.Sivakumar, A.Kaja Mohideen, "Automatic Detection of Microcalcifications in Mammograms- A Review", ICGST, 2005.

H.D. Cheng, Xiaopeng Cai, Xiaowei Chen, Liming Hu and Xueling Lou, "Computer-aided Detection and Classification of Microcalcification in Mammgrams: A survey", *Pattern Recognition, Vol 36*, pp. 2967-2991, 2003.

Damir Sersic and Sven Loncaric, "Enhancement of Mammographic Images for Detection of Microcalcifications", Fac. of Electrical Engineering and Computing, Zagreb, Croatia, 1998.

Chun-Ming Chang and Andrew Laine, "Coherence of Multiscale Features for Enhancement of Digital Mammograms", IEEE Tran. on Information Technology in Biomedical, vol. 3, n 1, pp. 32-46, 1999.

H.S. Zadeh, S.P. Nezhad and F.R. Rad, "Texture Feature Extraction Methods for Microcalcification Classification in Mammgrams", *Proc. SPIE 3979*, pp. 982-989, 2000.

Raul Mata, Enrique Nava, Fransisco Sendra, "Microcalcification Detection Using Multiresolution Methods", *icpr, vol. 04, no. 4*, pp. 4344, 2000.

S.Sentelle, C.Sentelle and M.A.Sutton, "Multiresolution-Based Segmentation of Calcifications for the Early Detection of Breast Cancer", Elsevier Science Ltd, Tran. on Real-Time Imaging, vol. 8, pp. 237-252 2002.

Peter Heinlein, Johan Drexl and Wilfried Schneider, "Integrated Wavelets for Enhancement of Microcalcifications in Digital Mammograms", IEEE Tran. on Medical Imaging, vol. 22, n. 3, pp. 402-413 March 2003.

G.Lemaur, K.Drouiche and J.DeConinck, "Highly Regular Wavelets for the Detection of Clustered Microcalcifications in Mammograms", IEEE Tran. on Medical Imaging, vol. 22, n. 3, pp. 393-401 March 2003.

Michael Unser, Akram ALDROUBI and Andrew Laine "Wavelet in Medical Imaging", IEEE Tran. on Medical Imaging, vol. 22, n. 3, pp. 285-288 March 2003.

Paul Sajda, Andrew Laine and Yehoshua Zeevi, "Multi-resolution and wavelet representations for identifying signatures of disease", IOS press, pp 339-363, 2002.

Carissa ERICKSON, "Automated Detection of Breast Cancer using SAXS Data and Wavelet Features", Master dissertation, University of saskatchewan. Saskatoon, July 2005.

Ali. M.Reza, "Wavelet Characteristics", Lab UWM White paper, Oct. 1999.

Songyang Yu and Ling Guan, "A CAD System for the Automatic Detection of Clustered Microcalcifications in Digitized Mammogram Film", IEEE Tran. on Medical Imaging, vol. 19, n. 2, pp. 115-126 February 2000.

Marlin L. GENDRON and Dr. Juliette W. IOUP "Wavelet Multi-scale Edge detection for extraction of Geographic Features to Improve Vector Map Databases", Master dissertation, University of New Orleans Physics Department, vol. 53, pp.79-92.

EFFECT OF HIGH FREQUENCY ELECTROMAGNETIC FIELD ON HUMAN HEAD USING MULTI-LAYER MODEL

Ossama E. Gouda
Faculty of Engineering
Cairo University, Egypt

Adel Zein E. M
Higher Institute of Energy
Aswan, Egypt

Ghada M. Amer
Higher Institute of Technology
Benha University, Egypt

KEYWORDS
Method of moment, Effect of HF, EMF, Human head.

ABSTRACT

This paper describes the research work done by using the method of moment in investigating the effects of high frequency electromagnetic field (EM) on the human head. The behavior of the human head under EM radiation is modeled as a multilayer model in order to assess biological effects on the human head. The specific absorption rate (SAR) in the human head model is calculated, where the SAR is the main parameter used for indicating the effects of EM field.

INTRODUCTION

The increasing use of electromagnetic (EM) devices in our society for a variety of purposes has caused growing concern about possible health hazards produced by EM radiation. This concern has led to an increased intensity of research aimed at identifying possible hazards due to EM radiation. In particular, a considerable amount of theoretical work has been devoted to the investigation of EM effects on human being using various shapes [1]. In this paper, the head model is inhomogeneous and classified into only three layers of material (average skin dray/wet properties for first layer, average skull properties for second layer and average brain properties for third layer). The tissue parameters are derived by Gabriel, et al. [2]. This data is available on Federal Communication Commission's website in the United States. Table (1) shows the real part of the dielectric permittivity (ε_r), conductivity (σ S/m) and mass density (ρ kg/m^3) of tissues used in the simulation of three layer model and homogenous model at high frequency electromagnetic field [2]. The applied antenna consists of a quarter-wavelength monopole of radius 0.0025m at 900MHz and 0.0012m at 1800MHz mounted on a mobile handset (treated as a metal box of 5cm*8cm*18cm), and radiated power of 0.32 watt. The purpose of this paper is to investigate the interactions between the handset antenna and the human head. Where the SAR is the main parameter used for indicating the effects, one gram average SAR on the above systems is calculated, which is recommended its limit value 2W/kg in the Federal Communications Commission, FCC and International Commission on Non-Ionizing Radiation protection, ICNIRP. In addition to these results, ten grams average SAR is calculated [3]. Also the results of the three layer model are compared with those of homogenous model [4].

Table 1: Real Part of the Dielectric Permittivity (ε_r), Conductivity (σ) (S/m), and Mass Density (ρ) kg/m^3 of Tissues used in the Simulations at 900 and 1800MHz.

Properties of tissues	dielectric permittivity (ε_r)	conductivity (σ) (S/m)	mass density (ρ) kg/m^3
900MHz (homogenous)	45.8	0.77	1030
1800MHz (homogenous)	43.5	1.15	1030
900MHz Skin dray/wet	43.8	0.86	1100
900MHz Skull	20.8	0.34	1850
900MHz Brain average	45.8	0.77	1030

FEKO SIMULATION AND VALIDATION

The FEKO program is based on the Method of Moments. Electromagnetic fields are obtained by first calculating the electric surface currents on conducting surfaces and equivalent electric and magnetic surface currents on the surface of a dielectric solid. The currents are calculated using a linear combination of basis functions, where the coefficients are obtained by solving a system of linear equations. Once the current distribution is known, further parameters can be obtained e.g. the near field, the far field, radar cross sections, directivity or the input impedance of antennas [5]. The simulation procedure is as follows:
1-Create the human geometry model
2-Define the frequency, human parameters and meshing parameters,
3-Create the monopole and mobile handset; define parameters for segmentation, excitation and radiation power
4-Solving the problem
5-Calculate the near field and SAR.
Table (2) shows the calculation information from FEKO program.

RESULTS AND DISCUSSION

Calculation Position

As it cannot be expected that the user will hold the mobile phone exactly in one well defined position, therefore there are different operational conditions. Let a reference line describing the phone is defined as a line which connects the center of the ear piece with the center of the bottom of the case and the human head position is given by means of a reference plane defined by the following three points: auditory canal opening of both ears and the center of the closed mouth [6]. With these definitions the calculation position is given by: The telephone line shall lie in the reference plane (40 degrees around x-axis).

Table 2: Calculation Information

FEKO Program	900MHz homogenous	1800MHz homogenous	900MHz (3-layers)
The total computation surface: -wire segment of dipole antenna -metallic triangles of mobile handset -dielectric triangles of three layer human head model	 9 188 1480	 9 502 2868	 9 368 6560
Total number of basis function	4730 unknown	9365 unknown	20240 unknown
Memory requirement on disc	341.383 MB	1.307 GB	6.104 GB
Total time required for calculations	6.482 hours	12.677 hours	38.862 hours

The angle between the phone line and the line connecting both auditory canal openings shall be reduced (10 degrees around y-axis) until the device touch the human head. A FEKO simulation of the human head and the handset antenna interaction is shown in figures (1-a) and (1-b).

Specific Absorption Rate

It is generally accepted that the Specific Absorption Rate (SAR) is the most appropriate metric for determining EM effect exposure in the very near field of a RF source [7]. The *SAR* (W/kg) at any point in the model can be determined from the calculated electric field (V/m) at that point by [8]

$$SAR = \frac{\sigma |E|^2}{\rho} \qquad (1)$$

Where:

E is the internal electric field (r.m.s) value (v/m),

σ is the conductivity (S/m) of the tissue in which the calculation is done,

ρ is its mass density (kg/m^3).

SAR can be expressed in two ways; one way is to compute average value of SAR in cell of one gram and the other way is to compute an average value in a cell of ten grams. Also SAR can be calculated over a whole body. SAR is important in the antenna design process since the value is restricted and it is not to be exceeded.

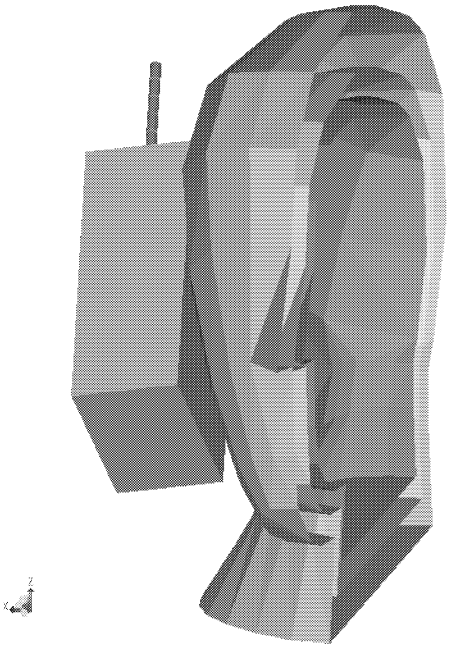

Figure 1-a: Front view of FEKO Model and Calculation Position, where the Phone Line Rotated 10 Degree Around y-axis.

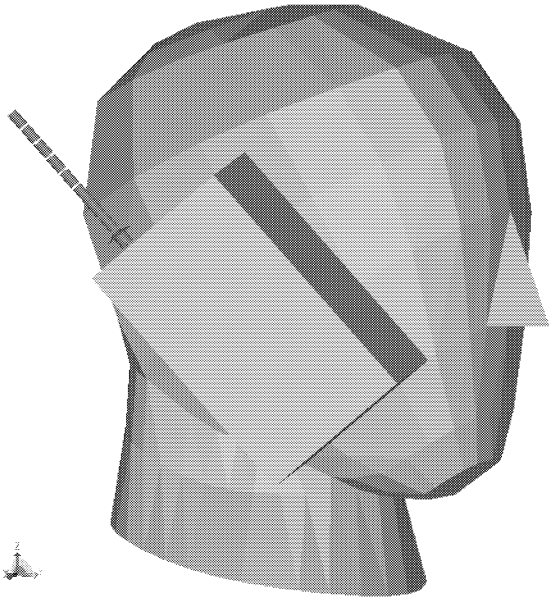

Figure 1-b: Side View of FEKO Model and Calculation Position, where the Phone Line Rotated 40 Degree Around x-axis.

In Sweden and the rest of Western Europe the maximum average value is set to 2 W/kg over ten grams by standardization organization European Committee for Electrotechnical Standardization, CENELEC. In United States and many other countries the maximum average value is set to 1.6W/kg over one gram by another standardization organization called – the Federal Communications Commission, FCC. [9]. Also SAR is a measure of the local heating rate dT/dt, viz.:

$$\frac{dT}{dt} = \frac{SAR}{c} \text{ C}^{o}\text{/s} \qquad (2)$$

Where c is the specific heat capacity of tissue in J/kgC^{o}. This assumes "ideal" nonthermodynamic circumstances, i.e., no heat loss by thermal diffusion, heat radiation, or thermoregulation (blood flow, sweating, etc).

RESULTS

Figures (2) and (3) show the SAR and internal electric field variation along x-axis, that is "from one ear to the other" of the three layer human head model, it is noticed that the SAR decreases within the second layer (skull), which have lower conductivity, then the SAR decreases rapidly with increasing depth from the phone head side as a result of the skin effect or penetration depth, where the penetration depth and reflection at the interface surface determine how much energy reaches deep into the body.

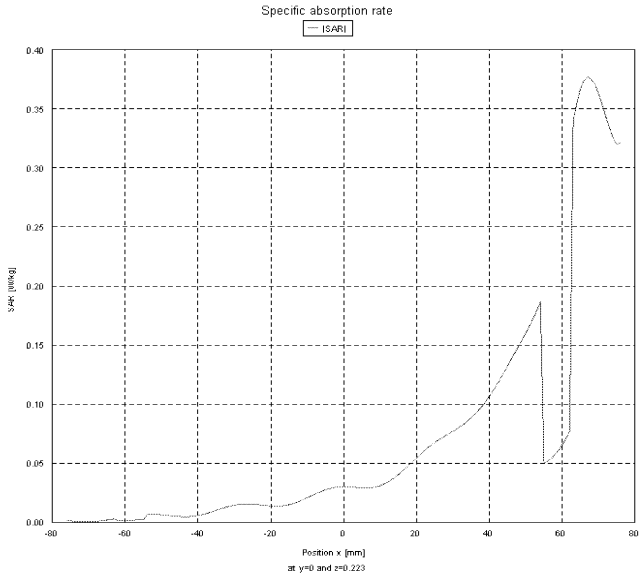

Figure 2: Penetration Curve of SAR Along x-axis

Figure (4) shows the SAR variation along *x*-axis, that is "from one ear to the other" of the homogenous human head model at 900MHz and 1800MHz, it is noticed that for 1800MHz the SAR decreases more rapidly with increasing depth from the phone head side than that for 900MHz . That can be explained as: at 1800MHz, where the penetration depth is reduced by about 50% than that at 900MHz, most of the induced fields are already absorbed in the peripheral layer (closed to the mobile) compared to 900MHz. Figure (5) show the distributions of the local SAR at y=0 plane for three layer human head at 900MHz, it is noticed that the first layer (skin) have higher local SAR values and the second layer (skull) have lower local SAR values. Figures (6) and (7) show the positions of the cubes o one gram and ten grams tissue, where max. SAR occurs. Results for average SAR in W/kg over whole head model max. SAR in one gram and ten grams tissue in the shape of a cube for homogenous model and three layer model at 900 and 1800MHz are presented in table (3).

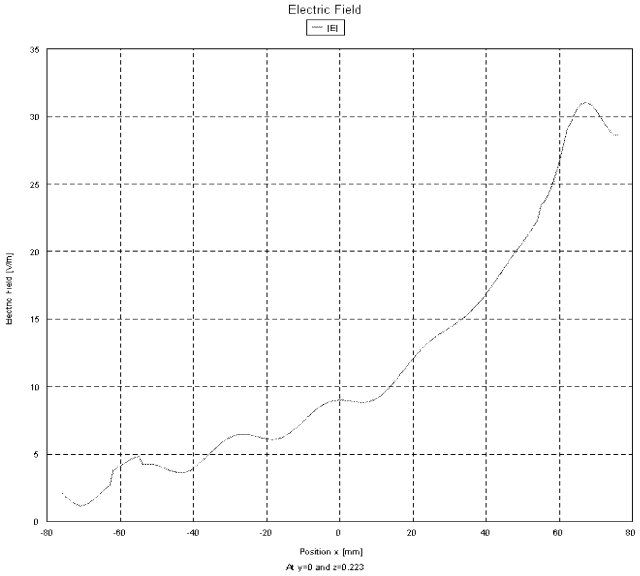

Figure 3: Penetration curve of Internal Electric Field Along x-axis

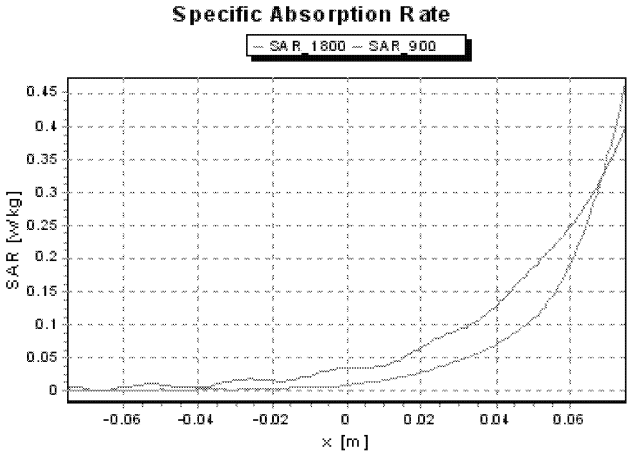

Figures 4: Penetration Curves of SAR Along *x*-axis

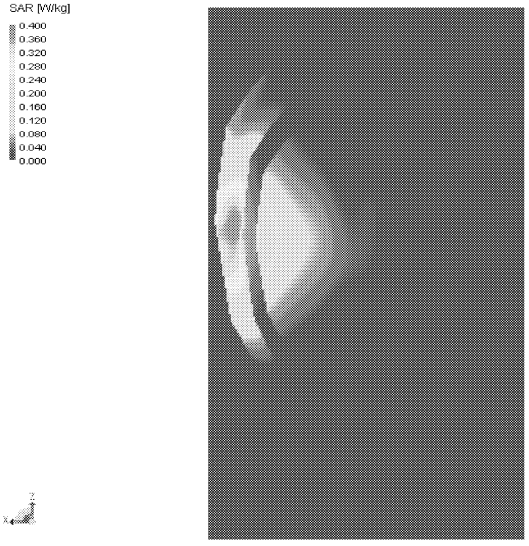

Figure 5: SAR Distribution at xz Plane and y=0

From table (3), for a homogenous models, it is noticed that, where the spatial-peak SAR values for (one gram and ten grams) tissue in the shape of a cube for 1800MHz are higher than those for 900MHz, the average SAR, over whole human head, at 1800MHz is less than that at 900MHz, that can be explained as the SAR regions produced by 900MHz monopole antenna are more extended as compared to those induced by 1800MHz monopole antenna. This is due to the fact that the higher rate of energy absorption for a high frequency does not allow much energy to penetrate to a region that is located towards the back of the body.

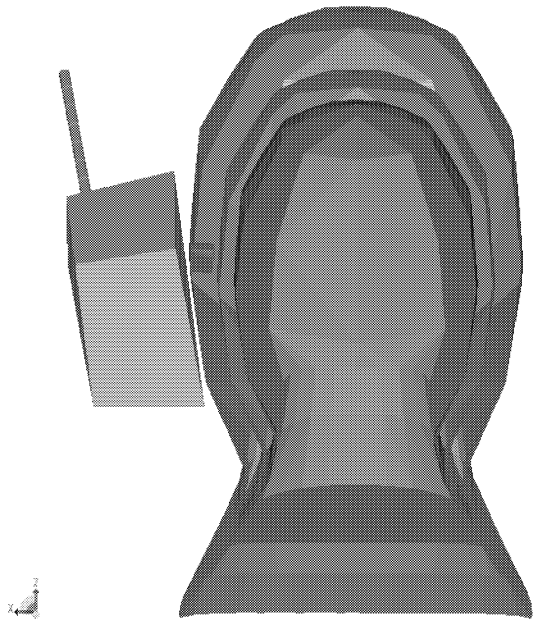

Figure 6: Presents the Cube of One Gram and Max. SAR

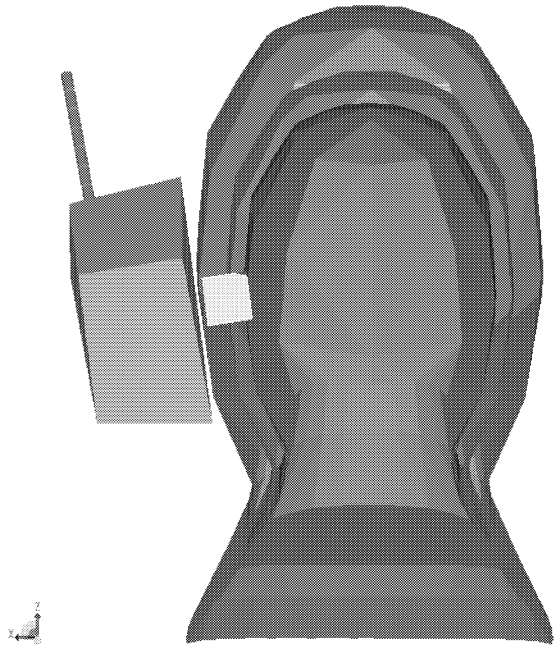

Figure 7: Presents the Cube of Ten Grams and Max. SAR

Table 3: Average SAR and Max. SAR in W/kg for (One Gram and Ten Grams Tissue in the Shape of a Cube for 900MHz and 1800MHz.

SAR	Average SAR Whole head	One gram SAR_{max} (W/kg)	Ten grams SAR_{max} (W/kg)
900MHz (homogenous)	0.02908	0.4221	0.3338
1800MHz (homogenous)	0.01301	0.8291	0.5432
900MHz (three layers)	0.01611	0.3826	0.2273

CONCLUSIONS

The obtained results show that the spatial-peak SAR values as averaged over one gram on the human head model obtained with a radiated power of 320 mW, are well below the limit of 2 W/kg. At max. SAR of 0.45W/kg, the associated heating rate will be less than $0.00013C^{o}/s$ in the human tissue where the average human body specific heat capacity $=3.47kJ/kgC^{o}$. This means the human tissue would take more than two hours to increase the temperature one degree Celsius, even without blood or other cooling system. The results have shown that it is possible to support experimental findings of phantom studies with numerical computer models. So there are possibilities to validate both the experimental results and the calculations. Finally the FEKO simulation package used in this study has been proved to be adequate in evaluating the interaction between a handset antenna and the human head, but it needs a long time and requires a large memory on disc to obtain the results.

REFERENCES

F. Akleman & L. Sevgi, "FDTD Analysis of Human Head Mobile Phone Interaction in Terms of SSAR Calculations and Antenna Design", Proc. of IEEE-APS Conference on Antennas & Propagation for Wireless Comm., pp. 85-88, November 1995,2-4, Waltham, MA, USA

C. Gabriel et al., "Compilation of the Dielectric Properties of Body Tissues at RF and Microwave Frequencies", http://www.brooks.af.mil/AFRL/HED/ hedr/reports/dielectric/Title/Title.html, 1999.

ANSI/IEEE, "IEEE Standard for Safety Levels with Respect to Human Exposure to Radio Frequency Electromagnetic Fields, 3 kHz to 300 GHz", ANSI/IEEE C95.1-1992 (see http://standards.ieee.org/cgi-bin/status), 1992.

Adel Zein E.M and O. S. Dautov " Application of FEKO program to the analysis of SAR on human head modeling at 900 and 1800 MHz from a handset antenna" VI international conference on electromagnetic compatibility and electromagnetic

ecology EMS-2005, St.-Petersburg, Russia, on June, 21-24,2005,in English.

FEKO program http://www.feko.info/contact.htm and http://www.emss.de.

EUROPEAN STANDAR EN 50361, Basic standard for the measurement of Specific Absorption Rate related to human exposure to electromagnetic fields from mobile phones (300 MHz – 3 GHz), CENELEC European Committee for Electrotechnical Standardization, rue de Stassart 35, B-1050 Brussels, July 2001.

Allen S G, "Radiofrequency field measurements and hazard assessment", Journal of Radiological Protection, Vol ll-1, 1996.

FCC, OET Bulletin 65, "Evaluating Compliance with FCC Guidelines for Human Exposure to Radiofrequency Electromagnetic Fields," Edition 97-01, released December, 1997.

"SEMCAD Reference Manual". Bundled with SEMCAD and available at: http://www.semcad.com/downloads_free/SEMCAD_RefManual.pdf.

MULTIMEDIA SIMULATION

HiperJanela, an Upper Dimension for the Society of Information

© J. Manuel Feliz-Teixeira

May 2006

GEIN – Section of Management and Industrial Engineering
Faculty of Engineering of the University of Porto, PORTUGAL
Email: feliz@fe.up.pt

KEYWORDS: Information Society, ambience simulation, horizontal communication, citizenship, media, global audience, global consciousness.

ABSTRACT

This article describes an idea for achieving a higher level of global visibility of certain events and for improving and stimulating citizens (in this first approach, European citizens) for a higher level of consciousness of the diversity of European reality. At present, each country or region of Europe is still living in a sort of psychological space circumscribed by the old sense of geographical border, and where information about other realities is mostly spread by means of conventional media, newspapers, magazines, TV, etc., as well as by the Internet and, in the latter case, by the information recorded by travellers. This is how the conceptions of Europe and of European citizenship are slowly developing. The proposal presented in this article, named "*HiperJanela*", aims to bring citizens to an upper level of on-time-real-information across the entire European space, by means of a global network of public video-interfaces which we call the *HiperJanelas* (notice that "*Janela*" is the Portuguese word for window).

1. Introduction

As a first notice, we would like to state that the idea presented in this article is to be considered anti-patent, that is, it is offered to the public by its author and anyone may implement it freely without the need for any special permission, other than a symbolic contribution in order to cover the author rights. Please contact the author at feliz@fe.up.pt, in such a case.

In these days of the *Information Society*, one of the main aspirations of the European Commission seems to be the creation not only of the institutional European space, but also of a certain European mind and citizenship (E.U., 2006). Although the European mind already exists, in its diversity, strong and well established, and based on a wisdom built along several centuries of a rich history, the visibility of such a mindset is not yet corresponding to the concept of "one-voice Europe". The weak knowledge about what is occurring in the various centres of Europe and the poor information reaching ordinary citizens are, in our point of view, obstacles to faster development. In one sense, ordinary citizens know very little about the places of other countries, how life runs in those places, how people work, what problems they face daily, and how they surmount them. Discussion and learning through comparison is therefore not stimulated. On the other hand, directives and incentives of European Union institutions hardly reach "normal" citizens, since they are usually broadcasted to the public by the media or by some country dependent institutions. Visibility of European directives, tendencies and proposals is also poor. Although such information can also be accessed via Internet, it is recognised that people often do not plan their lives based on getting constantly informed by those means, since they are fully focused in other aspects of their lives. At the same time, any polls or events that may be important for the population may well appear obstructed by regional information, since it is

usually delivered by the media. This way, both the information from European institutions to the public and from the public to the European institutions is, in the present approach, deficient, mainly because there is always a third party between the two interlocutors.

Therefore, aims like those of improving Commission ability to listen, improving communication in Europe, better perception of policies, institutions, task, etc., and especially facilitating the ability to communicate with any European region, will hardly be achieved by means only of the actual network of information, where a significant quantity of information is handled through a vertical structure. In the following sections, we will expose our vision of the actual situation and confront it with a simulated ambience based on a new communicational proposal, the *HiperJanela*, which may be considered the basis of a more flexible and popular horizontal network for the improvement of European citizenship.

2. The present situation

As previously said, the present situation of communications among citizens and institutions in European Union (E.U.) is very much based on peer-to-peer contacts, like email, telephone, etc., and, when the information is to be broadcasted, by introducing some natural third parties between the two interlocutors . These third parties are frequently regional institutions or even regional media operators. Anyhow, the practice shows that frequently a certain obscurity is maintained in the public concerning certain events of the Union, obviously because the media cannot be fully dedicated to broadcasting such information. On the other hand, citizens are also not commonly aware of the day-to-day life in other places, and therefore have no idea of how people normally live, no way of comparing and reflecting on their own lives, in order to improve them, and get a more realistic perspective of our common space. Figure 1 aims to represent the actual type of system, in terms of information sharing. In a certain sense, Europe at present still is a universe made up of several domains which are still very enclosed. We believe that this is an obvious obstruction to the intellectual perception of the whole and, therefore, also an obstruction to the evolution of a superior state of awareness.

In figure 1, these *domains* are schematically represented. Peer-to-peer communications are shown in the form of *dashed* links, and broadcasts in terms of *solid* lines. The E.U. institutions use these two types of approaches to interface with citizens. Third parties, as depicted in the figure, which in many cases operate with other objectives than solely to inform people, are usually responsible for broadcasting.

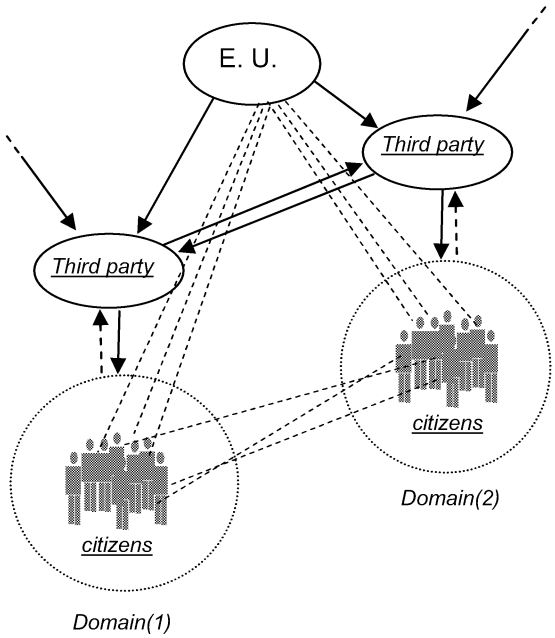

Fig. 1 Actual communication structure in the E.U.

A conclusion that can easily be drawn from this scheme is that citizens will be only informed (1) by what third parties deliver; (2) by informing themselves directly at the European Union Internet sites and institutions, or (3) by what the community of people will share by email, telephone, chat, etc. This is obviously a system which is not only far from being optimized but also susceptible to generating information noise. As we said, we claim that this is extremely obstructive to faster and cleaner development of European citizenship.

3. The *HiperJanelas* communication space

The prime aim of the *HiperJanela* concept is to make the communication of different realities in an extensive geographical space as reliable and horizontal as possible. In a sphere where visibility, flexibility, trust and reliability are key words for the development of a progressive society, this aim is appropriate. The *HiperJanela* space must therefore allow the following: (1) information from E.U. will

reach the citizens directly, and without being filtered or delayed by third parties; (2) citizens will be able to have an on-time real visual perception of life running in diverse locations of the Union, by simply looking through the windows; (3) citizens will be free to use such visual information for becoming more aware of events, proposals and possibilities, and even for personal contact with other members of the community.

In our view, this may be achieved by installing high resolution video-interfaces between the various domains belonging to the E.U. space. As suggested in the scheme of figure 2, each *HiperJanela* installed between domains *i* and *j* (HJ_{ij}) will ensure the exchange of an on-time video of the two realities to their citizens. Citizens *i* will literally have a view on the universe *j* and vice versa. In effect, people would then have the possibility of *looking into* the other side and observe, learn and communicate through the *HiperJanela*.

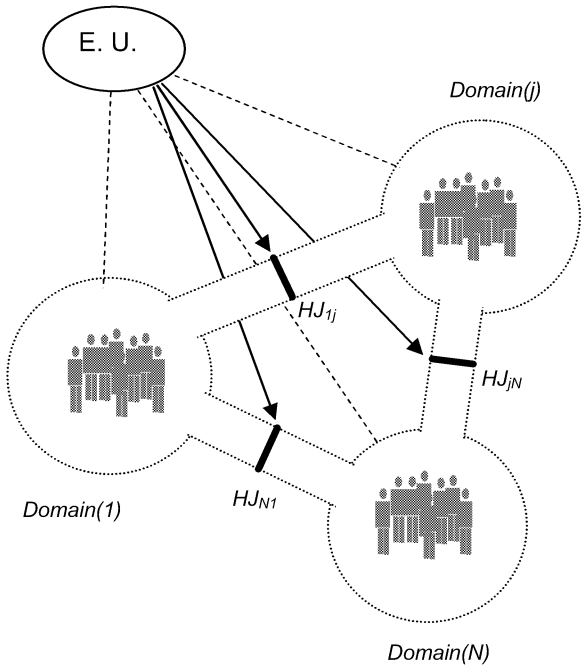

Fig. 2 Proposed structure using *HiperJanelas* (HJ)

At the same time, E.U. institutions will be now able to deliver specific information to a specific domain or even use these windows to directly broadcast information for all. The citizens' feedback can therefore be pumped up and simply completed by accessing the sites on the Internet proposed in the window, for more detailed information or actions. This scheme, which does not have to eliminate third parties from the process, but instead reduce their charge, establishes a direct feedback between citizens-citizens and citizens-E.U.

It is obviously not practical to maintain a link to each domain in all the domains at the same time, however, it is perfectly possible to commute these links after a certain period of time in order that all the domains can be scanned and become visible. The system is therefore a sort of rotating presentation of pairs of video-images, through which people will slowly get to know and develop a stronger sense of community. A *HiperJanela* in Nuremberg can, for instance, be connected during a week to Porto, and then be commuted to Madrid and stay there for the next week, for example. At the same time, other *HiperJanelas* installed in the European space would be operating in the same manner, giving people a better sense of how life runs in the overall communitarian space, while letting E.U. institutions achieve an excellent efficiency on broadcasting information.

4. A simple *HiperJanela* system

It is possible that this kind of space can be implemented in various ways, but here we propose a system which is very simple and reliable. It is based on a simple *video-panel*, perhaps made of several plan TV screens, to which a digital video-camera system is adapted. The images from the *Domain(i)* are captured by the camera C_i and then transmitted to the *Domain(j)*, and vice versa, at the same time, as represented in figure 3.

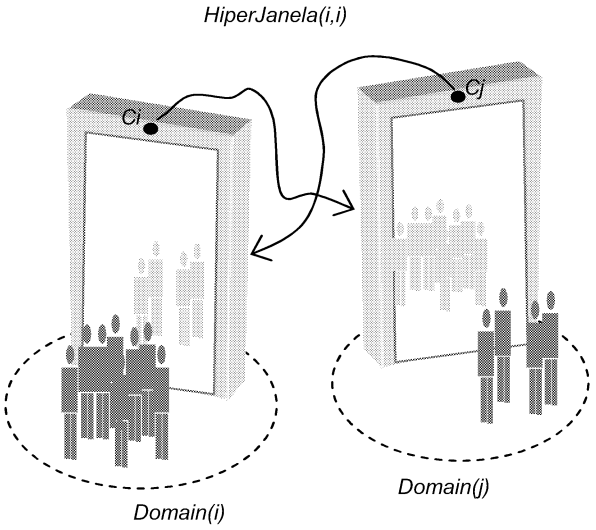

Fig. 3 The *HiperJanela* system

As we now see, at the very same moment that

people can be informed about E.U. by some text messages presented over the image, in the form of running banners, or in a corner of the panel, for example, people can also *look into* the other side and say greet other people, or even communicate other messages visually, almost instantaneously. Friends, for instance, may sometimes meet at the *HiperJanelas* and send fast messages, arranging meetings, exchanging numbers or sentences written in a paper, and so on. People will learn to use this resource as they require, while developing their own creativity. The sense of a common space will quickly emerge as an upper dimension of our *Information Society*. Politically, there will be also many advantages for the democracy, since the visibility of the diverse realities will be tremendous, and the information shared almost free of noise. This can be done either by fast Internet connections or by using satellite communications, for example. And people will simply feel the diverse reality in which they are living in. The following simulated images aim to give a better idea about what can be achieved by means of the implementation of such a concept.

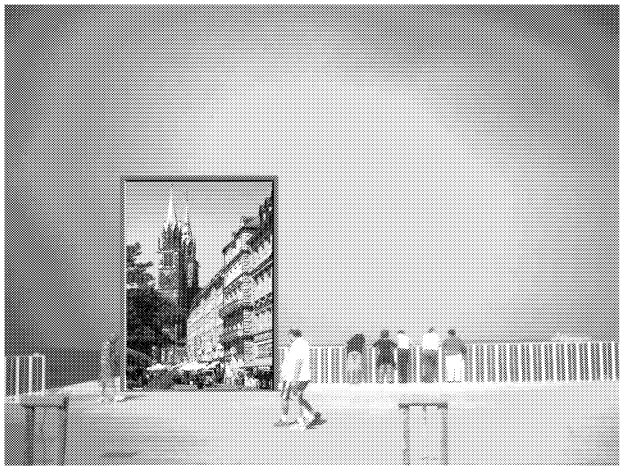

Fig. 4 *HiperJanela* between a street of Nuremberg, Germany, and a location near the sea in Porto, Portugal

Notice that the *HiperJanela* dimensions can also be diverse, and therefore these tools will be easily adaptable to the spaces where they are to be installed. A *HiperJanela* can be simply installed as a panel in a plaza or in a street, or inserted in the space of a real door or window of a building, in a café, for example. This, of course, already gives an idea of the powerful vehicle of information contained in the *HiperJanela*. Technologically, it is a concept that presents no challenges for the actual information technology, and, at the same time, the tendency will be to improve the quality of its images as time passes and technology develops even more.

Fig. 5 *HiperJanela* installed at a corner of a building of *Maximilianstrasse*, in München, Germany

Fig. 6 *HiperJanela* installed in a street of Porto connected to *Marienplatz*, München, Germany

Fig. 7 *HiperJanela* installed at the *Plaza Mayor* of Madrid, Spain

The most interesting aspect of this proposal, however, is that it introduces such a high level of information on many levels of citizens' lives. In effect, one can imagine an esplanade of Lisbon linked to an esplanade of Vienna; a metro station of

Paris linked to a metro station of Napoli; a public café in Brussels linked to a public café in Roma or Barcelona, etc. The ability to join all these ambiences while broadcasting the messages (or some small images) from the E.U. institutions to all of them is the precious potential of this system.

5. *HiperJanelas* and Arts

As another interesting curiosity of this system, we would like to point out the effects that can be achieved by arts in these windows, which can even make each *HiperJanela* a sort of attractive touristic element.

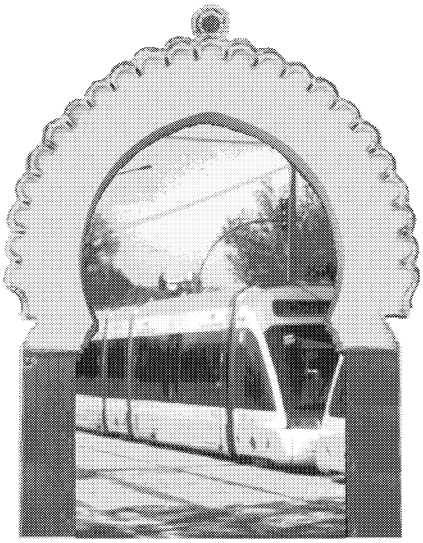

Fig. 8 *HiperJanela* bordered by an Arabic door

Fig. 9 *HiperJanela* with a running banner moulded by a Portuguese door with *azulejos*

In figure 8, is simulated a *HiperJanela* of Andaluzia connected to a surface tram somewhere in another location in Europe. On the other hand, in figure 9, a *HiperJanela* enclosed in a Portuguese door with *azulejos*, with messages passing in a running banner, is linked to a view on the Plaza Mayor of Madrid.

6. *HiperJanela* operators and advertisement

Finally, it is also interesting to make some considerations concerning the utilization of these windows by private operators and, consequently, for the use of advertisement. Although in our point of view the primary objective would be completely perverted if *advertising* would invade such a precious space (we expect that it will not happen), private operators could be given a little space for advertising and, therefore, for maintaining the system, as long as such advertisement would not interfere with the principle of the *HiperJanela*. In such a small space reserved to them, private operators could be induced to advertise only something related to the region or the place where the *HiperJanela* was installed. For instance, if at a certain moment the *HiperJanela* is connected to a place in Italy, then the priority would be given to the advertisement of products from that region or country, therefore improving also the visibility of regional products and tourism. This serves not only to improve the visibility of how people live, but also the visibility of each people's culture.

7. Conclusions

We may conclude that the *HiperJanela* concept is expected to promote and help to implement not only a direct and a horizontal information structure between citizens, but also the ability of the European institutions to quickly and reliably listen and communicate with the population. The *HiperJanela* may therefore be considered a hyper-window linking different realities across Europe and, that way, contributing to the development of a superior state of conscience and of the European mind as a whole. The importance of these windows will be even more noticed in the peripheral regions, since these are usually the last ports reached by waves of information. So, the actual peer-to-peer contacts between people and the broadcast of E.U. information through the normal media operators will be complemented by the *HiperJanela* features, which include a horizontal type of information share for connecting different people and different cultures.

References:

E.U. (2006). *Annual Work Programme on Grants and Contracts in the Field of Communications for 2006*. Brussels: European Union.

Author Biography:

J. Manuel Feliz-Teixeira graduated in Physics in the Faculty of Sciences of University of Porto, Portugal, and MSc and PhD from the Faculty of Engineering of the same university. His work has been related to various matters, from optical communications, solar energy and seismology to, more recently, the simulation of complex systems in management science, like warehouse and supply chain. His PhD thesis is on “Flexible Supply Chain Simulation”.

Experimental Web Content re-authoring System [EWCRS]

May Haikel Riadh
Iraqi Commission for Computers and Informatics, Informatics Institute for Postgraduate Studies.
Baghdad, Iraq.
E-mail: mayhr60@yahoo.com

Prof. Dr. Hilal M. Yousif
Graduate College of Computing Studies, Amman Arab University For Graduate Studies,
Amman, Jordon.
E-mail: hilal@aau.edu.jo

Dr. Akram M. Othman
Applied Science University
Amman, Jordon
akram.othman@asu.edu.jo

KEYWORDS

Computing Device, Content Adaptation, Re-authoring technique, XML, XSL.

ABSTRACT

In this paper we present an experimental Web content re-authoring system [EWCRS] for mobile devices. The system enables the presentation of Web content by considering the problem of small screen display of mobile computing devices, also independent-device access to web content is considered.

The focus has mainly been on the adaptation of HTML web page content to make it viewable on mobile devices, constraint that no server-side content adjustments are assumed.

The adaptation is done by using the re-authoring technique started by parsing the HTML web page and converting it to tree structure.

This conversion will separate presentation from content which will be more efficient in dealing with content, then converting to XML document that is a well structured document.

The result is a device independent user interface that could be shown on any device. The output shows TOC that consists of list of hyperlinks, each either the header of the web page or a title of a paragraph or using the first sentence elision as hyperlink and a link to image that will be resized to fit on mobile screen.

A major advantage of this adaptation is to deliver content with multiple versions and XML/XSL transformations to a number of mobile devices and save time and power by eliminate scrolling vertically and horizontally the page content.

INTRODUCTION

Computing devices such as Personal Digital Assistants (PDAs) and mobile phones have been increasingly used and getting more powerful every day. Although the latest PDAs are even able to display frames, it is still important to adapt the content for these devices in order to provide a satisfactory surfing experience for users. Web content access will not only have to support mobile access, but will also have to deal with other forms of web access such as voice interfaces. [EK02]

The common assumption was that a web site would always be accessed by a browser found on a personal computer or a laptop. Recent developments in mobile computing software and hardware not only have changed this view, but have also increased the importance of *device-independent* access to Web content: The ability to access web sites using a wide variety of *web devices*. [HF03]

Web content and applications should be generated or adapted for a better user experience. Device independence principles are independent of any specific markup language, authoring style, or adaptation process. So HTML is not a device independent markup language due to its mixture elements of content and presentation. A good device independent application is one where content can be specified in a unified, optimized way on many different kinds of devices. [TB96]

One way, according to device independence principles, is to use styling languages CSS or eXtensible Stylesheet Language (XSL) to add style and presentation information to content written in XML, and then the web output will be a suitable content format for a mobile browser. [RG03]

EXPERIMENTAL WEB CONTENT RE-AUTHORING SYSTEM [EWCRS]

We try to build an Experimental Web Content Re-authoring System (EWCRS) that can be used for independent-device access to Web content taking into consideration the types of adaptation, method of adaptation, and adaptation technique. There are several ways to adapt a conventional desktop HTML page to better fit on a device; web page re-authoring taken as an example system that can be of great interest.

The concepts of HTML page parsing is introduced, extract content from the page, and convert these content to XML document, content processing and XSL stylesheet preprocessing to render the new content to be displayed on mobile devices.

This introduces a system for a device-independent web content adaptation, the system is structured as follows:-
First, a requested to web page in HTML format is made.
Second, an overview of the re-authoring system is given.
Third, the concepts of page parsing, content processing technique and XSL stylesheet pre-processing are presented and discussed.

SYSTEM DESCRIPTION

The experimental system introduces and uses three techniques, *page parsing, content processing technique,* and *render to mobile device* that allow mobile users to access web content and the sizes of generated pages will be according to the characteristics of a device that is being used. These techniques overcome the problem of displaying web pages on devices with small displays and memory sizes. The adaptation of content for a web page and rendering the content to mobile devices is performed during the processing stage by the administrator which has full control over the whole system; Figure (1) shows the complete system diagram.

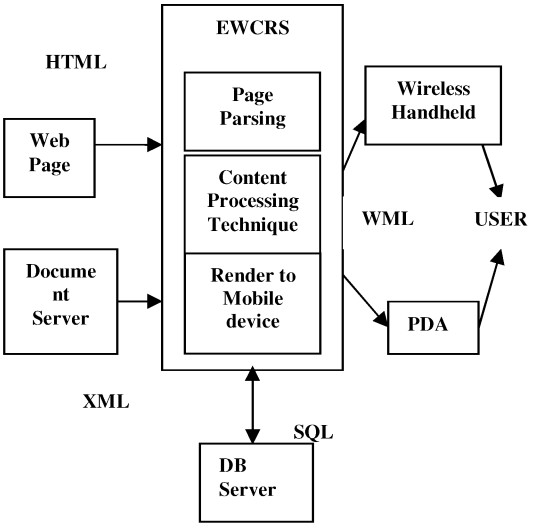

Figure 1: The complete system

THE EXPERIMENTAL SYSTEM ARCHITECTURE

The experimental system is to analyze the web page, examine its structure, extract content, re-engineer a page, and then display the modified web page on a mobile device. This usually creates a multi-dimensional document structure from the flat two-dimensional web document.

Figure (2) shows the main parts of the experimental system [EWCRS], theses are: the parse engine part that parses the requested web page in HTML format and extracts the content from the web page, the content re-authoring part that will convert the extracted content from the parse engine part to XML document and apply the content re-authoring processing, the user interface generator that will render the adapted content from the previous part to device-independent type to display the new content on different mobile devices and the services part which consist of email and SMS.

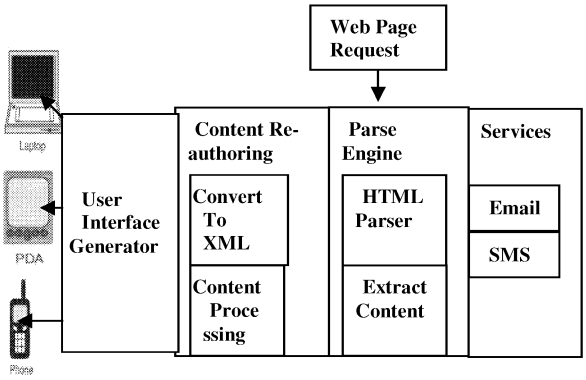

Figure 2: EWCRS architecture

The Parse Engine

This part of the system accepts a request from the user to display a web page which is in HTML format on their mobile devices; the parse engine will analyze the web page structure and extract the content from web page as shown below:

HTML Parser

HTML represents a certain range of hypertext information, it is a simple markup language used to create hypertext documents that are platform independent. Since this type of pages is used to be displayed on PC's screens that do not fit in to mobile devices screen, so it needs to be adapted.

The first step is to enter the web page to HTML parser that will parse it as:

- Handles HTML frames, Frameset and Frame tags describe the frame structure in HTML, for each frame whenever the parser encounters a Frameset element, it recursively calls itself to iterate through each Frame element, inserting it into the tree and effectively flattening the structure.

- Constructs an Abstract Syntax Tree (AST), which many web pages use extensively to partition pages into separate areas. Starting with the root, labels each node of the AST with a unique identifier and starts with the text part by identifying each <p> tag, i.e. paragraph, then iterates through section headers from <h1> … <h6> if there is any, then retrieves any embedded images so that their size can be determined (as

necessary) as shown in Figure (3), this process is done on the client side.

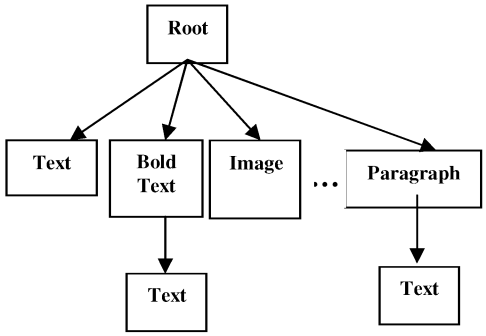

Figure 3: Parse tree of HTML Page

Parsing HTML web page is not an easy task, since most of them (pages) do not have a standard structure, so many tags, logos, tables, banners … etc are difficult to manipulate during parsing, all the previous work done in this field uses the parse engine of their proxy server and not build a parse engine to parse the HTML. Our parse algorithm is shown below.

The parse algorithm for the HTML document (Algorithm 1) is shown:

Algorithm (1)
Parse (in Q: sentence; G: set of rules; out T: parse tree)
Begin: initialize T to be a tree with root "S";
Loop while there are non-terminal leaves in T
Pick a non-terminal leaf L of T;
Choose a rule in G of the form "L -> RHS"
If RHS is a word W
Then choose an occurrence O of W in Q;
Associate O with L;
If the order of leaves in T violates the order of
Associated words in Q then fail
End if;
Else
Make children for L corresponding to RHS
End if;
End loop
If not all words in Q are attached then fail;
End.

Extracting the Content
The second important part of the parse engine is the capability to extract content from AST, and save these contents in a database file to be processed in the next step.

- This involves structural analysis of the Abstract Syntax Tree (AST) by exploiting the HTML data structure from the AST.
- Once segmented, content extraction can be attempted by classifying these segments into various classes, such as image, text, story (large contiguous chunk of text), titles, side bars, tables, top bars, advertisements and so on.
- Extraction and processing images also play a large part in this process. Classification of these images into various classes has also been attempted.

Clearly there is a need to keep content and presentation separated from the beginning of the information chain for flexibility. Information should stick to the principle of "single content, multiple accesses", i.e. it should be originated in a common form which is automatically interpretable and transformable to different presentations for a wide range of requesting clients with different capabilities. Thus the presentation level must not be fixed, but flexibly interchangeable. In addition, the content, which is the core of information, should consist of data and metadata. Metadata is the description of the actual data, additional information about what the data is representing. Data and metadata should be coupled together at the source and be available as a complete content before any style formatting.

All the HTML tags are deleted, each node in the parse tree will be represented by another user defined tags that will be converted to a record and these records are stored in tables to be accessed later. The description of these records (i.e. the metadata) will be stored in temporary file, which is the structure description for XML data file. The content extraction algorithm is shown below.

The content extraction algorithm (Algorithm 2) is shown.

Algorithm 2
Initialize: Extract (open [start]; closed [ ] ;
While open < > [ ] do
Begin:
Remove the next state from the left open;
Call it X;
If X is a goal then return [success];
Generate all possible children of X;
Put X in closed;
Eliminate children of X already on either open or closed, as those will cause loops in the search;
Put the remaining children of X in order of discovery on the left of open:
End if;
End.

Content Re-authoring

This part accepts the new structured document from the content selection part, converts to XML document, applies re-authoring technique and prepares it to be presented on user-interface device.

Converting to XML Document
A new meta language is XML, a subset of SGML optimized for Web use. XML is an extensible meta language defining markup languages that describe structured data, not visual presentation.

In this part, the new data record file from the previous step is converted to XML document which is structured and well formed data, XML suits well for transmission of information, as individual documents that can be easily requested and transferred by HTTP between applications or from server to browser.

Content Processing for Re-authoring
The content is extracted from HTML web page and then segmented into classes in XML document will be processed more by the re-authoring technique, and using the client-side adaptation with these specifications.

Table of Content
The document is re-created based on extracted content and a list of *heading* is created. This heading hides a hyperlink, which if selected, can load up details associated with the headline.

So the first display per web page is always a table of content (TOC) with hyperlinks. In this model, there can be any number of abstractions, but practical considerations dictate that any more than two levels are confusing for most users.

TOC techniques provide a very good method for reducing the required display size for structured documents. The contents of each section is elided from the document and the section header is converted into a hypertext link which, when selected, loads the elided content into the browser. The approaches to perform the elision works by keeping only the section headers and eliding all content, with the results looking like a table of contents for a book. Figure (4) shows the HTML page request in PC computer.

Figure 4: the total HTML page

The same HTML page if requested on pocket PC2002 will show in Figure (5).

Figure 5: Non EWCRS of HTML page on pocket PC2002

By using the re-authoring technique the TOC of this web page will displayed on a pocket PC2002 as in Figure (6).

Figure 6: TOC of HTML page

First Sentence Elision

Since most pages have text blocks, even when no section headers are present, first sentence elision can be a good way of reducing required screen area. In this technique, each text block is replaced with its first sentence (or phrase up to some natural break point), and this sentence is also made into a hypertext link to the original text block, as shown in Figure (7-a) the second hyperlink is first sentence elision to the paragraph shown in Figure (7-b).

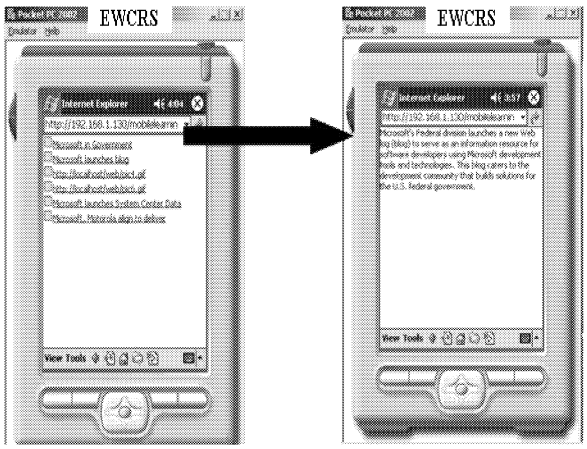

(a) TOC **(b) First sentence elision**

Figure 7: HTML Content

Image Reduction and Elision

Images present one of the most difficult problems for re-authoring, because the decision of whether to keep, reduce, or eliminate a given image should be based on an understanding of the content and role of the image on the page. However, image reduction and elision can be applied without content understanding, as long as users are provided a mechanism by which they can retrieve the original image. The approach taken is to provide a set of techniques which transform images of these types (.bmp, .gif, .jpg) in a page by pre-defined scaling factors (25%, 50%, and 75%), and making the reduced images hypertext links back to the originals [ST04, TP05], as shown in Figure (8-a) the third hyperlink of image and the image reduction shown in Figure (8-b).

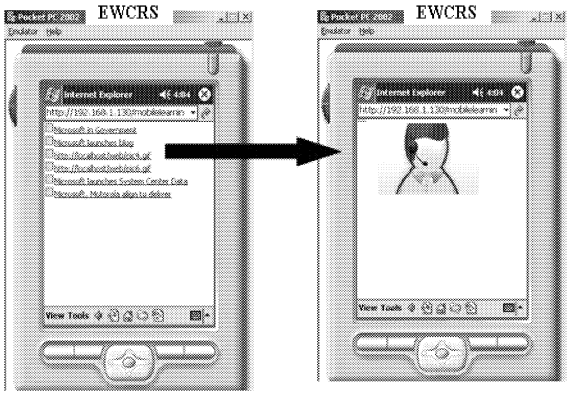

(a) TOC **(b) Image display**

Figure 8: HTML Content

Understanding the Re-authoring Process

In conclusion, to perform document re-authoring two things are required: a set of re-authoring techniques, and a strategy for applying them. Of the techniques used in the manual re-authoring study, those most important and meanable are the syntactic elision techniques (section outlining, first sentence elision, image elision) and the syntactic transformation techniques (image size reduction, font size reduction). The design strategy learned during the study consists of a ranking of the transformation techniques (i.e., *try this before that*) and a set of conditions under which each transformation or combination of transformations should be applied.

User Interface Generator

The user interface generator will render the content to the user according to the capability of the mobile device which is defined in the system. The user interface generator begins by identifying the type of device making the request. It then determines the appropriate type of response markup and dispatches it to a markup handler.

Transformation from XML to XSLT

In an XSL transformation, an XSLT processor reads XML data and an XSLT stylesheet which is also an XML

document; that is, all instructions of the language are expressed in the form of XML elements.

Based on the instructions the processor finds in the XSLT sheet, it outputs a new XML document or fragment thereof. Although XSLT is designed primarily for XML-to-XML transformations, there is also support for outputting non-XML documents, such as HTML and plain text. [ST04] XSLT is applied to the layout content to meet the device characteristics.

Services

Some other services that will complete all the types of device access to web content that could be added also to the experimental system are:

- **Email**: An e-mail interface can be used for small content update and service use. Commands are given by sending e-mails to a certain e-mail address on the web server.

- **SMS:** Being limited in length, an SMS interface suits only for small content update and service use. SMS connections to the system are made via an external SMS gateway application which forwards the client's SMS by HTTP to the platform using HTTP headers, body or both, depending on the architecture. The server sends back the content using methods required by the SMS gateway.

SYSTEM IMPLEMENTATION

To implement the EWCRS system, a design of a mobile application that will reflect the use of mobile device access to web content is done as a kind of mobile-learning (m-learning) that will let the user with mobile devices access web content documents from their devices. Connecting to a network depends on the type of connection their devices accept (i.e. wireless LAN card, Bluetooth, cradle…etc) and navigate through courses that are dedicated by administrator who is responsible for specifying the web document related to the course by request HTML page, parsing to (AST), extracting the content and converting to XML document, XSL pre-processing and the new content will render to the user mobile device related to the device capability.

Using the visual studio.net 2003 tool to design the system, a visual basice.net and ASP.net as a programming language is used also a JavaScript is used as a scripting language with ASP.net, with the platform of Microsoft Windows Server 2003 with (IIS) to implement the system.

This work is done by using both the server-client adaptation, using the ASP.net with the IIS to perform all the server side work, and the JavaScript language for the client side and the visual basic.net for the CGI interface.

CONCLUSIONS AND SUGGESTIONS FOR FUTURE WORK

The following conclusions reached from the implementation of the proposed experimental system.

Conclusions

1. Simple content adaptation of HTML web pages with multiple versions and XML/XSL transformation methods for selecting the appropriate presentations and changing image sizes is done and implemented on Pocket PC 2002.
2. Instead of building different webs for different devices, we strongly believe that the right direction is to convert and deliver the same content in different ways to different devices, by using the re-authoring technique for content adaptation.
3. Separating content from presentation which is important for each element in a given web page and generating multi dimensional customized “web” for mobile devices.
4. A table of content (TOC) from HTML web page is generated with a hyperlink that hides the content of the page.
5. First sentence elision technique is used when the text is a big paragraph and not under any heading.
6. Image resize technique is used to show the image on mobile devices, or an ALT text is displayed if the image is not shown.
7. Experiments show that in the vast majority of cases the experimental system provides the expected results for a range of web pages that are well structured, like the pages that contain texts, images, header and tables but problems are found in the web pages that have too many tags, banners, and links.
8. The result was shown that the adapted content on the reduced display gain good impression on the users approach to retrieve web page on their mobile devices.
9. There is no perfect solution to adapt content for different mobile phones available yet with current technologies, no matter whether a phone is WAP, or i-mode with their different platforms.

Suggestions for Future work

The following is a suggestions for a future work.

1. Upgrading the system to be used for different types of HTML web pages taking in consideration all the HTML tags to be adapted to mobile devices.
2. Image format conversion: When a mobile phone preferred image format is not available on the server, an image format conversion function should be performed to convert the existing image format to a proper image format particularly for the mobile phone.
3. This research is made on text and image types of content, multimedia content could be added and its

content could be adapted in the Infopyramid content selection technique.

4. Summarization of web pages is another approach of web page re-authoring techniques. In this approach, the content is not separated into separate layers; the textual part of the content is summarized using natural language techniques.
5. The SMS service could be added also by adding new mobile controls to the system.
6. The service should be fully tested when the server is under heavy load and used by many simultaneous users, to see how long a user needs to wait for the navigation.

REFERENCES

[EK02] Engin Kirda, "Engineering Device-Independent Web Services", Ph.D. Thesis, Technical University of Vienna, 2002.

[HF03] Hassan Alam and Fuad Rahman1 ,"Web Document Manipulation for Small Screen Devices: A Review" BCL Technologies Inc, 2003.

[RG03] Rui Guan "Content Adaptation on Mobile Phones", Master's Thesis, CTI Technical University of Denmark Kgs. Lyngby, Denmark, August 2003.

[ST04] Sudhir Dixit, Tao Wu ,"Content Networking in The Mobile Internet", 2004 by John Wiley &Sons,Inc.

[TB96] Timothy W. Bickmore , Bill N. Schilit , and FX Palo Alto Laboratory "Digestor: Device-independent Access to the World Wide Web", 3400 Hillview Avenue, Bldg. 4 Palo Alto, CA 94304 USA, 1996 .

[TP05] Timo-Pekka Viljamaa,"Types and Methods of Content Adaptation", T-110.456 Next Generation Cellular Networks, 2.3.2005.

SELF LEARNING USING WEB 3D PROTOTYPES

Jesus Felez, Maria L. Martínez, Gregorio Romero and Joaquin Maroto
Dep. of Mechanical Engineering. ETS Ingenieros Industriales.
Universidad Politécnica de Madrid (UPM)
José Gutiérrez Abascal, 2. 28006 Madrid. Spain
e-mail: [jfelez, muneta, gromero, jmaroto]@etsii.upm.es

KEYWORDS

WEB3D, Virtual Reality, computer aided learning, interactive graphics, Internet. Collaborative Design

ABSTRACT

The goal of this paper is to develop and evaluate modules of design engineering through Internet where the use of 3D and interactive graphics are the most innovative aspect and attractiveness.

This paper presents a development consisting of course for teaching mechanical design and the development of a virtual reality application based on internet used to move, view and manipulate mechanisms. These mechanisms can be assembled or disassembled and checked if work properly.

An application based on virtual reality techniques has been developed allowing the construction of geometric models of the assemblies. These models have been implemented in virtual reality software aimed at the computer simulation of those assemblies. With the developed software, two actions can be implemented: the possibility to put together and dismantle the assembly, and being able to operate the assembly according to its natural movements, which means studying how it works, so that the students will be able to understand the geometric characteristics of the assembly and to view it on a drawing. Finally, evaluation of the training developed tools is presented.

INTRODUCTION

One of the main goals of technical drawing is to reach an understanding of how assembly drawings work. During the whole of this subject we place special emphasis on different concepts, such as the interpretation of assembly drawings, distinguishing between the functions developed by each element, and the reasons for using a specific part and its shape. We show that a individual part has no meaning unless it is located in its corresponding assembly. The shape and dimension of each part depends on the other elements next to it (an assembly is like a mechanism where each part has its fixed function and must fit exactly in its position).

One of the main problems that has to be faced, is that as real drawings are usually worked with, sometimes their difficulty or complexity, and other times people's lack of spatial vision, make it difficult to understand the subject properly.

A good solution is to physically have the real machines, as well as the parts that configure the drawings. With these assemblies it is possible to physically observe what they are like and observe the shape of the elements under any point of view. We can study the way they are fixed, how certain ones fit in with others, and as a result, it will be possible to study how the assembly works in order to achieve a better understanding.

However, due to the extension and variety of the assemblies used, and in some cases, their physical size and weight, they become unmanageable, and being able to have all of them is almost impossible.

In order to solve these kinds of problems a computer solution seems appropriate. Computers have no problems of accessibility and use except for those imposed by the program. They allow an application to be developed to reconfigure the assemblies and be able to modify them easily.

With this project, it is intended to develop an application based on virtual reality techniques that allows the construction of geometric models of the assemblies. These models have been implemented in virtual reality software aimed at the computer simulation of those assemblies. With the developed software, two actions can be implemented: the possibility to put together and dismantle the assembly, and being able to operate the assembly according to its natural movements, which means studying how it works, so that the students will be able to understand the geometric characteristics of the assembly and to view it on a drawing.

LEARNING WITH INTERNET

The Internet has become one of the best tools in the educational field. The possibility of arranging almost limitless textual and graphical information is the first sign of its potentiality. Very many approaches have been realized in graphics development in the Internet. From the most simple 2D graphics based on ASCII codes to

streaming jpg graphics. But all of these are always "plain material". Expensive hardware was required to obtain nice graphics and videos. But not all of them were user interactive. The possibility of building virtual worlds arose with the implementation of VRML language. The first specification of VRML 1.0 began at the end of 1994. This language was the first step to obtaining low cost interactive virtual worlds by means of the Internet. Since standard VRML 2.0 in 1997 (Tittel, 1997) arose, many educational applications have been made from the Internet taking advantage of the improvements provided by 3D graphics. The CosmoPlayer (CosmoSoftware, 2003) browser popularized its use. Currently, any CAD program offers a VRML output of the 3D design in course (Web3D Consortium, 2006).

WEB3D TECHNOLOGIES

The main goal of the project was to evaluate the possibilities offered by WEB3D Internet technologies in the field of training. From VRML, a standard specification did not come about until the middle of 2002, creating a void that a large number of software companies (around 45 companies have been detected) decided to fill by developing the so-called WEB3D technologies. At first these technologies were focused towards being 3D product viewfinders for Internet sales. In general, they include several technologies that optimize the mesh of the 3D models, thus obtaining very low rates of downloading. They also use streaming and optimized textures. The render kernels are very good and offer a higher quality than the ones obtained with VRML. On the other hand, the preparation of a 3D graphics standard, the X3D for Internet, was not completed until the end of 2002, which is why WEB3D graphics occupy much of the market (Web3D Consortium, 2006).

WEB3D graphics show the following characteristics: they are fast to create because usually models can be created with other programs like 3D Studio MAX or Alias Wavefront; they either require a small size plug-in or they do not require one (if they are based on Java); impressive appearance: better than VRML or X3D; easy to integrate in Web pages; reduced downloading time; and finally, based on standards such as XML

These technologies can be grouped in:

- XML-based technologies: One file contains the geometry and another file the transformations and any possible interactions of the user with the virtual world. These require plug-ins for their display.
- Java3D-based technologies. Plug-ins are not necessary although they are slower.
- Own technologies developed by the commercial companies requiring a plug-in

By means of these technologies, and in particular by those offered by Viewpoint (Viewpoint Corporation, 2006) and Spinfire (Actify, 2006) , more than 700 3D interactive models have been developed and applied to different scopes:

- To display simply 3D objects (with zoom functions, pan and rotation). In figure 1 the high quality obtained is observed.
- To offer interactive assemble/disassemble of devices (figure 2). We use collision detection and transparencies to improve students' skills.

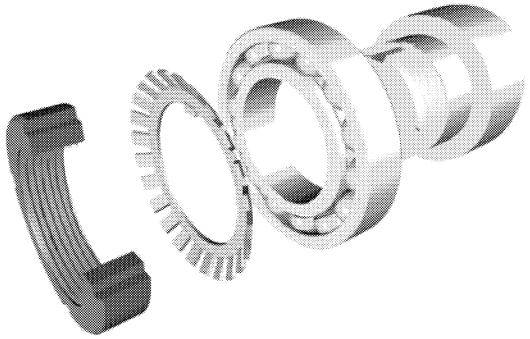

Figure. 1 : Visualization of some accessorize elements

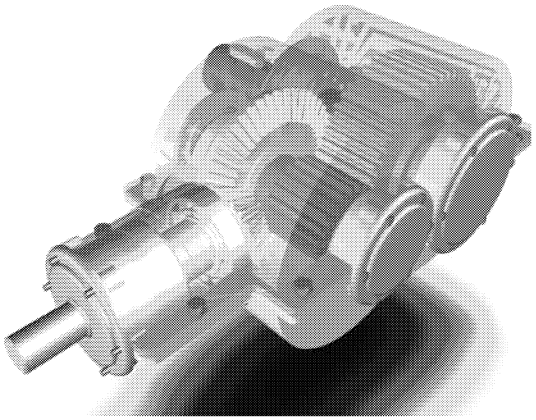

(a)

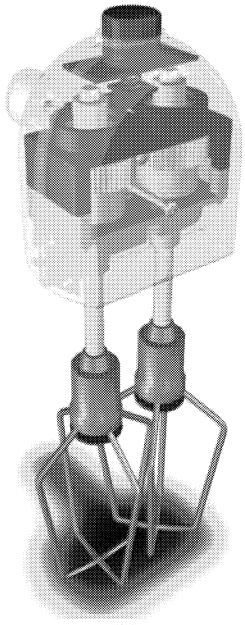

(b)

Figure. 2 : Different assemblies.
(a) with transparencies to show the inner parts
(b) other devices that can be disassembled

Very attractive 3D worlds for the user have been developed, where in addition, the behavior of those worlds is included. The most stable technologies seem to

be Viewpoint (Viewpoint Corporation, 2006) and Cult3D (Cult3D, 2006).

For the project, the models are made from 3Dstudio Max optimizing the mesh. Also, animations have been defined if necessary. The companies themselves provide programs or procedures to convert to WEB3D formats. In order to add interactivity, it is necessary to program either in agreement with the specific syntax of each program, or by adding routines in JavaScript, since these technologies were aimed at electronic commerce and have limited capacities of interactivity, mainly of programming.

PROJECT DESCRIPTION

Software based on virtual reality techniques will be developed to allow interaction with the assemblies.

The project goal is to develop a software tool that allows working with a physical assembly and interacting with it in a virtual environment. A set of mechanisms, as can be seen in figure 2, will be defined and built.

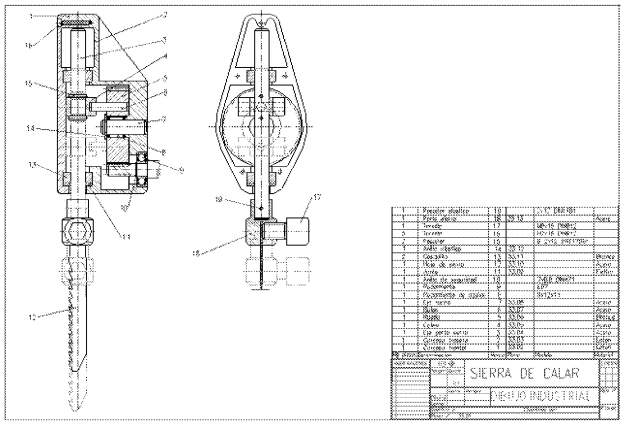

Figure 3 : An assembly drawing

Based on these assembly drawings (figure 3), 3D models need to be constructed with geometric modeling software that represents the assembly in three dimensions, as shown in figure 4.

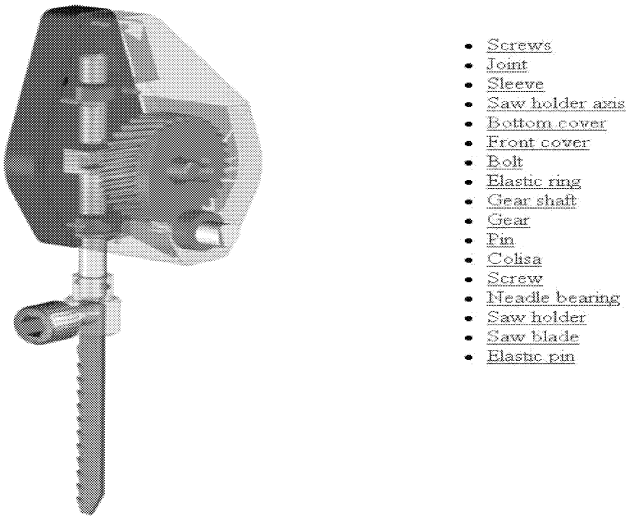

Figure 4. Three-dimensional model

Afterwards, the geometry will be imported by the virtual reality application to develop and apply features to each object such as interference and collision detection, paths and tasks. Collision detection will let interference between objects be studied, and when it happens it will not let one object get into the other. With this procedure the pieces can only move as the other elements next to them let them move. Therefore, it can be shown how the assembly really moves when it is working by simulating the different possible movements of the assembly in accordance to its geometry (figure 5).

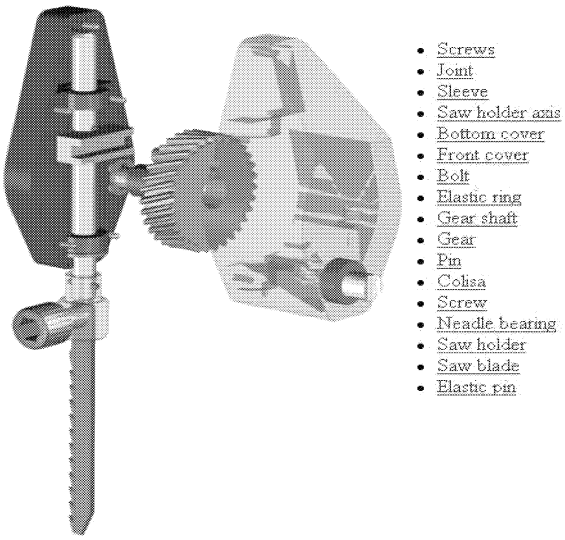

Figure 5. Exploded assembly model

Once the 3D model has been built, it is necessary to define a hierarchical structure of the objects including two types of constraints.

The first type of constraint is the assembly constraint. This constraint serves to set out the way to assemble or disassemble the machine. An assembly constraint is defined by means of a direction of assembly and a relative movement of an object with respect to another object. By correctly defining the assembly constraints it is possible to establish the order and way of assembly / disassembly of a machine. It is also possible to establish complex constraints, for example, in the way of “do not disassemble the chassis until all the screws have been removed”. This type of constraint is used when the program is used to train people in assembly sequences.

The second type of constraint is the kinematic constraint. Kinematic constraints serve to define machine movement. They define the way the pieces move when the user moves the degree of freedom of the system. The definition of these constraints serves to define the movement of the mechanism and to train people in the way machines work.

Nevertheless, at this moment the developed application has no feedback between the virtual reality model and its corresponding assembly drawing.

OBJECT HIERARCHY AND SCENE GRAPH

In order to display the mechanism, a scenario is defined where the action is developed. The objects are placed in the scenario constituting a hierarchical tree structure

defined as scene graph. The "Scene graph" is a structure that contains all the elements in the scenario: geometries, lights and position information in an ordered way.

The elements that made up the scene graph are called nodes. A node is an element that contains information such as geometric information, positional information and lights. The geometric information is stored in the geometric nodes, the situation information is stored in the transformation nodes, and the light information in the light nodes.

The nodes are structured in a hierarchical way. The nodes are joined to each to other upside down in a tree form. In figure 6, a scene graph is shown, its structure and the order of evaluate nodes.

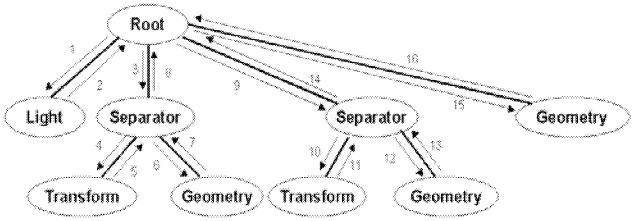

Figure 6. A scene graph

The root node is the first node of the tree. Once inside the tree graph, it is followed from top to bottom and left to right, so the child nodes inherit the properties of the parent nodes.

MODEL ACTIONS

Three types of actions working with the virtual mechanism can be carried out:

Navigation

Navigation is interactively moving the viewpoint of the objects with a pointing device (a mouse for example). To do this a "motion link" of the input sensor with the position of the camera viewpoint is used. In accordance with this, if the mouse is moved, the program interactively changes the scene viewpoint.

Assembly of the Parts

To assemble the mechanism, some assembly constraints are defined. The assembly constraints prevent an object from being able to be moved through its assembly direction at the same time that the object collides or interferes with others. Once an object is selected, by clicking on it, a motion link is associated to the mouse to move that object.

In figure 7, a scene graph with the assembly constraints has been represented.

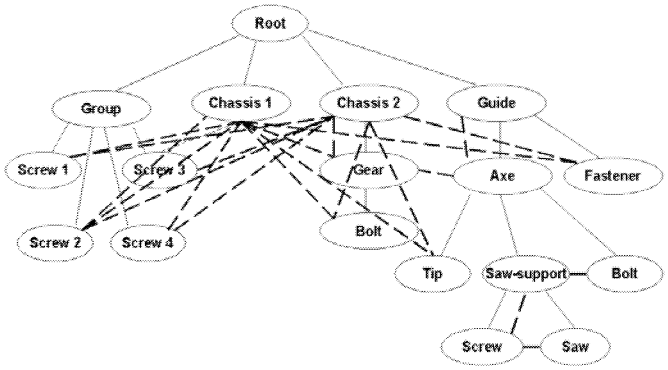

Figure 7. Scene graph with assembly constraints.

Kinematic Simulation

A module that permits the kinematic calculation of the movement of the parts of the mechanism has been developed. Once the mechanism has been assembled, the kinematic module produces movements according to the kinematic constraints.

To define the mechanism's kinematic behavior, it is necessary to establish the inputs of the system and the kinematic constraints that make the movement of the system compatible with the assembly constraints. The way to do this is by establishing link blocks of the type of kinematic constraints that are applied to the nodes joined by the constraints (figure 8).

The program includes a module to simulate the kinematics of the mechanism. This analytical tool permits the mechanism movement to be reproduced according to the established kinematic constraints.

A collection of kinematic constraints such as translational, revolute, spherical, cylindrical, screw, etc., have been defined as formal models. It is only necessary to define the type of constraint that appears and the affected objects.

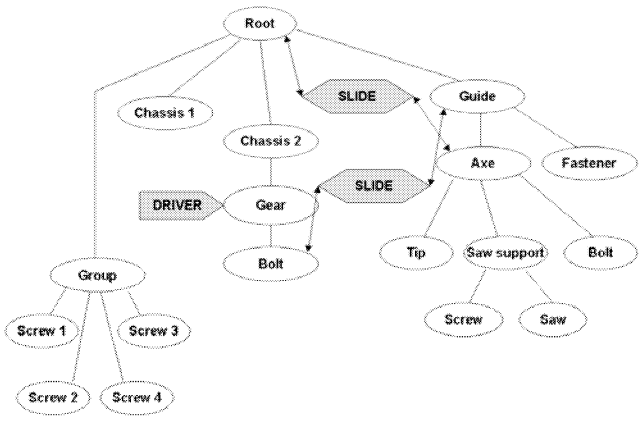

Figure 8. Scene graph with kinematic constraints.

THE WEBSITE

A Website container (www.webd.etsii.upm.es) has been developed, including all the educational materials to

implement the project. Five types of materials can be described.

- Textual educational material
- 2D graphics
- 3D interactive graphics
- Tests in order to allow the user access to the advanced modules.
- Management of access.

The access of the site is free requiring only a simple user registration.

Preparation of Textual Educational Material

Contents of design engineering modules have been developed. These contents had to be made in ASP pages, specifying that 2D images had to be present and suggesting interactive 3D virtual models that could be interesting (Martinez et all, 2002).

The subjects developed for the design engineering module are:

- Basic level: Descriptive Geometry, Basic Drawing, Drawing of Basic Sets and CAD.
- Advanced level: dimensional tolerances, TG&D and standardized elements (rivets, gears, bearings, screws, springs, etc) are offered.

Preparation of 2D graphics

2D graphics have been inserted accompanying the contents as 2D images in classic formats for Internet (GIF and JPEG). In addition, due to the necessity of using vectorial drawings, these are displayed in EDRW format (edrawing) (Solid-works, 2006). With this format it is possible to use the zoom facility or display layers without loss of quality. Also technical drawings have been transformed into images using high-resolution bitmaps, which means focusing can be used to see details. Many zoomview (Viewpoint Corp. 2006) images have been used to see details in large drawings (figure 9). In this format the image can be enlarged without loss of quality. Some features can be added such as Flash animations included in the images.

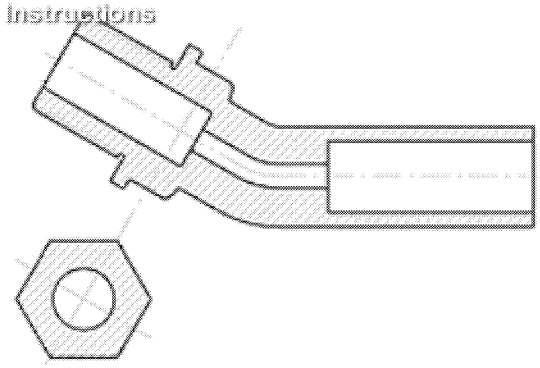

(a)

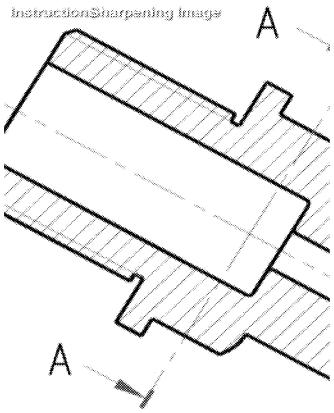

(b)

Figure. 9 Zoomview (a) original size (b) after zoom

EVALUATION

An evaluation has been carried out by the Federico II University of Naples. There are various methods for evaluating e-learning projects. Many organizations have developed standards and protocols based on trying to evaluate their resources and their reuse by the whole community. Some have focused their attention on systems specifications and others on the interoperability between different platforms. Of all these systems, the ones worthy of mention are the Nishikant Sonwalker Method (Sonwalkar, 2006), Quality Criteria Courseware (EuroPACE, 2004) and the Michigan Virtual University Course Evaluator (Michigan Virtual University, 2006). All of these systems offer web-based learning site evaluation criteria, but only the first one considers pedagogical aspects to be paramount.

The Federico II University of Naples analyzed these methods and adopted some indicators to evaluate the project activities and results (Lanzotti et all, 2003). In accordance with the global objectives, the project's management activities evaluation took the following points into account:

- Innovation as a way to introduce the new methodologies or teaching strategies
- Transferability as a possibility to use or adapt the results to other fields.
- Coherence which allows the results to be checked against the project's initial objectives.
- Relevance, as the results have a high chance of affecting learning.
- The ever increasing number of computers with an Internet browser at the student's disposal, that allow access to these e-learning sites.

Widely recognized indicators such as clarity, accessibility, interface, and user support, are also taken into account as part of the evaluation, as well as feedback and self-assessment.

When the project was running, an expert monitored all the indicators so that management of the project could be changed at any point where an increase in quality was needed. A matrix position is given, where all the marks

for the product and the management activities connected with it, provide the level reached by the project.

In the monitoring phase, which lasted approximately 2 months, the involvement was checked in-depth, along with the results, the Web site, dissemination and other points. The relative costs statements were taken into account, together with the organization, the multimedia production, and the information exchanged among partners, etc.

With the chosen indicators, the project turned out to be totally in line with the initial proposals and the innovation introduced is clear and obvious, even when the workloads were not evenly distributed among the partners.

The Web site content was positively appraised, as it was well organized using a logical sequence and small modules, although there were small syntactical and spelling errors. Evaluation results can be seen in figure 10.

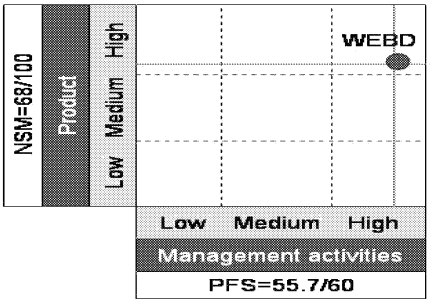

Figure 10. Project Evaluation Matrix

CONCLUSIONS

A virtual reality application has been presented. This application allows the display and simulation of mechanical assemblies. These mechanisms can be assembled or disassembled interactively using a conventional computer mouse and keyboard.

A kinematic module has been also developed in order to simulate the movement of the model mechanism.

In this project a set of design engineering learning modules through Internet has been developed where the three-dimensional and interactive graphics are the most innovating and attractive feature.

The last objective of the project is to demonstrate the benefit of the use of these technologies in education. WEB3D Technologies have been used to develop these models, providing them with a high degree of realism and interactivity. These technologies are characterized by a high level of realism and by a high rate of image compression, which makes for an optimum use in the Internet. For this project more than 700 3D models have been developed. Nevertheless, the modeling work was laborious and slow, and although these technologies have the highest capacities, they are in a continuous state of improvement that sometimes causes confusion in their application.

To manage the courses, a Website has been developed, including a control of student visits, and access to the different levels from contents based on the self-evaluation tests.

REFERENCES

Actify, 2006, http://www.actify.com

CosmoSoftware, 2003,. http://www.cosmosoftware.com

Cult3D, 2006 http://www.cult3d.com/

EuroPACE, 2004, Quality Criteria for e-Learning, http://www.ecc.org.sg/cocoon/ecc/website/qualitycriteria2.pdf

Lanzotti, A.; Savarese, M.; 2003, "Quality evaluation of a learning and training project: The WEBD Project". Int. Workshop in "New WEB technologies for collaborative design, learning and training". Torino Italy.

Martínez, M. L.; Félez, J.; Romero; G. "Ultimas tendencias en gráficos WEB3D para Internet". XIV Congreso Internacional de Ingeniería Grafica INGEGRAF. Santander 2002.

Michigan Virtual Univ, 2006, http://standards.mivu.org/

Solid-works, 2006, www.solidworks.com

Sonwalkar, N.; 2006, http://www.uwex.edu/disted/desien/2002/0205/focus.htm

Tittel, E., Sanders, C., Scott, C., Wolfe, P., 1997, "Building VRML Worlds", McGraw-Hill, 1997

Viewpoint Corp., 2006, http://www.viewpoint.com

Web3D Consortium, 2006, "Open Standards for Real-Time 3D Communication", http://www.web3d.org/

AUTHOR BIOGRAPHY

Jesus Felez received his Mechanical Engineer and Doctoral degrees from the University of Zaragoza in 1985 and 1989. He started as Associate Professor at the Technical University of Madrid in Spain (UPM) in 1990 and becomes Full Professor in 1997. His main activities and research interests are mainly focused in the field of simulation, computer graphics, virtual reality and mechanical design.

M. Luisa Martinez received her Mechanical Engineer Master degree from the Technical University of Madrid in Spain in 1990. Since 1990 she started to work as Associate Professor at the Technical University of Madrid. She got her PhD Degree in 1997. She usually works in the field of computer graphics, virtual reality and CAD.

Gregorio Romero has received the Ph. Degree in 2005 and the Control Engineer Grade in year 1999 both at the Technical University of Madrid. He is Assistant Professor at the Technical University of Madrid in Spain. His main research activity is based on computer simulation models, virtual reality and computer vision.

Joaquin Maroto has received the Ph. Degree in 2005 and the Control Engineer Grade in year 2000 both at the Technical University of Madrid. At present, he is Assistant Professor at the Technical University of Madrid in Spain. His main research activity is based on traffic simulation models, computer graphics and computer vision.

SCICOS

A survey of Scilab simulation tools

François Delebecque

Abstract— **This paper presents an overview of the basic simulation tools available in Scilab. Scilab provides standard ode solvers, implicit (DAE) solvers, and a comprehensive set of functions for the simulation of linear systems, possibly controlled.**

I. INTRODUCTION

Scilab is a general purpose numerical CACSD package which in particular collects a number of simulation tools. Designed as an open package devoted to control applications, the Scilab/Scicos software provides a comprehensive environment for modeling, control and simulation of dynamic systems. The basic tool for simulation in Scilab is the Scicos toolbox which is an editor for modeling a system using a block diagram description. Once the system has been described graphically, it is easy to simulate it for given inputs and display the results into a scope. In addition, Scilab offers other specific simulation tools that are described in this paper. All the functions described here can be illustrated by examples which are given in the online help.

II. SIMULATION OF EXPLICIT SYSTEMS

Scilab provides several functions for solving systems of differential equations. The main function is `ode` which can be used for solving systems given in the following form:

$$\dot{x} = f(t, x) \tag{1}$$

with initial state $x(0) = x_0 \in \mathbb{R}^n$. Equation (1) admits a unique solution on an open domain of time containing 0 if f satisfies a local Lipchitz condition. As Scilab solves (1) numerically, an approximate solution is calculated and the user has to check that the solution is satisfactory or not. For instance, an accurate solution can be found even in cases where f is discontinuous but on the other hand the numerical solution found can be very sensitive to parameter variations in other situations. A simple example is given by the linear system $\dot{x} = Ax$ with $A = \begin{bmatrix} 0 & 1 \\ 100 & 0 \end{bmatrix}$. Although f is Lipchitz (with constant $L = 100$), the problem is ill-conditioned.

A. Ode function

The simplest syntax of the ode function is the following:

```
x=ode(x0,t0,T,f)
```

The first input `x0` is the initial state (column vector with n entries) and the second input `t0` is the initial time (often `t0=0`). The third input `T` is a row vector containing the times at which a solution is to be computed, i.e. if `T=[t1, ..., tk]` the output `x` will be a n x k matrix such that its ith column contains the solution vector `x(ti)`. The RHS function `f` is a Scilab function `f(t,x)`. Note that the variable `t` must appear in the calling sequence of `f`, even for autonomous systems. As a simple illustration, one can solve the linear system $\dot{x} = Ax$ as follows:

```
-->x0=[1;-1]; t0=0; T=[1,2,3];
-->function xdot=f(t,x)
-->xdot=A*x;
-->endfunction
-->x=ode(x0,t0,T,f)
```

Here, the solution has been computed for at instants $(1, 2, 3)$. Note that the A matrix is defined outside the definition of `f`.

B. Passing parameters

Variables are semi-global in Scilab. In particular a function can make use of a variable which is not in its calling sequence. This feature is convenient in the `ode` function framework, since a parameter can be passed by the context. However in some situations it can be necessary to pass explicitly parameters to the RHS function f. In this case, f can be defined as a function of $(t, x, p1, p2...)$ where the pi's are arbitrary Scilab variables. The additional parameters $(p1, ..pn)$ can be passed to the solver by using the syntax:

```
x=ode(x0,t0,T,list(f,p1,...,pn))
```

Another way is to wrap the call to `f` into a another function:

```
-->function xd=g(t,x)
-->p1=...
-->xd=f(t,x,p1,...)
-->endfunction
-->x=ode(x0,t0,T,g)
```

It is also possible to read in the Fortran or C routine a variable defined in the current Scilab workspace. Examples are given in the file `externals.s` in the "basic-test" directory of Scilab, distributed with the Scilab source code.

C. Syntax details

The syntax of the Scilab ode function follows the Odepack solvers. The Odepack library can be found in Netlib. It implements the Lsode code of Hindsmarch which uses Adams-Moulton formulas for non stiff problems and BDF's formulas for stiff problems. We refer to [1] for details. When the user does not give the solver to be used, ode uses by default the Lsoda routine. This routine uses an automatic

F. Delebecque is with Inria, Metalau Project, Domaine de Voluceau, 78150 Le Chesnay, France. `Francois.Delebecque@inria.fr`

switching strategy between stiff and non-stiff formulas. The basic syntax is as follows:

```
x=ode('method',x0,t0,T,rtol,atol,f,Jacobian)
```

The `method` can be choosen among

```
'adams'
'stiff'
'RKF'
'RK'
```

The Adams method uses Adams-Moulton formulas of order at most 12, which is the default value. The tolerance parameters `rtol,atol` is used in such a way that the solvers tries to match the inequality:

$$e(i) \leq rtol(i)|\bar{x}(i)| + atol(i)$$

where $\bar{x}(i)$ is the solution computed by the solver at time t, and $e(i)$ is an estimate of the error between the exact solution and the computed solution. Default values for `rtol` and `atol` are set to 10^{-7} and 10^{-5} respectively. The Jacobian is a matrix valued function which is used for better performance particularly in case of stiff problems. If the jacobian is not provided the solver will internally compute it using finite differences. Thus both for performance and accuracy it is recommended to pass the jacobian to the ode solver. When the `RK` or `RKF` flag is passed to `ode` a Runge Kutta method is used. RK is an adaptive Runge-Kutta of order 4, and RKF implements the Shampine and Watts program based on Fehlberg's Runge-Kutta pair of order 4 and 5 (RKF45). This is for non-stiff and mildly stiff problems when derivative evaluations are inexpensive. This method should generally not be used when the user is demanding high accuracy.

D. Options

The global variable variable `%ODEOPTIONS` controls the various options available with the ode solver. It is a vector with the following elements:

```
%ODEOPTIONS=[itask,tcrit,h0,hmax,hmin,...
 jactyp,mxstep,maxordn,maxords,ixpr,ml,mu]
```

The set of parameters allows a complete control over the solver. For instance `itask` defines the task to be done by the solver (normal computation at specified times, computation at meshpoints, one step at one internal mesh point, normal computation without overshooting `tcrit`, one step without passing `tcrit`). The other parameters specify the order of the solver, the minimal and maximal step time, the bandwith of the jacobian matrix, the maximal number of calls to the rhs function allowed, etc...

E. Hot restart

In some applications it is necessary to compute the solution over different time intervals. For instance, one may want to get the solution for t in [t0,t1], examine the solution at time t1, and restart the solver for a new time interval [t1,t2]. As the solver contains many implicitly defined variable (such as the current order or the current internal work array), restarting the solver can be time-consuming. It is possible to get the complete internal state in two work arrays w and iw as extra lhs parameters.

```
[x,w,iw]=ode(...)
```

These arrays can be passed to the solver for a hot-restart as follows:

```
ode(...,w,iw)
```

In this way the solver continues integration with its current internal state.

F. C or Fortran coded functions

For large problems with thousands of equations it is necessary to implement the functions in C or Fortran. Indeed, Scilab is an interpreted language and the computation time becomes critical for large problems. It is of course possible to call a C or Fortran coded function by defining a wrapper Scilab function which call the C or Fortran function. It is also possible to call directly the C of Fortran function. It that case the syntax of the function is imposed: for C functions one must define the RHS function as follows.

```
void extf(int *n, double *t, double y[],
          double ydot[])
```

To use this function within Scilab one should first compile the file `extf.c` containing the source code of `extf` and build a dynamic library. This is done by a Scilab command:

```
ilib_for_link('extf','extf.o','C')
```

This command builds a dynamic library (.so file in Linux platforms or .dll file in Windows platforms) and produces a generic Scilab script called `loader.sce` which contains the commands necessary to link the library with Scilab. Finally, the ode is solved by the command

```
x=ode(x0,T0,t,'extf')
```

The only difference with the usual syntax is that the last parameter of ode is now a character string. The same way is used for using a C coded jacobian.

G. Stopping time

It is possible to use the ode function for solving stopping time (or event location) problems. A typical example is a problem which can be written:

$$\dot{x} = f_1(x) \text{ if } g(x) > 0$$
$$\dot{x} = f_2(x) \text{ if } g(x) < 0$$

The function g is called a switching function. The syntax for solving such problems is:

```
[x,rd]=ode('root',x0,t0,T,f,ng,g)
```

Other parameters can be given (tolerance, jacobian function) as for the usual calling sequence. The parameter ng is an

integer and g is the crossing function. It is an external function i.e. a function with a specified syntax or the name of a Fortran subroutine or a C function, or a Scilab list. If g is a Scilab function, it syntax should be `g(t,x)` where t is the time (real scalar) and x is a real vector (state). It should return a vector of size ng which correspons to the ng constraints. If g is a character string it refers to a C function or a Fortran subroutine, with the following calling sequence:

```
void g(int *n,, double *t, double x[],...
      int *ng, double gout[])
subroutine  g(n,t,x,ng,gout) (Fortran)
```

If parameters should be passed to g, the function g can be plugged into a list and the same conventions as for f apply. Output rd is a k-vector. The first entry containts the stopping time (the time τ at which the surface is crossed for the first time, $g_i(\tau, x(\tau]) = 0$. other entries indicate which componets of g have changed sign. Some care should be taken when using `root`for event location. The solver adjust the steps according to the tolerance required. When the ode is particularly smooth and easy, the solver can take large steps and miss some zeros of the function. The remedy is to adjust the number of steps and the maximal allowed step used by the solver. This is done by redefining an appropriate `%ODEOPTIONS` variable.

H. Csim function

This function is devoted to the simulation of linear systems. A linear system

$$\dot{x} = Ax + Bu$$
$$y = Cx + Du$$

is represented in Scilab by a single object, collecting the four matrices A,B,C,D or in transfer function representation. For example, the linear system `Sys` can be built by the command `Sys = syslin('c', A, B,C D)`. The simulation for given input u is given by the `csim` function. The simplest calling sequence is

```
y=csim(u,T,Sys)
```

Here, u can be a Scilab function or a vector of numerical values representing the inputs at instants given in T. As for ode, the u entry can be wrapped into a list for passing parameters. The implementation of the function relies on a block-diagonalization of the dynamic matrix of the system. Then the ode solver is called for each block; Since the eigenvalues are clustered in , the solver is used with an Adams numerical scheme. Systems given in transfer matrix representation are transformed into state-space. For specifoc time response the first argument of csim can be given as a string such as `'step'` or `'impulse'`.

I. Odedc function

This function `odedc` is mainly desiged for the simulation of a continuous time system controlled by a digital (discrete time) controller. It aims at simulation a system dynamics changing at sampled instants. To be more specific, the state of the system has implicitly two components $(y_c, y-d)$ and simulated system equations are given by

$$\dot{y_c} = f_0(t, y_c(t), y_d(t)) \text{ for } t \in [t_k, t_{(k+1)}[$$
$$y_d(t_k) = f_1(y_c(t_k^-), y_d(t_k^-), 1)$$

$$y_c(t0) = y_{c0}; \quad y_d(t0) = y_{d0}$$

The code is implemented in C and make calls to the lsode Fortran code. The external function can be given as a Scilab function or as a C function.

As an illustration of the usage of `odedc` in Scilab, we consider the a non linear continuous system

$$\dot{x_c} = f_c(t, x_c, u) \quad y = h_c(t, x_c)$$

with the digital feedback:

$$xd+ = f_d(x_d, y) \quad u = h_d(t, x_d)$$

To perform a simulation of the closed-loop system, assuming an input function $e(t)$, and given 4 Scilab functions `fc,fd,hc,hd` we first define the external function:

```
xcd=f(t,xc,xd,iflag)
if iflag==0 then
   xcd=fc(t,xc,e(t)-hd(t,xd));
else
   xcd=fd(xd,hc(t,xc));
end
```

Then the call to `odedc` is done as follows:

```
-->xcd=odedc([x0c;x0d],nd,h,t0,t,f);
```

Here `nd` is the size of the discrete state and h is the sampling period.

J. 2D simulations

For ode with trajectories in the plane, Scilab offers functions wich display the phase portrait of the trajectories. These functions are named `champ` and `fchamp`. The syntax is `fchamp(f,t,xr,yr)` where f is a function compatible with the `ode` external. Here is an example of how to plot the direction field of the Van der Pol oscillator.

```
function xdot = vanderpol(t,x)
xd1 = x(2)
xd2 = -x(1) + (1 - x(1)**2)*x(2)
xdot = [ xd1 ; xd2 ];
xf= -1:0.1:1;yf= -1:0.1:1;
fchamp(derpol,0,xf,yf)
```

Several examples are provided as built-in demos in Scilab. The user is invited to choose a starting point by a mouse click.

III. Discrete time simulations

There are several function in Scilab which can be used for simulation of discrete time systems.

A. The 'discrete' flag

The ode function can be used with the `x=ode("discrete",x0,t0,T,f)` for the fast evaluation of the sequence defined by

$$x_{n+1} = f(n, x_n)$$

Note that the external function f can be a Scilab function, or a function coded in C or Fortran. Parameters can be passed to f by using a list argument. Also, the parameters can be retrived from the Scilab workspace.

B. ltitr, rtitr, flts

Function `ltitr` is used for the fast evaluation of the time response of the discrete time system:

$$x_{n+1} = Ax_n + Bu_n$$

with the calling sequence `x=ltitr(A,B,U)` where the inputs ui's are the coluns of the matrix U=[u0,...,un].

Function `rtitr` computes the discrete time response of a MIMO linear system given in transfer form. `y=rtitr(N,D,u)` returns the time response of the discrete time linear system with transfer matrix $D^{-1}N$ for the input u, i.e y and u are such that

$$D(z)y = N(z)u$$

where $D(z)$ and $N(z)$ are polynomial matrices, $D(z) = D_0 + D_1 z + ... + D_{d1} z^{d1}$, $N(z) = N_0 + N_1 z + ... + N_{d2} z^{d2}$. The above equation is interpreted as

$$D(0)y(t) + D(1)y(t+1) + ... + D(d1)y(t+d1) = N(0)u(t) + ... + N(d2)u(t+d2)$$

Function `flts` is a versatile function for the simulation of a linear system defined as a `syslin` list. Here are examples of usage:

```
Sys=syslin('d',1,1,1);u=1:10;
y=flts(u,sl); //State-space

z=poly(0,'z'); D=1+z+z^2;
Sys.D=D;   //Polynomial D matrix
y=flts(u,sl);

H=(1-2*z)/(z^2+0.3*z+1); //Transfer form
u=zeros(1,20);u(1)=1;
y=flts(u,H);  //Impulse response
u=ones(1,20);
y=flts(u,H);  //Step response

Sys=syslin('d',A,B,C,D);  //MIMO example
u=[1;-1]*(1:10);
rh=flts(u,ss2tf(Sys)); rs=flts(u,Sys);
```

Finally, function `dsimul` built over `ltitr`, can also be used for discrete time simulation of linear systems.

IV. Simulation of implicit systems

The `odepack` package provides the routine `lsodi` for the simulation of implicit systems. This function has been interfaced with Scilab and can be called by the `impl` built-in function. The system of equations is given by:

$$\begin{aligned} A(t,y)\frac{dy}{dt} &= g(t,y) \\ y(t0) &= y_0 \end{aligned}$$

where A is a matrix-valued function and g a vector-valued function. The simplest calling sequence is:

```
y=impl(y0,ydot0,t0,T,res,adda)
```

The user should provide a consistent (y0,y0dot) pair. Two external functions are required. `res` must follow the syntax `function r=res(t,y,ydot)` and should return $r = g(t,y) - A(t,y)\dot{y}$. `adda` should be `function r = adda(t,y,p)` and returns $r = A(t,y) + p$ where p is a matrix with same dimensions as $A(t,y)$. The external functions `res` and `adda` can also be defined as C or Fortran routines, with a specific calling sequence. As for ode, parameters can be passed to these functions, either by the list mechanism or by reading variables in the Scilab workspace. There exist of course many other parameters which can be used with `impl` such as tolerances, jacobian functions, step control etc. Also it is possible to perform a hot restart of the solver?

A. Dassl and Dasrt function

Scilab has an interface with the DAE solvers Dassl and Daspk codes [7]. The DAE to be solved has the form:

$$\begin{aligned} g(t, y, \dot{y}) &= 0 \\ y(t0) &= y_0 \\ \dot{y}(t0) &= ydot_0 \end{aligned}$$

The simplest calling sequence for `dassl` is

```
R=dassl(x0,t0,T,res)
```

where x0 is either y0 (in this case, ydot0 is estimated by Dassl) or the matrix [y0 ydot0] (in that case, the vector pair (y0,ydot0) must meet the constraint g(t,y0,ydot0)=0). T is the vector containing the instants at which the solution is desired. The external function `res` must be defined by:

```
function [r,ires]=res(t,y,ydot)
```

This function should return in vector `res` the residue g(t,y,ydot) and an error flag `ires` with value 0 for normal computation. The output of `dassl` is a matrix R with 2n+1 rows. The first row contains the instants at which the solution has been computed (this vector can be different from T, unless a specific `info` parameter is passed to dassl). The bottom rows of R contain the components of the solution y and its derivative $\dot{y}$, one column for each instant of computation. For large problems it is possible to use a g function written in C or Fortran. We refer to the on-line

help for their syntax. Agin, parameters can be sent to this routine. It is also possible to provide additinal parameters, in particular the Jacobian of `g`. As for the ode function `dassl` admits a first optional argument which gives the kind of numerical scheme to be used (stiff, Adams).

The implementation of `dasrt` is very similar to `dassl`. This is a DAE solver with stopping time. The solution is computed and the instant at which a given surface is crossed is returned. The function receive an additional argument which is a vector valued function defining a set of surfaces. The output of dasrk gives the instants at which the surface is crossed and which particular surface has been crossed.

Both `dassl` and `dasrk` have a mechanism for hot restart.

V. Conclusion

There exist a large set of simulation functions available in Scilab. Specific functions have been designed for control applications and the simulation of possibly controlled linear systems. Systems can be discrete, continuous time or hybrid, given in explicit or implicit form. There exist also numerical codes for solving general differential boundary value problem. In Scilab, the code colnew.f [6] is interfaced as the built-in function `bvode`. Future work should include a built-in solver for delay differential equations ans updating the basic ode solver for based on the odepack package by switching to the recently released sundiag package [5].

References

[1] A. Hindmarsch and G. Byrne. Odepack, a systematized collection of ode solvers. In Eds. Scientific Computing, R. Stepleman et al., Editor, Scientific Computing, North-Holland, 1976.

[2] B. Pinçon, Une Introduction à Scilab, IECN 2002.

[3] L. F. Shampine, Numerical Ordinary Differential Equations, Chapman and Hall, 1994.

[4] L. F. Shampine, What everyone solving solving differential equation numerically should know, In Computational Techniques for ODEs, pp 1-17, 1980.

[5] Sundials, A collection of Ode solvers, http://www.llnl.gov/sundials.

[6] Fortran subroutine colnew.f, U. Ascher and G. Bader.

[7] L. R. Petzold, A description of DASSL, A differential/algebraic system solver, in Scientific Computing, eds. R.S. Stepleman et al., North- Holland, Amsterdam (1983).

[8] K. E. Brenan, S. L. Campbell, and L. R. Petzold, Numerical Solution of Initial Value Problems in Differential-Algebraic Equations, SIAM, 1996.

GreenScilab: A toolbox simulating plant growth in the Scilab environment

MengZhen KANG [a,b,c], Rui QI [c,d], Philippe de REFFYE [b,e], BaoGang HU [c]

[a] *Capital Normal University, BeiJing, China, 100037*

[b] *INRIA-Rocquencourt, B.P. 105, 78153 Le Chesnay Cedex, France*

[c] *LIAMA, Institute of Automation, Chinese Academy of Sciences, BeiJing, China, 100080*

[d] *Laboratory of Applied Mathematics, Ecole Centrale Paris, 92295 France*

[e] *AMAP, CIRAD Montpellier, 34398 France*

Abstract

In this paper we present a toolbox, "GreenScilab", which simulates plant growth based on GreenLab model with the open-source software Scilab ((c)INRIA-ENPC). GreenLab is a functional-structural plant model (FSPM) that computes plant growth and development. Such kinds of models are receiving more and more attentions in the domain of plant modeling. Bug proof and heavy computation are problems for FSPMs, and only few of them are able to be calibrated. GreenLab is one of these exceptions. While modelers are using different languages to fulfill their job, like C, matlab, C++, Scilab provides free, efficient and easy-to-use environment for modeling. GreenScilab(www.GreenScilab.org) is then born being the first open-source software that fulfill model simulation and calibration. It can simulate different botanical plant architectures, plant growth process, effects of climate conditions on plant growth, and fit the real plants with the model. The toolbox has been tested with a lot of parameter files representing different virtual plants. A graphical user interface is developed using TCL/TK to facilitate model I/O. Some functions are written in C to speed up simulation.

Key words: GreenLab, functional-structural plant model, Scilab toolbox, MESM

1 Introduction

Plants, including crops and trees, have been modeled with different aims(visualization [12],prediction[17], optimization [14]) and different methodologies (L system [11], automata, Markov chain[4]...). Scientists from various domains (applied mathematics, computer science, agronomy, forestry) work with different tools and programming languages(C, C++, Matlab, PowerSim) in doing their work, giving difficulty in teaching and cooperation.

It is commonly recognized nowadays that both plant architectural development and physiological process need to be integrated in modeling, leading to so-called functional-structural plant model[13]. In this new and multi-disciplinary subject, there are mainly approaches based on L-system, with L-studio software[1], and GreenLab model[16], with software CornerFit, DigiPlante and GL1. Except that GL1 was originally written in Matlab, others were written in C++.

The open-source Scilab software provides many equivalent functions as Matlab for matrix operation, optimization and graphics. It is easy to use compared to language C: the developer is not necessary to know a lot about programming. In order to facilitate sharing knowledge betweens different people, the GL1 code was translated into Scilab,leading to a toolbox named 'GreenScilab'. In this paper, we are going to present this toolbox. The GreenLab model theory has been presented in [16] and [5], thus they are explained here.

Email addresses: mzkang@liama.ia.ac.cn (MengZhen KANG), rqi@nlpr.ia.ac.cn (Rui QI), philippe.de reffye@inria.fr (Philippe de REFFYE), hubg@nlpr.ia.ac.cn (BaoGang HU).

2 GreenLab model

GreenLab model is a discrete system defined on the organ level. The plant grows cycle by cycle. Each growth cycle corresponds to a growth season, which can be several days or weeks for crops, or one year for trees. During each cycle, the terminal bud of the plant shoot produces a growth unit (GU). A GU contains one (often for crops) or several (for trees) metamers, a metamer being the elementary botanical unit in plant structure. A metamer is a set of organs: an internode, a node, one or more lateral buds and leaves, and sometimes flowers.

The plant shows organ differentiation during its life time. For example, the wheat produces vegetative organs (internodes and leaves) at young stages, and productive organs (ears) appear later on the top of stems. A weak tiller of wheat is not necessary to arrive the productive stage. In trees, some branches shows obviously less vigor than the others, for example, some short shoots can never grow longer. A botanical concept, physiological age(PA)[2], is used to describe such difference in a plant structure. It is different from the concept chronological age(CA),which means number of cycles since the appearance of an organ or a branch. Thanks to these two concepts, the plant structure can be organized in a hierarchical way.

In GreenLab model, the development pattern of plant is ruled by a dual-scale automaton[19]. The macrostate corresponds to the level of GU, while the microstates corresponds to the level of metamer. The transition between macrostate describes the organ differentiation along an axis, while the transition between microstates describe the acrotony of branches along a GU. The parameters for this model has clear botanical meaning, for example, number of lateral branches per metamer. The model deals also with case of reiteration(the branch being a copy of mother structure) and inflorescence structure. It is shown that it can simulate most of the botanical architectures as defined in [6]. Thus it can be used not only for crops, but also for trees, since the architectural model in [6] covers most of the plants.

Another part of the GreenLab model is the functional model. The plant growth is based on sink-source relationship. In each cycle, all organs (leaf, pith, ring, fruit, root) compete for biomass according to its sink strength , which is linked to its PA,CA and branching order. Sink variation of organs are described with Beta law. The total demand (requirement of biomass) of the plant,can be computed knowing the CA,PA and number of organs from the automaton. Biomass supply is computed from the leaves. When plant grows, the biomass supply and demand relationship changes, leading to different organ size in plant structure. In each cycle, the new and growing organs compete for biomass from a common biomass pool, whose initial value being the seed biomass. Organ size is computed from the renewed weight and the allometric law that links size and weight the renewed weight. The plant photosynthesis is computed macroscopically based on leaf area[16] or leaf area index[5] with Beer-Lambert law. New biomass becomes the reserve for next cycle, and so on.

For visualization, individual organs are organized in space according to the phyllotaxy angle, branching angle, bending parameters and so on, and the growth result can be visualized in 3D. In GreenScilab, the 3D structure is not used for computing light interception, but just for showing the plant.

Thanks to the notion PA and CA, the tree structure can be decomposed into substructures, supposing substructure of the same two features are similar. Compared to bud by bud simulation, this substructure algorithm can fasten a lot tree computation, [15][9].The plant organogenesis, growth and morphogenesis were formalized with dynamic equations in[3]. According to [3], the dynamics of the structure can be expressed as:

$$S_p(0) = s_p \ , \tag{1}$$
$$S_p(k) = R_p(k,S)S_p(k-1) \ , \qquad 0 < k < \tau_p \ , \tag{2}$$
$$S_p(k) = T_p(k,S)S_{\mu(p)}(k-\tau_p) \ , \qquad \forall k \geq \tau_p \ , \tag{3}$$

with

$$R_p(k,S) = \prod_{q>p} \left\{ m_{pq}(k) S_q(k-1)^{b_{pq}} \right\}^{r_{pq}} \ , \tag{4}$$

$$T_p(k,S) = \prod_{l=k-\tau_p+1}^{k} R_p(l,S) \ . \tag{5}$$

where S represents a substructure, $p \in \mathcal{P} = \{1, \cdots, P\}$ is the PA,P being the maximum PA of the plant, and k the CA. s_p denotes a bud of PA p, which is the stating condition of a substructure S_p.$m_{pq}(k)$ is a symbol representing a metamer of PA p and CA k,that bear buds of PA q. q is not younger than p, as the branches of higher order are physiologically older. The substructure is seen as a word by concatenating alphabets from the set of metamers $\Sigma = \{m_{pq}(k,n) \mid p,q \in \mathcal{P}\}$. b_{pq} is the number of buds on a metamer m_{pq}, and r_{pq} is number of metamer m_{pq} in a GU of PA p. τ_p is the number of repetitions of GUs of PA p before changing into another PA,μ_p. R_p

3 The GreenScilab toolbox

This toolbox simulates plants based on GreenLab model. It computes number, size, weight and 3D positions of all organs inside plant structure at each cycle. It is written mainly in Scilab language, using lots of Scilab functions for matric manipulation, visualization, optimization, etc. A user interface, made in TCL/TK, is developed to help parameter input, see Fig.1.

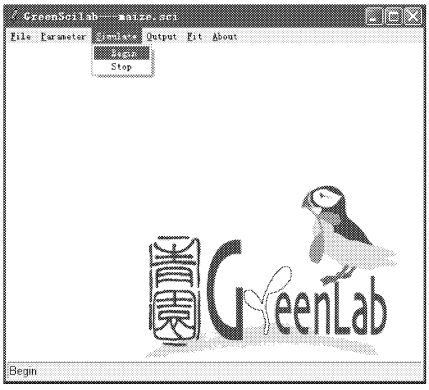

Fig. 1. GreenScilab interface

3.1 Simulation

The input of the simulation are model parameters for plant organogenesis, photosynthesis ,morphogenesis (and environmental data if needed). The parameters can be monitored through the TCL/TK interface. An example of the functional parameters is displayed in Fig.2, where users can choose two ways of computing biomass, and modify the sink functions of organs.

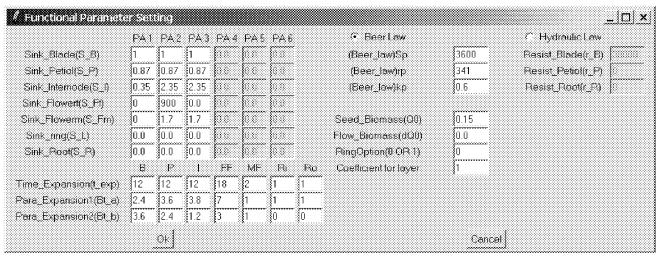

Fig. 2. Example of parameter dialog

Choosing menu 'Simulate/Begin', GreenScilab computes the following data in each cycle:

(1) the number of all organs;
(2) the demand of biomass from each organ;
(3) the biomass acquisition of each growing organ;
(4) the new sizes of organs;
(5) the geometrical shape of plant;
(6) the new biomass supply;

3.2 Model Calibration

Most of model parameters are observable, or can be obtained through statistics,like number of leaves per metamer, or thickness of leaves. Others are hidden properties, such as the rule of sink of expansion of organs, the sink strength of organs. These model parameters are calibrated by fitting the model output with the real plant data. This concerns how to prepare data and how to calibrate the model with given data. It is preferable to have detailed data on organ size and weight, as what the model outputs. For plants of single-stem structure, like Corner model, it is relatively easy to do measurement on each metamer.However, for a branching structure,like a tree, it is tedious to measure all metamers. But GreenScilab can accept sparse data, or measurement on compartment level, if one has good estimation of about the parameters. The aim of the fitting process is to find the best values of hidden parameters, to make the model output closest to the measured data. The non-linear least square method is suitable for this purpose[18]. In this toolbox, the function *lsqrsolve* from Scilab optimization toolbox is used for fitting, where functions (based on Levenberg-Marquart algorithms) from Argonne National Laboratory is used.

The input of the calibration process are the real plant data (the target) and initial values of model parameters to be fit. The initial values are important to have a quick convergence. To reach satisfactory fitting results, in practice, prior knowledge,like organ expansion duration, are needed. Fitting is often not successful at the first strike because of various reasons. However, model calibration has been done successfully on several crops, like sunflower, maize[5], wheat, chrysanthemum[8], etc. In GreenScilab, the fitting process runs by choosing 'Fit/Begin'.

3.3 Case study : maize

An example of maize [5] is presented here to show the usage of GreenScilab toolbox. Field data of maize have been collected destructively at several growth stage. The task is to fit all the data simultaneously with one set of model parameters, as shown in Fig.3. With parameters

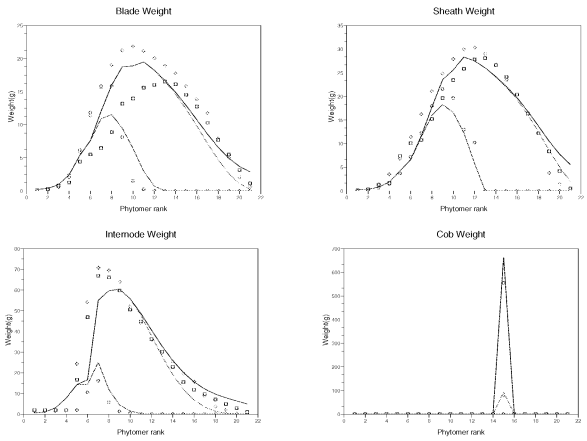

Fig. 3. Weight of organs in maize at GC 12, 21 and 30. (symbols:measured data, lines:model output)

gotten by fitting process, one can simulate the plant. The computed results can be displayed either with numerical values, curves, like in Fig.4, or with 3D shape of plants, like in Fig.5.

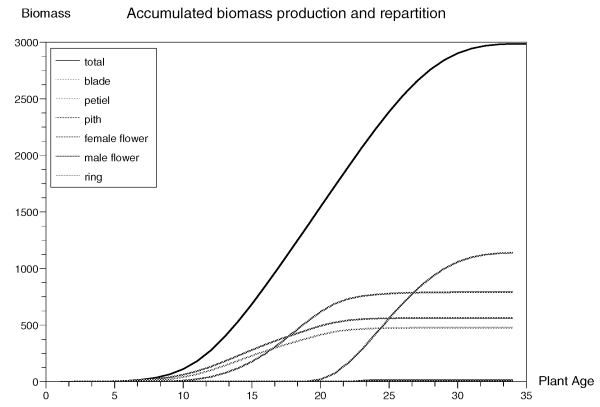

Fig. 4. Biomass production and allocation of maize

Fig. 5. 3D visualization of maize

One can change the parameters to study the plant growth. For example, by changing the S_p value in the Fig.1, which is project area(cm^2) of a plant computed from the planting density, one can simulate the effect of density on the cob wight per plant and per square meter, as shown in 6. This tendency is close to the real measurement (data not shown), even if change of parameters at different densities are not considered yet.

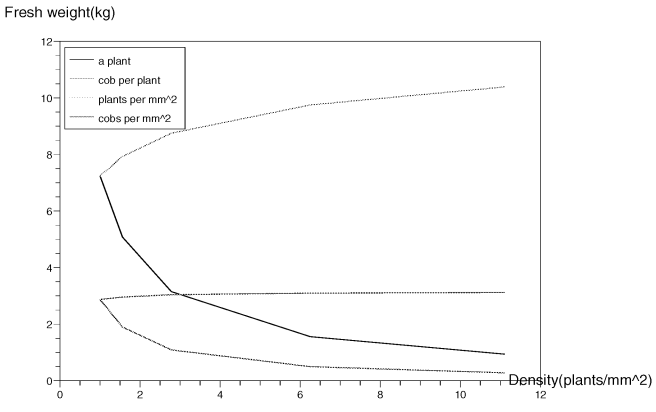

Fig. 6. Simulating effect of planting density on production in GreenScilab

3.4 Efficiency

As Scilab provides an interpret language, the computation speed is slower in nature compared to those written in C. Moreover, a lot of hypermatrices are used to describe the number, size, weight of organs of different PA,CA, plant age, and reiteration order, which slows down the computation. This problem is more evident when simulating a plant of high branching order, say, 5, or a plant of big age. When the plant contains a lot of polygons,like in Fig. 7, the visualization itself will takes several minutes too. High efficiency is especially important in fitting real data, as the simulator will be called many times. To improve the efficiency, some computations that concerns high-dimensional hypermatrice are translated into C. In Scilab, function *profile* can be used to test the cost of function, so it is easy to find which sentence is costly. These translated functions run faster than previous Scilab code. Fig.8 shows the result on a function computing sizes of organs in each cycle. The difference in time becomes more obvious when the plant age is bigger.

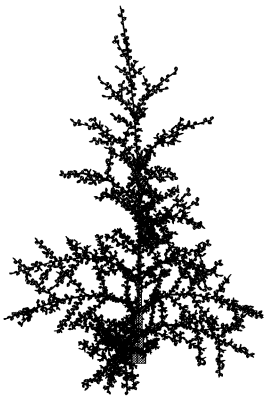

Fig. 7. An example of a plant with branches of order 5

4 Conclusion

We presented here the GreenScilab toolbox and some examples. More possible applications can be explored by referring the articles on GreenLab model. As scilab code is not difficult to learn and use for non-computer scientists, it is possible that other researchers modify part of the codes for their specific purpose, for example, the module for biomass production.

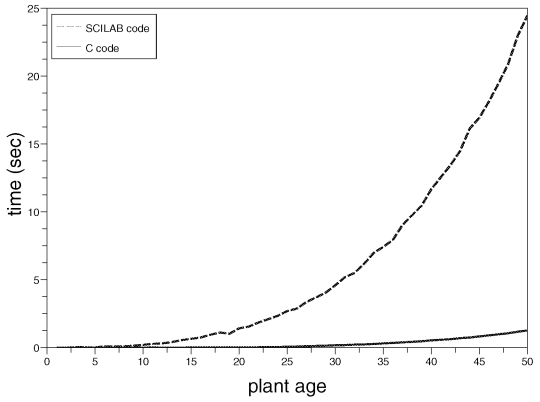

Fig. 8. Time efficiency for a GreenScilab function using hypermatrix

This toolbox is currently based on deterministic model, that is, the plant topology is fixed, and there is no feedback from plant photosynthesis. The next work will be introducing bud probability,as done in [7], and the effects of plant production on the plant development in the following cycle, as described in [10]. It is also interesting to apply optimization tools, to study the optimal model parameters, such as sink strength, or topological structure, for the expected output: weight of fruit, or weight of leaves. A website(www.GreenScilab.org) has been applied to for this toolbox, and it will also be uploaded soon to the site of Scilab distribution (www.scilab.org).

5 Acknowledgement

Many thanks to F. Delebecque for C interface program and S. Steer for help in Scilab. This work is supported in part by LIAMA, NSFC(60073007) and PostDoc scholarship for M.Z. Kang from INRIA.

References

[1] http://algorithmicbotany.org/.

[2] D. Barthelemy, Y. Caraglio, and E. Costes. Architecture, gradients morphogenetiques et age physiologique chez les vegetaux. In J. Bouchon, P. de Reffye, and D. Barthelemy, editors, *Modélisation et Simulation de l'Architecture des Végétaux*, pages 89–136, Paris, France, 1997. INRA, Science Update.

[3] P. de Reffye, M. Goursat, J.P. Quadrat, and B.G. Hu. The dynamic equations of the tree morphogenesis greenlab model. In *Research report 4877*. INRIA, 2003.

[4] Barthélémy D. Caraglio Y. Costes E. Guédon, Y. Pattern analysis in branching and axillary flowering sequences. *Journal of theoretical biology*, 212:481–520, 2001.

[5] Y. Guo, Ma Y.T., Z.G. Zhan, B.G. Li, M. Dingkuhn, D. Luquet, and P. de Reffye. Parameter optimization and field validation of the functionalcstructural model greenlab for maize. *Annals of Botany*, 97:217–230, 2006.

[6] F. Hallé, R.A.A. Oldeman, and P. B. Tomlinson. *Tropical trees and forest:An Architectural Analysis*. Springer-Verlag, New York, 1978.

[7] M. Z. Kang, Ph. de Reffye, J. F. Barczi, B.G. Hu, and F. Houllier. Stochastic 3d tree simulation using substructure instancing. In B. G. Hu and Jaeger M., editors, *Plant Growth Modeling and Applications*, pages 154–168, BeiJing,China, 2003. Springer and Tsinghua University Press.

[8] M. Z. Kang, E. Heuvelink, and Ph. de Reffye. Building virtual chrysanthemum based on sink-source relationships: Preliminary results. Acta Horticulture,Accepted.

[9] M. Z. Kang, H.P. Yan, P. de Reffye, M. Jaeger, B.G. Hu, and F. Houllier. A fast algorithm for calculating stem and branch radial growth in a tree. In *IUFRO colloque*, Vancouver, Canada, 2002.

[10] A. Mathieu, P.-H. Cournède, and P. de Reffye. A dynamical model of plant growth with full retroaction between organogenesis and photosynthesis,. In *7ème Colloque Africain sur la Recherche en Informatique (CARI'04)*, Hammamet, Tunisia,, 2004.

[11] P. Prusinkiewicz and J. Hanan. Developmental models of herbaceous plants for computer imagery purpose. *Computer Graphics*, 22(4):141–150, 1988.

[12] P. Prusinkiewicz, L. Muvndermann, R. Karwowski, and B. Lane. The use of positional information in the modeling of plants. In *ACM SIGRAPH 2001*, pages 289–300, Los Angeles, CA, USA, 2001.

[13] R. Sievänen et al. Components of functional-structural tree models. *Ann. For. Sci.*, 57:399–412, 2000.

[14] L. Wu, F.X. le Dimet, B.G. Hu, P.H. Cournède, and P. de Reffye. A water supply optimization problem for plant growth based on greenlab model. In *7ème Colloque Africain sur la Recherche en Informatique (CARI'04)*, Mammamet, Tunisia, 2004.

[15] H.P. Yan, J. F. Barczi, P. de Reffye, and B.G. Hu. Fast algorithms of plant computation based on substructure instances. In *International Conferences in Central Europe on Computer Graphics, Visualization and Computer Vision*, volume 3, pages 145–153, 2002.

[16] H.P. Yan, M.Z. Kang, P. de Reffye, and M. Dingkuhn. A dynamic, architectural plant model simulating resource-dependent growth. *Annals of Botany*, 93:591–602, 2004.

[17] X.Y. Yin and H.H. van Laar. *Crop systems dynamics*. Wageningen Academic Publishers, The Netherlands, 2005.

[18] Z. G. Zhan, P. de Reffye, F. Houllier, and B.G. Hu. Fitting a funtional-structural growth model with plant architectural data. In B. G. Hu and Jaeger M., editors, *Plant Growth Modeling and Applications*, pages 108–117, BeiJing,China, 2003. Springer and Tsinghua University Press.

[19] X. Zhao, P. de Reffye, F.L. Xiong, B.G. HU, and Z.G. Zhan. Dual-scale automaton model of virtual plant growth. *Chinese Journal of Computers*, 24(6):608–615, 2001.

SCICOS: USE OF HARDWARE IN THE LOOP SIMULATION IN CONTROL

Simone Mannori , Ramine Nikoukhah
INRIA-Rocquencourt, Domaine de Voluceau,
78153 Le Chesnay Cedex, France
e-mail: simone.mannori@inria.fr

KEYWORDS
Dynamic system simulation, Hybrid systems, Simulation software, Real time control, Hardware in the loop control

ABSTRACT

Scilab/Scicos is an open-source and free software package for design, simulation and implementation of industrial process control systems. It can be used as the center of an integrated platform for the complete development process, including running controllers with real plants (Scicos Hardware In the Loop) and automatic code generation for real time embedded platforms (Linux-RTAI, RTAI Lab, RTAI-XML, J-RTAI Lab). Scilab/Scicos is a mature, stable, working alternative to closed source, proprietary solutions for educational, academic, research and industrial applications. In this paper, we present a complete development software/hardware chain for the control of the ball and beam experiment.

Introduction

Scicos is a Scilab toolbox[1] for modeling and simulation of dynamical systems. It provides a block diagram graphical editor for the construction of complex dynamical systems including hybrid systems.
The main usage of Scilab/Scicos is in the area of systems and control. A typical application consists of designing controllers using the routines available in the Scilab control toolbox, which are then validated in Scicos by simulation. This of course requires that a model of the plant be constructed in Scicos. Once the controller has been validated, Scicos code generator can be used to obtain a C code to be used for the actual implementation of the controller.
With computers becoming more and more powerful, for many applications, it is possible to consider validating the controller not only on a model of the system but also directly on the system itself using a hardware in the loop approach. In this case, the computer plays the role of the controller as Scicos simulation runs.
In this paper, we present, through the ball and beam experiment, the use of Scicos in hardware in the loop applications. The main steps in realizing this project, have been to

- construct a mathematical model of the plant,
- validate the model of the plant through simulation and open-loop measurements,
- design a suitable controller,
- simulate the full system and optimize controller parameters,
- construct a real model of the plant,
- run the controller inside the standard simulator while connected to the real plant in ”soft-real-time” mode (Scicos Hardware In the Loop).

We also

- use an automatic code generator to create stand-alone controller program that could run stand-alone in ”hard-real-time” mode (Linux-RTAI Code Generator,
- implement graphical user interfaces (RTAI Lab, J RTAI Lab) to remotely interact with the controller using network connections;

we do not discuss these latter points in this paper.

Software packages used

One - if not the most important - critical issue for the development of modern digital control systems is the software tools used for the design and the implementation. We use Scilab as the main development environment. Scilab [8] is a scientific software package for numerical computations providing a powerful open computing environment for engineering and scientific applications. Since 1994 it has been distributed freely along with the source code via the Internet. It is currently used in educational and industrial environments around the world. Scilab includes hundreds of mathematical functions with the possibility to add interactively programs from various languages. It has sophisticated data structures (including lists, polynomials, rational functions, linear systems), an interpreter and a high level programming language. It is possible to write simulation programs as Scilab scripts but it is very time consuming, inefficient, error prone and none modular. To simplify this job, Scilab includes Scicos [8] a graphical dynamical system modeler and simulator toolbox. Scicos has been used for applications in signal processing, systems control, queuing systems, and to study physical and biological systems. Within the Scicos graphical editor it

[1] Scilab is a free open-source software for scientific computation, see www.scilab.org and www.scicos.org.

is possible to place, configure and connect blocks, in order to create diagrams to model hybrid dynamical systems, and simulate them.
Most of the Scicos graphical user interface is written in Scilab language, for complete integration with Scilab, easy customization and maximum flexibility. The simulation engine and the computational functions associated to the blocks are written in C and compiled. Pre-compiled and customizable C routines are supported. To use the latter, a supported C compiler must be present on the system (for example GCC under Linux or Visual C++ under Windows). If the execution speed is not a priority, it is also possible to write computational functions for new blocks in the Scilab language.
Scicos simulations could be used to interact with real systems in many ways:

- Scicos HIL (Hardware In the Loop). With some limitation, it is possible to use Scicos simulation to control a real plant in real time. This solution is presented in this paper.

- Stand-alone C code. The Scicos "Code Generator" translates Scicos diagrams into stand-alone, general purpose C code. This code uses by default the standard I/O (terminal) as interface; it is up to the end user to customize the C code in order to interact with I/O data acquisition devices and to resolve the timing issues.

- SynDEx code generation. A special code generator can be used to generate SynDEx[13] code. SynDEx is used to implement hard real time code on multiprocessor architectures.

- Code generation for Linux RTAI. This solution combines the hard real time capabilities of RTAI [16] with the creation of a stand-alone program from Scicos; ideal for embedded systems with limited hardware resources.

To implement HIL in Scicos, we use the Comedi library. Comedi is the standard way to use I/O interface devices with Linux. The Comedi project develops open-source drivers, tools, and libraries for data acquisition card. Comedi is a collection of drivers for a variety of common data acquisition plug-in boards (more than 300 devices are supported). The drivers are implemented as a core Linux kernel module providing common functionality and individual low-level driver modules. To use the driver, the application program should use Comedilib functions. Comedilib is a user-space library that provides a developer-friendly interface to Comedi devices. Included in the Comedilib distribution is documentation, configuration and calibration utilities, and demonstration programs. Kcomedilib is a Linux kernel module (distributed with Comedi) that provides the same interface as Comedilib in kernel space, suitable for real-time tasks.
The Linux kernel is the foundation over which this building is constructed. The Linux kernel provides a level of flexibility and reliability simply impossible to achieve with any other (free or commercial) operating system. For this reason, many commercial providers of real time and embedded systems (Wind river, Montavista) offer support for Linux.
The real time performances of the latest 2.6.1x Linux kernel are very close to real time (for sampling time in the milliseconds range) but the "plain, vanilla" Linux is NOT a real time operating system: with the standard Linux kernel it is not possible to have guaranteed timing. There are many projects that modify (patch) the Linux kernel in order to create a "parallel" hard real time kernel (and user) space where the tasks have deterministic activation timing, while leaving the other "normal" tasks running in the standard Linux user's space. We use RTAI because it offers direct support for Scilab/Scicos, but it is also possible to use Xenomai.

Construction of the plant

To validate our approach, we wanted to test the full process on a real plant. There are many companies on the educational market that offer such products [1]. We decided to build one ourselves. We chose the classical ball and beam experiment (Fig. 1 (a)) because its intrinsic instability and non linearity make it a recognized benchmark and it is possible to build it using readily available cheap parts. For most of the mechanical parts we used LEGO Technique/Mindstorm [2] components (less than 200 Euro for a complete kit).

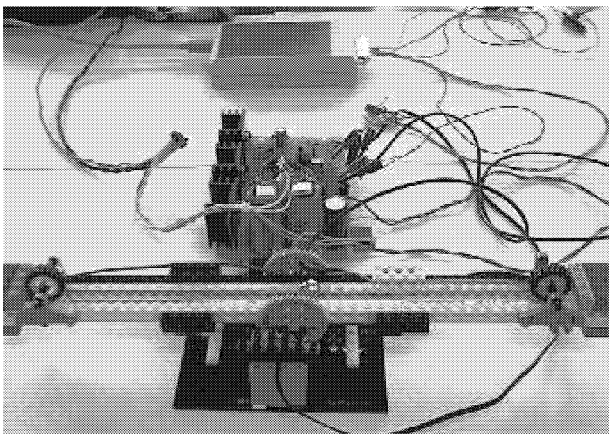

Figure 1: Complete system. From the bottom: (a) ball and beam; (b) amplifiers and power supplies; (c) USB-DUX data acquisition card.

The ball is made of stainless steel. The ball rolls on two brass rails salvaged from a model train set and glued on the Lego bricks (Fig. 1(a)). We built the input amplifier, the power output amplifier and the power supplies using a single experimental printed circuit board (Fig. 1(b)). We used the USB-DUX ([1]) for data acquisition.

Ball position sensor

The ball position is measured using one of the rails as a variable voltage source (Fig. 2). A floating 5 Volts voltage and a

series resistor, supply a constant 700 mA current to the reference rail. This arrangement is simple but inefficient: almost all the electrical power is dissipated in the linear regulator and in the external 6.8 ohm / 5 Watt power resistor. To avoid this waste of electrical power, we plan to use a constant voltage (100mV), low noise, switching power supply in the future. The metallic (stainless steel) ball works as a sliding contact; the second rail closes the circuit, sending the low level signal (0-40 mV, 0-30 cm) to the input amplifier.

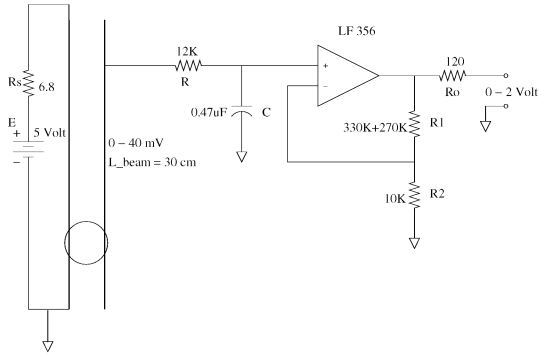

Figure 2: Input Amplifier.

The contact resistance is very noisy (moving contact noise). The input amplifier (Fig. 2) has high-input impedance and uses a low pass filter (R and C) that cuts out part of the noise from this sensor. With the high-impedance of the JFET operational amplifier LF356, if the ball loses electrical contact, the input filter works as a "sample-and-hold" device: the capacitor C "remembers" the last valid value of voltage/position. This non linear behavior of a fully linear filter and amplifier is a "collateral effect" of the non-linear, random properties of the contact resistance, which represents the internal impedance of our position sensor. Having two moving contacts (reference rail/ball and ball/reference rail) in series aggravates the problem. A common cure to reduce the moving contact noise is to use carbon based (electrical conducting) grease to lubricate the ball.

Actuator

For actuator we use the LEGO Mindstorm standard motor model "71427". The specifications of this motor are available [3] from experimental tests. The inductance of the motor armature ($L_A = 2.07mH$, average value, measured with an impedance bridge) is not included in the model because it introduces a time constant

$$\tau_e = L_A/R_A = 0.83ms$$

which can be neglected.
The limited electromechanical conversion efficiency factors of the motor: K_T (torque constant) and K_V (speed constant) are different here. These two constants are equal in the case of "perfect" 100% efficient motor, where all the electrical power is converted into mechanical work. The constants are different also because inside the Lego motor there is a reduction gear that lowers the efficiency but increases the torque (reducing the maximum speed) and improves the linearity of the DC motor in the low speed region.

In the model, we neglect all the possible sources of friction.

The motor has more than sufficient speed and torque to move the ball and the beam directly. We use an external reduction gear to better use the speed range of the motor.

Power Amplifier

The output of an operational amplifier is boosted with a complementary pair Darlington transistors. This linear power amplifier has more than sufficient bandwidth (10kHz), voltage (+/- 15V) and current (+/-1.5 A) capabilities to drive the loaded motor. The output voltage is limited to +/-9V to avoid motor overload (which could permanently damage the motor). We choose to set $A_V = 1$ for the power amplifier because we found that the +/- 4V dynamic range of the USB-DUX output voltage is enough to drive the motor (the output amplifier works only as current booster).

Encoder Input

Using the bidirectional counter input of the data acquisition card (USB-DUX), it is possible to connect an encoder measuring the real angle of the beam. We have not used this input in the experiment because we chose to use an observer to recreate the full state of the system. With an observer, it is possible to avoid the necessity of a sensor to measure the angle of the beam.

Data Acquisition Card

We use the USB-DUX [4] interface. We choose this device because it has sufficient resources to monitor and drive the plant. USB-DUX uses a Universal Serial Bus connection thus it can be used with any recent computer, including laptops. USB-DUX uses Comedi [5] device driver suite that allows the use of different hardware without a customized API. In the spirit of free and open-source development, the USB-DUX is fully documented (hardware and software), including schematics and source code of the firmware of the micro-controller that runs the board. Finally the cost is limited: 250 euro. With the Linux/Comedi/USB combination, it is also possible to use other platforms than x86 (e.g. Apple PPC, Arm,...).

The only real limit of this board is the USB bus: unfortunately it is not yet possible to run it in true hard real time. To do so, it is necessary to rewrite the full USB Linux stack [6]. In most cases, with recent 2.6.1x kernels, this is not a serious limitation for applications with sampling times of 10ms or higher. To allow full hard real time guarantee behavior, it is necessary to use ISA/PCI/PC-CARD I/O board [7]

Modeling and simulating the system

The non linear model of the plant is obtained from elementary physical laws; see the Appendix. The controller is obtained from the linearized model. The linearization around the steady-state position of the ball at the center of the beam can be done analytically or numerically.
The continuous-time linear state-space model of the plant is represented by the matrices `A`, `B`, `C` and `D`. The `A` matrix has dimension 4×4 (the model has four states see the Appendix), the matrix `B` is 4×1 (there is only one input: the motor voltage), `C` is 1×4 (the position of the ball is the only output) and `D` is zero.
The eigenvalues of the A matrix show that the linearized model is unstable at the equilibrium point (there is an eigenvalue with positive real part).

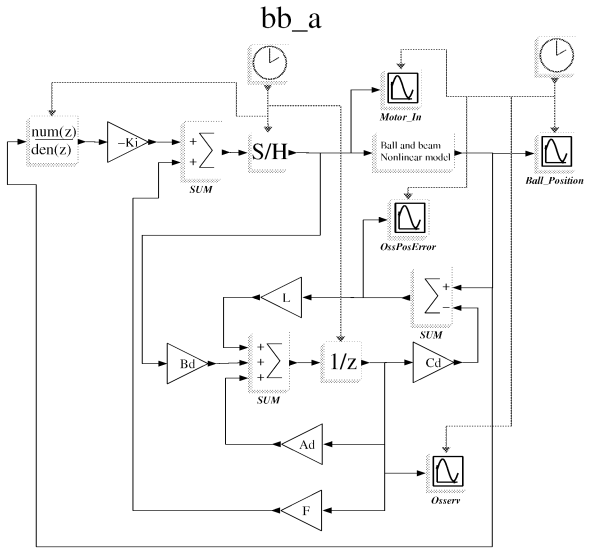

Figure 3: Scicos diagram `bb_a.cos` with complete, continuous non linear model of the plant and the linear discrete controller.

Controller design

The controller implemented inside a PC is a discrete-time system, but the real plant is a continuous-time system. Various approaches are possible: we choose to transform the continuous model of the plant into a discrete one and design the controller in the discrete-time domain. The first thing to do is choose a sampling time. Usually the sampling time is chosen looking at the closed loop expected performances. If T_r is the desired 10-90 response time to a step reference, then $T_s = T_r/10$ or less. The sampling time should be high enough to cover, within the $F_s/2$ Nyquist limit, all the "fast" poles of the plant in order to avoid inter-sampling oscillation.

It is important to check also the power of the actuator present in the real system. In our plant, the Lego motor has an intrinsic bandwidth in the range 10-40 Hz, depending on the load inertia. We choose Ts = 10 ms because it is a good compromise between this requirement and it is realizable with the available hardware and software components in soft and hard real time modes.
Input amplifier, data acquisition and output amplifiers can be considered fully "transparent".
With the full, linearized, model of the plant

```
sys = syslin('c',A,B,C,D);
```

and the sampling time Ts, the equivalent discrete time plant is computed with

```
sys_d = dscr(sys,Ts);
```

The system matrices are obtained as follows:

```
[Ad,Bd,Cd,Dd] = abcd(sys_d);
```

The classical approach to the design of a regulator is to use the separation principle. First, a state feedback is designed, then it is applied not to the state, which is not measured, but to an estimate of the state obtained using an observer. We use the LQG method where the feedback is obtained using the LQR method and the observer is a Kalman filter.
In order to improve the steady state accuracy of the system, an external discrete integrator is added in the loop. The matrices of our new "augmented" feedback system are:

$$F_i = \begin{pmatrix} F & K_i \end{pmatrix}, Ad_i = \begin{pmatrix} Ad & 0 \\ -Cd & I \end{pmatrix}, Bd_i = \begin{pmatrix} Bd \\ 0 \end{pmatrix}$$

With this arrangement it is possible to compute the gain of the integrator K_i and the stabilizing feedback matrix F at the same time. The value of R and Q are found experimentally using R = 1 and Q = [1 1 1 1 1] as a starting point.

```
F_lqr_i = bb_dlqr(Adi,Bdi,Qi,R) ;
F =  -F_lqr_i(1:4) ;
Ki = -F_lqr_i(5) ;
```

Observer

As an observer, we use the Kalman filter with appropriate parameters. The added integrator does not change the design of the observer because it is external to the plant.
Scilab function `lqe` is used to design the observer (Kalman filter in this case).

Testing the controller with the real plant: Scicos HIL

With some limitations, it is possible to use Scicos to control a real plant. The first step is to create input blocks to acquire the feedback signals and output blocks to drive the system. Using the examples found in the Scicos [9] and

Comedi [10] documentations, we have developed the interfacing and computational functions that realize the I/O facilities using Scicos blocks. Within Scicos it is possible to run the simulation in "real-time" using the menu option `[Simulate]->[Setup]` and setting "Real-time scaling" equal "1". With this parameter set Scicos "waits" for the right time to read the inputs, make the calculations and updates the outputs. It is clear that the time required to complete all the actions should be less than the sampling time. Normally this is not a problem with modern PCs. The latest 2.6.1x Linux kernel, with the low latency features active and with the internal timer set to the maximum resolution (1 ms, 1000 Hz) could be considered real-time at 99% for a sampling time of 10ms. This performance is more than enough for laboratory applications with electromechanical systems where sampling time in the range of 4-20 milliseconds.
The respect of the sampling time is a very critical issue for a digital controller because the position of poles and zeros are functions of sampling time Ts. If Ts changes, the position of poles and zeros change, with potential dangerous consequence in the transient, steady state and stability properties of the closed loop hybrid system.
It is also important to limit the number of Scicos scopes and traces: they use CPU resources. Increasing the scope's internal buffers reduces the CPU loads, at the expense of the real time update of the display.

Compensation of the mechanical non linearity

The very cheap Lego parts create a non linear "sticky friction" (sticktion) that block the movement of the beam for very low values of the motor voltage. As a result of this "dead zone" effect, the motor is totally incapable of making the small movements needed to place the ball in the perfect equilibrium position with zero ball speed. We use a custom Scicos block to create an artificial non linearity to compensate the "dead-zone", using a fixed voltage "step" in the correct direction.
This non linearity is realized by the block `Mathematical Expression` using the equation:

```
sign(u1)*a+u1
```

The parameter `a`, defined in the script or in the `Context`, represents the equivalent voltage of the the dead zone of the motor (the minimum voltage required to start a motor movement). The full regulator is shown in Fig. 4. We used a non linear block `Saturation` to limit the motor voltage during the start up: during the normal operation, the voltage computed form the controller is never beyond the saturation levels (+/- 2V).

Results

The set up described in this paper works perfectly despite low cost components used in the construction of the hardware. The ball and beam mechanism works: the ball is stabilized and the system has satisfactory performance. See Figs. 5 and 6 for the scope outputs, which here correspond to real oscilloscopes.

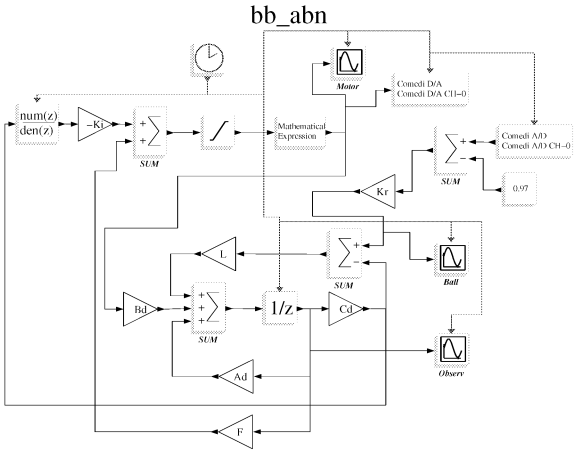

Figure 4: Scicos Hardware In the Loop .

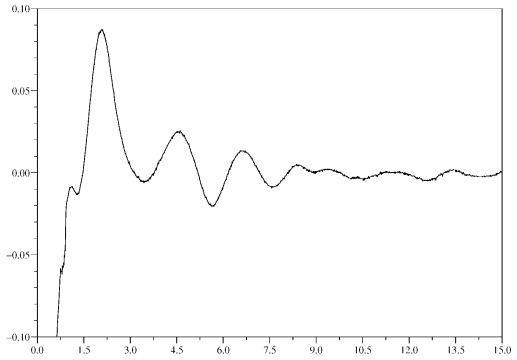

Figure 5: Ball position (m), time (s).

Scicos RTAI Code Generator

In some situations, the performance of the Scicos HIL solution is not sufficient, in particular if a controller requires a sampling time below 4 ms. In other cases, it is not possible to install the full Scilab/Scicos package on the controller hardware. For these situations, code generation option must be used to obtain stand-alone codes. For example for code generation for RTAI, it suffices to replace the I/O blocks with blocks from the RTAI Scicos palette. This procedure is fairly simple but it is not described in this paper due to space limitation.

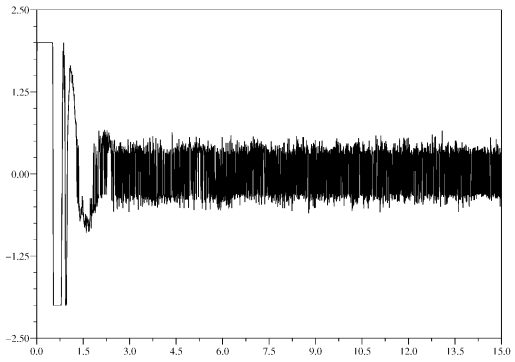

Figure 6: Motor voltage (Volt), time (s).

Conclusion

In this paper we have presented a full working system to illustrate the use of the modeling and simulation software Scicos in hardware in the loop control applications.

REFERENCES

[1] Quanser [Online].
Available: *http://www.quanser.com*.

[2] TQ Education and Training Limited [Online].
Available: *http://www.tq.com/*.

[3] LEGO [Online].
Available: *http://www.lego.com/*.

[4] LEGO Mindstorm [Online].
Available: *http://mindstorms.lego.com/*.

[5] LEGO motor parameters [Online].
Available: *http://www.philohome.com/motors/motorcomp.htm*.

[6] USB-DUX [Online].
Available: *http://www.linux-usb-daq.co.uk/*.

[7] Comedi [Online].
Available: *http://www.comedi.org/* .

[8] USB-RTAI stack: works in progress [Online].
Available: *https://www.rtai.org/*.

[9] PC-CARD DAS16/16-AO Measurement Computing [Online].
Available: *www.measurementcomputing.com* .

[10] J.P. Chancelier, F. Delebecque, C. Gomez, M. Goursat, R. Nikoukhah and S. Steer, *Introduction à Scilab*, Springer, 2001.

[11] C. Bunks, J.P. Chancelier, F. Delebecque, C. Gomez, M. Goursat, R. Nikoukhah and S. Steer, *Engineering and Scientific Computing with Scilab*, Birkhäuser, 1999.

[12] Scilab [Online].
Available: *http://www.scilab.org/*.

[13] SynDEx [Online].
Available: *http://www.syndex.org/*.

[14] Scicos documentation [Online].
Available: *http:www.scicos.org*.

[15] S. L. Campbell, J-Ph. Chancelier and R. Nikoukhah, *Modeling and Simulation in Scilab/Scicos*, Springer, 2005.

[16] R. Bucher [Online].
Available: *http://www.dti.supsi.ch/~bucher/scilab-howto.pdf*

APPENDIX
Mathematical model of the plant

The mathematical model of the mechanical system has three "internal states": the ball position x, the ball's rotation angle ϕ, and the beam angle, θ. The equation relative to the dynamics of the ball is

$$mg\sin(\theta) = m\ddot{x} + J_s\ddot{\phi}/r$$

where r is the ball radius (meter), m the ball mass (Kg) and $J_s = 2mr^2/5$ is the rotational moment of inertia.
Using the relation $x = \phi r$ obtained thanks to the hypothesis that the ball rolls without sliding, the dynamics of the ball is simplified as follows

$$\ddot{x} = 5g\sin(\theta)/7.$$

The dynamics of the beam is:

$$T = -mg\cos(\theta)x + J_b\ddot{\theta} + mx^2\ddot{\theta}$$

where T represents the torque on the beam's axis.
Using the simplified model of the motor (one that does not consider the inductance):

$$T_M = K_T i_A$$

where T_M is the motor torque (Nm), K_T the torque constant (Nm/A), and i_A the motor current (A).
Denote the kinematics ratio of the gears that couple the motor and the axis of the beam by K_C. Then

$$K_C = 40/8 = \omega_M/\omega = T/T_M$$

where ω_M is the rotational speed of the motor axis and $\omega = \dot{\theta}$.
The equation of the motor is

$$U_M = R_A i_A + K_V \omega_M,$$

we thus obtain

$$K_C K_T i_A = -mg\cos(\theta)x + J_b\ddot{\theta} + mx^2\ddot{\theta}$$

where

$$i_A = \frac{U_M - K_V\omega_M}{R_A}.$$

Replacing $\dot{x}$ by v, we obtain the complete model of the system:

$$\begin{aligned}
\dot{\omega} &= \frac{mgx}{J_b + mx^2}\cos(\theta) - \\
&\quad \frac{K_V K_C^2 K_T}{R_A(J_b + mx^2)}\omega + \frac{K_C K_T U_M}{R_A(J_b + mx^2)} \\
\dot{\theta} &= \omega \\
\dot{v} &= \frac{5}{7}g\sin(\theta), \\
\dot{x} &= v.
\end{aligned}$$

Modeling and simulation of chaotic communication systems in Scilab/Scicos environment

Alan Layec
INRIA Rocquencourt
Le Chesnay, France
e-mail: alan.layec@inria.fr

Danièle Fournier-Prunaret
LEISA, INSA Toulouse
Toulouse, France
e-mail: daniele.fournier@insa-toulouse.fr

Laurent Larger
FEMTO-ST/Optoelectronics group
University of Franche-Comté
Besançon, France
e-mail: laurent.larger@univ-fcomte.fr

Raymond Quéré
XLIM
University of Limoges
Limoges, France
e-mail: raymond.quere@xlim.fr

KEYWORDS Communications, Computer Aided Design (CAD), Hybrid simulation

ABSTRACT

The paper reports recent advances in regularly clocked chaos communication systems focusing on the problems encountered in modeling and simulation of such systems. We will show that Scicos is an appropriate tool for this purpose. The reason lays in the way hybrid systems are modeled and in particular the way the events are treated in Scicos formalism. Some examples are presented in the last part of the paper.

INTRODUCTION

Problems of modeling and simulation encountered in systems which use chaotically modulated carriers lay mainly in the difference between time-constants of the low and high frequency stages, and the treatment of mixed-signal. Moreover, development of such communication systems requires flexible Computer Aided Designed (CAD) working environment. Indeed, this environment must be suitable to implement custom models and be capable of considering both discrete and continuous time signal.

In this paper, we present the free an open-source scientific software Scilab/Scicos, to solve the high technical level of modeling and simulation of chaotic communication systems. First, we give a brief description of principles of synchronization of chaotic systems and then some examples of modern systems based on chaos. Some features of the modeler/simulator software Scicos, revelant to the use of event for modeling mixed-signal system, are then presented. The resolution of some discrete equations that we are using to generate chaotic and pseudo-chaotic behavior are realized and presented in the graphical editor. Finally, we give a description of a quasi-chaotic frequency-hopping communication system that we have entirely developed in Scicos. We will try to show the effectiveness of Scicos in modeling and simulation of such a complex communication system.

BACKGROUND

Complex dynamics of chaotic oscillators are issued from time domain integration of systems of non-linear state equations. During the past fifteen years, these behaviors have been studied in a wide range of applications in the scientific and engineering communities to realize secure communications. Indeed, waveforms produced by chaotic oscillator have a wide band power spectrum and approximately have the same correlation properties as the White Gaussian Noise (WGN). Many applications have been found in noise generator design or Pseudo random Noise (PN) in digital applications.

The possibility of synchronization of chaotic systems, as illustrated in the Figure 1 with the general approach of the master-slave synchronization set-up, has been first demonstrated in 1991 by the use of low frequency analogical circuits (Carroll and Pecora 1991).

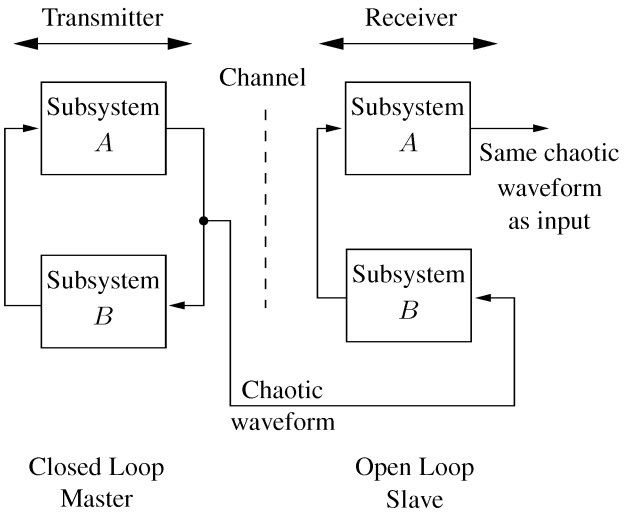

Figure 1: Master-slave synchronization.

Initially, chaotic transmission has been then accomplished by hiding the message in the waveform produced by a chaotic oscillator. This oscillator, included in the transmitter, is traditionally a closed loop system that is a collection of sub-systems. As shown in the Figure 1, the synchronization is achievable by constructing an open loop receiver with sub-systems which are included in the oscillator of the emitter. The main goal is to internally duplicate the same chaotic waveform that the waveform viewed at input. When the level of message introduced at the output of the transmitter is not predominant (in comparison with the level of the chaotic waveform), the information is then recovered by subtracting input and output signals of the receiver.
In fact, such a technique of transmission is not very efficient in current communication systems. Indeed, when traveling through the various stages of the transmitter, the receiver and the channel, chaotic waveform is subjected to different disturbances which make synchronization difficult to realize.

A second possibility has been then investigated to exploit chaotic waveform to drive a high frequency carrier as in the optical system (Gastaud *et al.*) shown in the Figure 2.

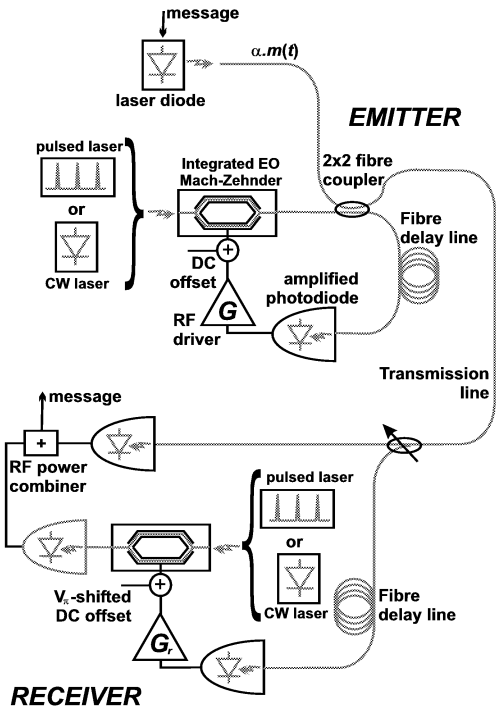

Figure 2: Optical communication system.

Emitter and receiver consist of two identical nonlinear delayed opto-electronic differential processes. The ”key” nonlinear process is performed through an electro-optic modulation transfer function, which should exhibit at least one extremum to allow for chaotic oscillations. The emitter is organized in a closed loop configuration, and acts as both wide band chaotic oscillator (> several GHz), and information encoder (through the 50/50 fiber coupler). The receiver is in open loop, performing the replica of the emitter chaos generation process, as well as the information decoding operation (through a subtractor). It was recently demonstrated (Larger *et al.* 2005) that, depending on the kind of the laser source -a Constant Wave (CW) laser or a pulsed laser source-, two different kinds of dynamics can be used to produce chaos: a continuous analog chaotic carrier for a CW laser, or a regularly clocked but chaotic amplitude optical pulses when a pulsed laser source is used. This could open the way to the integration of such ultra-fast optical chaos communication techniques, into the data packet format of modern optical networks.

Other methods use chaos in digital domain to realize chaotic digital encoding and to generate PN sequences for applications in spread spectrum communications.
Chaotic encoding approaches use encoder/decoder pairs sub-systems and have been studied more especially by (Frey 1993) and (Werter 1998). We will give an example and some properties of such sub-systems in the section dedicated to Scicos.
PN sequences generation has been tested for Direct Sequence Code Division Multiple Access (DS-CDMA) systems and in particular in (Varadan and Leung 2002). They have been tried to improve the Bit Error Rate (BER) by substituting traditional Maximal Linear Shift Register (MLSR) and Gold sequence generators with non-linear recursive discrete equations. An example of a single-user transmitter scheme of such a communication system is given below in Figure 3.

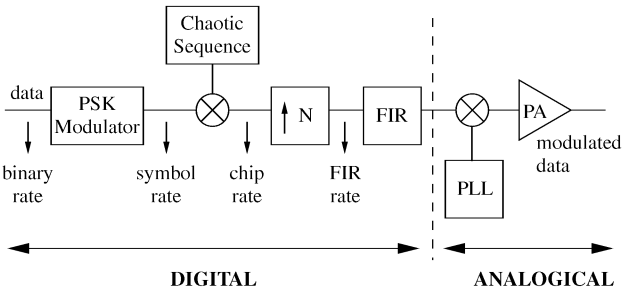

Figure 3: Spread Spectrum transmitter system.

The first part of this diagram is digital. It realizes baseband treatment when binary data becomes filtered chip. In this part, the signals are described in a discrete-time domain because of the sequential nature of digital sub-systems. Moreover, the digital part is composed of sub-systems working at different sampling rates. In high data rate systems, the binary period is first converted in a symbol period. DS spread spectrum technique consists in an oversampling of the symbol rate. Finally, filtering process with Finite Impulse Responses (FIR) needs a rate increase to work properly.
The second part realizes the frequency translation and the power amplification of the modulated carrier. These functions are always realized in a continuous manner and signals are then considered in a continuous-time domain.

So, we can see that the evolution of these various techniques significantly increases the level of complexity of communication systems. Designers which wants to model such large systems will probably prefer the block-diagrams approach than the "rough" approach (i.e. Scilab/Matlab scripts or a fortran/C program). Moreover, a CAD working environment suited to the design of communication systems based on chaos must :

1. Have differential equations solver.
2. Be able to realize simulation of closed-loop system.
3. Process dynamical and fast simulation in time domain.
4. Manage both discrete and continuous time signal.

In the wide range of CAD software, Scicos[1] is avialable with the free and open source scientific software package Scilab. Scicos already meets the previously quoted needs. But with its event driven simulator core, it offers miscellaneous features that are convenient for modeling stages of communication systems.

SCICOS FEATURES

Scicos is a modeling and simulation software for hybrid dynamical systems (Campbell *et al.* 2005). It is able to handle both discrete and continuous system in a same simulation process. It has a graphical editor where the user can build systems by interconnecting blocks. For example, the following system of discrete state equations

$$\begin{cases} x_{n+1} &= y_n \\ y_{n+1} &= a \sin^2 (b + x_n - y_n) , \end{cases} \quad (1)$$

is easily implemented by using the provided standard palettes, as shown in the Scicos diagram given in Figure 4.

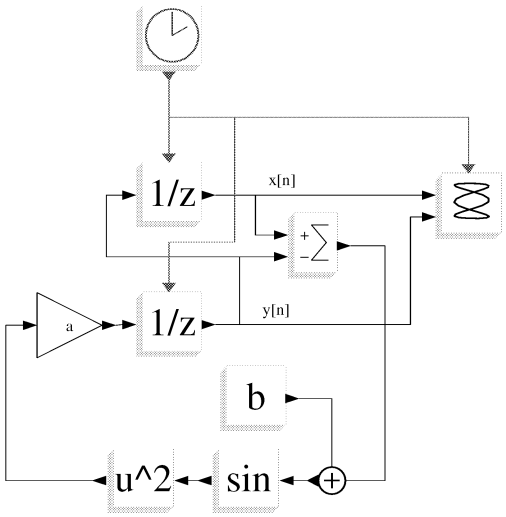

Figure 4: Scicos diagram of a discrete-time system.

[1] SCICOS : SCIlab Connected Object Simulator.

This discrete system is activated by only one event clock generator that describes the simulated sampling rate of the system and also the dates of activation of all blocks composing this diagram.

In Scicos, parameters and initial conditions of systems can be defined with symbolic variables. The values of this variables allow adjustment of constants of the system at each simulations. This functionality is interesting, in particular in search of instabilities, in the context of the simulation of chaotic system. For example, with parameters $[a; b] = [1.9; 0.7]$ and initial conditions $[x_0; y_0] = [1.5; 0.5]$, the simulation of the system (1) shows the chaotic attractor (Larger and Fournier-Prunaret 2005) given in the Figure 5.

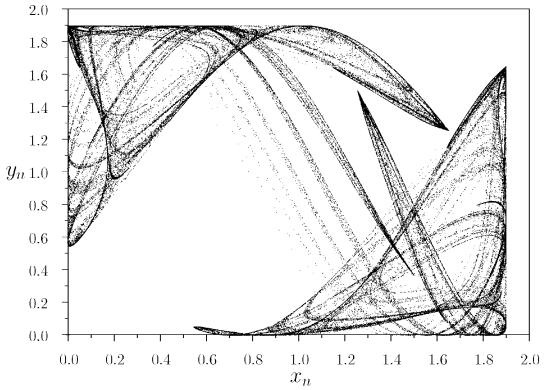

Figure 5: Chaotic attractor.

Of course, Scicos also offers the possibility of developing additional models by writing computational functions of basic blocks. This computational functions can be written in C, Fortran or Scilab language and thus provides facilities of interfacing with external computational libraries. A diagram of a continuous block, which is the type of block the most used in Scicos, is shown in Figure 6.

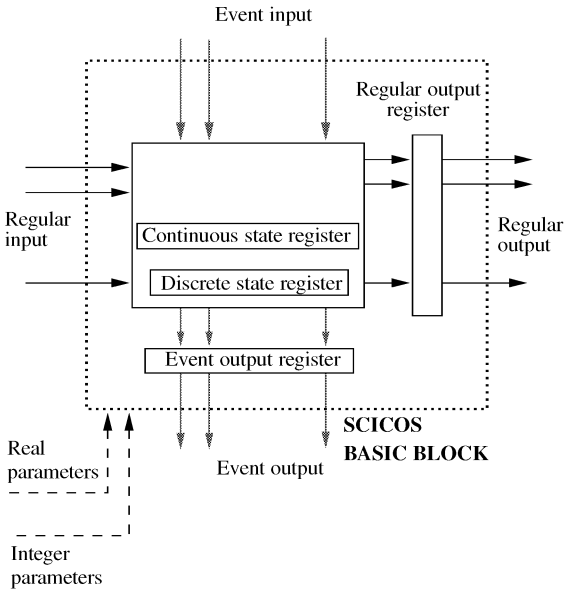

Figure 6: Scicos basic block.

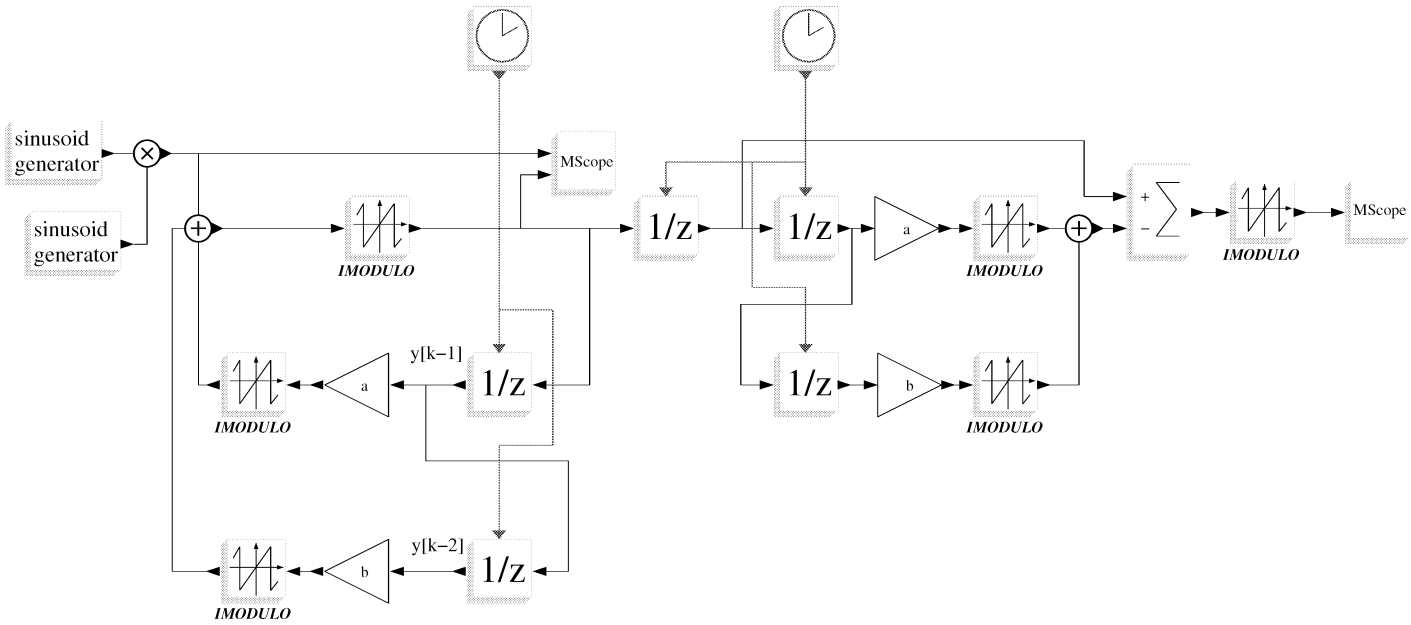

Figure 7: Scicos diagram of a quasi-chaotic encoder/decoder pair.

In Figure 6, we can see all objects that the user can handle to develop new models. Regular inputs and outputs are used to drive and to compute the values of data flow. Event inputs serve as discrete activation of the computational function in his continuous activation process. Continuous-time state registers x and x_d are used by the Ordinary Differential Equation (ODE) solver or the Differential Algebraic Equation (DAE) solver in simulation of continuous-time systems. And finally, the z register is mainly used to store values of preceding discrete states.

The event driven simulator of Scicos uses a scheduling table to run simulation. This scheduling table is dynamically informed during the simulation by output event registers of blocks which compose the diagram. In computational function, the user has then access to this register to generate events.
In our considerations, events can be used to :

1. Set time index of signal. Indeed, Scicos makes it possible to define signals with values furthermore with the date when the signal may change. This time-based formalism allows managing asynchronous samples that is a modeling approach closer to the reality of dynamical systems than sample-based modeling approach as it is used in Simulink.

2. Detect zero-crossing of state variables. This detection can be realized in the continuous-time domain of Scicos with the help of the differential equations solvers as well as in discrete-time domain. Edges detection in a noisy oscillator is a good example of discrete-time zero-crossing which has been explained in (Quéré *et al.* 2005).

3. Model local oscillator and multi-rate clock signals. This is easily done by using an event clock generator. In the case of a fixed period oscillator, it can be followed by frequency divider blocks for the generation of multi-synchronous clock signals. This operation is always almost necessary in order to correctly model the digital stages of communication systems.

EXAMPLES OF REALIZATION

Currently, a growing request focus on the security of the digital communications field. That is due to the explosion of the personal communications market, in particular with the expansion of the mobile telephony sector, Internet and as well as the Local Area Networks (LAN). The examples of realization that we will describe should be viewed as an alternative of traditional cryptography methods which are used in the contemporary digital systems.

Digital encoder/decoder pair

A first example of an all-digital secure communication scheme is given by the Scicos diagram shown in Figure 7.

The left part is the encoder that can be viewed as a second order recursive Infinite Impulse Response (IIR) filter. It is described by the following system of discrete state equations

$$\begin{aligned} y_{1_k} &= F\left(a y_{1_{k-1}} + b y_{2_{k-1}} + x_k\right) \\ y_{2_k} &= y_{1_{k-1}}. \end{aligned} \tag{2}$$

In autonomous mode (x_k=0), these simple equations are capable of generating complex dynamics, when the IIR filter is set to be unstable (Chua and Lin 1988).

In the system (2), note that the function $F()$ comes from the hardware implementation. Indeed, in digital subs-systems that work with integer numbers, operators are non-ideals, and for example, in digital adders and multipliers, an overflow occurs when values exceed the maximal capacity of registers. The function $F()$ is most of the time a modulo function.

The right part of the diagram of the Figure 7 is the decoder. This is an open loop model of the second order IIR filter and the operation realized by this decoder is given with the equation

$$x_k^{'} = F\left(y_k^{'} - ay_{k-1}^{'} - by_{k-2}^{'}\right). \quad (3)$$

This architecture is also called self-synchronized decoder and is easily implementable (Penaud *et al.* 2000) on a Digital Signal Processor (DSP).

Figure 8 shows results of a simulation in time-domain, for the preceding Scicos diagram. The encryption key is defined with the values of gain blocks (a=0.5;b=-1) and with the working wordlength (16 bits). In Figure 8-(a), we can see that the message (dashed line) is completely hidden in the output waveform of the encoder (solid line). In Figure 8-(b), we can see that the output of the decoder correctly restores the encrypted information after a laps of time that characterizes the self-synchronized process.

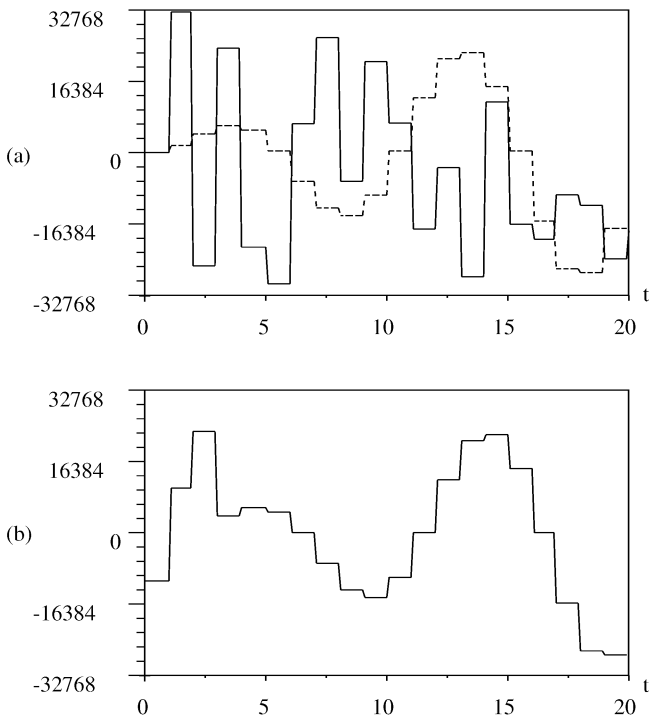

Figure 8: Time domain waveforms of the encoder/decoder pair. (a) Transmitted information (dashed line), output of the encoder (solid line). (b) Decoded information at the output of the decoder.

This principle of such an encoder/decoder pair needs in fact many numbers of states to produce a good encryption of the message to be transmitted. Indeed, a finite-state machine can behave in a chaotic way only if its wordlength is sufficiently large (Lin and Chua 1991).

Frequency-hopping communication system

Frequency-hopping systems are extensively used in military applications and they are now found in commercial applications as in the Bluetooth wireless communication systems.

Modern frequency-hopping systems are most of time based on frequency synthesizers. These sub-systems are used to provide low phase noise carrier in the frequency translation stages but also directly as transmitter system because of the accuracy of the produced output frequencies and the possible connection with other digital chips. Synthesizers are an extension of traditional Phase Locked Loops (PLLs) but they include a digital frequency divider in the feedback path. A typical frequency synthesizer used in emission is composed of :

- a Local Oscillator (LO),
- a Phase Frequency Detector (PFD),
- a Loop Filter (LF),
- a Voltage Controlled Oscillator (VCO),
- a feedback frequency divider.

Previous works have been shown that such a mixed-signal sub-system could be fully implemented in Scicos (Layec *et al.* 2004). In this paper, we assume now the design of a chaotic frequency-hopping system based on frequency synthesizers as illustrated in the Scicos diagram of the Figure 9.

The transmitter is based on fractional $\Delta\Sigma$ frequency synthesizer working at 2.5GHz with a spreading band of 20MHz. The synthesizer is driven by a digital encoder built with the second order IIR filter of the preceding sub-section. The message is a digital word directly introduced in the chaotic behavior of the encoder. The large wordlength of the encoder is break with a shift register and thus reduces the number of hops in the frequency channel. To disable the hop transients which are a source of spectral splatter in synthesizers (Filiol *et al.* 1998), a Gaussian FIR filter is applied on the emitted symbol before being modulated by the $\Delta\Sigma$ modulator. This results in a Gaussian Frequency Shift Keying (GFSK) modulation.

The receiver is built from a frequency divider, included in the computational model of VCO that reduces the high frequency of the modulated carrier at 2.5GHz to 20MHz. This is done to realize a frequency demodulation with an integer frequency synthesizer. The input voltage of the VCO which is a replica of the input voltage of the VCO of the

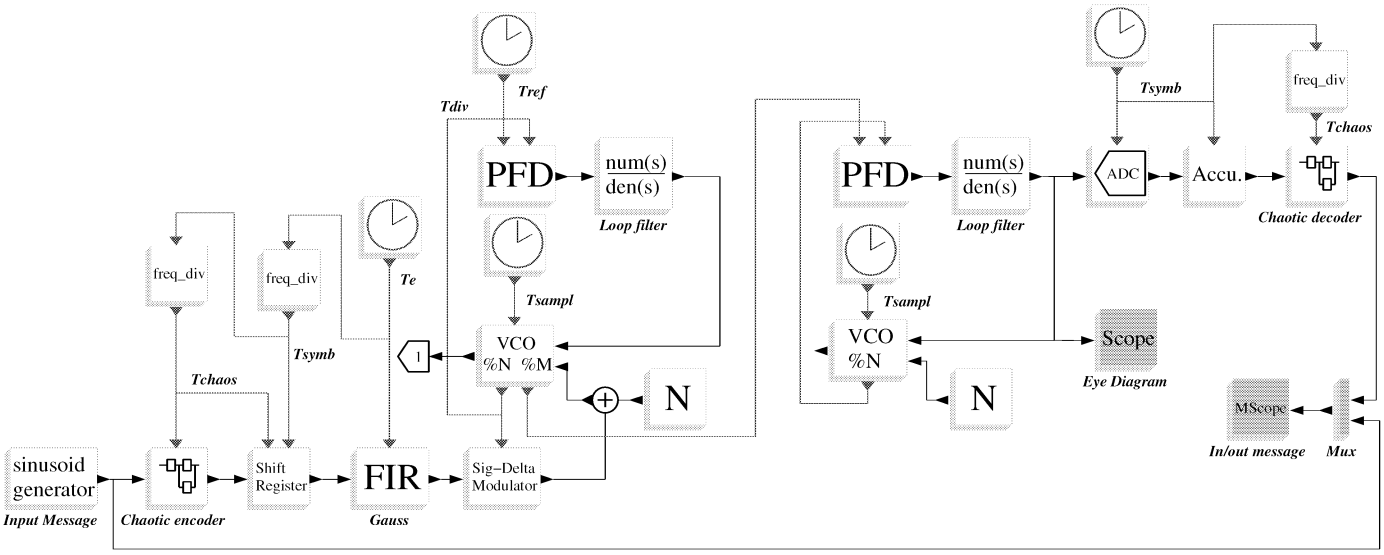

Figure 9: Scicos diagram of a chaotic Gaussian Frequency Shift Keying communication system.

emitter, is converted with an Analogical to Digital Converter (ADC).

The information that is contained in the frequency hops is then retrieved with the use of a binary accumulator and a self-synchronized digital decoder.
Note that this communication system is a multi-rate clock signals system. This can be viewed in the Figure 9 with the digital stages of the transmitter where three synchronized clocks are needed to achieve the transmission of a large length digital word with a fractional synthesizer.

An asynchronous event is generated by the computational models of VCO, when carriers are reaching zero. This event is used both to activate the computational function of the $\Delta\Sigma$ modulator, where this activation is the oversampling rate of the modulator, and to activate the PFD model of the synthesizer.

The simulation process in Scicos of this system is both discrete and continuous because of the time-domain integration of the loop-filter models. Figure 10 gives the transient behaviors of the synthesizers at the beginning of the simulation, when the loops are going towards the initial frequency target.

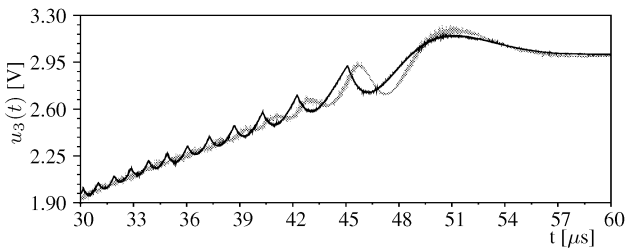

Figure 10: Transient waveforms of input voltage of VCO. Emitter (black line). Receiver (gray line).

Figure 11 shows some time waveforms when the system is in steady state : Figure 11-(a) shows the digital information to be transmitted, 11-(b) is encrypted information at the output of the encoder, 11-(c) is the control voltage of the VCO in the transmitter and finally 11-(d) shows the received information at the output of the receiver and that ensures that we have succeeded a good transmission.

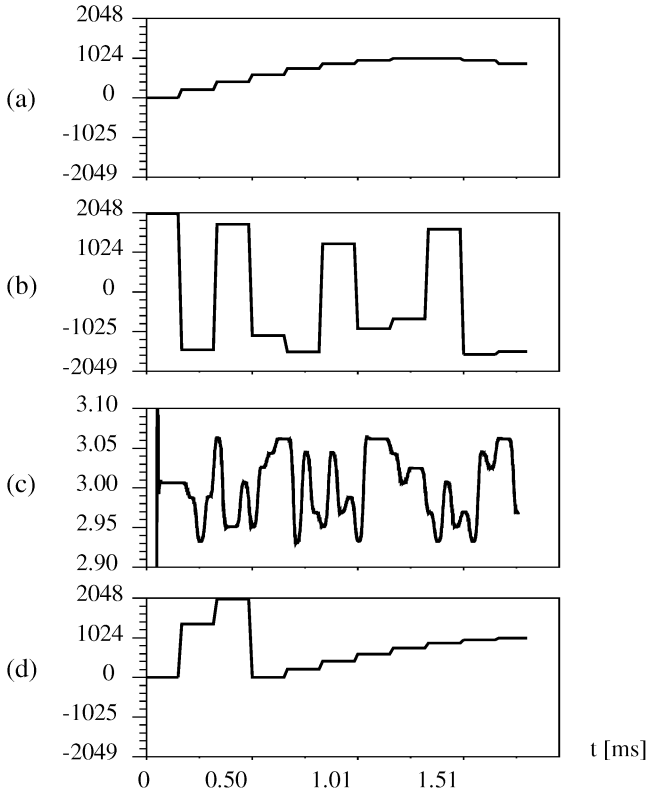

Figure 11: Steady state time waveforms.

Scicos provides also the possibility to run simulation in batch mode from the Scilab prompt. We have used this feature in order to store the time-domain waveforms during the simulation and realized the following post-treated spectrum of the output of the transmitter. This spectrum shows that we are using a 8-GFSK modulation to achieve this chaotic transmission.

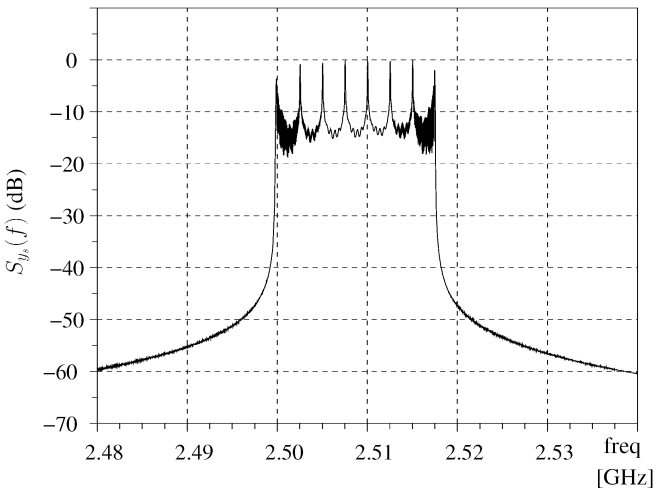

Figure 12: Post-processed output spectrum of synthesizer.

CONCLUSION

In this work, we have reviewed architectures of communication systems based on chaos and detailed problems concerning modeling and simulation. We have also explained that such systems become more and more mixed-signal systems. That is due to the explosion of the digital communications and because of the growing request for secure transmissions. The open working environment Scilab/Scicos provides many development facilities (blocks diagram editor, differential equations solvers, event driven simulator core,...) for the modeling and simulation of hybrid dynamical systems. The designs that we have made in this environment, clearly show that Scicos is very well suited to the design of modern chaotic communication systems.

REFERENCES

Carroll, T.L. and Pecora, L.M. 1991. "Synchronizing chaotic circuits". *IEEE Transactions on Circuits and Systems*, Vol.38, No.4 (Apr), 453-456.

Campbell, S.L.; Chancelier, J.P. and Nikoukhah R. 2005. *Modeling and Simulation in Scilab/Scicos*, Springer Verlag.

Chua, L.O. and Lin T. 1988. "Chaos in Digital Filters". *IEEE Transactions on Circuits and Systems*, Vol.35, No.6 (June), 648-658.

Filiol, N.M.; Plett, C.; Riley T.A.D. and Copeland, M.A. 1998. "An Interpolated Frequency-Hopping Spread-Spectrum Transceiver". *IEEE Transactions on Circuits and Systems–II*, Vol.45, No.1 (Jan), 3-12.

Frey, D.R. 1993. "Chaotic Digital Encoding: An Approach to Secure Communication". *IEEE Transactions on Circuits and Systems–II*, Vol.40, No.10 (Oct), 660-666.

Gastaud N. *et al.*, 2004. "Electro–optical Chaos for Encoded Multi-10Gb/s Optical Transmissions". *Electronics Letters*, Vol.40, No.14 (Jul), 898-899.

Larger L. *et al.*, 2005. "From flow to map in experimental high dimensional electro–optic nonlinear delay oscillator". *Physical Review Letters*, Vol.95, No.4 (Jul), 043903.

Larger, L. and Fournier-Prunaret, D. 2005. "Route to chaos in an opto-electronic system". In *European Conference on Circuit Theory and Design*. Irland, Cork, (Aug).

Layec, A.; Quéré, R.; Nallatamby J.C.; Mons, S. and Guittard, J. 2004. "Behavioural Model of Integer-N Frequency Synthesizer". In *Procedings 2004 International Workshop on Electronics and System Analysis*. Spain, Bilbao, (Oct) 29-32.

Lin, T. and Chua, L.O. 1991. "On Chaos of Digital Filters in the Real World". *IEEE Transactions on Circuits and Systems*, Vol.38, No.5 (May), 557-558.

Penaud, S.; Guittard, J.; Bouysse, P. and Quéré, R. 2000. "DSP implementation of self-synchronized chaotic encoder decoder". *Electronics Letters*, Vol.36, No.4 (Feb), 365-366.

Quéré, R.; Nallatamby, J.C.; Layec, A. and Prigent, M. 2005. "Low phase noise oscillator modeling in a system environment". In *IEEE MTT-S International Microwave Symposium*, United States, Long Beach.

Varadan, V. and Leung, H.; 2002. "Design of Piecewise Maps for Chaotic Spread-Spectrum Communications Using Genetic Programming". *IEEE Transactions on Circuits and Systems–I*, Vol.49, No.11 (Nov), 1543-1553.

Werter M.J. 1998. "An Improved Chaotic Digital Encoder". *IEEE Transactions on Circuits and Systems–II*, Vol.45, No.2 (Feb), 227-229.

SCILAB TOOLS FOR SIMULATION OF SYSTEMS WITH NON STATIONARY MODAL PARAMETERS.

Maurice Goursat and Laurent Mevel
INRIA, Domaine de Voluceau
Rocquencourt BP 105 78153 Le Chesnay Cedex, France
Email: maurice.goursat@inria.fr
INRIA-IRISA, Campus de Beaulieu, 35042 Rennes Cedex, France
Email: laurent.mevel@irisa.fr

KEYWORDS: Mechanical systems, Vibrations, Modal parameters, Covariance driven subspace method, Non-stationary systems, Simulation software.

ABSTRACT

In many cases modal parameters of mechanical systems are time varying. This is the case of space launchers, bridges, airplanes, stadia... This can be the effect of mass changes, temperature... It is very important to do appropriate simulations if we want to derive adapted algorithms for the identification of modal parameters of such systems and if we want to develop methods for the monitoring (health monitoring, flutter testing...). We present here the covariance driven subspace identification method and some specific cases of the use of simulations in order to get numerical results similar to real experiments; all the computations are made with Scilab and the specific modal analysis toolbox Cosmad.

INTRODUCTION

The development of airplanes requires a full exploration of the dynamical behavior of the structure subject to vibration and aero-servo-elastic forces. Modal analyzes are performed for ground and in-flight tests.
The analysis can be achieved by using some specific (and limited) measured excitation inputs and more easily with output-only methods, with the natural excitation (e.g. turbulent) ([3] , [9] , [7]).
The modal characteristics of airplanes vary during the flight for example with the change of mass (fuel consumption, rocket for military aircrafts, water of aircrafts fighting against fire...) and the changes due to flight conditions may lead to the critical instability phenomenon, known as *"aero-elastic flutter"*, that results in structural failure ([8]).
This is a common case for use of methods to prevent a failure: how to design an in-flight method to predict the speed limit at which flutter can occur. ([8], [6], [10]).
Another usual example is given by the thermal effects on the modal parameters of a structure; there are many cases as bridges, parts of in-operation machines. The problem of monitoring of structures under different thermal conditions is to decide whether some changes are due to a failure or are the effect of the variation of the ambient temperature.
The first section summarizes the main lines of the covariance driven subspace identification method investigated in earlier papers ([2]).
In the next section we show some results illustrating the evolution of modal parameters. In the third section we show some simulation results corresponding to previous examples.
All the numerical results are obtained with Scilab and COSMAD, a toolbox designed for modal identification, monitoring and diagnosis.
Finally, some conclusions are drawn.

IDENTIFICATION PROCEDURE

Modeling

The mechanical system is supposed to be a stationary linear dynamical system:

$$\left\{ \begin{array}{rcl} M\ddot{\mathscr{Z}}(t)+C\dot{\mathscr{Z}}(t)+K\mathscr{Z}(t) & = & v(t) \\ Y(t) & = & L\mathscr{Z}(t) \end{array} \right.$$

where the variables are :
$\mathscr{Z}$: displacements of the degrees of freedom
M, C, K: mass, damping, stiffness matrices
t: continuous time;
v: excitation (external non measured forces) modeled as a non-stationary white noise
L: observation matrix giving the observation Y (corresponding to the locations of the sensors on the structure).

The modal characteristics are:
μ vibration modes or eigen-frequencies
ψ_μ modal shapes or eigenvectors

$$(M\mu^2+C\mu+K)\Psi_\mu = 0 \ , \ \psi_\mu = L\Psi_\mu$$

By stacking $\mathscr{Z}$ and $\dot{\mathscr{Z}}$ and time discretization the rate $1/\delta$:

$$X_k = \left[\begin{array}{c} \mathscr{Z}(k\delta) \\ \dot{\mathscr{Z}}(k\delta) \end{array} \right] , \ Y_k = Y(k\delta)$$

we get the following equivalent state-space model:

$$\left\{ \begin{array}{rcl} X_{k+1} & = & FX_k+V_k \\ Y_k & = & HX_k \end{array} \right.$$

with

$$F = \exp(A\delta) \quad \text{and} \quad H = \left[\begin{array}{cc} L & 0 \end{array} \right]$$

where

$$A = \left[\begin{array}{cc} 0 & I \\ -M^{-1}K & -M^{-1}C \end{array} \right]$$

The input noise V_k is zero-mean and its covariance is:

$$Q_V(k) = \int_{k\delta}^{(k+1)\delta} \exp(As)\tilde{Q}(s)\exp(A^T s)ds$$

$$\tilde{Q}(s) = \left[\begin{array}{cc} 0 & 0 \\ 0 & M^{-1}Q_v(s)M^{-T} \end{array} \right]$$

$Q_v(s)$ is the covariance matrix of v.

The dimensions of the state X and the observations Y are respectively $2m$ and r with r much smaller than $2m$ (it is usual to have more than 10000 degrees of freedom and less than 100 sensors in practice).

The modal characteristics (μ, ψ_μ) are given by the eigenstructure (λ, Φ_λ) of the state transition matrix F :

$$\begin{aligned} e^{\delta\mu} &= \lambda \\ \psi_\mu &= \phi_\lambda \triangleq H\Phi_\lambda \end{aligned}$$

For an eigenvalue λ the corresponding modal frequency f and damping coefficient ρ are given by:
$f = a/2\pi\delta$
$\rho = 100|b|/\sqrt{(a^2+b^2)}$
with
$a = |arctanIm(\lambda)/Re(\lambda)|$ and
$b = ln|\lambda|$

Subspace-based identification methods

The basic observability-controllability relationship is:

$$\mathscr{H}_{p+1,q} = \left[\begin{array}{cccccc} R_0 & R_1 & \cdots & R_p & \cdots & R_{q-1} \\ R_1 & \cdots & \cdots & \cdots & \cdots & R_q \\ \cdots & \cdots & \cdots & \cdots & \cdots & \cdots \\ R_p & \cdots & \cdots & \cdots & \cdots & R_{p+q-1} \end{array} \right]$$

$$\mathscr{H}_{p+1,q} = \mathscr{O}_{p+1}\mathscr{C}_q$$

$$\mathscr{O}_{p+1} = \left[\begin{array}{c} H \\ HF \\ HF^2 \\ \cdot \\ \cdot \\ \cdot \\ HF^p \end{array} \right], \mathscr{C}_q = \left[\begin{array}{ccccc} G & FG & F^2G & \cdots & F^{q-1}G \end{array} \right]$$

$$R_i \triangleq \mathbf{E}(Y_k Y_{k-i}^T)\ ,\ G \triangleq \mathbf{E}(X_k Y_k^T)$$

By singular value decomposition we get:

$$\mathscr{H}_{p+1,q} = (PP^\perp) \left(\begin{array}{cc} D & 0 \\ 0 & 0 \end{array} \right) V^T$$

with

$$\mathscr{O}_{p+1} = PD^{1/2}T \ \text{ and } \mathscr{C}_q = T^{-1}D^{1/2}V^T$$

$$\mathscr{O}_{p+1}(H,F) = W_1^{-1}PD^{1/2}T$$

It is possible to pre and post multiply by weighting matrices. There are many papers on such identification techniques. A complete description can be found in [5]), [11], [4], [1] and the related references.

Global algorithm

The algorithm follows the theoretical steps:

- Compute the empirical Hankel matrix $(\hat{\mathscr{H}}_{p+1,q})$
- Compute the following SVD

$$\hat{\mathscr{H}}_{p+1,q} = (U_1 U_2) \left(\begin{array}{cc} S_1 & 0 \\ 0 & S_2 \end{array} \right) V^T$$

  where S_1 corresponds to the m dominant singular values. We keep these values for the model and neglect S_2. There is no good procedure to decide what part S_1 we can choose. The best way is an a priori knowledge of the structure giving the number of significant modes and to weakly over-estimate this number.

- We get the estimate of the observability matrix with:

$$\hat{\mathscr{O}}_{p+1}(\hat{H},\hat{F}) = U_1 S_1^{1/2} T$$

- We use the usual trick in identification procedures: increase the order of the SVD and get the stabilization diagram. Use frequency windows for the selection of alignments. We do a rough selection with the use of the frequency and the final choice is done with the evolution of damping coefficients and the MAC criterion (normalized scalar product of the eigenvectors).

THE COSMAD TOOLBOX

We have developed a Scilab toolbox COSMAD. The features of this toolbox have been designed and adapted in order to solve the problems encountered in different examples (airplanes, cars, civil structures...).

The Fig. 1 shows the Scilab window environment with the on-line help during a filter design with the signal processing toolbox.

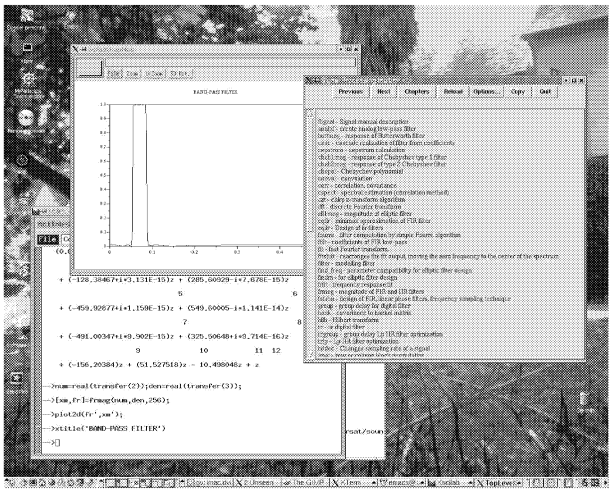

Figure 1: Averaged Spectra of 2 Records

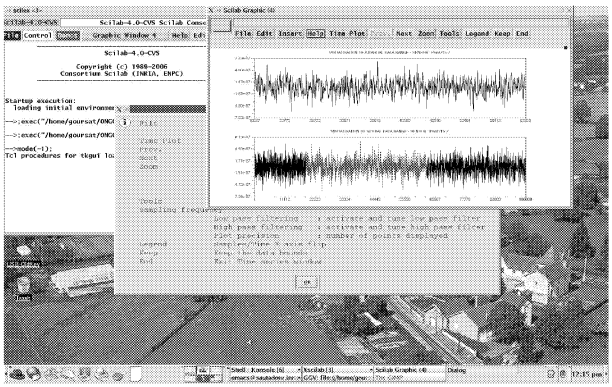

Figure 2: Basic signal processing and selection

Identification with COSMAD

Main computing

Data manipulation and preprocessing. The first step is to define a project and the location of the associated data. Then we have to choose the records used for the identification process that we want to execute. How many sensors and which sensors: this has to be done on the first dialog window. The best results for a global analysis are obtained with a low number of sensors: 2 to 10; in general 4 and 6 are the best choices.

At this step we have 2 basic features; the first one is the selection of the desired part of the record. The second is the a filtering process: low-pass, high-pass or band-pass.

The Fig. 2 shows the screen for the selection of the part of the record used for the identification process. The different windows are the Scilab window, the basic window of the toolbox, the window for the signal processing of the record and the associated help window (at every step of the toolbox, a help button opens a window giving the role of the different buttons).

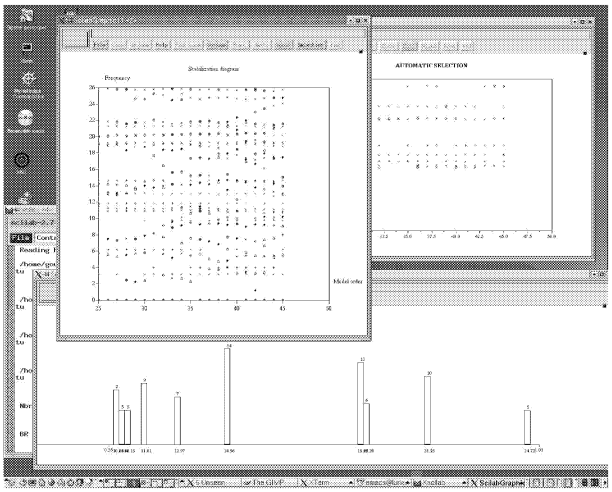

Figure 3: Result of the Automatic Selection Procedure

The algorithm: example of classical subspace. The second step is the main part: choose the identification method of the algorithm with some parameters. If we choose the subspace basic method the algorithm is: compute the empirical estimates of the covariance matrices, build the Hankel matrix and compute the SVD and derive the observability matrix; then we get the system matrices for increasing orders and their eigenstructures. By this way we get a collection of signatures (modal parameters).

Visual examination of the results

We have now a large collection of redundant modal characteristics corresponding to the different increasing orders and in many difficult cases the final selection cannot be done by an automatic procedure and needs a visual examination. But a rough automatic selection can be used to get a good starting condition for the manual process.

Stabilization diagram. All the obtained frequencies are plotted on an "histogram" called the stabilization diagram. The "true" eigenfrequencies are present for the different orders and so we get a possible signature by the alignments of the diagram.

Many other frequencies are due to spurious modes given by the numerical computations and are easy to discard with the help of the damping coefficient (generally close to zero).

Local examination. For every frequency previously selected we plot w.r.t. the order the result of the identification i.e. the eigenfrequency, the damping coefficient and the MAC criterion. It is a good strategy to choose loosely parameters for the automatic selection and then reject results, if necessary, with the damping coefficient and MAC results. Of course this step is easier if we have computed the modal shapes with a finite element model: we can then do a comparison and see what is the corresponding identified

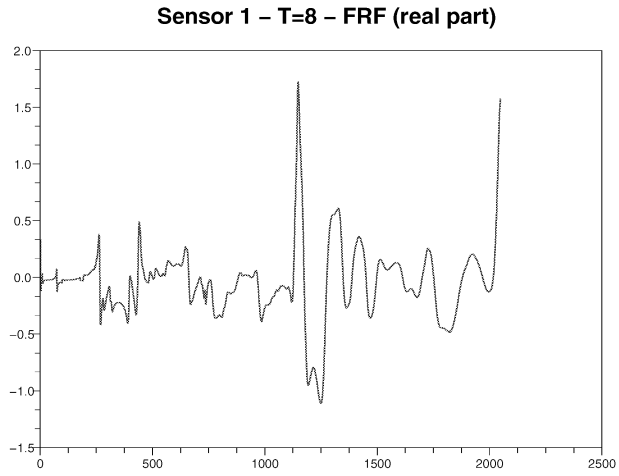

Figure 4: An example of FRF (real part - sensor 1)

mode.

It is also possible to zoom on a frequency, plot the corresponding modal shape, run its animation and plot the histogram of modes.

RESULTS

We give here some results illustrating the problem of the modal analysis of the oil pan and the effect of the temperature.

The Figs. 4 and 5 show the real part and the imaginary part of a FRF (sensor number 1). The frequency response (FRF) of the mechanical structure is the spectrum of the vibration of the structure divided by the spectrum of the input force to the system. To measure the frequency response of a mechanical system, one must measure the spectra of both the input force to the system and the vibration response, and this is most easily done with a dual-channel FFT analyzer. Frequency response measurements are used extensively in modal analysis of mechanical systems.
It is possible to use directly the FRFs in the identification procedure. In our case we have chosen to build the impulse responses and to use these responses to easily compute the correlations and compute the Hankel matrix. The Fig. 6 shows the impulse response corresponding to the FRF of Figs. 4 and 5.

We work here with the impulse responses because in the second phase we want to do simulations, for example with the impulse responses and to compare the results.

The next tables give some examples of the evolution of the eigenfrequencies and the corresponding damping parameters for the different temperatures.

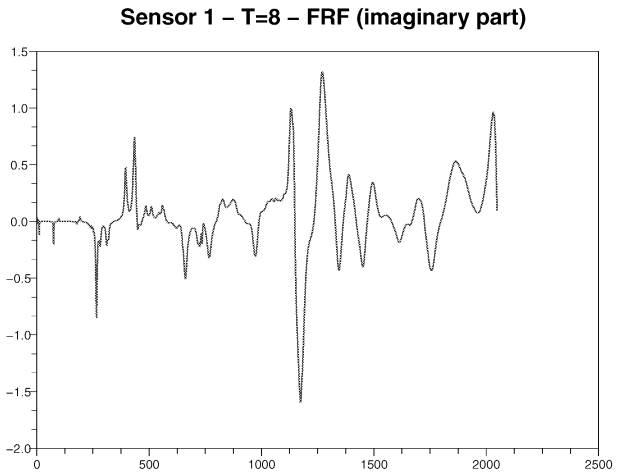

Figure 5: An example of FRF (imaginary part - sensor 1)

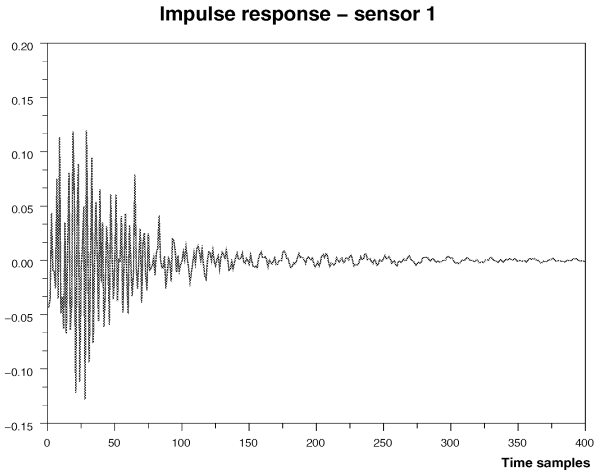

Figure 6: An example of impulse response (sensor 1)

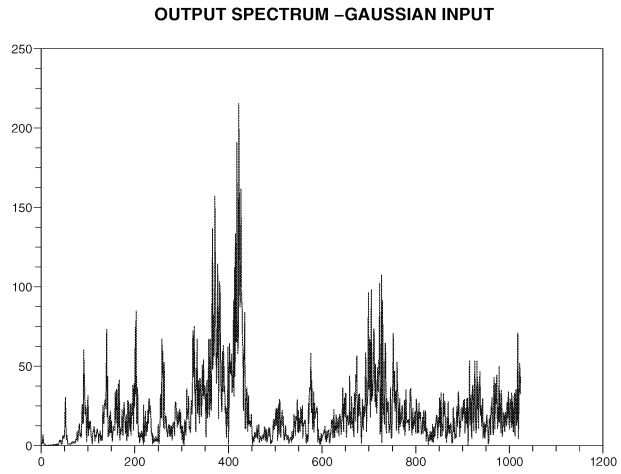

Figure 7: Output spectrum for a Gaussian input

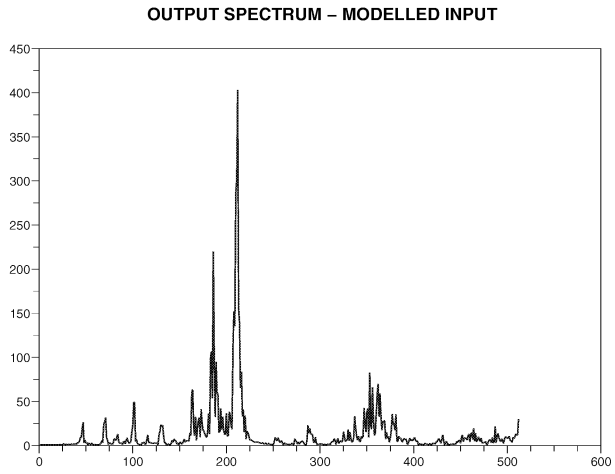

Figure 8: Output spectrum for a colored input

Temperature	Fr1	Fr2	Fr3
8	37.2	50.5	197.5
20	37.0	48.9	195.9
33	35.9	46.9	186.2
45	34.9	44.9	175.1
58	33.6	43.1	164.7
70	32.2	41.3	154.8

Temperature	D1	D2	D3
8	1.2	1.2	1.4
20	1.4	1.5	1.8
33	1.8	1.9	2.2
45	2.0	2.2	2.5
58	2.2	2.3	2.7
70	2.8	2.5	2.7

The tables show clearly the evolution of the modes: the frequencies are decreasing and the damping parameters are increasing when the temperature increases.

Simulation of stationary systems

The first experiments are made for stationary systems. The first way is to use the finite element model. There are many problems in this case: the first one is to do a very good identification and even in this case the main problem remains: how to do the simulations of damping.

In a first step we choose to use one of the impulse responses and to get the output of this filter for a Gaussian input.
The Fig. 7 shows the spectrum of the output.
By this way we get a very bad output and it is impossible to use it for identification.
A better way is to do a filtering of the output or to use a "modeled" input: in this case we use the spectrum we want to get for the output and we use it for the modeling of the input: the corresponding result is shown on Fig. 8.

Simulation of time varying systems

Many systems are time varying (aircrafts during flights, space launchers, bridges...) and we want to design algorithms for the monitoring of such structures and adapted tests to detect failures or dangerous phenomena (e.g. flutter). We need data to develop the algoritms.
In this case the use of the (FEM) finite element model or the impulse responses are quite impossible. With the FEM it is possible to change the mass and the stiffness matrices but it will need an important computing time and we still have the problem of the simulation of damping.
Another main problem is that it is impossible to do simulations of the common case of flutter. In this case we have only changes for two frequencies and the corresponding damping coefficients. We want to have the crossing of the two frequencies with the damping coefficients going to zero. It is impossible to modify the FEM model in order to get such effects.

So we use here a simulator with the state-space model described in the modal basis.
The identification phase gives us the modes of the structure: the eigenvalues λ and the modal shapes ϕ_λ.
Our data are collected by the simulation of the system:

$$\left\{ \begin{array}{rcl} X_{k+1} & = & F(\lambda,k)\, X_k + V_{k+1} \\ Y_k & = & H(\phi)\, X_k + W_k \end{array} \right. \quad (1)$$

where the system matrix F is block-diagonal of the identified eigenvalues λ, the observation matrix H is composed by the identified modal shapes, V and W are white noises. We supposed that the modal shapes are stable during the process and the simulation of the variation of frequencies or damping coefficients is simply achieved by time varying simulation of the corresponding elements of the diagonal

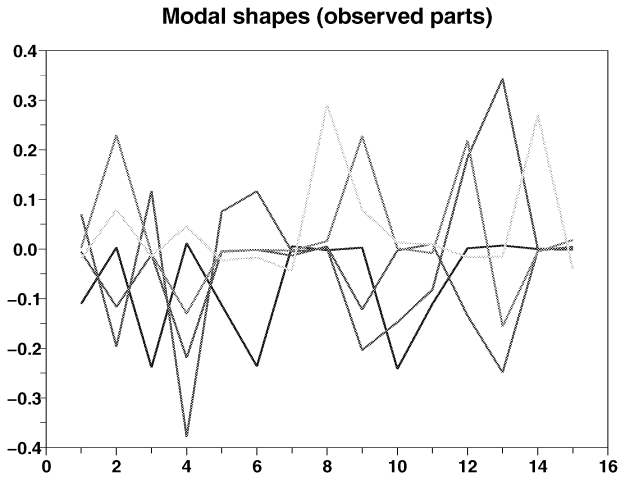

Figure 9: Modal shapes used for simulation

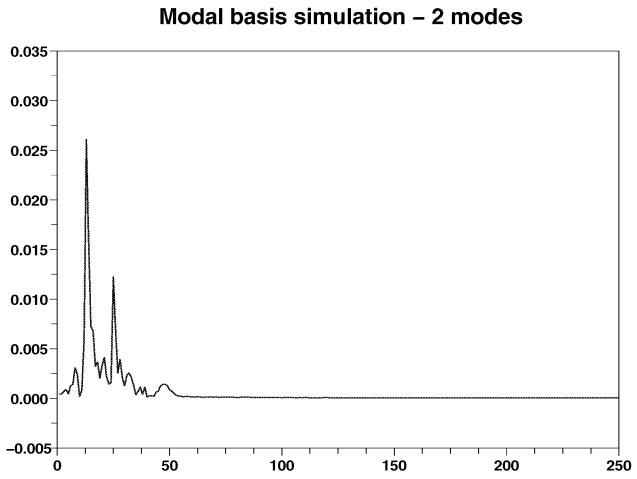

Figure 10: The 2 simulated frequencies on one of the 15 output

matrix F. The identified eigenvalues and the eigenvectors are not real. We can operate a simulation with the complex values or after an appropriate rotation of the eigenvectors get "near real" values and perform a simpler simulation.

The results presented here are obtained with the Scilab "ode" function where we used default options: in fact we do not need severe thresholds for the estimated errors because the input is not smooth and the system is not stiff.

We consider a simple example with 15 sensors, 5 identified eigenfrequencies and we retain only 2 frequencies for the simulation; the modal shapes are shown on Fig. 9. The imaginary parts of these eigenvectors is zero.

With an appropriate input the spectrum of the output is represented on Fig. 10.

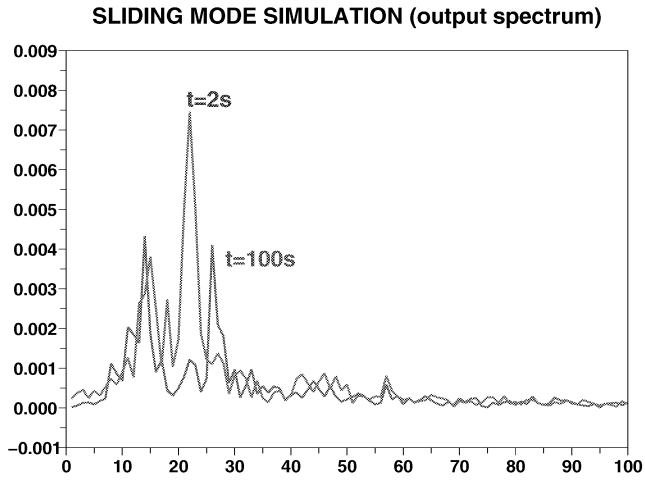

Figure 11: Simulation of sliding frequencies

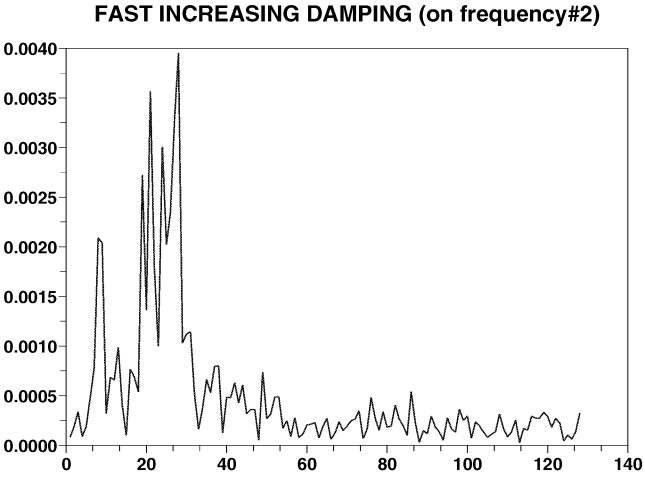

Figure 12: Mode number 2 with fast increasing damping parameter

With this procedure it is easy to obtain the simulated observations for non stationary frequencies or/and damping coefficients. The Fig. 11 shows the case where the lower frequency is slowly decreasing and the higher one is more quickly increasing.

The Fig. 12 shows the behaviour of the output in the case of a fast increasing damping parameter.

CONCLUSION

We have illustrated some capabilities of Scilab and a specific toolbox COSMAD to do identification of modal parameters and to have realistic simulations for non stationary systems. It is an important point in many cases: the flutter phenomenon is an example where the measured data are of course not available because the flight domain is defined in order to avoid such a problem. The loop with the identifica-

tion procedure is a good measure of the quality of the simulations in the stationary case and leads to a good tuning of new procedures. There are many adaptations of the computations presented here: it is possible to change the ODE solver method and parameters, to do different procedures to have a colored input and to make different filtering operations on the input and the output.

References

[1]Basseville, M., Abdelghani, M., and Benveniste, A., "Subspace-based fault detection algorithms for vibration monitoring," *Automatica*, Vol. 36, No.1, 2000, pp.101-109.

[2]Basseville, M., Benveniste, A., Goursat, M., Mevel, L., "Subspace-based algorithms for structural identification, damage detection, and sensor data fusion," *Journal of Applied Signal Processing, Special Issue*, 2006.

[3]Basseville, M., Benveniste, A., Goursat, M., Hermans, L., Mevel, L. and Van der Auweraer, H., "Output-only subspace-based structural identification: from theory to industrial testing practice,"*ASME Journal of Dynamic Systems Measurement and Control*, Vol. 123, No.4, 2001, pp.668-676.

[4]M. Basseville and others "Damage Monitoring in Vibration Mechanics: Issues in Diagnostics and Predictive Maintenance" *Mechanical Systems and Signal Processing*, vol. 17, no 5, pp. 401-423, 1993

[5]A. Benveniste and J.-J. Fuchs "Single Sample Modal Identification of a Non-stationary Stochastic Process " *IEEE Trans. Aut. Cont.*, vol. AC-30, pp. 66-74, 1985

[6]Brenner, M.J., Lind, R.C., and Voracek, D.F., "Overview of recent flight flutter testing research at NASA Dryden," NASA TM-4792, April 1997.

[7]M. Goursat, L. Mevel, A. Benveniste (2005). Using Subspace on a large aircraft dataset, a case study. *IMAC-XXIII, International Modal Analysis Conference*, Orlando, Fl.

[8]Kehoe, M.W., "A historical overview of flight flutter testing," NASA TM-4720, October 1995.

[9]Mevel, L., Goursat, M., and Benveniste, A., "Using subspace on flight data, a practical example," *Proceedings of the Twenty-First International Modal Analysis Conference*, SEM, Kissimmee, Florida, 2003.

[10]Pickrel, C.R., and White, P.J., "Flight flutter testing of transport aircraft: in-flight modal analysis," *Proceedings of the Twenty-First International Modal Analysis Conference*, SEM, Kissimmee, Florida, 2003, pp.

[11]Van Overschee, P. and De Moor, B., "Subspace Algorithms for the Identification of Combined Deterministic-stochastic Systems" *Automatica*, vol. 30, no 1, pp. 75-93, 1994

A LEARNING BASED STOCHASTIC APPROACH FOR FAULT DIAGNOSIS IN A CONTINUOUS STIRRED TANK REACTOR

Tarik. AL-ANI, Yskandar HAMAM
ESIEE-PARIS- A2SI Laboratory, Cité Descartes, BP 99, 3162 Noisy-le-Grand Cedex, France
emails: t.alani@esiee.fr, y.hamam@esiee.fr

KEYWORDS
Machines Learning, Stochastic Process, Hidden Markov Models, Diagnosis, Continuous Stirred Tank Reactor.

ABSTRACT

Many approaches have been developed to detect and diagnose the different types of faults that may occur in a complex process. Most of these approaches have traditionally been based on linear modeling techniques, which restricts the type of practical situations that can be modeled. Recently, many learning based non linear modeling using neural and other on-line approximation models have been developed. This paper presents a learning based stochastic methodology for constructing automated fault detection and diagnosis architecture for Continuous Stirred Tank Reactor (CSTR). The main idea behind our approach is to use Hidden Markov Models (HMMs). By applying off-line training procedures, different fault models may be constructed using only system measurements. Based on these models, on-line fault diagnosis may be achieved. A *Maximum Likelihood* approach is used for fault detection. Some practical aspects of the different algorithms are discussed and simulation results using Scilab are presented.

INTRODUCTION

In order to achieve high performance with increased reliability in the dynamical systems, the field of Fault Diagnosis and Accommodation (FDA) have been actively developed during the past two decades. The FDA in complex industrial plants have acquired a great importance due to the increase of automation (Isermann 1992), (Isermann and Raab 1993), (Isermann et al. 1993). This task is assigned to the supervision computers and has as objective to detect sudden faults. It may avoid in some cases catastrophes, and in other cases reduces maintenance costs. This has been the main motivation for most of the existing works. Many results are now applicable to production systems, whether on or off line, where the availability of the machinery is critical from an economic point of view. The process of system failure may be broken up into three phases: (1) *detection* of malfunction in the different parts of physical system; (2) *diagnosis* for failure isolation; and (3) *accommodation* attempts to self-correct a particular failure via the control system. Most of the computer controlled systems contain some type of detection and diagnosis procedures based on the comparison of some variables with their nominal or threshold values. Despite that, the threshold values give only the detection warnings of dangerous situations and allow neither to foresee the faults, nor to analyse their cause. Nevertheless, present computing techniques allow the development of more sophisticated methods.

Fault detection problems may be defined as the resolution of an inverse problem of the cause-effect relationship (Frank and CLARK 1989), (Isermann 1993). When a fault or degradation takes place, the effects may be observed in the measurements of the process. Only in simple systems, these measurements may determine the state of the system. These may be considered as symptoms which permit fault detection and isolation. In the literature, many fault diagnosis in complex chemical plants are explored. Many approaches are concerned with the use of Knowledge based approaches (Pau 1986), (Dexter 1986) and Neural networks (Napolitano et al. 1993), (Hoskins and Himmelblau 1991), (Venkatasubramanian and Chan 1989), (Watanabe et al. 1989). Their generalization ability renders them attractive diagnostic tools. Learning based stochastic modeling allows the use of probabilistic models to deal with the problems of uncertain or incomplete information. One of the most efficient approaches is *Hidden Markov Models (HMMs)* discussed later. This kind of fault detection does not use a mathematical system model but only observations associated to the process. The various observations are classified in a nominal or in a faulty state (Bunks et al. 2000), (Smyth 1994), (Heck and McClennan 1991). *Fault isolation* is possible if a prior classification of the faulty states is available. In what follows we will consider only this approach.

This work presents a learning based stochastic methodology for constructing automated fault detection and diagnosis architecture for Continuous Stirred Tank Reactor (CSTR) (Lopez 1973). The main idea behind our approach is to use Hidden Markov Models (HMMs) (Rabiner 1989). Based on off-line training procedures, different fault models may be constructed using only system measurements. On-line fault diagnosis may be then achieved using these constructed models.

This paper is organized as follows. After introducing a briefly the state of art in fault classification by neural and learning based stochastic approaches, we describe the CSTR reactor modeling and control. Afterwards, the fault detection of CSTR using hidden Markov models is developed. Then,

some results, conclusions and perspectives are given.

CSTR MODELING AND CONTROL

Fault detection theory can be used in several fields. Before selecting a detection method it is important to make a good description of the system. The following question should first be asked: is it possible to model the system? The objective of a good modeling is on the one hand to predict the behaviour of the system, and on the other hand to select a detection method that fits better to the system requirements. In the present work the fault detection is applied to the continuous stirred tank reactor (CSTR) shown in figure 1. The elements which compose a CSTR are: the reaction vessel, the jacket vessel, entry and exit pipes of feed, coolant and products, valves, the stirring system, heat exchange surface. A chemical reactor is a tank in which a reaction is produced with various reactants to obtain a certain product. The reactor to be considered operates in a continuous mode. There is a continuous feeding flow of reactant which enters into the vessel and a continuous product flow that leaves it. The reaction takes place within the reactor. A stirring system maintains the mixture among the reactants and products, and a good homogeneous degree of physical and chemical properties (Lopez 1973).

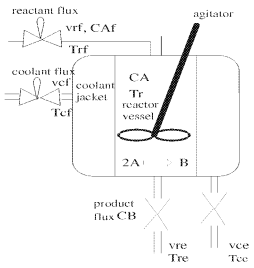

Figure 1: CSTR schedule.

The process is described by a deterministic system with mathematical equations corresponding to mass and energy conservation. These mathematical equations are based on the mass and energy conservation principles (Bird et al. 1960). The model chosen for simulation purposes is a macroscopic description where only the time remains as an independent variable. The dependent variables, such as concentration and temperature, are not function of the position and, they represent average values for all the volume of the reactor.

The Mathematical Model

The nomenclature and the subscripts described in Appendix will be used to describe the model. Consider a continuous Stirred Tank Reactor cooled by a coolant that flows through a jacket around it (Froment and Bischoff 1990), (Bird et al. 2002) as shown in figure 1. The reactor vessel is a cylinder. Inside the vessel, an exothermal irreversible reaction of two molecules of the feed component A takes place to produce one molecule of the component B: $2A \longrightarrow B$. The dynamic behaviour of a CSTR reactor is described by the following system equations (Lopez 1973),

$$\begin{aligned}
\frac{dh_r(t)}{dt} &= \frac{1}{S_r}\left(v_{rf}(t) - k_r\sqrt{h_r(t)}\right), \\
\frac{dc_{Ae}}{dt} &= \frac{1}{\tau_r}(c_{Af} - c_{Ae}) - K_r(T_r)c_{Ae}^2, \\
\frac{dT_{re}}{dt} &= \frac{1}{\tau_r}\Delta_{T_r} - JK_r(T_r)c_{Ae}^2 \\
&- \frac{Q}{S_r h_r(t) C p_r}, \\
\frac{dh_c(t)}{dt} &= \frac{1}{S_c}\left(v_{cf}(t) - k_c\sqrt{h_c(t)}\right), \\
\frac{dT_{ce}}{dt} &= \frac{1}{\tau_c}\Delta_{T_c} + \frac{Q}{S_c h_c(t) C p_c} \\
&- \frac{wastes}{S_c h_c(t) C p_c},
\end{aligned}$$

where $k_r = \frac{v_{re}(t)}{\sqrt{h_r(t)}}$, $k_c = \frac{v_{ce}(t)}{\sqrt{h_c(t)}}$, J=-$\frac{H_r}{Cp_r}$, $\Delta_{T_r} = T_{rf} - T_{re}$, $\Delta_{T_c} = T_{cf} - T_{ce}$, τ_r is the *residence time* in the reactor vessel defined by $\tau_r = \frac{V_r}{v_{rf}} = \frac{S_r h_r(t)}{v_{rf}(t)}$ and τ_c is the *residence time* in the coolant jacket defined by $\tau_c = \frac{V_c}{v_{cf}} = \frac{S_c h_c(t)}{v_{cf}(t)}$. The wastes term is calculated by $wastes = U_{wastes} \times S_{ee} \times (T_{cf} - T_a)$ where $S_{ee} = \pi \times D \times h_c$ and U_{wastes} is the global coefficient of heat transmission between the coolant jacket and the outside. $Q = U \times S_{ex} \times (T_{re} - T_{ce})$.

CSTR operation simulation using Scilab or Scicos

The above described set of equations represents a *non linear Ordinary Differential Equations (ODE)*. For Simulation purposes, they must be solved using numerical methods. The Runge-Kutta method of 2nd and 3rd order has been used with good results. The following system has been calculated by the Scilab-function "ode" (Scilab 2006), (Al-ani and Hamam 2000).

During the CSTR operation it is possible to recognize two stages. the first stage, is the non equilibrium state, where the variables vary along the time. Its dynamic evolution is described by the conservation differential equations of the mass and energy. The reactor evolves until reaching the equilibrium state, where the variables remain constant along the time . The equilibrium stage is described by algebraic equations obtained when the accumulation value in the differential equation is null. A reactor CSTR works during most of its life in equilibrium state. For this state concentration and temperature variations are minimal. The fault detection is applied in the equilibrium point. However, it is necessary to take into account the differential equations in order to know the system evolution when a fault occurs. The assembly of differential equations takes into account the level in the reactor vessel and in coolant jacket, the temperature in both tanks

and the concentration.

Level of the reactor

The level of the reactor at the equilibrium point is that for which the volumetric flow that enters is equal to the volumetric flow that leaves. The same considerations may be considered for the volume inside the coolant jacket

$$v_{rf} = k_r\sqrt{h_{r0}},\ v_{cf} = k_c\sqrt{h_{c0}}.$$

Temperature and Concentration

The discussion of the reactor equilibrium temperature, coolant temperature and concentration is not so evident since the three variables are related. A good way to verify the stability of a system is by using the diagram of elimination and generation of energy. This diagrams permits the observation of the effects of the perturbations on the CSTR. They must be on the one hand, the cause of instability and on the other hand, the cause of deviations of their operation point and therefore the loss of production quality.

CSTR Control

The control is required to stabilize the system around a set of operating points and to reject perturbations. In (Stephanopoulos 1984), (Coulson 1991), (Al-ani and Hamam 2000), the stability of the reactor has been studied, with the conclusion that the reactor operates as a stable point. In a reactor the most important variable is the concentration from a production point of view. Normally the concentration is not available for measurement and it is necessary to relate it to another process measured variables.

Fault Simulation

In this section, some of the faults that may occur are considered. The behaviour of the system is calculated by means of the ordinary differential equation system described above. In order to simulate the different faults, some parameters are modified and two coefficients are added to the initial differential equation system. In both vessels, the most probable fault is a leak caused by material deterioration along the operation time. The material deterioration simulation is not available by the mathematical CSTR model described above. However, the leak produced in the exit valves may be simulated by changing the nominal values of k_r and k_c to a smaller values; when $k_{rd} < k_r$ a leak in the reaction vessel is simulated. It is possible to do the same for the jacket tank when $k_{cd} < k_c$. The fault may be sudden or transient. In the latter case $k_{rd} = k_{rd}(t)$ and $k_{cd} = k_{cd}(t)$. The no fault (nominal) situation is considered when $k_{rd} = k_r$ and $k_{cd} = k_c$. A valve obstruction is simulated when the valve constants are bigger than the nominal values. The obstruction may evolve gradually (transient evolution) when a progressive deposit of viscous substances occurs, or suddenly as a result of a deposit of a big solid impurity. The reactant feeding flux as well as the coolant flux are modified. A leak in both flux may be simulated by means of the new coefficients α_1 and α_2 whose values are $0 < \alpha_i \leq 1$. The modified differential equation are

$$\begin{aligned}
\frac{dh_r(t)}{dt} &= \frac{1}{S_r}\left(\alpha_1 v_{rf}(t) - k_{rd}\sqrt{h_r(t)}\right),\\
\frac{dc_{Ae}}{dt} &= \frac{\alpha_1}{\tau_r}(c_{Af} - c_{Ae}) - K_r(T_r)c_{Ae}^2,\\
\frac{dT_{re}}{dt} &= \frac{\alpha_1}{\tau_r}\Delta_{T_r} - JK_r(T_r)c_{A_e}^2 - \frac{Q}{S_c h_r(t) Cp_r},\\
\frac{dh_c(t)}{dt} &= \frac{1}{S_c}\left(\alpha_2 v_{cf}(t) - k_{cd}\sqrt{h_c(t)}\right),\\
\frac{dT_{ce}}{dt} &= \frac{\alpha_2}{\tau_c}\Delta_{T_c} + \frac{Q}{S_c h_c(t) Cp_c} - \frac{wastes}{S_c h_c(t) Cp_c}.
\end{aligned}$$

Under nominal conditions $\alpha_i = 1$. The performance may change suddenly or gradually when α_i is a function of time. In the first case the fault is modeled as a step function while the flux changes from its nominal value to its fault value during a time period t_d in the second case.
Under nominal conditions $\alpha_i = 1$. The performance may change suddenly or gradually when α_i is a function of time. In the first case the fault is modeled as a step function while the flux changes from its nominal value to its fault value during a time perid t_d in the second case. The heat exchange surface has normally a transient degradation caused by the dirt on both sides of the wall. Its simulation is possible by introducing a global heat exchange coefficient as a function of time, $U = U(t)$.

System performance

The faults have been simulated using the controlled reactor model, and it is necessary to study the system evolution in order to validate the results. It is difficult to classify the kinds of simulated faults. We consider the faults that occur in valves as a multiplicative component fault, and the entrance flux faults as an additive fault, although in some cases they may be multiplicative. It is considered that the fault occurs suddenly and is simulated by a step function. The fault is introduced as a percentage value of the nominal one. The percentages chosen are 80%, and 120%. The variation of the variables is sometimes difficult to observe since it may produce several changes at the same time. In this paper, five faults are simulated: Reactant feed flux fault (F1), Coolant feed flux fault (F2), Reactor valve fault (F3), Coolant valve fault (F4) and Heat exchange coefficient fault (F5).

BASIC HIDDEN MARKOV MODELS (HMMs)

Hidden Markov models (HMM) have been widely applied in automatic speech recognition. In this field, signals are encoded as temporal variation of short time power spec-

trum (Rabiner 1989), (Baum and Eagon 1967), (Baum et al. 1970), (Liporace 1982), (Bahl et al. 1986), (Ephraim et al. 1987), (Al-ani and Hamam 1996), (Al-ani and Hamam 2004). HMM applications are now being extended to many fields such as pattern recognition, signal processing, modeling and control of dynamic systems. In general, the HMMs approach seems to be promising in other fields such as in medical diagnosis and in other types of system monitoring (Al-ani et al. 2004), (Al-ani et al. 2005), (Novk et al. 2004d), (Novk et al. 2004b), (Novk et al. 2004a), (Novk et al. 2004c), (Al-ani and Hamam 2003), (Al-ani and Hamam 2005), (Bunks et al. 2000), (Smyth 1994), (Heck and McClennan 1991). They are well suited for the classification of one or two dimensional signals. A HMM is a double stochastic process with one underlying process that is not observable but may be estimated through a set of processes that produce a sequence of observations. A Hidden Markov Model is defined by the triplet $\lambda \Rightarrow \{\mathbf{\Pi}, \mathbf{A}, \mathbf{B}\}$, where $\mathbf{\Pi}$, $\mathbf{A}$ and $\mathbf{B}$ are the initial state distribution vector, matrix of state transition probabilities and matrix of measurement probability distribution, respectively citepRabi.

$$\begin{aligned} \mathbf{\Pi} &= [\pi_1, \pi_2, ..., \pi_N],\ \pi_i = P(q_0 = i), \\ \mathbf{A} &= [a_{ij}], \qquad a_{ij} = P(q_{k+1} = j | q_t = i), \\ \mathbf{B} &= [b_j(\mathbf{O}_t)], \quad b_j(\mathbf{O}_t) = P(\mathbf{O}_t | q_t = j), \end{aligned}$$

$i, j \in \{1, 2, ..., N\}$, $t \in \{1, , ..., T\}$. $\mathbf{O}_t$ may be discrete $\mathbf{O}_t = l$, $l \in V = \{1, 2, ..., M\} \subset \mathbf{N}$ or continuous $\mathbf{O}_t \in \mathbf{R}$. In general, at each instant of time t, the model is in one of the states q_i. It outputs v_t (Discrete (DHMM) or continuous observation (CHMM)) with probability $b_j(\mathbf{O}(k))$ and then jumps to state q_j with probability a_{ij}. The model λ may be obtained off-line by training. The state transition matrix represents the structure of the HMM. In Fault Detection, we usually assume N Faults to be recognized, a training set of L observations corresponding to each fault, and an independent testing observations set. One HMM is built for each Fault. In Fault detection of continuous dynamic systems, we may represent the evolution of one system component by three hidden states: nominal, transient and faulty state respectively. For this process, the observation may be the estimated system parameters or the ystem output signals.

Structures of HMMs

It is possible to obtain two principal structures of models according to the restrictions of the elements in the state transition matrix $\mathbf{A}$. These models are:

Ergodic Models: In these models there is no transition restriction on the elements of the matrix A. All the states can be reached from whatever other state with only one transition.

Left-right models: These models have the following properties:
- the first observation is produced when the Markov chain is in the first state.
- the last observation is generated when the Markov chain is in the final state.
- there is not possibility to come back to a precedent state.

For our dynamic system, the two types of models may be used. The major problem with the left-to-right models is that one cannot use a single observation sequence to train the model. This is because the transient nature of the states within the model only allow a small number of observations for any state. Hence, in order to have sufficient data to make reliable estimates of all model parameters, multiple observation sequences must be used.

Implementation of HMMs

In Fault detection of continuous dynamic systems, we may represent the evolution of one system component by three hidden states: nominal, transient and faulty state respectively. For these systems, the observation may be the estimated system parameters vector or system output measurements vector. To use HMM we need to do two phases; training phase and recognition phase:

- **Training phase**: build one or many HMMs for the process (or processes $w = 1, ..., W$) to be modeled. Use the observations from the set of L nominal and faulty operation events to estimate the optimum parameters for each event, i.e. creating λ^w for the w-th event, $1 \leq w \leq W$.
- **Recognition phase**: For each hidden sequence in the test set characterized by an observation sequence $\mathbf{O} = (\mathbf{O}_1, \mathbf{O}_2, ..., \mathbf{O}_t)$, the occurrence probability $P_w = P(\mathbf{O}|\lambda^w)$ is calculated for each process model λ^w. The unknown observation $\mathbf{O}$ is then classified as the process

$$w^* = \arg \max_{1 \leq w \leq W} P_w.$$

For the recognition phase, the forward probability function that evaluates probability of a partial observation sequence at node i may be used (Rabiner 1989),

$$\alpha_t(i) = P(\mathbf{O}_1 \mathbf{O}_2 ... \mathbf{O}_t, q_t = i | \lambda^w),$$

$1 \leq i \leq N$, $1 \leq t \leq T$, i.e. the probability of being in state i at time t given the model λ^w. $\alpha_t(i)$ may be recursively computed. The occurrence probability is obtained by

$$P(\mathbf{O}|\lambda^w) = \sum_{i=1}^{N} \alpha_t(i).$$

In some applications of HMM, the most probable state sequence $Q_t^* = q_1^* q_2^* ... q_t^*$ that generates a given observation ($\mathbf{O} = \mathbf{O}_1 \mathbf{O}_2 ... \mathbf{O}_t$) is desired. To estimate the optimum state sequence, the Dynamic Programming Viterbi

algorithm (Viterbi 1967) may be used. For the training phase, there are many algorithmes with different efficient approaches (Rabiner 1989), (Hamam and Al-ani 1996).

Dimension of the observation vector: The elements of the observation sequence are obtained from the simulation of the system. It is necessary to select those variables that are related to the faults. The observation at a given time $\mathbf{O}_k$ is a vector formed by four component: the reactor temperature T_{re}, jacket temperature T_{ce}, product flow v_e and exit coolant flux v_{ce}. All these variables are measurable. The dynamic behavior of these or some of these variables when a fault has occurred, varies for each fault type. This condition is necessary to isolate faults.

Kind of observation probability density in a given state: The HMM may be discrete or continuous according to the kind of observation probability density in a given state. Before creating a HMM model for a given process it is necessary to choose the observation type of this model: continuous or discrete observation model. For our continuous model we use a single Gaussian density in each state.

Type and structure of HMM to be employed: Before creating a HMM model to a process it is necessary to choose also the structure of the model. This choice is depends on the number of chosen states and the fault evolution nature, 2.

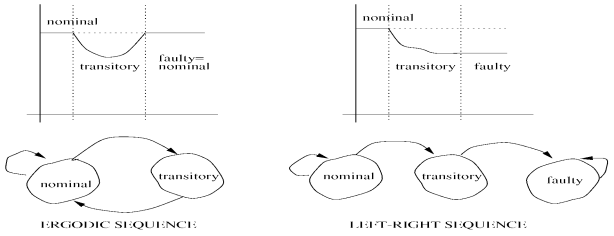

Figure 2: Comparison between Ergodic (case of a minor fault cancelled by the control process) and Left-Right models (case of a major fault).

Number of States: Since the system is controlled, in some cases, after a fault the system will go back to the initial conditions, 2. In this cases there will be two states: nominal and transient. In other cases, the process does not reach its initial conditions so we consider three states nominal, transient and faulty. In the first case, it is necessary to use an ergodic model while in the second, a right-to-left model is possible. In this work we have used an ergodic model.

SIMULATION AND RESULTS

Scicos and Scilab were used to simulate the CSTR model with different operation events (nominal and faulty events). The physical parameters of the CSTR model are given in (Al-ani and Hamam 2000). The collected system output data (observation sequences) were then used to train and to test the models.

Training phase

The training phase is carried out using sets of observation sequences obtained by simulation. These sets are representative of the different system operations. The measurements (observations) are taken for each 36 seconds and during five hours. The faults are introduced at time 2 hours. In this simulation, the occurrence of ten faults was simulated, each with its own evolution. The problem in learning phase is to create the HMM parameters $\lambda(\mathbf{\Pi}, \mathbf{A}, \mathbf{B})$ for each fault. This may be obtained by maximizing recursively $p(\mathbf{O}_t/\lambda_{it})$, the probability that the measured observation belongs to a the current HMM model λ_{it}. Several sequences may be employed for each HMM trainig. In order to obtain a good generalization, these sequences are obtained by introducing different faults, the same fault but with different values of the components change and by introducing different noise levels. If the number of faults to be detected is k, it is necessary to create $k+1$ HMM models, one for the nominal case and the others for the faults. At the beginning, we give initial values for the HMM parameters and then the parameters are re-estimated by Baum-Welch algorithm. As an example, the HMM model for two sequences is created, one corresponding to the nominal state and other corresponding to a fault of type F1 occurred in the input reactant flux with $\alpha_1 < 1$. The change that has occurred is an 80% of its nominal value, as shown in figure 3.

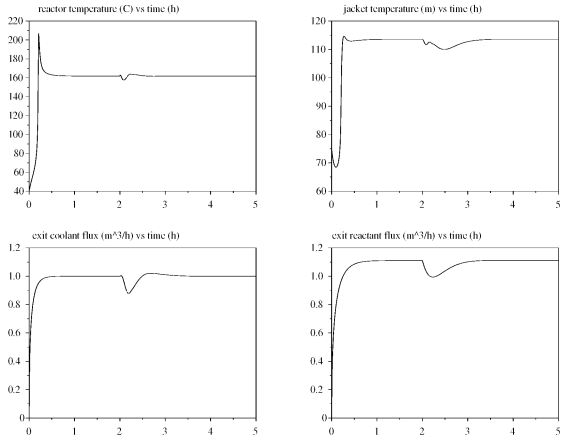

Figure 3: Observation sequence for the transition between the states: nominal - fault in reactant flux - nominal. From left-to-right and up to down: reactor temparature, jacket temparature, exit coolant and exit reactant flux respectively.

If the sequence has several states, it is necessary to define the intervals of each state. For example, two sequences of five hours were generated. The observations are given for each 0.01 hours. each observation sequence has a mean length of

500.

The HMMs obtained for each sequence are:

- **Sequence 1, no fault**. For this sequence only one state (one interval) is considered, so the initial probability at this state is equal to one.

- **Sequence 2, fault in** α_1. For this sequence there are two states (two intervals) nominal and faulty.

$$HMM(i) = [\pi, A, \mu, \Sigma, LP, length)]$$

where π: initial state probability vector. It contains the initial probability of the nominal state which is maximal and the initial probability of the faulty state which is minimal. A: state transition matrix.The probability of transition between the two states in this example is formed by a square matrix (2×2). μ and Σ are the Gaussian mean vector (1x4) and the covariance matrix (4x4)respectively employed by the probability distribution B, $LP = logP(\mathbf{O}|\lambda)$: likelihood of HMM and $length$: is the set of observation sequence lengths used in each state.

Detection phase

The fault detection consists of two phases: first we estimate the state of the system (fault detection); second we determine the fault type (isolation).

An external observation sequence is taken that usually contains some noise. The Maximum Likelihood Criterion is used for isolation. It is defined as $p_w = p(\mathbf{O}/\lambda^w)$, where λ^w represents the HMM for the fault w. The observation sequence $\mathbf{O}$ in this case is defined by a sliding window which contains a set of observations including the current time observation. For each λ^w the likelihood of the sequence $\mathbf{O}$ is calculated. The current fault is then given by w^* as described above.
For fault isolation, the forward probability $\alpha_t(i)$ of the partial observations given by the sliding window at each time t is evaluated. This probability of the state may be recursively calculated at every time instant as described above.

In our simulation, the HMM toolbox (Al-ani and Hamam 2004), (Scilab 2006) has been used for training, fault detection and isolation. To illustrate the fault detection, we use the two HMMs obtained in the above explained example.
Two observation sequences have been generated, one for the nominal case and other for the faulty one.
The results obtained are satisfactory, see figures 4 and 5, which represent the $Log(p(\mathbf{O}/\lambda^w))$ vs. time. The same experience was made by using all the HMM set for all the faults. The results were satisfactory for all the sequences and a good generalization was obtained.

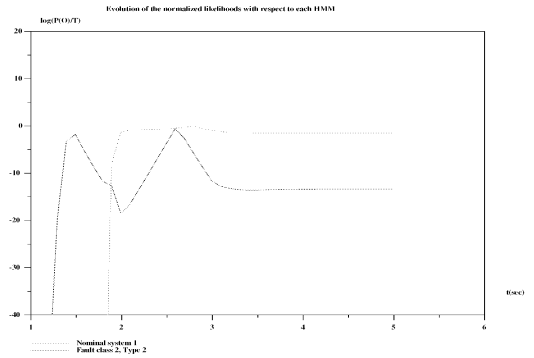

Figure 4: Maximum likelihood representation $(Log(p(\mathbf{O}/\lambda^w))$ vs. time in hours) when there is no fault . The nominal likelihood is greater than the faulty one.

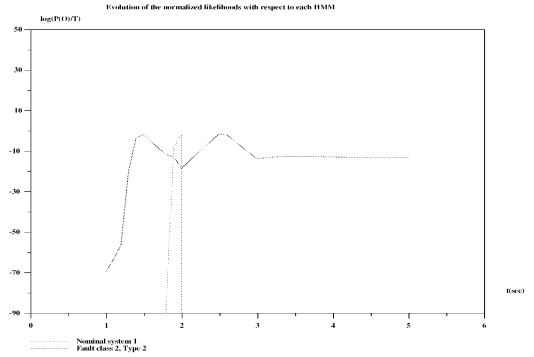

Figure 5: Maximum likelihood representation $(Log(p(\mathbf{O}/\lambda^w))$ vs. time in hours) when there is a fault of type F1 introduced at time 2 hours. . The nominal likelihood is smaller than the faulty one.

CONCLUSION

In this paper the domain of on-line fault detection of complex CSTR reactor system using Hidden Markov Models (HMMs) has been explored. HMMs provide an effective approach for incorporating the temporal context. They may be employed directly using the output external signals of the process. HMMs based approaches may also be employed using internal methods of fault detection. In this case, the observation will be the internal symptoms (e.g. parameters) that may be calculated using a discrete time linear difference equations relating inputs and outputs.
The HMMs may be used to provide a predictive estimate of failures. However, to use them, some hypothesis must be satisfied. In this paper the following assumptions are used:

- The process is described by a first order Markov chain.

- The faults are assumed to be discrete and a prior knowledge on the failure states and their fault system output data are supposed available for model training purpose.

REFERENCES

Al-ani T. and Hamam Y., 1996. *An Integrated Environment for Hidden Markov Models - A Scilab Toolbox.* In *IEEE Int. Conf. on CACSD.* Dearborn.

Al-ani T. and Hamam Y., 2000. *A learning based stochastic approach for fault diagnosis in a continuous stirred tank reactor.* Research report, esiee.

Al-ani T. and Hamam Y., 2003. *A Hidden Markov Models - based Scilab Diagnosis Toolbox. Simulation News Europe (SNE).*

Al-ani T. and Hamam Y., 2004. *A Learning Based Stochastic Modeling Toolboxes in Scilab Environnement.* In *Scilab04.* INRIA Rocquencourt, France.

Al-ani T. and Hamam Y., 2005. *A Stochastic Learning Based Approach For Automatic Medical Diagnosis Using HMM Toolbox In Scilab Environment.* In *IEEE Conference on Control Applications (CCA05).* Toronto, Canada.

Al-ani T.; Hamam Y.; Fodil R.; Lofaso F.; and Isabey D., 2004. *Using Hidden Markov Models For Sleep Disorderd Breathing Identification. Simulation Practice and Theory, Special Issue, Elsevier*, 12, 117–128.

Al-ani T.; Hamam Y.; Novk D.; Mendoza P.T.P.; Lhotsk L.; Lofaso F.; Isabey D.; and Fodil R., 2005. *Noninvasive Automatic Sleep Apnea Classification System.* In *Fourth International Conference on Simulation in Medicine, Biology, Biomedical Engineering, and Systems Biology (BioMedSim'05).* Linkping, Sweden.

Bahl L.R.; Brown P.F.; SOUZA P.V.D.; and Mercer R.L., 1986. *Maximum mutual information estimation of hidden Markov model parameters for speech recognition.* In *Proc. ICASSP'86.* Tokyo, 49–52.

Baum L. and Eagon J., 1967. *An inequality with application to statistica estimation for probabilistic functions of Markov processe and to a model for ecology. Bull Armmer Soc*, 77, 360–363.

Baum L.E.; Petrie T.; Soules G.; and Weiss N., 1970. *A maximization technique occurring in the statistical analysis of probabilistic functions of Markov chains. Ann Math*, 41, no. 1, 164–171.

Bird R.B.; Edwirn W.E.S.; and Lightfoot E.N., 1960. *Transport Phenomena.* John Wiley & Sons.

Bird R.B.; Stewart W.E.; and Lightfoot E.N., 2002. *Transport Phenomena 2nd edition.* John Wiley & Sons.

Bunks C.; McCarthy D.; and Al-ani T., 2000. *Condition-Based Maintenance of Machines Using Hidden Markov Models. Mechanical Systems and Signal Processing, Academic Press*, 14, no. 4, 597–612.

Coulson J.M., 1991. *Chemical process control. An introduction to Theory and Practice.* Pergamon Press.

Dexter A.L., 1986. *Fuzzy model based fault diagnosis. IEEE Proc-Control Theory Appl*, 142, no. 6, 545–550.

Ephraim Y.; Dembo A.; and Rabiner L.R., 1987. *A minimum discrimination information approach for hidden Markov modeling.* In *Proc. IEEE Int. Conf. Acoust. Speech and Signal Process.* Dallas, 25–28.

Frank P. and CLARK R., 1989. *Fault Diagnosis in Dynamic Systems.* Ron Patton, Prentice Hall.

Froment G.F. and Bischoff K.B., 1990. *Chemical Reactor Analysis and Design.* John Wiley & Sons.

Hamam Y. and Al-ani T., 1996. *Simulated annealing approach for Hidden Markov Models.* In *4th WG-7.6 Working Conference on Optimization-Based Computer-Aided Modeling and Design.* ESIEE-Paris, France.

Heck L.P. and McClennan J.H., 1991. *Mechanical system monitoring using Hidden Markov Models.* In *ICASSP-91.* Toronto, vol. 3, 1697–1700.

Hoskins J. and Himmelblau D., 1991. *Fault Diagnosis in Complex Chemical Plants Using Artificial Neural Networks. American Institute of Chemical Engineering Journal*, 37, 137–141.

Isermann R., 1992. *Estimation of physical parameters for dynamic processes with application to an industrial robot. Int J Control*, 55, no. 6, 1287–1298.

Isermann R., 1993. *Fault Diagnosis of Machines via Parameter Estimation and Knowledge Processing-Tutorial Paper. Automatica*, 29, no. 4, 815–835.

Isermann R. and Raab U., 1993. *Intelligent Actuators-Ways to Autonomous Actuating Systems. Automatica*, 29, no. 5, 1315–1331.

Isermann R.; Reib T.; and Wanke P., 1993. *Model Based Diagnostic Machine Tools.* In *Proceedings of the 30th Conference on Decision and Control.* Brington, England, 2574–2579.

Liporace L.R., 1982. *Maximum likelihood estimation for multivariate observations of Markov sources. IEEE Trans Inform Theory*, IT-28, 729–734.

Lopez J.C., 1973. *Análisis de reactores.* Editorial Alhambra 1 Edicion.

Napolitano M.R.; Chen C.I.; and Naylor S., 1993. *Aircraft Failur Detection and Identification Using Neural Networks. AIAA J Guidance Control Dynam*, 16, no. 6, 999–1009.

Novk D.; Al-ani T.; Hamam Y.; Cuesta-Frau D.; M.Aboy; and Lhotsk L., 2004a. *Morphology Analysis of Biological Signals Using Hidden Markov Models*. In *17th conference of the International Association for Pattern Recognition (ICPR 2004)*. Cambridge,UK.

Novk D.; Al-ani T.; Hamam Y.; and Lhotsk L., 2004b. *Electroencephalogram processing using Hidden Markov Models*. In *5th EUROSIM Congress on Modelling and Simulation (EUROSIM'04)*. Paris.

Novk D.; Cuesta-Frau D.; Al-ani T.; Aboy M.; Mico P.; and Lhotsk L., 2004c. *Speech Recognition Methods Applied to Biomedical Signals Processing (EMBS 2004)*. In *26th Annual International Conference of the IEEE Engineering in Medicine and Biology Society*. San Francisco, USA.

Novk D.; T.Al-ani; Hamam Y.; Cuesta-Frau D.; Mico P.; and Lhotsk L., 2004d. *Unsupervised Learning of Holter ECG signals using HMM optimized by simulated annealing*. In *BIOSIGNAL 2004, 17th international EURASIP conference*. Brno, Czech Republic.

Pau L.F., 1986. *Servey of expert systems for fault detection, test generation and maintenance. Expert Systems*, 3, no. 2, 100–111.

Rabiner L.R., 1989. *A Tutorial on Hidden Markov Models and Selected Application in Speech Recognition. Proc IEEE*, 77, no. 2, 267–296.

Scilab, 2006. *A free CACSD Package by INRIA: http://www-rocq.inria.fr/scilab/*. Tech. rep.

Smyth P., 1994. *Hidden Markov Models for fault detection in dynamic systems. Pattern Recognition*, 27, no. 1, 149–164.

Stephanopoulos G., 1984. *Chemical process control. An introduction to Theory and Practice*. Prentice -Hall,Inc.

Venkatasubramanian V. and Chan K., 1989. *A Neural Networks Methodology for Process Fault Diagnosis. American Institute of Chemical Engineering Journal*, 35, no. 12, 1993–2002.

Viterbi A.J., 1967. *Error bounds for convolutional codes and asymptotically optimum decoding algorithm. IEEE Trans Inform Theory*, IT-13, 260–269.

Watanabe K.; Matsuura I.; Abe M.; Kubota M.; and Himmelblau D., 1989. *Incipient Fault Diagnosis of Chemical Processes via Artificial Neural networks. American Institute of Chemical Engineering Journal*, 35, no. 11, 1803–1812.

APPENDIX

Nomenclature for the CSTR model:
c_{Af}: feed molar concentration (mol/m^3),
$c_{Ae} = c_B$: exit molar concentration (mol/m^3),
c_{Ao} nominal concentration (mol/m^3),
Cp_r: heat capacity of the reacting mixture, $(Kcal/Kg.^\circ K)$,
D: reactor diameter (m),
k_r: outside reactor valve constant $(m^{5/2}/hour)$,
k_c: outside jacket valve constant $(m^{5/2}/hour)$,
K_r: reaction rate kinetic constant $(m^3/mol.hour)$,
H_r: reaction heat $(Kcal/m^3.hour)$,
$h_r(t)$: reaction vessel height (m),
$h_{rm}(t)$: minimum reaction vessel height (m),
$h_c(t)$: jacket height (m),
h_{r0}: nominal reaction vessel height (m),
h_{c0}: nominal jacket height (m),
Q: exchange heat between reactor and jacket (Kcal/hour),
J: the relation between H_r and Cp_r,
m: mass (kg),
$\dot{m}$: massic flux $(Kg/hour)$,
ρ: density (kg/m^3),
S_r: surface of reactor vessel base (m^2),
S_c: surface of the jacket vessel base (m^2),
S_{ex}: heat exchange surface (m^2) calculated as the surface of the wall between the two vessels, reactor and jacket: $S_{ex} = \pi \times D \times h$, where h is the smallest level between the reactor tank and the jacket tank,
S_{ee}: outside surface of the jacket (m^2) calculated as: $S_{ee} = \pi \times D \times h_c$,
T_r: reactor temperature $(^\circ K)$,
T_{cf}: feed coolant (jacket) temperature $(^\circ K)$,
T_{ce}: exit coolant (jacket) temperature $(^\circ K)$,
T_{rf}: feed reactor temperature $(^\circ K)$,
T_{re}: exit reactor temperature $(^\circ K)$,
T_{r0} nominal reactor temperature $(^\circ K)$,
T_{c0} jacket temperature $(^\circ K)$,
T_a: ambient temperature, considered constant,
t: time
t_p: sampling time
t_s: stabilization time,
τ_r: residence time in the reactor vessel (hour),
τ_c: residence time in the coolant jacket (hour),
U: global heat exchange coefficient $(Kcal/hour.m^2.^\circ K)$,
v_{rf}: reactant feed volumetric flux $(m^3/hour)$,
v_{re}: reactant exit volumetric flux $(m^3/hour)$,
v_{cf}: coolant feed volumetric flux $(m^3/hour)$,
v_{ce}: coolant exit volumetric flux $(m^3/hour)$,
V_r: reactor volume (m^3),
V_c: jacket volume (m^3).
Subscripts:
c: in coolant, r: in reactor, e: exit, f: feed, i: component i, 0: nominal conditions, d: fault conditions and t: discret time index.

Nomenclature for HMMs:
π_i: initial probability of state i, $1 \leq i \leq N$
$q_t = i$: state at time t
a_{ij}: state transition probability from state i to state j,
O : sequence of observations $(\mathbf{O}_t)$ (scalars or vectors of dimension K),
$b_j(\mathbf{O}_t)$: observation probability distribution in state j.

AUTHOR LISTING

AUTHOR LISTING